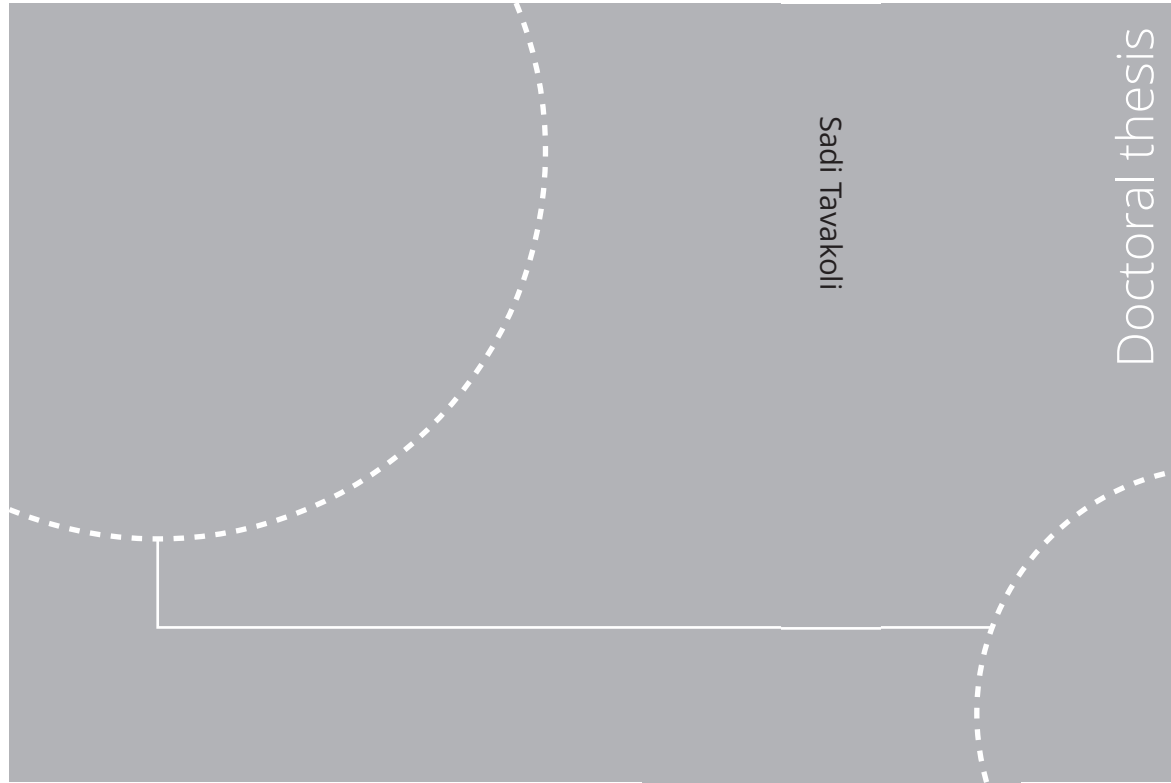


ISBN 978-82-326-5665-3 (printed ver.)
ISBN 978-82-326-6664-5 (electronic ver.)
ISSN 1503-8181 (printed ver.)
ISSN 2703-8084 (electronic ver.)



Doctoral theses at NTNU, 2021:261

Sadi Tavakoli

Ship Propulsion Dynamics and Emissions

Gas Engine Methane Slip Reduction at Dynamic Loads

Doctoral theses at NTNU, 2021:261

NTNU
Norwegian University of
Science and Technology
Thesis for the degree of
Philosophiae Doctor
Faculty of Engineering
Department of Marine Technology

 **NTNU**
Norwegian University of
Science and Technology

 NTNU

 **NTNU**
Norwegian University of
Science and Technology

 **DTU** Technical University
of Denmark

Sadi Tavakoli

Ship Propulsion Dynamics and Emissions

Gas Engine Methane Slip Reduction at Dynamic Loads

Thesis for the degree of Philosophiae Doctor

Trondheim, "August" "2021"

Norwegian University of Science and Technology
Faculty of Engineering
Department of Marine Technology

Technical University of Denmark
Department of Mechanical Engineering



NTNU

Norwegian University of Science and Technology

Thesis for the degree of Philosophiae Doctor

Faculty of Engineering
Department of Marine Technology

© Sadi Tavakoli

ISBN 978-82-326-5665-3 (printed ver.)
ISBN 978-82-326-6664-5 (electronic ver.)
ISSN 1503-8181 (printed ver.)
ISSN 2703-8084 (electronic ver.)

Doctoral theses at NTNU, 2021:261



Printed by Skipnes Kommunikasjon AS

Abstract

Continuous discharging of greenhouse gases into the atmosphere has motivated researchers to develop prime movers for working with less polluted energy sources. The low cost of natural gas relative to diesel and gasoline combined with various emissions-related regulatory measures drew attention toward natural gas as an alternative fuel for internal combustion engines.

Natural gas fuel utilization is regarded as the right choice due to its low-carbon emission, lower NO_x , and almost zero smoke and particulate matter. Among several categorizations of the natural gas engine, including stoichiometric Otto cycle, lean burn, and dual fuel, there is a particular interest in lean burn gas engines where the excess air ratio is almost two, and the emission target is achievable without applying an after-treatment system.

However, there are also several challenges with lean combustion. The knock phenomenon limits the engine performance in high loads and rich mixture, and in contrast, misfires occur when the mixture is too lean. Working in a narrow operating area with high-efficiency combustion requires sufficient stability and control of the engine.

For an engine encountering a time-varying load in a marine application, load on the engine continuously varies in either a fixed or a variable frequency. Depending on the magnitude of load fluctuation, the response of the engine changes. Moreover, despite the low emission level provided by a lean burn natural gas engine, the lean mixture combustion suffers from high methane slip.

This study developed a model for a spark-ignition engine that uses natural gas as the fuel and is applicable for the marine sector. The work in this thesis investigates the effect of sea state on ship propulsion systems.

Accordingly, the thesis consists of four major parts. First, the influence of time-varying load on the lean burn gas engine is discussed, and the response of the engine and the importance of methane slip sources are presented. Second, engine-propeller interaction has been studied in a range of wave characteristics, and the engine response has been discussed in all sea states for the specific vessel. Third, considering methane slip as the main issue of lean burn gas engines, several controlling methods have been performed to overcome the methane slip increase during transient conditions. Furthermore, the part-load operation of the engine has been modeled by a non-harmonic transient condition in almost one hour of the vessel journey.

Preface

This thesis is submitted in partial fulfillment of the requirements for the Ph.D. degree. The Ph.D. candidate is under the Double Doctorate Degree agreement between the Norwegian University of Science and Technology (NTNU) and the Technical University of Denmark (DTU). The work has been mostly performed at the department of marine technology, NTNU, Trondheim, with Professor Eilif Pedersen as the main supervisor and partly at the department of mechanical engineering, DTU, Copenhagen, with Professor Jesper Schramm as the co-supervisor.

The Ph.D. project was part of the joint project “Ship propulsion dynamics and emissions”, and it was based on collaboration between the Norwegian University of Science and Technology and the Technical University of Denmark. The joint project required the integration of two disciplines: marine machinery and marine hydrodynamics. Thus, the current Ph.D. student actively cooperated with another Ph.D. student, Simone Saettone, during the research study. The collaboration was necessary to investigate the dynamic interaction between the engine and propeller loads of a ship.

This thesis is divided into two parts: the main thesis, which comprises six chapters, and a compilation of papers. The first part of the thesis will provide the context of the research with regard to the backgrounds, the research questions, methods, and the main results, while the second part includes the publications.

Acknowledgments

First of all, I would like to express my special appreciation and thanks to my advisor Professor Eilif Pedersen for being an excellent supervisor. I would like to thank you for encouraging my research and allowing me to grow as a research scientist. I have enjoyed all our discussions, which were always productive and informative.

Besides, I would like to thank Professor Jesper Schramm for the inspiring guidance, insightful comments, and encouragement. He spent lots of time reading my reports and improved my research with his worthwhile comments.

My sincere thanks also go to Professor Sverre Steen and Professor Poul Andersen for all their supports.

I would especially like to thank my friends, Simone Saettone and Michael Vincent Jensen, for their successful collaboration, which helped me extend the boundary of my research.

I very much appreciate the advises and supports I received from Assoc. Prof. Amir Nejad and Isar Ghamari, particularly during the first months of this journey.

I would also like to thank my friends and Ph.D. colleagues ShuaiShuai Wang, Farid Moghadam, Chana Sinsabvarodom, Kamyar Maleki, and Espen Krogh for making a pleasant working environment.

Words can not express how grateful I am to my parents for all of the sacrifices that they have made on my behalf. I wish to express my deepest gratitude to my sister and brothers for their support and for always being there for me as friends.

Last but not least, my most heartfelt thanks to my wife, Fariba. She has always been faithful, supportive, and compassionate. I owe a great debt to her in this long journey, and I am so happy that we can celebrate the end of this work together.

Contents

Contents	ix
List of Tables	xi
List of Figures	xvi
1 Introduction	1
1.1 LNG propulsion systems	4
1.2 Background and motivation	6
1.3 Objectives of the thesis	8
1.4 Publications	9
1.5 Thesis outline	12
2 Natural Gas Engine	13
2.1 Natural gas engines	13
2.1.1 Stoichiometric combustion	13
2.1.2 Homogeneous charge compression ignition	15
2.1.3 High pressure direct injection	15
2.1.4 Lean burn combustion	15

2.2	Natural gas plus an additive	16
2.2.1	Dual-fuel natural gas engines	16
2.2.2	Reactivity controlled compression ignition	17
2.3	Marine gas engines	17
2.4	Installation modes	17
2.5	Vessel and engine specification	19
3	Modeling and Simulation	23
3.1	Steady-state vs. transient condition	25
3.2	Main components in the modeling	26
3.2.1	Combustion chamber	26
3.2.2	Power transmission	33
3.2.3	Controlling system	34
3.2.4	Intake and exhaust manifold	35
3.2.5	Intake and exhaust valves	36
3.2.6	Intercooler	37
3.2.7	Turbocharger	38
3.2.8	Boundary condition of inlet and outlet	39
3.3	Establishment of engine simulation	39
3.4	Co-simulation	40
4	Unburned Hydrocarbon Formation	43
4.1	Engines in relation to UHC emission	44
4.2	Available technologies for methane slip reduction	47
4.3	Methane slip modeling	48
4.3.1	Model 1	49
4.3.2	Model 2	51

5	Results and Discussion	57
5.1	Research objective 1 (Paper 1 and Paper 4)	57
5.2	Research objective 2 (Paper 2 and Paper 3)	61
5.3	Research objective 3 (Paper 4, Paper 5 and Paper 7)	64
5.4	Research objective 4 (Paper 6)	75
6	Conclusion and Recommendations	81
6.1	Summary and conclusions	81
6.2	Recommendations for future work	83
A	Appended Papers	105
B	List of previous PhD theses at Dept. of Marine Tech	217

List of Tables

1.1	Properties of alternative fuels for marine engines [1].	3
1.2	Emission reduction percentage of two-stroke and four-stroke NG-engines [2].	4
2.1	Engine specification.	21
2.2	Vessel specification.	21
5.1	Periodic waves characteristics	61
5.2	Performance and emission of the engine after applying the UHC reduction methods.	71
5.3	Performance and emission of the engine after retarding the spark ignition timing.	72

List of Figures

1.1	Natural gas storage for internal combustion engines in the transportation system.	4
1.2	Increase in the total number of LNG carriers due to more demand on using natural gas engines [3].	5
1.3	Percentage of the gross tonnage of the newbuildings LNG fleet [4]. A sharp increase occurred after 2012, from 2% to almost 14%.	5
1.4	The ideal operating area of lean burn gas engines [5].	6
1.5	Interconnection between the papers and the objectives of the PhD project.	11
1.6	An intuitive overview of the current work. The numbers in parentheses refer to the relevant paper.	12
2.1	All types of available natural gas engines.	14
2.2	Stoichiometric combustion process. a is $(X + Y/4)$	14
2.3	Marine gas engines classification [6].	18
2.4	Marine gas engines in the shipping industry [7]. Lean burn gas engines and dual-fuel high-pressure four-stroke engines have the most considerable contribution by around 90%.	18
2.5	Marine gas engines propulsion mode.	20

3.1	Engine modeling complexity from minimum fidelity and computation time (down) to maximum (top) [8].	25
3.2	Temperature zones of the cylinder head and piston top surface. . .	28
3.3	The instantaneous indicated torque is a function of pressure in each crank angle and the in-cylinder surface area.	34
3.4	PID controller block diagram. Three parameters (K_p , K_i , and K_d) can be manually or automatically tuned based on the setpoint and output.	35
3.5	The intake and exhaust valves lift in an engine cycle. The values are normalized to be fitted in the maximum amount of one.	37
3.6	Engine modeling schematic. All essential elements influential on flow and dynamic are implemented in the engine model using two-zone zero-dimensional modeling for the combustion, one dimensional for pipes and connections, and a look-up table for the turbocharger.	39
3.7	Comparison of measured data and engine simulation in steady-state. The X-axis shows the load percentage, and the Y-axis gives the measured-modeled output. The results are normalized by the measured value in 100% load.	40
3.8	Comparison of measured data and engine simulation in transient conditions. The X-axis shows the time, and Y-axis shows the measured-modeled output.	41
3.9	Propulsion system modeling in a co-simulation platform developed in MathWorks Simulink.	42
4.1	Methane reaction pathway diagram at high combustion temperature. A temperature lower than 1500 K results in CO and CH_2 formation as well. The detailed reaction and reaction rate is presented in [9].	44
4.2	Flow chart mechanism of unburned hydrocarbon formation for a typical gasoline engine in steady-state [10].	47
4.3	Post-combustion zones. The burned and unburned mixtures are combined into a single mixture. The crevice volume is assumed to be constant. Gas exchange only occurs when both of the valves are open.	49

4.4	Connecting the engine model to Model 2 for determining UHC source contribution.	52
5.1	Regular harmonic, sinusoidal torques around the full load.	58
5.2	Increase of methane slip with load fluctuation.	58
5.3	Methane slip source contribution during load fluctuation.	59
5.4	Quenched flame has the most variation during time-varying load.	60
5.5	Variation of excess air ratio due to engine response delay during propeller load fluctuation.	60
5.6	A medium harmonic torque. The mean value is 70% nominal torque at 750 rpm.	61
5.7	The sources of UHC. The UHC percentage of crevice volume and quenched flame are contrasted during the time, while part of the variation on crevice contribution is due to remarkable change of quenched flame source.	62
5.8	The calculated torque by the propeller modeling, which is an input to the engine model.	63
5.9	The contour representation of the mean values of the model output with various wave characteristics.	65
5.10	The imposed torque for investigation of turbocharger shaft moment of inertia on engine response.	66
5.11	Increasing the mass moment of inertia from Lag 1 to Lag 6 with Base as the inertia of the original shaft has negligible influence on methane slip.	66
5.12	Total NO _x value is higher with a higher mass moment of inertia due to the slower response of the turbocharger.	66
5.13	Schematic of two of the controlling methods.	69
5.14	Spark ignition timing for promoting flame propagation and reducing the UHC formation. The red section shows the spark timing as a function of excess air ratio, and the blue section shows the distance to the top dead center.	71

5.15	A new set of spark ignition timing for reducing NO _x . The timing is imposed based on the air-fuel ratio between 28 to 34 (to cover all lambda variation between 1.6 to 2.0).	72
5.16	The implemented steady loading and a severe transient torque for comparing the response of the engine with and without a throttle during the lower loads.	73
5.17	The influence of the air throttle in both steady-state and transient conditions.	73
5.18	Hybrid propulsion system configuration.	74
5.19	Smoothed load using a hybrid configuration.	75
5.20	The amount of unburned hydrocarbon reduced considerably with the hybrid propulsion concept.	75
5.21	Notable reduction of NO _x during load increase with the hybrid implementation.	76
5.22	The frequency of occurrence of the torque percentage of the vessel.	77
5.23	Target torque and speed based on the real imposed data of the ship.	78
5.24	UHC formation during the real operational condition in sea state.	78
5.25	NO _x compound during the real operational condition in sea state.	78
5.26	Average values of UHC- A comparison of steady-state and transient conditions. There is a big gap between the two states during the lower load operation.	79
5.27	Average values of NO _x - A comparison of steady-state and transient conditions.	79

List of Abbreviations

BDC	bottom dead center
BMEP	brake mean effective pressure
BOG	boil-off gas
BSFC	brake specific fuel consumption
BTDC	before top dead center
C ₂ H ₆	ethane
C ₃ H ₈	propane
CFD	computational fluid dynamics
CH ₄	methane
CNG	compressed natural gas
CO	carbon monoxide
CO ₂	carbon dioxides
CPU	central processing unit
DI	direct injection
DOC	diesel oxidation catalyst
DPF	diesel particulate filter
EGR	exhaust gas recirculation

ESD	energy storage device
f MEP	friction mean effective pressure
FPSO	floating production storage and offloading
GHG	greenhouse gases
GWP	global warming potential
H ₂ O	water
HC	hydrocarbon
HCCI	homogeneous charge compression ignition
HFO	heavy fuel oil
HIL	hardware-in-the-loop
HPDI	high pressure direct injection
IC	internal combustion
IFO	intermediate fuel oil
IMO	international maritime organization
LNG	liquefied natural gas
MDO	marine diesel oil
MGO	marine gas oil
MPC	model predictive control
MV	manipulated variable
NO _x	nitrogen oxides
OHC	oxygenated hydrocarbon
PID	proportional-integral-derivative
PM	particulate matter
PSC	partially stratified charge
PTI	power take in

PTO	power take off
RCCI	reactivity controlled compression ignition
SCR	selective catalytic reduction
SI	spark ignition
SO _x	sulfur oxides
TDC	top dead center
TWC	three-way catalyst
WHO	world health organization

Chapter 1

Introduction

Internal combustion (IC) engines are almost the primary driver of all the road transports and a substantial majority of the off-road services [11]. The history of converting the fuel chemical energy into mechanical rotating work in IC engines with commercial success traces back to the 19th century when Lenior [12] developed the engine to burn a mixture of coal gas and air in two directions without compression stroke. Later, in 1864, Nicolaus Otto [13] patented the first atmospheric gas engine, which is very similar to the recent reciprocating piston engines. Almost a century after the appearance of the first vehicles, the link between air pollution and IC engines was recognized, and after verifying the link between health and air pollution, the air pollution standards began with Clean Air Act in 1970 [14]. Until 2016, based on a report by the World Health Organization (WHO), the number of registered vehicles increased to 281 million in the United States and 3.9 million in Norway [15, 16].

The utilization of IC engines is not limited to transport vehicles, but refers to ships, airplanes, and trains as well. Due to the increase of global scale trade and advantages of carrying capacity, over 80% of global trade by volume and more than 70% of its value was carried by a total of 93161 commercial fleet throughout the world in 2017 [4]. This weight on transport places the shipping industry as a significant source of emission, where 15% of global anthropogenic NO_x and 5-8% of global SO_x emissions are owing to the maritime ships [17, 18]. The marine sector mostly uses heavy fuel oil (HFO) rather than marine gas oil (MGO), marine diesel oil (MDO), and intermediate fuel oil (IFO). HFO fuel is a high-viscosity residual oil, and due to the low quality grade, is one of the main causes of high emission level in maritime transport [19].

Therefore, the national and international standards came into force to restrict the pollution sources. SO_x emissions from ships first came into force in 2005, under Annex VI [20], and the limits on this compound have been progressively tightened from the previous limit of 3.50% to 0.50% m/m (mass by mass) in January 2020 for the ships operating outside designated emission control areas. Moreover, the International Maritime Organization (IMO) applied a maximum specified NO_x in various regulations. For instance, a medium-speed diesel engine was limited to produce almost 20% of NO_x in 2016 by Tier III compared with 1st of January 2000 by Tier I [21]. International efforts such as the Paris agreement in addressing greenhouse gases (GHG) emissions will contribute to carbon intensity reduction of over 70% in 2050 compared with 2008 [22, 23].

The desired emission levels in ship transportation are achievable by either employing the latest technologies or using alternative fuels.

A catalytic converter, an exhaust emission control device to convert the emissions, mitigates carbon monoxide, hydrocarbon, nitrogen oxides, and particulate matter (PM) compounds [24]. But, the reduction of emissions using the aftertreatment systems is still a major challenge. Diesel oxidation catalyst (DOC), diesel particulate filter (DPF) and selective catalytic reduction (SCR) are usually associated with the fuel quality, exhaust temperature, and the engine application plus an expensive service and replacing necessity [25–28].

Exhaust gas recirculation (EGR) is another NO_x emission reduction technology that recirculates a fraction of exhaust gas to the combustion chamber. The addition of EGR either with an internal or external circuit increases the mixture heat capacity and consequently reduces the flame temperature. Moreover, the decline in the NO_x by EGR rates ends with an unsatisfactory reduced thermal efficiency, higher PM emissions, and a brake specific fuel consumption (BSFC) footprint [29].

Adding water into the combustion chamber influences NO_x emission in exhaust gas due to thermal, dilution, and chemical effects by decreasing the concentration of atomic oxygen. Injection of the water directly into the hot compressed air at the outlet of the turbocharger, increasing the humidity of the charge air, direct water injection, water-cooled residual gas, and fuel–water emulsion injection are applicable methods for including water in the flame propagation [30]. Cost, effectiveness and risk of water drops are the main challenges for each specific method.

Regarding the alternative fuels to achieve the emission goals, the properties of alternatives fuels are listed in Table 1.1. MGO and MDO are alternative fuels of HFO [31]. However, these fuels cost more compared to HFO with a cost of refinery

change [32], and they also produce more carbon dioxides (CO_2) [33]. Biodiesel with a positive impact on the environment can partly replace fossil fuels due to the main drawbacks of limited raw materials and high production costs. In addition, the IMO study concluded that low blends of biodiesel of up to 20% (B20) could be used without any fuel system adjustments [34]. Methanol is an oxygenated and sulfur-free fuel, but engine modification, including injection systems, fuel tanks and piping is required for use in a marine diesel engine [1]. Natural gas with relatively little processing after the refinery is becoming an essential alternative for conventional fossil fuels. Moreover, natural gas has an octane number of approximately 120. This specification gives methane a high resistance to knocking in combustion [35, 36], although the natural gas composition varies considerably over time and location [37]. Thus, utilizing natural gas is one of the effective ways in terms of high-efficiency combustion with the potential of emission reduction [38, 39]. The utilization of natural gas gives emissions reduction up to 85% on NO_x , 30% on CO_2 , and 95% on carbon monoxide (CO). Smoke and PM of this fuel are also around zero [40].

Table 1.1: Properties of alternative fuels for marine engines [1].

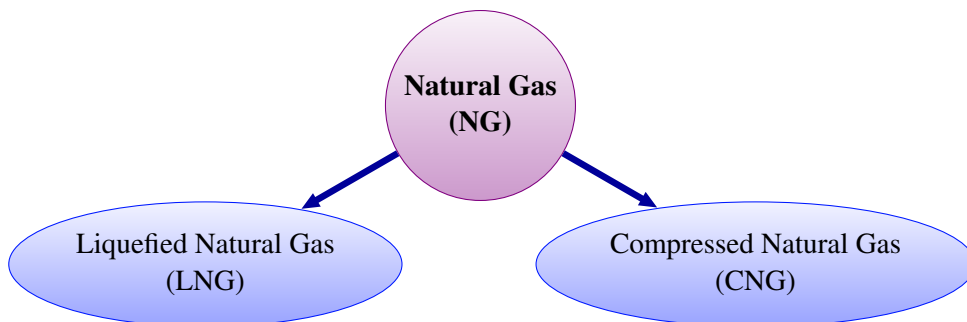
Property	Unit	Diesel	HFO	MDO	Biodiesel	Methanol	Natural gas
Calorific value	MJ/kg	42.5	41.26	42	37.5	20.26	50
Cetane number	-	51	>20	>35	50	3	-
Density at 15 °C	kg/m ³	847	934.8	<900	890	795	0.7-0.9
Viscosity at 40 °C	mm ² /s	2.72	24.27	<11	4-6	0.58	-
Ash content	%	<0.01	0.042	<0.01	-	-	-
Sulphur	ppm	<350	<500000	<200000	<10	-	-

Global warming potential (GWP) for different time horizons expressed relative to CO_2 shows that the GWP 20 years and GWP 100 years of methane is 72 and 25, respectively [41]. This high GWP factor of methane reduces the GHG-emission reduction potentials of a natural gas engine. Table 1.2 shows the emission reduction potentials for the two types of the natural gas engine. The CO_2 emissions are presented as CO_2 equivalents where methane slip is accounted for. Natural gas engines have the potential to contribute significantly, apart from the notable benefits in terms of air quality for lean burn combustion engines, to the GHG reduction target. However, methane slip must be reduced to the lowest level to enhance the benefits.

Moreover, due to the low density of natural gas, for use in internal combustion engines, natural gas ought to be stored either as compressed natural gas (CNG) or be cooled down to liquid form in non-pressurized storage, Fig. 1.1. CNG occupies

Table 1.2: Emission reduction percentage of two-stroke and four-stroke NG-engines [2].

Engine type	CO ₂ equivalent	NO _x	PM	SO _x
4-stroke low-pressure	5	90	98	100
2-stroke high-pressure	20	90 (with NO _x reduction measures)	98	100

**Figure 1.1:** Natural gas storage for internal combustion engines in the transportation system.

less than 1% of the volume at standard atmospheric pressure with a 200-250 bar in cylindrical shapes metallic cylinder [42]. However, weight, cost, and safety factors strongly favored liquefied natural gas (LNG) for marine application [43].

1.1 LNG propulsion systems

Boil-off gas (BOG) from LNG cargo appeared first on the LNG-fuelled ships in 1964 [43], and the first gas-fuelled ship using CNG on the coast of Norway was launched in 2000 [44]. The total number of LNG carriers exceeded 500 by 2020 in the world, as shown in Fig. 1.2. By 2016, more than 50% of gas fuelled ships were working in the Norwegian sea [45]. Moreover, the gross tonnage of the newbuildings has shown a sharp increase in recent years, as shown in Fig. 1.3. The gross tons percentage of liquefied natural gas-capable was approximately steady at around 2% from 2002 to 2013. It rose to 5.8 % in 2014 and stayed almost constant for the next three years. The trend becomes noticeable after 2016, with more than 13% of the gross tonnage. The gross tonnage of 2017 was delivered by over 325 liquefied natural gas-capable vessels, while 110 liquefied natural gas-capable ships were on order.

Combustion of natural gas for marine applications supports three concepts [3, 46]:

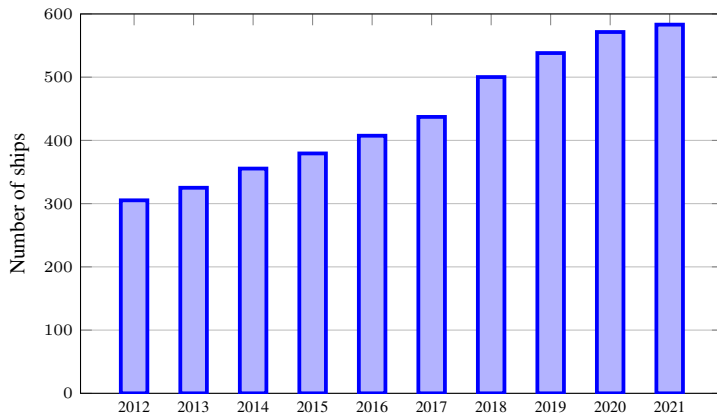


Figure 1.2: Increase in the total number of LNG carriers due to more demand on using natural gas engines [3].

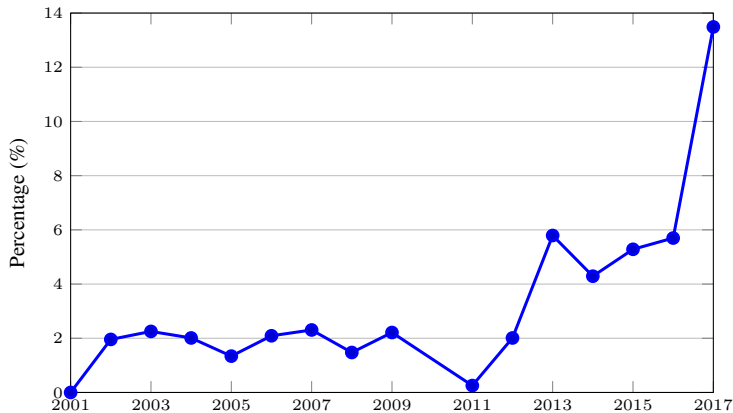


Figure 1.3: Percentage of the gross tonnage of the newbuildings LNG fleet [4]. A sharp increase occurred after 2012, from 2% to almost 14%.

1. High-pressure dual-fuel engines
2. Low-pressure dual-fuel engines
3. Lean burn spark-ignition engines

Lean burn engines and low-pressure dual-fuel engines have, by far, the most substantial contribution of the operational cases [7], where low-pressure dual-fuel engines can hardly meet the mandatory emission standards (Euro V, Euro VI) with the present available technology. The dual-fuel engine uses both conventional diesel and gaseous fuels. The low running costs and use of alternative fuel

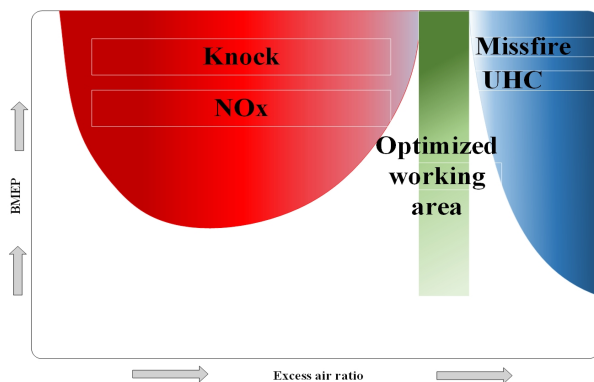


Figure 1.4: The ideal operating area of lean burn gas engines [5].

contributed this engine to be applicable in various applications [47, 48]. The drawback of this engine is releasing total emissions of GHG higher than diesel engines [49]. It also suffers from increases in CO and hydrocarbon HC emissions. In addition, due to operating unthrottled, the fuel efficiency is lower at light load and the mixture becomes very lean when the load reduces [50].

Lean burn spark-ignition gas engines with an excess air ratio of $\lambda = 2$ reduce the thermal load and the level of NO_x emission to meet Euro V/EEV emission requirements without an additional after-treatment system [51, 52]. However, as shown in Fig. 1.4, there is a narrow area that the engine works with the optimized excess air ratio with high thermal efficiency. The widened operating area is restricted to the low brake mean effective pressure (BMEP), which gives a lower combustion efficiency. With a high BMEP, the variation of air-fuel ratio drives the engine on either misfire or knock phenomenon, especially when the load varies continuously in ship propulsion.

1.2 Background and motivation

Current emissions legislation in the marine sector has led the manufacturers to place the lean burn natural gas engines into the application. Traditionally this type of engine is considered mainly in a stationary condition and for power plants [53–55]. In a stationary condition, the power is expected to maintain within limited loads. Voltage and frequency are generally restricted within predefined quantities, and the engine or parallel engines must bear the load steps without stalling. Therefore, keeping the engine in the optimized area is more accessible. In the presence of the waves in the marine propulsion system, the engines are exposed to considerable varying loads due to rolling or windmilling, whereas they must operate close to their nominal propeller curve. The oscillated load is a continuously

varying load with various frequencies and amplitude. This variation of load plays a dominant role in engine response. The transient response behavior of an engine is commonly described by the ability to cope with a sudden increase in load [56,57].

Moreover, the elements of ship propulsion include the ship hull, the propeller, and the engine. The traditional way was to consider these three elements separately. A real ship operates in waves that induce motions, give a time-varying inflow, and load on the propeller that again interacts with the engine. In severe weather conditions, the propeller might even entirely out of the water and cause a sudden drop in the engine torque and result in over-speed on the engine.

Modeling of a ship travel at sea with the wave and wind resistance using a co-simulation for a two-stroke diesel engine and the propeller was performed by Yum et al. [58]. The study aimed to find the dynamic load effect compared to a constant load and confirm a quasi-steady mapping method to estimate efficiency and NO_x emissions. The simulation of the propulsion system performance by Kyrtatos [59] indicated the influence of components on the ship hydrodynamic performance. The detailed implementation of the engine elements coupled to the propulsion systems proved that the fuel limiters change the vessel speed and the ship developed forces. Campora and Figari [60] tried to find a reliable prediction of the ship system behavior in transient conditions to optimize the propulsion system components choice in such conditions. Neilson and Taret [61] simulated a marine propulsion system to support the design process, including machinery performance analyses, vibration analyses, maneuvering, and sea-keeping analyses. Taskar et al. [62] discussed the influential parameters on a wave in a ship trip and identified the propulsion performance drop. Altosole et al. [63] showed the need to use marine propulsion simulator in real-time for control system design and training the diesel engine dynamics with low computation time. The methodology proposed was based on 5-D matrices to predict engine behavior. Moctar et al. [64] performed maneuvering motions in a simulation of the engine propeller model, test scale model, and real scale measurement. The model output illustrated the impact of engine dynamics on the entire system and the engine time delay due to the response time.

Converting the traditional engines to spark ignition natural gas in lean mixture demands studying the marine gas propulsion system in transient conditions, particularly in harsh weather conditions. It is paramount to understand how the different condition affects the performance, efficiency, and emissions of a lean burn gas engine in the marine propulsion system [65–67].

Therefore, this project designated a lean burn gas engine performance, i.e., the dynamic response, fuel consumption, and emission, resulting from oscillating

propeller loads due to the waves. A particular interest is to examine how the methane slip changes during such fluctuating loads. Presenting practical solutions to stabilize the engine, optimizing the combustion by the latest available controllers, and smoothing the imposed torque are further goals of this study.

1.3 Objectives of the thesis

This thesis has been motivated by an interest in spark-ignition gas engines, which are becoming one of the most critical contributors to marine propulsion systems in the early future. However, they were lacked attention from emission aspects, especially the methane slip is not yet investigated during the transient sea conditions. To draw an ideal conclusion of the impact of the transient conditions on the lean burn gas engine response and particularly the amount of the methane slip, full-scale experiments with sufficient instruments are needed. Moreover, the unsolvable challenge is determining the sources of methane slip while there is a time delay in measuring the methane slip during the rapid transient conditions [68]. To cope with these issues and recognize the methane slip primary sources, developing numerical methods has been ideal for reducing the project risk and cost and providing a clear methane slip trend.

Different possible sources for methane slip in the internal combustion engine are proposed [69–71], where the three main sources of methane slip for the lean burn gas engine are gas exchange, crevice volume, and quenched flame [72, 73]. They are the primary sources in steady-state, but what if the load suddenly changes. Does the percentage of the load variation influence the amount of methane slip? On this basis, the following research objective can be formulated:

- **Research objective 1**

What are the primary sources of methane slip in lean burn spark-ignition engines, especially during transient conditions?

The lean burn gas engine load fluctuation is caused by external disturbance represented by the propeller torque in waves [74]. The disturbance is the wavelengths, wave heights, and wave directions. In order to evaluate the fluctuations, a coupled modeling of engine-propeller is needed. This idea is the basis for the second objective of the project:

- **Research objective 2**

What is the influence of wave characteristics on transient loads and marine gas engine response in terms of combustion efficiency and emissions?

The operating of spark-ignition engines on a lean mixture has several positive features such as improvement of combustion efficiency and reducing the fuel consumption [75,], but the engine response may suffer from instability [77, 78] and even misfire [79]. To offset the disadvantages of the lean mixture, improving the engine stability gets even more attractive, and becomes our third research objective:

- **Research objective 3**

How to stabilize the engine during transient conditions and improve the combustion?

The maximum efficiency occurs around the full load, and there is a decrease in engine efficiency during part-load operating. This reduction for SI engines normally occurs due to an increase in pumping loss and throttle closure [80, 81]. Emission rise due to the incomplete flame propagation of lean mixture [82, 83] provided our third research objective as follow:

- **Research objective 4**

How is the engine response concerning sea transient conditions in part-loads?

Answering these questions has constructed the main goals and scope of this research. As a consequence, nine journals and conference papers are published.

1.4 Publications

The following publications constitute a part of the thesis:

1. **Authors:** Tavakoli S., Jensen M. V., Pedersen E., Schramm J., **Title:** Unburned Hydrocarbon Formation in a Natural Gas Engine Under Sea Wave Load Conditions. **Journal:** Marine Science and Technology. **Editor:** Springer. **Year:** 2020. **Status:** Published. **Type:** Journal Paper. <https://doi.org/10.1007/s00773-020-00726-5>.
2. **Authors:** Saettone S., Tavakoli S., Taskar B., Jensen M. V., Pedersen E., Schramm J., Steen S., and Andersen P. **Title:** The importance of the engine-propeller model accuracy on the performance prediction of a marine propulsion system in the presence of waves. **Journal:** Applied Ocean Research. **Editor:** Elsevier. **Year:** 2020. **Status:** Published. **Type:** Journal Paper. <https://doi.org/10.1016/j.apor.2020.102320>.

3. **Authors:** Tavakoli S., Saettone S., Steen S., Andersen P., Schramm J., and Pedersen E. **Title:** Modeling and Analysis of Performance and Emissions of Marine Lean-Burn Natural Gas Engine Propulsion in Waves. **Journal:** Applied Energy. **Editor:** Elsevier. **Year:** 2020. **Status:** Published. **Type:** Journal Paper. <https://doi.org/10.1016/j.apenergy.2020.115904>.
4. **Authors:** Tavakoli S., Schramm J., and Pedersen E. **Title:** Strategies on Methane Slip Mitigation of Spark Ignition Natural Gas Engine During Transient Motion. **Journal:** SAE Automotive Technical Papers. **Editor:** SAE. **Year:** 2021. **Status:** Published. **Type:** Journal Paper. DOI:<https://doi.org/10.4271/2021-01-5062>.
5. **Authors:** Tavakoli S., Schramm J., and Pedersen E. **Title:** Influence of Turbocharger Inertia and Air Throttle on Marine Gas Engine Response. **Journal:** Journal of Fluid Flow, Heat and Mass Transfer (JFFHMT). **Editor:** AVESTIA. **Year:** 2021. **Status:** Published. **Type:** Journal Paper. DOI: [10.11159/jffhmt.2021.013](https://doi.org/10.11159/jffhmt.2021.013).
6. **Authors:** Tavakoli S., Schramm J., and Pedersen E. **Title:** Effects of Propeller Load Fluctuation on Performance and Emission of a Lean-Burn Natural Gas Engine Operating at Part-Load Condition. **Status:** Under revision. **Type:** Journal Paper.
7. **Authors:** Tavakoli S., Maleki K., Schramm J., and Pedersen E. **Title:** Emission Reduction of Marine Lean-Burn Gas Engine Employing a Hybrid Propulsion Concept. **Journal:** International Journal of Engine Research. **Editor:** SAGE. **Year:** 2021. **Status:** Published. **Type:** Journal Paper. <https://doi.org/10.1177/14680874211016398>

The work conducted during the Ph.D. also resulted in the following papers:

- **Authors:** Tavakoli S., Pedersen E., and Schramm J. **Title:** Natural Gas Engine Thermodynamic Modeling Concerning Offshore Dynamic Condition. **Book:** Proceedings of the 14th International Symposium, PRADS 2019, September 22-26, 2019, Yokohama, Japan- Volume II. **Status:** Published. **Type:** Conference Paper.
- **Authors:** Tavakoli S., Schramm J., and Pedersen E. **Title:** The Effect of Air Throttle on Performance and Emission Characteristics of an LNG Fuelled Lean Burn SI Engine in Steady and Unsteady Conditions. **Book:** In Proceedings of the 5th World Congress on Momentum, Heat and Mass Transfer (MHMT'20). **Year:** 2020. **Status:** Published. **Type:** Conference Paper

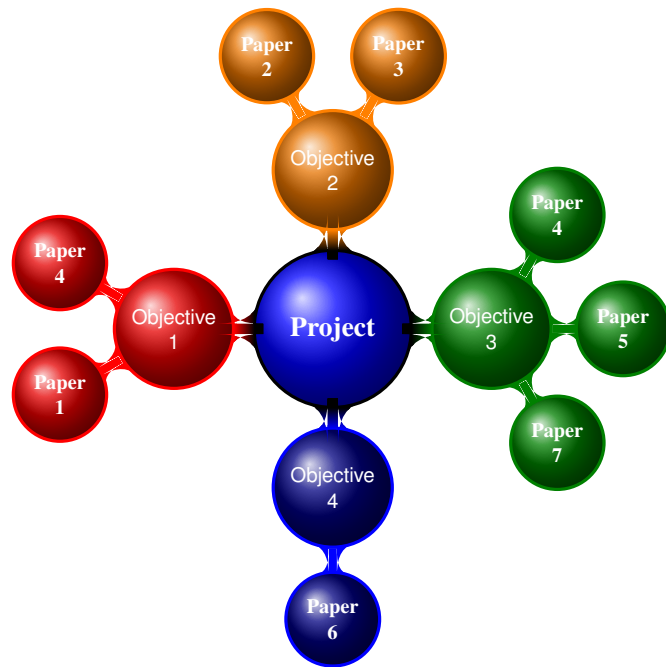


Figure 1.5: Interconnection between the papers and the objectives of the PhD project.

The interconnection between the papers and the objectives of the Ph.D. project is presented in Fig. 1.5. The author tries to address all the knowledge required in each objective and the relevance of the published papers to the four main objectives.

Furthermore, the output of the current work is arranged in an intuitive diagram shown in Fig. 1.6. The starting point was developing an engine model platform. Next, the implemented equations were confirmed by using available measured data. The verified model was the original configuration of all the investigations in this study. Based on the imposed torque, two separate paths were considered: transient condition around the full load and transient condition around the part-load. The full load concept is presented in papers number 1, 2, 3, 4, 5, and 7 with harmonic sinusoidal torque. The part-load concept is only presented in paper number 6, where the modeling is for an actual transient condition. In the full load concept, papers 2 and 3 have experienced a wide range of waves, while papers number 1 and 4 presented an additional coupled emission model for methane slip. Strategies for controlling combustion and improving the engine response are presented in papers number 4, 5 and 7.

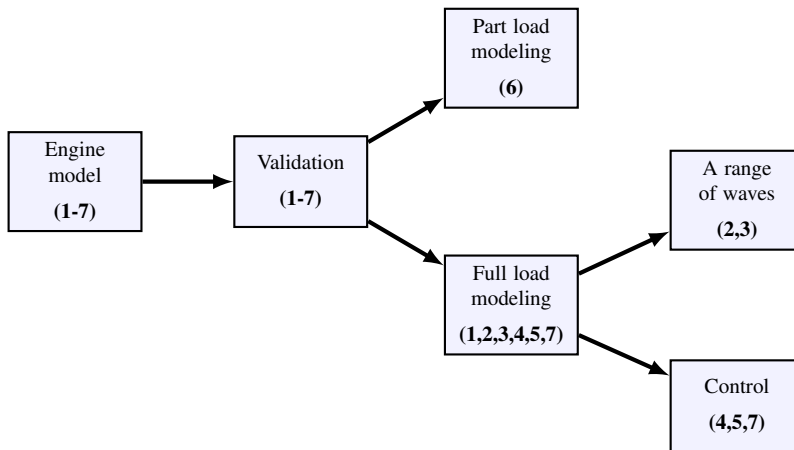


Figure 1.6: An intuitive overview of the current work. The numbers in parentheses refer to the relevant paper.

1.5 Thesis outline

This thesis is divided into two parts. The first part is the main body of the thesis, which comprises six chapters:

1. Introduction
2. Natural gas engine
3. Modeling and simulation
4. Unburned hydrocarbon formation
5. Results and discussion
6. Conclusion

In the first chapter, the motivation of the work and the research objectives are presented with the main questions. The second chapter introduces natural gas combustion in several applications with a specific focus on marine application. The third chapter develops the models of the engine and introduces the co-simulation. The fourth chapter identifies methane slip modeling, and all the results are discussed in chapter five. The last chapter of the first part concludes the main results and recommends suggestions for further works.

The second part contains the selected publications that are the main results of the thesis.

Chapter 2

Natural Gas Engine

Natural gas is a fossil energy source that formed deep beneath the earth surface consisting primarily of methane (CH_4) and ethane (C_2H_6), with also propane (C_3H_8) [84], and was first identified in America in 1626 [85]. The utilization of CNG for vehicle application in Europe traces back to early 1930 in Italy [86]. The report by BP Statistical Review of World Energy [87] shows that the consumption of natural gas in the world global energy consumption has the highest growth among all fuels in recent years with a 43% increase. Furthermore, the number of vehicles using natural gas as the main fuel has shown a rapid increase in the world [88]. Natural gas has a laminar flame speed of about 38 cm/s [89] and a turbulent flame speed of about ten times higher than its laminar flame speed [90]. This slow-burning velocity [91] results in poor lean burn combustion [92]. Therefore, two concepts are employed to use natural gas as the main fuel. As shown in Fig. 2.1, the first concept uses natural gas as the only fuel, and another uses additives to provide stable and controllable combustion. Discussing these concepts comprises the main part of this chapter.

2.1 Natural gas engines

2.1.1 Stoichiometric combustion

A normal combustion process includes the fuel and oxidizer. If the oxidizer quantity undergoes combustion and burns all the fuel, and forms only CO_2 and water (H_2O) as the products, this chemical reaction is stoichiometric. A stoichiometric natural gas engine burns the fuel, as shown in the schematic of Fig. 2.2.

Stoichiometric natural gas engines are commonly ignited with a spark plug with

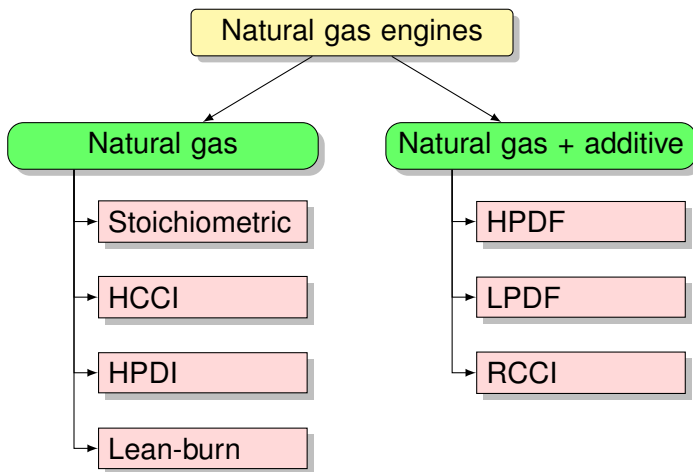


Figure 2.1: All types of available natural gas engines.

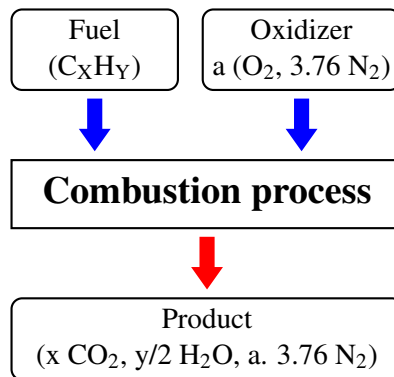


Figure 2.2: Stoichiometric combustion process. a is $(X + Y/4)$.

no excess fuel or excess air. The drawback of this engine is its higher combustion temperature. [93]. The high temperature means higher heat losses, higher pumping work at low to medium loads, higher thermal stress on the engine, and higher knock tendency [94–96]. A higher knock tendency requires redesigning the combustion chamber for a lower compression ratio, and thus the engine work with a lower brake efficiency [97]. NO_x also increases drastically when the flame temperature rises [98]. The technique of stoichiometric combustion with **EGR** and three-way catalyst (**TWC**) is recommended to reduce this harmful exhaust emission if the excess ratio is carefully controlled [99].

2.1.2 Homogeneous charge compression ignition

Homogeneous charge compression ignition (HCCI) is a homogeneous premixed charge, which is compressed to a higher compression ratio and auto ignited without any external supply of ignition sources. The concept of HCCI was initially investigated for gasoline applications by Onishi et al. [100], but in comparison with gasoline, natural gas has a higher octane number (up to 120) and high auto-ignition temperature (600 °C) [101]. This feature leads the mixture to reach a high heat release rate inherently, and the combustion may result in heavy knocking [102]. HCCI combustion contributes to rapid and low-temperature combustion of the very-lean mixture. High thermal efficiency and low NO_x formation is the desirable feature of this combustion.

There are, however, a few deficiencies intrinsic to HCCI combustion [103–106]:

1. Direct control over combustion timing
2. Releasing a high quantity of HC and CO emissions
3. Controlling the engine during transient condition
4. Excessive engine noise caused by knocking

2.1.3 High pressure direct injection

In order to have a high thermal efficiency comparable to high compression ratio diesel engines without smoke and PM compounds, direct injection (DI) of natural gas in the engine is an alternative by high pressure direct injection (HPDI) [107]. Compared with the premixed natural gas engine, the fuel composition has shown the least influence on the performance of HPDI engines [108]. However, this method's primary challenge is the fuel slow flammability during the delay phase [109] as well as providing high pressure gas.

2.1.4 Lean burn combustion

There is an excess air ratio of up to twice needed for stoichiometric combustion in a lean burn natural gas engine. This extra quantity of air typically does not participate in the combustion process, but the excess air contributes to a lower maximum temperature in the post-oxidation process. A major part of the NO_x formation is due to the high temperature [110–112]. Therefore, the excess ratio effectively reduces the amount of NO_x. Due to the lower temperature of the flame propagation, a higher compression ratio compared with a typical SI engine is feasible, and as a consequence, the thermal efficiency is higher than a similar

gasoline engine [113]. Combustion stability and the cyclic variation are two primary challenges since a standard spark plug cannot operate with this excess air ratio [114]. To stabilize the combustion process, installing a pre-chamber with an enrichment mixture or a partially stratified charge (PSC) is proposed to increase fuel conversion efficiency and brake mean effective pressure [45, 115]. In lean burn combustion, a pre-chamber can stimulate ignition and combustion by burning a small portion of the mixture. This flame produces multiplied kernels ignition than the regular spark plug. The influence of ignition energy, affected by temperature, size, and equivalence ratio, is striking on the flame development [116].

2.2 Natural gas plus an additive

2.2.1 Dual-fuel natural gas engines

In dual-fuel natural gas engines, natural gas plays the primary role by providing up to 98% of total energy. The compression pressure and temperature prevent the auto-ignition of the premixed natural gas inside the main combustion chamber. Therefore, a pilot injection of conventional diesel fuel with the fuel system like the standard diesel engine starts the ignition [117, 118]. With some simple modifications, a standard diesel engine can operate in gaseous mode. The advantage of this method is the possibility of using diesel fuel as the primary source of power if the storage of natural gas is depleted [119]. The gaseous fuel in dual-fuel engines can either be added to the mixture in low pressure or injected directly in high pressure:

2.2.1.1 Low-pressure dual-fuel engines

In the low-pressure dual-fuel engines, the gaseous fuel has a low-pressure supply and is premixed, while the liquid fuel is injected into the chamber with high pressure. The liquid fuel is atomized and distributed through the spray cone. The sprayed fuel and the gaseous mixture will be mixed inside the main chamber. The amount of the entrained mixture is a function of the injection condition, the pilot fuel quantity, and the ratio of air-fuel [117].

The primary purpose of using low-pressure dual-fuel engines is the backup fuel and the ability to operate on diesel oil, but the engine still suffers from a low compression ratio and upper excess air ratio during the low load. The former results in lower efficiency, and the latter lead the engine to misfire [45].

2.2.1.2 High-pressure dual-fuel engines

In high-pressure dual-fuel engines, the air is compressed with a compression ratio equal to the diesel engine. The diesel fuel is injected before the gas injection, and

the main characteristics, such as output power and load response, are identical with a similar diesel engine.

Although it releases a negligible quantity of the unburned fuel, to reach the Tier III limitation for NO_x , a combination of EGR or SCR is needed [120–122]. Another challenge with this engine is providing a high-pressure gaseous fuel in the injector. Diesel fuel pressure changes between 1500 to 3000 bar, and gas injector vary between 300 and 600 bar [45].

2.2.2 Reactivity controlled compression ignition

In HCCI, the mixture auto ignites at a high temperature after a high compression ratio, and the drawback is the high peak pressure and knocks phenomenon. Reactivity controlled compression ignition (RCCI) strategy is developed to overcome these issues and provide a solution for the high levels of natural gas substitution, particularly at low and medium loads of dual-fuel engines [123]. In this method, two types of fuel are used with high reactivity and low reactivity. The fuel with low reactivity is added into the main chamber as a premixed fuel, while the high reactivity fuel injects directly into the combustion chamber [124]. Natural gas with a low cetane number has become an appropriate fuel in the RCCI strategy. The drawbacks of this method are the higher adiabatic flame temperature of natural gas, which may result in higher heat losses, and lower gross efficiency than those fueled with gasoline/diesel [125]. Moreover, controlling the timing and magnitude of heat release rate is critical for operating at a high load [126, 127].

2.3 Marine gas engines

Marine gas engines can roughly be divided into two main groups: lean burn gas engines and dual-fuel engines [6]. The principles of the marine gas engine classifications are shown in Fig. 2.3. The high-pressure four-stroke engine is operated only in floating production storage and offloading (FPSO) and onshore power generation units, but not in the ship propulsion [7]. The proportion of each type of gas engine is shown in Fig. 2.4, where the lean burn gas engines and low-pressure dual-fuel engines have by far the largest contribution.

2.4 Installation modes

Among the largest offshore application for natural gas engines, the companies ‘MAN diesel & Turbo SE’, ‘Wärtsilä’, ‘Caterpillar Inc.’, ‘Hyundai Heavy Industries’, ‘Kawasaki Heavy Industries’, ‘Rolls Royce’ are the pioneer. The installation mode of these manufacturers can be summarized as follows.

Conventional

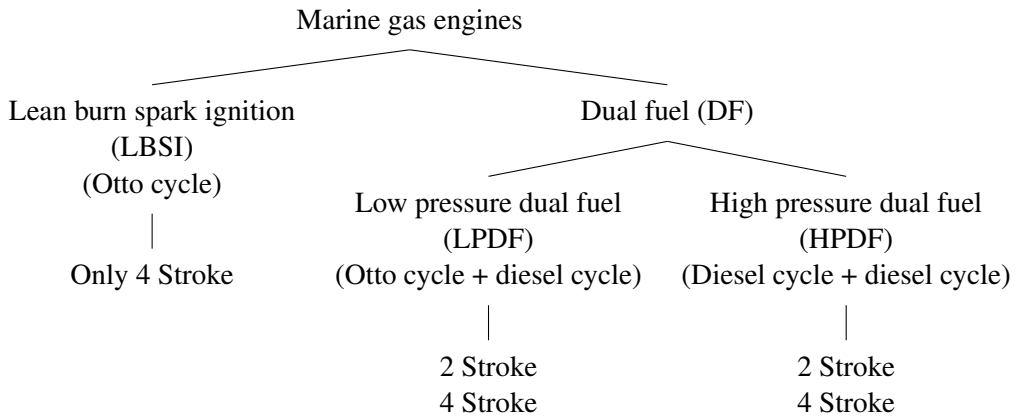


Figure 2.3: Marine gas engines classification [6].

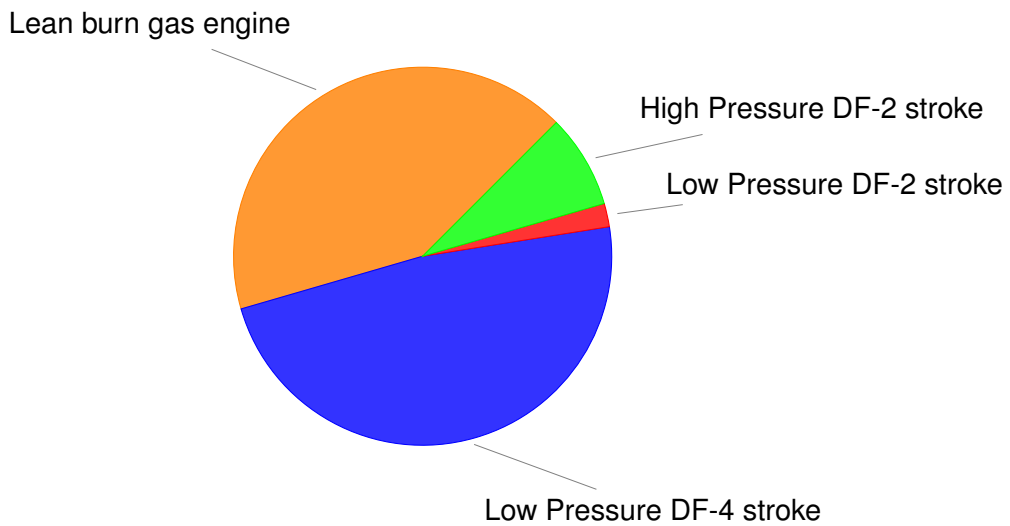


Figure 2.4: Marine gas engines in the shipping industry [7]. Lean burn gas engines and dual-fuel high-pressure four-stroke engines have the most considerable contribution by around 90%.

A conventional mode of a gas engine propulsion system consists of three main components: a prime mover, a connecting high inertia shaft, and a propeller. There is a gearbox as well to adjust the engine speed and the vessel speed. The schematic is shown in Fig. 2.5(a).

Constant speed

A constant speed mode consists of the same main components of the conventional mode plus a power take-off shaft (PTO) to the genset. Part of the power produced by the natural gas engine will drive the generator to supply the hotel load, battery recharge, and other supplementary systems. The schematic is shown in Fig. 2.5(b).

Booster

In a booster mode, the generator plays as a Power take in the shaft (PTI) and reduces the engine required torque. In this case, a fraction of the load is supplied through the genset, and the rest will be provided using the engine. The schematic is shown in Fig. 2.5(c). If the constant speed and booster mode have an energy storage device (ESD) in their arrangement, a smooth loading on the engine is applicable. Therefore, the engine can always operate in the optimum operating area of the engine designed map.

Power plant

A power plant mode is another arrangement of the natural gas engine in the shipping industry; however, its load change is not relevant to the marine sea wave. The schematic is shown in Fig. 2.5(d).

2.5 Vessel and engine specification

In summary, all the available papers and reports in the field of marine gas engines are about the description of the working principles, performance, and emissions; however, none of them considers the strong potential of real operational conditions on engine response. From these considerations, it can be inferred how it is essential to study a marine gas engine. Since an on-board measurement campaign is required to obtain the emission outline and performance data in real conditions, in order to provide a low-cost solution, comprehensive modeling of the propulsion system is performed.

This modeling is done on a ship propulsion system consists of a gas engine named Bergen ACL B35: 40L9 of 3940 kW. The engine specification is presented in Table 2.1. The ship specification called Kvitbjørn as a cargo vessel owned by Nor Lines, constructed by Tsuji Heavy Industries in China and based on Roll Royce's concept is presented in Table 2.2.

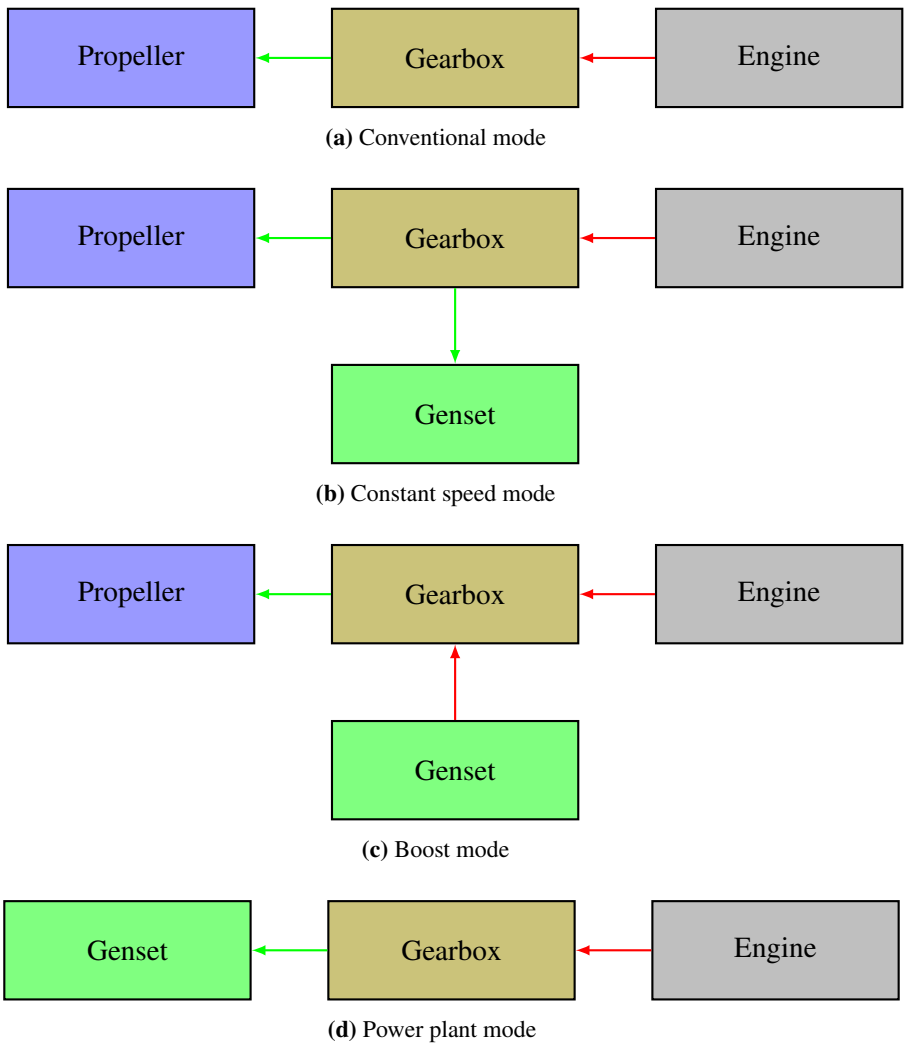


Figure 2.5: Marine gas engines propulsion mode.

Table 2.1: Engine specification.

Item	Unit	Specification
Engine model	-	B 35:40L9PG
Number of cylinders	-	9
Cylinder bore	mm	350
Cylinder stroke	mm	400
Connecting rod length	mm	810
Rated power	kW	3940
Maximum Torque at rated speed	Nm	50200
Rated speed	rpm	750
Displacement	L	346
Fuel type	-	Natural gas
Ignition type		Spark plug/ pre-chamber

Table 2.2: Vessel specification.

Item	Unit	Specification
Length oa	m	B 119.95
Length bpp	m	117.55
Width	m	20.80
Design draft	m	5.5
Design shaft submergence	m	3.3
Service speed	kts	15

Chapter 3

Modeling and Simulation

The complexity of experimental measuring and the uncertainty of the measuring instrument have always highlighted the simulation and modeling importance and potential. During the last decades, engine modeling has paved the way for an in-depth study of engines. It has also played a dominant role in showing the engine response during transient conditions due to more uncertainties in the measuring process. A significant number of engine modeling has already been conducted to show the importance and correctness of the simulation and modeling in an internal combustion engine, whether in steady-state or in transient condition [128–132]. The modeling approach of these two states, however, includes different detailed strategies. A transient condition refers to speed and loads variation, acceleration, and engine warm-up. In the transient condition, the torque, fuel quantity, heat transfer, and fluid flow vary, and the engine response during time-varying load plays a more critical role than the steady-state. Such conditions are expected for the vehicle application and marine propulsion systems, where the latter possesses a lot of wave and wakefield changing the engine load. An accurate engine modeling for the transient condition ought to consider the main and influential components in high fidelity. However, this would considerably raise the computational time, cost, and effort. Larimi developed a low-speed diesel engine model to predict the engine's response when the load on the directly coupled engine-propeller fluctuates largely. The modeling proved that transient response simulation could appropriately respond to the load fluctuation with a Wiebe function for the heat release rate, thermodynamic control volume for the air and exhaust gas receivers, and constant friction mean effective pressure (*f_{mep}*) [133].

In general, the requirements of the simulation can be outlined as [134]:

1. Sufficient detail to reflect any changes in design, environment and fuel properties,
2. Accurate prediction of the performance,
3. Emission formation,
4. Low computation time and cost,
5. The minimum empirical data requirement.

The in-cylinder conditions during the time-varying loads are different from the steady-state conditions. Therefore, a crucial part is the correct prediction of combustion modeling during the transient condition. An accurate prediction determines the amount and rate of pressure and temperature in the cylinder. The output will subsequently influence the energy and enthalpy of the gases of the turbine. The turbocharger boost pressure will again interact with the combustion phenomenon.

Based on the concepts mentioned above, several modeling approaches are available, as shown in Fig. 3.1.

Quasi-linear modeling uses empirical coefficients and neglects the nonlinear nature of the flow and combustion phenomenon. The advantage is the simplicity and limited computational time of the model but dependent on the empirical data [135].

0 D is a standard method of engine modeling and classifies in several sub-approaches. The main zero-dimensional modeling is the filling and emptying method and mean value model. In order to evaluate for a real-time in the hardware-in-the-loop (**HIL**) simulation system, the model must satisfy the demand of high prediction, precision, and real-time operating performance [136]. This approach can meet these requirements, and it has mainly been used in the **HIL** simulation system [137, 138]. This method considers the engine as a control volume series, connected through valves and junctions. The equations of mass and energy conservation are solved for each volume.

1 D or gas dynamic modeling is another modeling approach where the flow model involves the solution of the momentum equation. In this method, the whole fluid passage system is discretized into small volumes, and the conservation equations are solved in a concise time scale for all of the discretized volumes. The gas-dynamic model provides a reasonable estimate of the flow velocity in each boundary of control volumes, and therefore, a suitable prediction for the pulse

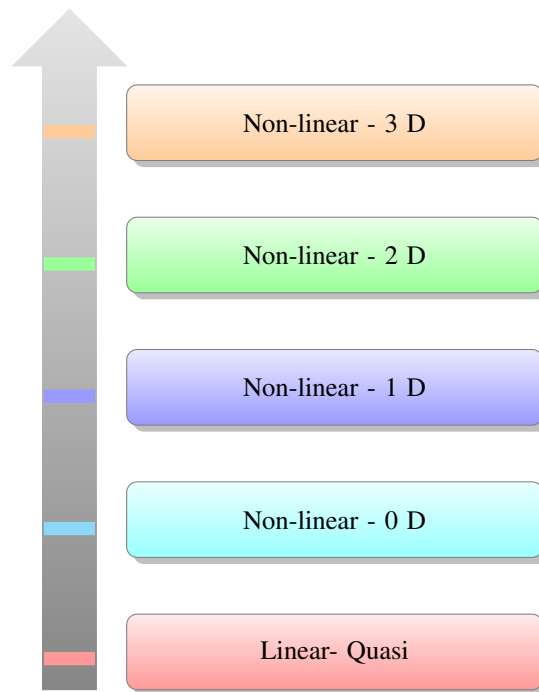


Figure 3.1: Engine modeling complexity from minimum fidelity and computation time (down) to maximum (top) [8].

turbocharged engines [139]. The CPU time using this method is by far more than real-time condition [140].

2-3 D named as **CFD** simulation simulates in order of turbulent time-scale. Solving the Navier Stokes equations in 2-3D in thousand of small volumes gives the most predictive simulation capability to this modeling. Simultaneously, the enormous computational time required for the components bounds the method application for simple components such as a combustion chamber or a manifold rather than the entire engine. Providing the detail of the flow field, distribution of pressure and temperature, and the possibility of considering the detailed chemical mechanisms is the advantage of the model. The inability to predict the engine performance, the system response, and connecting the subsystem are the disadvantages [141–143].

3.1 Steady-state vs. transient condition

In order to describe the impact of the transient condition, especially during the transient ramp-up of temperatures and transient build-up of boost pressure during accelerations, the leading causes of the disparity between steady-state and transient

conditions must be reflected. The differences can be classified into the mechanical delay, thermal delay, and dynamic delay of the engine [144].

Mechanical delay: All the rotating components, such as a flywheel, turbocharger shaft, and crankshaft, has a moment of inertia. During transient conditions, acceleration of the rotating mass needs additional energy; the larger the mass moment of inertia, the higher the energy requirement. Thus, a significant part of the energy during the transient condition, if the load increases, will be applied to accelerating the shafts to grasp the new speed. During the load reduction, the system responds contrariwise.

Thermal delay: As a result of the increasing or decreasing the fuel quantity due to the load changes, the wall temperature of the components at each consecutive cycle changes. The thermal variation is highly dependant on the type of combustion (SI and CI) and the air system response toward the fuel system variation. Usually, in diesel engines, this delay can be notably [134], while in the spark ignition engines with a constant air-fuel ratio, the oscillation of the exhaust temperature is small.

Dynamic delay: The fluid from the compressor inlet, passing through the intake and exhaust pipes and to the turbine outlet, follows the mass transfer function. The intake and exhaust manifold size, the pressure drop in the air and exhaust pipes, and the turbocharger type, whether pulse or constant pressure, influence the flow dynamic. The turbocharger variation is dominated by the rotational speed [145], and thus, any dynamic delay directly influences the turbocharger response. A diesel engine's transient duration may last from a few seconds up to several minutes [8, 58, 146].

3.2 Main components in the modeling

The marine gas engine model studied in this project is developed by considering the following influential componens:

3.2.1 Combustion chamber

A mixture of air and fuel with an excess air ratio is captured in a non-fixed control volume, and it is assumed to be perfectly mixed. Several thermal zones are imposed for more accurate heat transfer calculation.

3.2.1.1 Heat transfer modeling

During the intake, compression, combustion, and exhaust, there is always an exchange of thermal energy between gases and boundaries.

Heat convection modeling in the main combustion chamber followed the method

proposed by Woschni [147] in Equation (3.1):

$$h_{c(\text{Woschni})} = \frac{K_1 P^{0.8} W^{0.8}}{B^{0.2} T^{K_2}} \quad (3.1)$$

where K_1 and K_2 are constant, B bore and W is average cylinder gas velocity (m/s). The equation for the average in-cylinder gas velocity is:

$$W = C_1 S_p + C_2 \frac{V_d T_r}{P_r V_r} (P - P_m) \quad (3.2)$$

C_1 and C_2 are constants, S_p mean piston speed (m/s), T_r unburned mixture temperature, P pressure, P_m motoring pressure, P_r unburned mixture pressure, V_d the total displacement and V_r is the volume before combustion.

Woschni heat transfer model lumps the radiation portion, which is typically is estimated by the transmission of heat in the form of waves through space, into the convection portion inside the cylinder [148]. Moreover, radiative heat transfer from the hot burned gas in spark-ignition engines is tiny related to the convective heat transfer. Hence, Equation (3.1) is the only modeling theory for the heat transfer of the cylinder surfaces.

$$q_{\text{convection}} = h_{\text{Woschni}} (T_{\text{gas}} - T_{\text{wall}}) \quad (3.3)$$

In Equation (3.3), T_{wall} split into several zones.

The zones identified interior surfaces of the cylinder by: cylinder zone, piston zone, and head zone. Cylinder zone 1 is $\frac{1}{6}$ of the cylinder wall exposed when the piston is at BDC, cylinder zone 2 is $\frac{1}{3}$ of the cylinder wall exposed when the piston is at BDC and cylinder zone 3, covers the lower half of the cylinder wall exposed when the piston is at BDC.

The zones for piston surface and cylinder head are shown in Fig. 3.2.

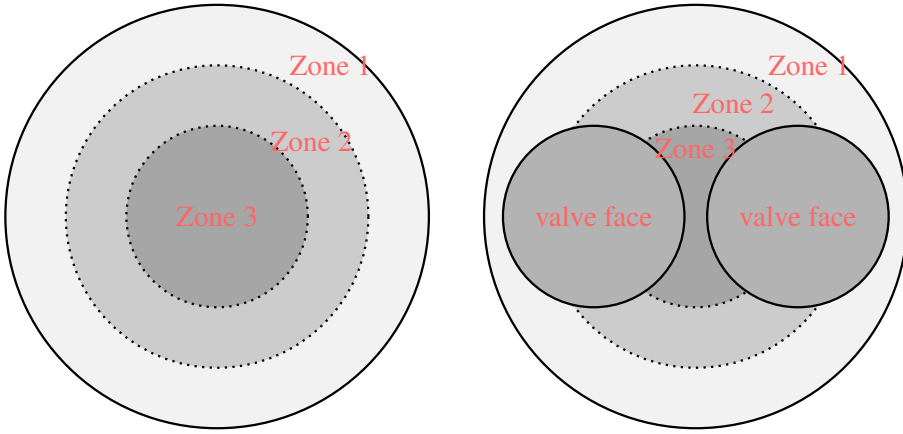
The temperature of the valve face surface is imposed and the total heat transfer is calculated for the valve surface area of:

$$area_{\text{valve}} = \frac{\pi}{4} D_{\text{valve}}^2 + 0.25 D_{\text{valve}} h_{\text{valve thickness}} \quad (3.4)$$

Where the average thickness of the valve head was chosen 16% of valve diameter.

3.2.1.2 Combustion

To predict the flame characteristics for the engine, the SI-turbulent flame model is employed. The model has the potential of predicting the combustion burning rate



(a) The three piston zones consisted of the piston zone 1 with 48%, piston zone 2 with 37% and piston zone 3 with 15% of the piston area. (b) The three head zones consisted of head zone 1 with 55%, head zone 2 with 35% and head zone 3 with 10% of the head area excluding valve faces.

Figure 3.2: Temperature zones of the cylinder head and piston top surface.

based on laminar and turbulent flame speed. It is assumed that there are two zones, burned and unburned zone, and the eddies of the unburned zone are entrained in the flame front at a turbulent velocity while the mixture of fuel and air is burning at laminar velocity. The rate of transformation of unburned to burned zone is calculated by Equation (3.5) and (3.6):

$$\frac{dM_e}{dt} = \rho_u A_e (S_T + S_L) \quad (3.5)$$

$$\frac{dM_b}{dt} = \frac{M_e - M_b}{\tau} \quad (3.6)$$

where index b symbolizes burned classification, u unburned classification, and e entrained classification.

It is also assumed that the reaction is quite fast with a thin layer of the burning zone [9]. To calculate the laminar flame speed (S_L), Heywood [109] recommended Equation (3.7) for several hydrocarbon fuels:

$$S_L = \left(B_m + B_f(\phi - \phi_m)^2 \right) \left(\frac{T_u}{T_0} \right)^\alpha \left(\frac{P}{P_0} \right)^\beta \cdot f_{\text{Dilution}} \quad (3.7)$$

where for natural gas fuel:

$$\alpha = 0.68\phi^2 - 1.7\phi + 3.18 \quad (3.8)$$

$$\beta = -0.52\phi^2 + 1.18\phi - 1.08 \quad (3.9)$$

and B_m is 0.490, B_f is -0.59, and ϕ_m is 1.390 [149].

f_{Dilution} is the dilution effect and is employed as:

$$f_{\text{Dilution}} = 1 - 0.75A(1 - (1 - 0.75A \cdot \text{Dilution})^7) \quad (3.10)$$

A is a multiplier, and Dilution is the mass fraction of the residuals in the unburned zone.

The time constant of combustion of fuel/air mixture entrained into the flame zone (τ) in Equation (3.6) was calculated by Equation (3.11):

$$\tau = \frac{\lambda}{S_L} \quad (3.11)$$

with the Taylor length scale of:

$$\lambda = a \frac{L_i}{\sqrt{Re_t}} \quad (3.12)$$

and turbulent Reynolds number:

$$Re_t = \frac{\rho_u \dot{u} L_i}{\mu_u} \quad (3.13)$$

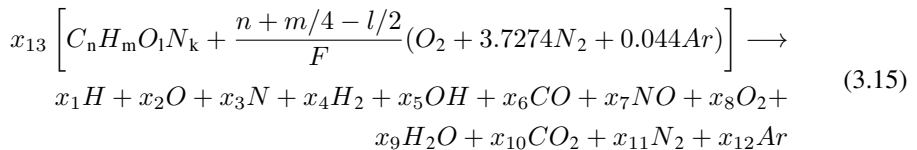
Calculation of turbulent flame speed is done by Equation (3.14):

$$S_T = b \cdot \dot{u} \left(1 - \frac{1}{1 + c \left(\frac{R_f}{L_i} \right)^2} \right) \quad (3.14)$$

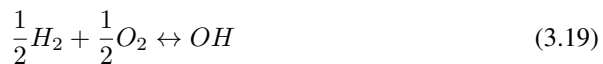
where a , b , and c are constants. Moreover, \dot{u} and L_i are turbulent intensity and turbulent length scale, respectively. They have been described in section 3.2.1.3. Calculation of surface area at the flame front (A_e) and flame radius (R_f) are presented in [150].

In order to calculate the concentrations of the species, chemical equilibrium is carried out for the entire lumped burned zone. This assumption is the state in which both reactants and products have no further inclination to change with time in the current pressure and temperature.

During the simulation, the main species and products of combustion are monitored in the main chamber by the relations between the composition of reactants and the composition of products by Equation (3.15):



Where x_1 to x_{12} are mole fractions of the products and x_{13} is the mole of fuel, giving one mole of the product. The atom balances plus the products add up to unity provides six equations. To solve for the 13 unknowns, seven other equations are solved using the equilibrium provided by the following equations:



Using the curve fitted from the JANAF thermodynamic table, the 13 equations of species are available and solvable in each pressure and temperature [151].

3.2.1.3 Flow model

The in-cylinder mean flow depends strongly on the chamber geometry, where the calculated values influence the burning rate. The sophisticated features of flow dynamics can be captured using detailed multidimensional Navier-Stokes models, but a simplified model of the combustion chamber is considered. The chamber is divided into three flow regions defined as the squish area above the piston crown, the cup volume, and the region above the cup lip. At each time step in each region, the mean radial velocity, axial velocity, and swirl velocity are calculated, taking into account the cylinder chamber geometry, the piston motion, and the incoming and exiting flow rates passes through the valves [152]. The turbulence model solves the turbulence kinetic energy equation and the turbulence dissipation rate equation. Two outputs of the model, turbulence intensity and turbulence length scale, are used directly in the turbulent flame velocity calculation in combustion modeling of Equation (3.5).

The turbulence length scale is calculated by:

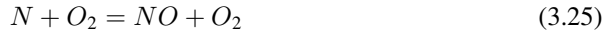
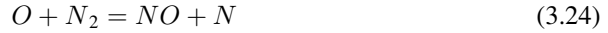
$$L_m = \frac{C_\mu^{\frac{3}{4}} \cdot K^{\frac{3}{2}}}{\epsilon} \quad (3.23)$$

C_μ is constant. The detailed equations are presented in [152]:

3.2.1.4 Emission

Natural gas engines produce four main emission compounds throughout the combustion: NO_x , UHC , CO_2 , and CO [153]. Generally, the concentration of these compounds differs in chemical equilibrium rather than the detailed chemical mechanism. Besides, implementing the detailed kinetics to find the emission level during combustion and post oxidation needs considering hundreds of reactions. Therefore, a basic formation mechanism is provided for the pollutants.

3.2.1.4.1 NO_x NO_x is nitrogen oxide, NO , and nitrogen dioxide, NO_2 , but NO is the prominent oxide of nitrogen of the internal combustion engine [109]. Therefore, the mechanism of formation of NO proposed by Zeldovich have been extensively applied for description of NO formation in engines [154]:



The rate of formation of NO via reactions of (3.24), (3.25) and (3.26) is:

$$\begin{aligned} \frac{d[\text{NO}]}{dt} = & k_1^+ [O][N_2] + k_2^+ [N][O_2] + k_3^+ [N][OH] \\ & - k_1^- [\text{NO}][N] - k_2^- [\text{NO}][N] - k_3^- [\text{NO}][H] \end{aligned} \quad (3.27)$$

With the steady-state approximation for $\frac{d[N]}{dt}$ and equilibrium for other species, a simplified one-way equilibrium is achievable with the following reaction rates respectively:

$$k_1 = F_1 \cdot 7.60 \cdot 10^{10} \cdot e^{-\frac{38000}{T_b}} \quad (3.28)$$

$$k_2 = F_2 \cdot 6.40 \cdot 10^6 \cdot T_b e^{-\frac{3150}{T_b}} \quad (3.29)$$

$$k_3 = F_3 \cdot 4.10 \cdot 10^{10} \quad (3.30)$$

F_1, F_2, F_3, A_1 and A_2 are constant coefficients for tuning the modeling, and T_b is the burned zone temperature.

3.2.1.4.2 UHC The implemented equations for **UHC** modeling to calculate the amount of methane slip is separately discussed in [chapter 4](#).

3.2.1.4.3 CO₂ **CO₂** is a greenhouse gas in the exhaust gases from **SI** engines as a main product of the combustion. Natural gas has chemical properties with a high H/C ratio of around 3.7. Thus, by changing the fuel from diesel with a ratio of 1.8 to natural gas, an immediate reduction of **CO₂** to half is achievable. As a result, the gas engines produce less **CO₂** and even 20% less than similar gasoline engines [72]. Thus the relative amount of this emission depends on fuel properties than the combustion mechanisms. Therefore, the output of the chemical equilibrium is used for the validation of the combustion, and the formation of this emission is not discussed further.

3.2.1.4.4 CO At lean equivalence ratios, like for the lean burn spark-ignition engine, a low amount of **CO** can be achieved [155, 156]. Moreover, the formation of **CO** emission is high primarily when the engine operates close to stoichiometric, or during warm-up when the wall is cold. Since the primary output from the **CO** is not verified, any further presenting of the modeling and output is neglected.

3.2.1.5 Knock

In spark-ignition engines, knock represents one of the most critical issues to reach optimal thermal efficiency. Therefore, to deal with any probable knocking occurrence, an air/fuel ratio and **EGR** based methodology aimed at evaluating the knock phenomenon. In the model presented here, the knock intensity is evaluated by the Kinetics-Fit-Natural-Gas model proposed by Gamma Technology and is based on the kinetic reaction mechanism of natural gas [157, 158]:

$$K_1 = M \cdot u(\alpha) \frac{V_{TDC}}{V(\alpha)} \exp\left(\frac{-6000}{T(\alpha)}\right) \cdot \max[0, 1 - (1 - \phi(\alpha))^2] \cdot I_{index} \quad (3.31)$$

Where M is a multiplier and can be found during the validation step. Induction time integral, I_{index} , is calculated by equation (3.32):

$$I_{index} = \int \frac{1}{\tau} dt \quad (3.32)$$

and the induction time, τ , is defined by equation (3.33) :

$$\tau = M_1 - \left[10^{-9} \exp\left(\frac{18659}{M_2 T}\right) \left(\frac{MN}{100}\right)^{0.978} \cdot (Fuel^{-0.578})(O_2^{-0.28})(Diluent^{0.03}) \right] \quad (3.33)$$

where MN is the fuel methane number, M_1 and M_2 are multipliers, equalized to 1, and diluent concentration is the sum of concentrations of N_2 , CO_2 , and H_2O . V_{TDC} is cylinder volume at the top dead center and ϕ is equivalence ratio of the unburned zone. $u(\alpha)$ is the percentage of cylinder mass unburned.

3.2.2 Power transmission

Sudden loading and unloading on the engine lead the engine to speed fluctuation and instability. Any idea to improve the engine stability is highly pertinent to the engine mass moment of inertia and the connected rotating components as power transmission [159, 160]. The degree of change of the system frequency regarding the external forces is inversely proportional to the magnitude of the inertia:

$$T_b(t) = T_s(t) - I \cdot \dot{\omega}_{ct}(t) \quad (3.34)$$

where, $\dot{\omega}_{ct}(t)$ is the instantaneous crank-train acceleration and I mass moment of inertia. $T_b(t)$ represents the torque available at the flywheel, after accounting for all friction and attachment losses as well as the acceleration of the crank train inertia.

The entire propulsion shaft is modeled as a single rigid, and the shaft torque, T_s , is calculated by:

$$T_s(t) = T_i(t) - T_{f(cyc)} + T_a \quad (3.35)$$

If there is any additional instantaneous torque of the other attachments, they can be added to the right of Equation(3.35) as T_a . $T_{f(cyc)}$ is friction torque for the current cycle, and $T_i(t)$ is the indicated torque and depends on the combustion chamber. The pressure inside the main chamber, calculated by the flame modeling, provides forces on the x-y direction on connecting rod as:

$$T_i(t) = \sum_1^9 \left(\frac{\pi}{4}\right) B^2 R_{crank} (\Delta P(t) \sin \theta_i(t) - \Delta P(t) \cos \theta_i(t) \tan \alpha_i(t)) \quad (3.36)$$

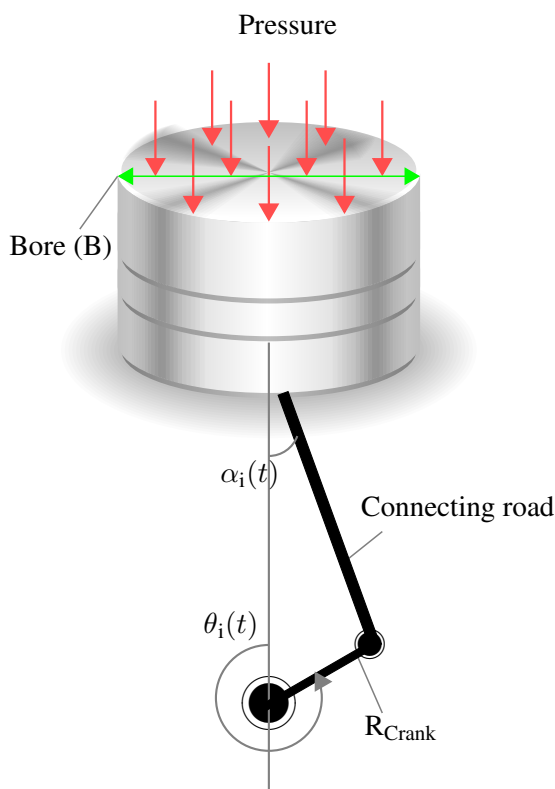


Figure 3.3: The instantaneous indicated torque is a function of pressure in each crank angle and the in-cylinder surface area.

$\theta_i(t)$ is the instantaneous angle of crank i in degree and $\alpha_i(t)$ is the instantaneous angle of connecting rod i in degree. The schematic shown in Fig. 3.3, indicates the pressure on the piston surface and the distribution of the forces.

The power transmission included the flywheel, crankshaft, main shaft, and gearbox to transmit the power to/from the engine. All are assumed to be rigid. Thus deformation of the crankshaft, corresponding to the immediate difference between the engine and load torque, is neglected. The inertia concerning the water resistance and the propeller is added to this model as well.

3.2.3 Controlling system

A proportional-integral-derivative controller (PID) consists of a proportional unit (P), an integral unit (I), and a derivative unit (D). The PID formula follows

Equation (3.37), and the schematic of the interconnections is shown in Fig. 3.4.

$$y(t) = K_p e(t) + K_i \int_0^t e(t) dt + K_d \frac{de(t)}{dt} \quad (3.37)$$

where $y(t)$ and $e(t)$ are the process input and error, respectively. The PID controller is used when the system has a linear response with dynamic characteristics. In a complex system with more degrees of freedom and nonlinear dynamic processes in calibration, new calibration approaches are needed [161, 162].

In this study, for the engine modeling, three regular PI controllers (PID with a coefficient of $D=0$) were required:

- The fuel flow regulator with engine speed feedback
- The VTG vane position with the feedback of air-fuel ratio
- The throttle opening angle with engine loading feedback

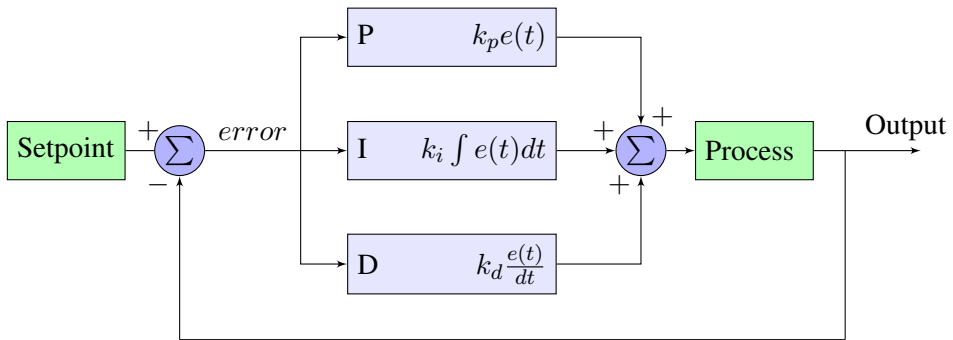


Figure 3.4: PID controller block diagram. Three parameters (K_p , K_i , and K_d) can be manually or automatically tuned based on the setpoint and output.

3.2.4 Intake and exhaust manifold

Since the fluid flow is important in calculating the dynamic delay and consequently the turbocharger response, the equation of conservation are involved the conservation of momentum as well as Equation (3.38) and (3.39) [157]. The dimensions for all the pipes and junctions are implemented based on the designed

components, and different discretized length scales for the straight pipes and bends are chosen.

$$\frac{dm}{dt} = \sum_{boundaries} \dot{m} \quad (3.38)$$

$$\frac{dme}{dt} = -\rho \frac{dv}{dt} + \sum_{boundaries} (\dot{m}H) - hA_s(T_{fluid} - T_{wall}) \quad (3.39)$$

$$\frac{d\dot{m}}{dt} = \frac{dpA + \sum_{boundaries} (\dot{m}u) - 4C_f \frac{\rho u |u|}{2} \frac{dx A}{D} - K_P (\frac{1}{2} \rho u |u|) A}{dx} \quad (3.40)$$

Where m is mass of volume, K_P pressure loss coefficient, D equivalent diameter, and \dot{m} is the boundary mass flux. A is the cross-sectional flow area and A_s is the heat transfer surface area.

In all discretized volumes, Equations (3.38) and (3.39) yield the mass and energy in each volume. With the available volume and mass, the density can be calculated. Afterward, the equations of state define density and energy as a function of pressure and temperature, and the solution will be continued iteratively on pressure and temperature until they satisfy the density and energy already calculated for this time step.

3.2.4.1 Fuel system

To address the fuel system response, it is imperative for the modeling to pursue the same fluid dynamics approach as the air in the intake and exhaust manifold. This is attained by adopting the use of conservation of mass, energy, and momentum equations, providing a high fidelity of fuel flow model, cost-effective, and ensuring the dynamic system response. To simulate the fuel delivery system dynamics, all fundamental components of this system, including the fuel tank, orifices, fuel lines, and fuel valves, are assembled. For simplicity, the fuel tank and fuel pump are assumed to be constant pressure sources. The fuel, natural gas, is mixed with the air just upstream of the intake valves.

3.2.5 Intake and exhaust valves

The intake and exhaust valve capacities ultimately restrict the total flow of the engine. A feasible approach for compressible flow over a flow restriction is proposed by Heywood [109] with a pressure upstream and downstream of the valve:

$$\dot{m} = A_{eff} \rho_{is} U_{is} = C_D A_R \frac{P_u}{\sqrt{RT_u}} \left(\frac{P_d}{P_u}\right)^{1/\gamma} \sqrt{\left[\frac{2\gamma}{\gamma-1} (1 - P_r)^{\frac{\gamma-1}{\gamma}}\right]} \quad (3.41)$$

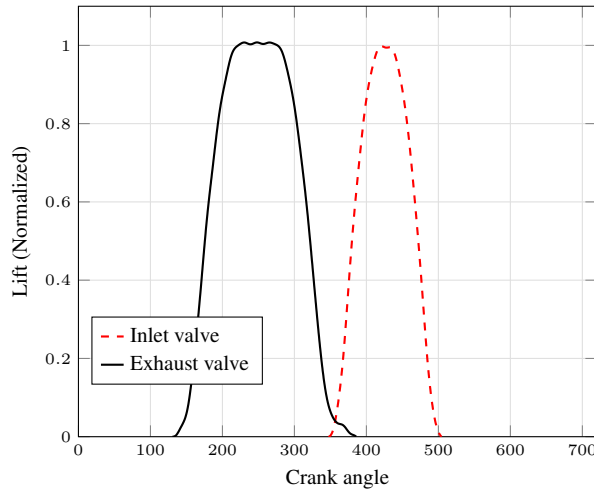


Figure 3.5: The intake and exhaust valves lift in an engine cycle. The values are normalized to be fitted in the maximum amount of one.

where u is upstream and d is downstream stagnation point. Here, C_D is an experimentally determined discharge coefficient of the valve lift presented in Fig. 3.5.

For choked flow, the equation modifies to:

$$\rho_{is} = \rho_o \left(\frac{2}{\gamma + 1} \right)^{\frac{1}{\gamma - 1}} \quad (3.42)$$

$$U_{is} = \sqrt{\gamma R T_o} \left(\frac{2}{\gamma + 1} \right)^{\frac{1}{2}} \quad (3.43)$$

3.2.6 Intercooler

Compressed air after turbocharger has higher internal energy with higher pressure and temperature. The drawback of the boosted fluid is now the low density due to the high temperature. For increasing the mass flow, it is essential to decrease the fluid density. An intercooler wastes the additional heat by multiple pipes. The infinite number of pipes is considered to provide an infinite heat sink for the modeling, and the outlet temperature leaving the intercooler equals the intercooler wall temperature and is equal to the measured value from the engine data. Calculation of total heat flux is performed by Equation 3.44, where h_g is the convection heat coefficient and is calculated using the Colburn analogy [163] by Equation 3.45.

$$q_{\text{convection}} = h_g(T_{\text{gas}} - T_{\text{wall}}) \quad (3.44)$$

$$h_g = \left(\frac{1}{2}\right)C_f\rho U_{\text{eff}}C_pPr^{\left(\frac{-2}{3}\right)} \quad (3.45)$$

where C_f is friction factor, C_p specific heat, and U_{eff} is effective fluid velocity.

3.2.7 Turbocharger

A turbocharger consists of three components: The turbine, which converts the high enthalpy gas to rotating energy, the compressor, which utilizes the excess power from the turbine, and finally, the connecting shaft. In developing the models for the turbocharger, a performance map is an alternative solution. Utilizing this method, the compressor and turbine information as a function of speed, pressure ratio, mass flow rate, and efficiency are implemented in the format of look-up tables. Turbocharger speed and pressure ratio are predicted at each time-step, and two other unknowns are taken from the look-up table [164]. The calculation starts with the predicted pressure ratio, calculating total temperature by Equation (3.46) and Equation (3.47):

$$T_{\text{total,in}} = T_{\text{in}} + \frac{u_{\text{in}}^2}{2c_p} \quad (3.46)$$

$$\Delta h_s = c_p T_{\text{total,in}} (PR^{\frac{\gamma-1}{\gamma}} - 1) \quad (3.47)$$

where u_{in} is inlet velocity. The outlet enthalpy will be calculated by Equation (3.48) and the compressor power by Equation (3.49) provides the torque of the compressor subsequently:

$$h_{\text{out}} = h_{\text{in}} + \frac{\Delta h_s}{\eta_s} \quad (3.48)$$

$$P = \dot{m}(h_{\text{in}} - h_{\text{out}}) \quad (3.49)$$

Subtext script in, out and s stands for inlet, outlet and isotropic, respectively. By Equation (3.50), the new calculated rotational speed is provided:

$$\Delta\omega = \frac{\Delta t(T_{\text{turbine}} - T_{\text{compressor}} - T_{\text{friction}})}{I} \quad (3.50)$$

A table of friction coefficients was considered for the turbocharger shaft for different rotational speeds, as T_{friction} .

For the turbine, the following equations are employed instead of Equation (3.47) and (3.48):

$$\Delta h_s = c_p T_{\text{total,in}} (1 - PR^{\frac{1-\gamma}{\gamma}}) \quad (3.51)$$

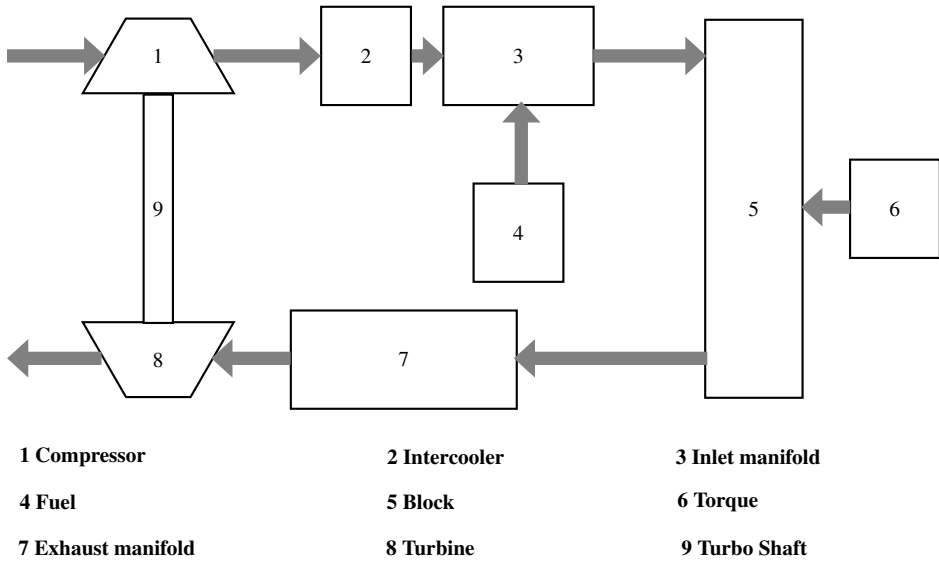


Figure 3.6: Engine modeling schematic. All essential elements influential on flow and dynamic are implemented in the engine model using two-zone zero-dimensional modeling for the combustion, one dimensional for pipes and connections, and a look-up table for the turbocharger.

$$h_{\text{out}} = h_{\text{in}} - \Delta h_s \eta_s \quad (3.52)$$

The computation will be repeated until the predicted parameters reach convergence.

3.2.8 Boundary condition of inlet and outlet

Sea reference condition states the free water surface boundary condition on an ocean. A static atmospheric pressure, temperature, and zero amplitude are utilized for the compressor inlet and the turbine outlet.

3.3 Establishment of engine simulation

The full-scale natural gas engine model, including all the engine components, was set up using the GT POWER from Gamma Technologies. The platform is designed for automotive fieldwork simulation and analysis. GT SUITE considers the components in a modular and visual logical calculation process. The schematic of the section modeled in this study can be represented, as shown in Fig. 3.6.

To evaluate the predictability of the model and the accuracy of the engine response, the model needs to be fully validated. For this purpose, the model results are compared with the data provided by the manufacturer. The results are in good agreement with the available data, and all errors between the simulated and measured outputs are within acceptable levels. The validation investigations confirm that the model is accurate and applicable for steady-state simulations within the fixed loading values as presented in Fig. 3.7 and transient conditions within a time-varying load as shown in Fig. 3.8.

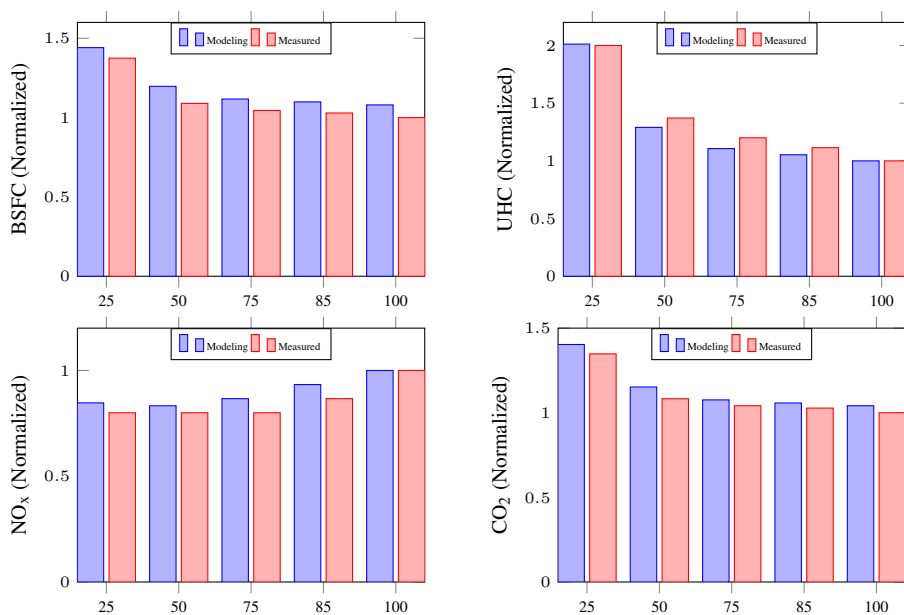
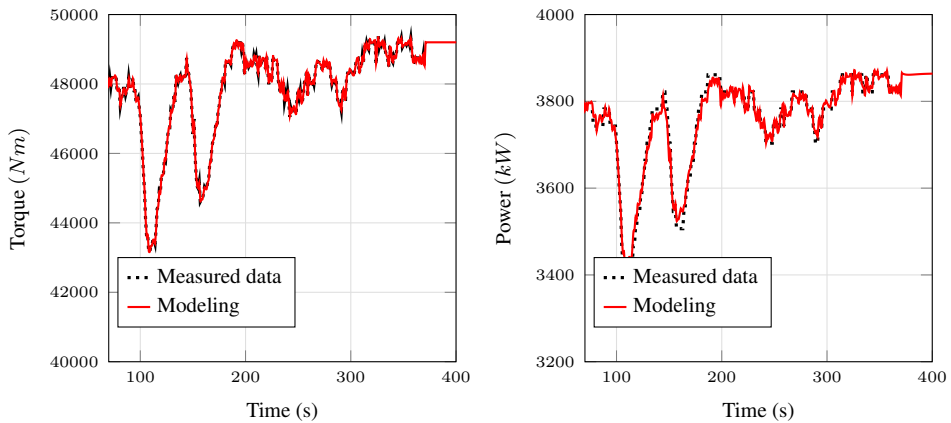


Figure 3.7: Comparison of measured data and engine simulation in steady-state. The X-axis shows the load percentage, and the Y-axis gives the measured-modeled output. The results are normalized by the measured value in 100% load.

3.4 Co-simulation

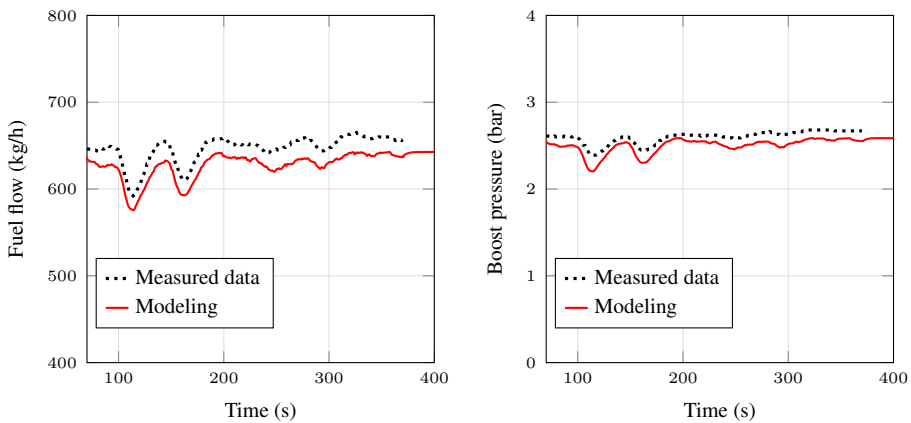
The engine model is not compatible with the propeller model, resulting in modeling the engine in a disagreement between the modeling results and real vessel data. Another challenge of simulating the individual engine for navigational purposes is considering a spectrum of wave amplitude and wave direction effect on the load magnitude. To properly simulate the entire system, an interface, co-simulation, is required to support both engine and propeller model [165].

A study of co-simulations is given in [166], and, therefore, just a short presentation for understanding the essence of co-simulations is presented here. In the



(a) The implemented torque is based on the five minutes of the vessel recorded torque from the real operational conditions.

(b) The calculated output power: Power is a function of the torque and speed, where the validity of the curve proves the validity of speed and torque during the transient condition.



(c) The fuel flow comparison. Even with a gap between two lines, the rate of change of variable given by simulation is acceptable.

(d) The Boost pressure provided by the turbocharger. The quantity is sensed from the pipe after the intercooler. So there is a pressure drop while passing the pipes and bends of the intake manifold and intake valves. The values are in the gauged pressure.

Figure 3.8: Comparison of measured data and engine simulation in transient conditions. The X-axis shows the time, and Y-axis shows the measured-modeled output.

co-simulation framework, different subsystems are modeled in a distributed manner, and the exchange of data between subsystems is restricted to discrete communication points. Each subsystem is then free to use the solver strategy and

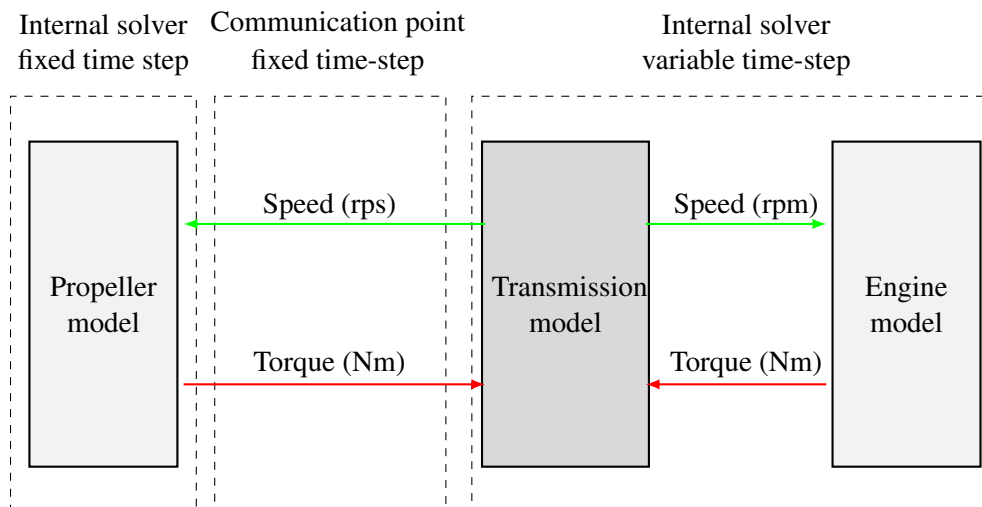


Figure 3.9: Propulsion system modeling in a co-simulation platform developed in MathWorks Simulink.

internal local time-step size, which is deemed most suited. This method improves the computational time of the full system simulation without sacrificing the fidelity of the model. Using co-simulation, one can solve complex multi-physics and multi-domain interactions of a single system using a simulation platform.

Different parts of the simulation may run on different processors or even different computers in a network to distribute the workload between them, but in this work, the co-simulation is performed on one computer, with the subsystems in the co-simulations are treated as separate processes.

The coupling and exchange of data between the engine and propeller have interacted based on the schematic is shown in Fig. 3.9. Both the engine model as the prime mover and the propeller were compiled and coupled in the MathWorks Simulink. Equations are solved independently with the internal solver with a fixed time-step for the propeller and a variable time-step for the engine model. The external time-step for exchanging the data between sub-models is fixed on 0.1 seconds. This time-step satisfies the shortest engine cycle and is adequate for addressing the full response of the engine.

Chapter 4

Unburned Hydrocarbon Formation

The word hydrocarbon refers to any compound consisting of carbon and hydrogen. Incorporating any other atoms disqualifies them from being considered as hydrocarbon [167]. The hydrocarbon chain may vary in molecular structure, but they have five specific families: alkanes, alkenes, alkynes, cycloalkanes, and aromatic hydrocarbons (arenes). This classification is based on the bonds between carbon(s) and hydrogen(s).

As predominantly discussed in previous chapters, internal combustion engines usually use diesel fuel, gasoline, and natural gas, which are nominated as hydrocarbon fuels. When the fuel does not participate during the combustion, part of the fuel remains unburned. Besides, the fuel may react during the combustion process and form formaldehyde [168]. In the presence of hydrocarbon compounds, a new formation of oxygenated hydrocarbon (OHC) may occur [169]. A schematic of the detailed combustion mechanism for methane is shown in Fig. 4.1. The pathway shows the conversion of methane to CO_2 at a high temperature, 2200 K. This temperature is close to the maximum flame temperature. Each arrow represents a set of elementary reactions based on a detailed mechanism [9]. With temperature reduction, the pathways change, and intermediate productions will appear. The new pathway usually is for a temperature less than 1500 K. To follow these pathways, implementing detailed mechanisms with 279 reactions is needed. This implementation requires a high computer performance time. Concerning the scope of this research, for modeling the engine response during dynamic loading, detailed kinetic modeling in association with the engine model is impossible.

Therefore, tracing the detailed reactions is neglected, and the unburned fuel is assumed as the only source of unburned hydrocarbon formation in this study. In natural gas engines, the unburned fuel has the same meaning as the methane slip since relative ratios of chemical components of methane are the highest among all [170].

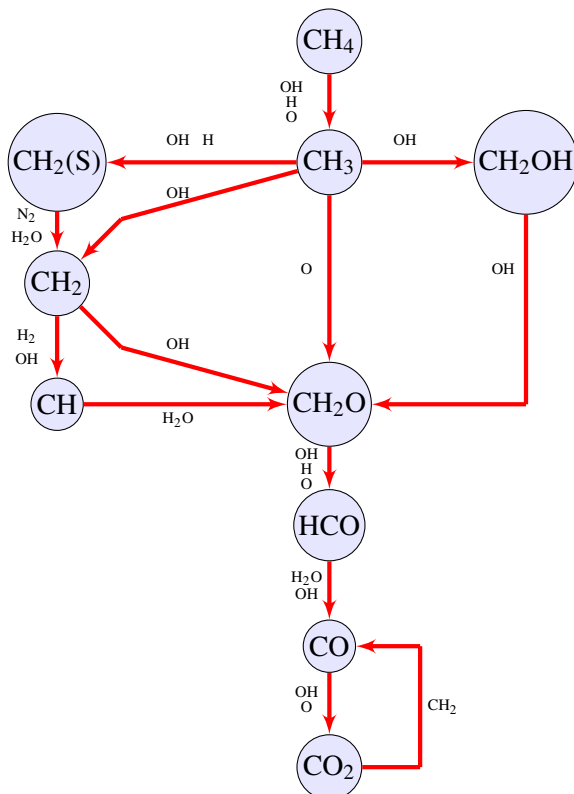


Figure 4.1: Methane reaction pathway diagram at high combustion temperature. A temperature lower than 1500 K results in CO and CH₂ formation as well. The detailed reaction and reaction rate is presented in [9].

The present section details the primary sources of unburned hydrocarbon emissions in conventional internal combustion engines. Afterward, modeling methods for methane slip formation are presented.

4.1 Engines in relation to UHC emission

In terms of unburned hydrocarbon emission formation, several engine categories are available.

Unburned hydrocarbon emissions of **CI** engines, mostly diesel engines, are attributed to the excess air ratio. In the too lean region of fuel spray, the flame stops propagating, and in the rich area of the fuel jet, the air is not sufficient to burn all the available fuel. Both of these conditions, too lean and too rich mixture, are the source of unburned fuel, and consequently, a probable **UHC** source. Moreover, this compound in a diesel engine is highly dependent on the fuel quality and the ignition delay [171–174]. When the ignition delay increases, a higher portion of the fuel will be in the over-lean area and results in the **UHC** formation [139]. A poor mixture formation due to the large droplets, low injection velocity, and cold crevices regions may also influence the total volume of **UHC** in diesel engines. The fuel spray-wall interaction is also reported as an influential potential source of **UHC** for diesel engines [175].

Dual-fuel engines exhibit higher **UHC** emissions than diesel, particularly at part-load conditions. During the full loads, the increase in the mixture strength and the improvement in the fuel utilization cause a reduction in total **UHC** emission, but the quantity is still higher than that of conventional diesel mode [176]. There are mainly four mechanisms in dual-fuel engines that result in **UHC** formation: crevice volumes, flame quenching, absorption and desorption of fuel in lubrication oil film, and the amounts of fuel remained in nozzle sac volume [177, 178].

In premixed **SI** engines, since the fraction of the unburned fuel may even reach 5% of total fuel, the **UHC** formation plays a more significant role in the combustion efficiency and total **GHG** emission of the engines [109]. In premixed **SI** engines, unburned hydrocarbon originates from various sources. The importance of the sources changes by the fuel phase, whether it is liquid or gaseous. Liquid fuel vaporization carburetor [179], oil-films, and wall wetting in the cold start [113, 180, 181] are reported as the main sources for liquid fuel **SI** engines. Injection of the liquid fuel in different places of the intake port showed a difference in **UHC** quantity. The liquid fuel entering close to the intake valve causes three times more **UHC** than the farthest injection probe from the exhaust valve. Heating by the hot residual gas back-flow that occurs at the intake valve opening reduces the estimated **UHC** emission of the liquid source [182]. It was also confirmed that liquid fuel flow produces between 3 to 7 times higher amounts of **UHC** than vapor fuel.

This is worse when the injection is direct. In the **DI** fuel injection system, liquid fuels will be injected directly into the chamber, and liquid drops will evaporate during moving toward walls. Depending on the chamber pressure and temperature, the vaporization rate varies, specifically during cold start when the wall is colder than normal operating conditions. The sources of unburned hydrocarbon emissions in **DI** engines also depend on the engine load and speed, where injection timing changes to provide homogeneous optimized combustion [183]. With an early

injection to provide a homogeneous mixture, a significant part of the fuel will be captured in the crevice volume, while with a late injection, the spray collides the piston surfaces and causes wall wetting before mixing in the air.

Hydrocarbon emissions arising from **HCCI** engines are expected to be the crevice volume, the fuel escaped from the primary combustion process, flame quenching, and the absorption and desorption of fuel vapor into oil layers of cylinder wall [184]. Moreover, it was shown that most of the unburned hydrocarbons from a port injected **HCCI** engine come from crevices [185].

Sources of **UHC** or methane slip in spark-ignition engines fuelled with natural gas are also reported as overlap, misfire, flame quenching, and crevices [186]. Changing a gasoline engine of vehicle application to a compressed natural gas engine showed a 50% reduction in terms of **UHC** [73]. The main reason for this change was the reduction of **UHC** in the oil film adsorption-desorption phenomena. Less wall fuel flow in the intake system of lean burn engines has also contributed to the gaseous engine having less **UHC** compared with a gasoline engine [72]; however, with the same power output compared with the gasoline engine, a gas engine was reported to have a 162% increase in **UHC** [187].

In general, seven classifications can be introduced for sources of **UHC** of internal combustion engines. Any specific type of fuel or combustion may consist of one or more sources in **UHC** emission production.

1. Crevice volume [188]
2. Wall layer quenching [185]
3. Pockets of partially reacted mixture [186]
4. Misfiring [189]
5. Oil films [190]
6. Deposits [191]
7. Overlap [192]

Figure 4.2 presents a flow chart of the distribution of the fraction of each of the sources on unburned hydrocarbon emission for a typical premixed spark-ignition gasoline engine. This flowchart can extensively stand for the **SI** natural gas engine except that the oil film and deposits have less influence than the other sources.

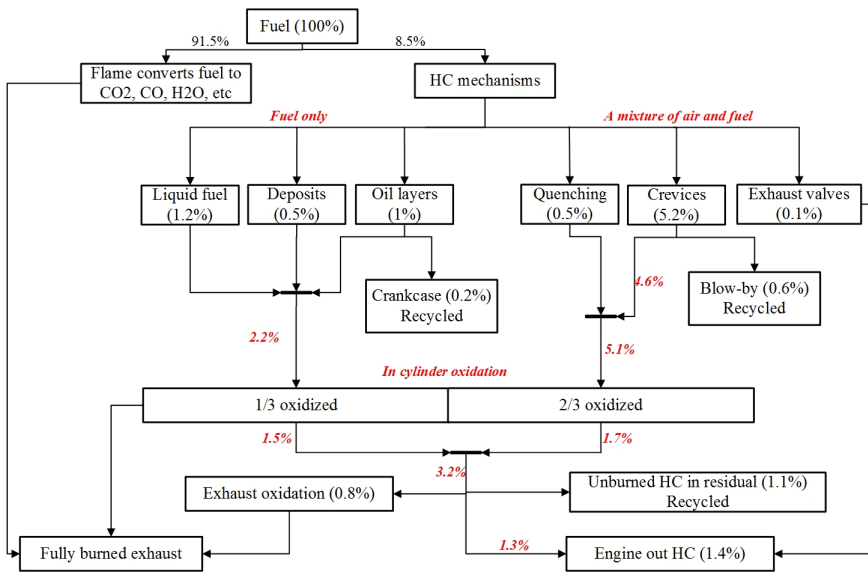


Figure 4.2: Flow chart mechanism of unburned hydrocarbon formation for a typical gasoline engine in steady-state [10].

As widely documented in the literature, the **UHC** sources are dominated by the fuel phase, combustion type, and injection properties. For a natural gas engine, where the fuel is in a gaseous mode and premixed with an injection valve before the intake valve, with some essential simplification, the **UHC** sources can be summarized into overlap, flame quenching, and crevices. Starting the initial flame by utilizing a spark plug and pre-chamber provides a high momentum gas jet entering the main chamber with good penetration. Thus, a misfire in a lean mixture with a pre-chamber rarely occurs during the normal operating condition.

4.2 Available technologies for methane slip reduction

There are three general ways to reduce methane slip from natural gas engines:

- Engine redesign
- Optimizing the combustion
- Using aftertreatment systems

Crevice volume is one of the primary sources and always gives a certain amount of methane slip. Reducing the dead volume of the combustion chamber, such as the gasket area between cylinder head and cylinder liner or clearance between

piston top and liner, reduces the amount of unburned fuel. Optimum intake and exhaust valve timing for reducing the gas exchange during the overlap is another applicable method suitable for natural gas engines compared with conventional diesel engines. However, these methods are already in use by the engine industry [45].

Optimizing the combustion includes but is not limited to a combination of performance improvements such as air-fuel ratio adjustment for various loads, developing the control systems, turbocharger matching, Miller cycle, EGR, and two-stage turbocharging. Many of these types of technology have been investigated already, but some are yet not commercialized due to complexity and high cost.

Exhaust aftertreatment systems have already been widely used to control the total emission of the engines. For gas engines with a lean mixture, palladium and platinum-based catalysts have shown a good performance of both methane and formaldehyde reduction [193] [194] [195]. However, the lifetime of these instruments limited the employment of an aftertreatment system for marine engines [45]. Wärtsilä reported acceptable methane conversion ratios in marine engines, although they also stated that the main challenge was the deactivation by sulfur [196].

4.3 Methane slip modeling

Since the challenges still exist in measuring the amount of methane slip, especially in defining the sources, methane slip modeling is represented. Only a few researchers conducted methane slip modeling, and the enhancement is demanded consistently. The review shows that a numerical model using CFD is developed to predict UHC emissions in gas engines. Results showed that increasing the air-fuel equivalence ratio and leading the mixture to leaner increases UHC from the near-wall regions due to the increased quench distance and reduced flame propagation speed [69]. Methane slip source distribution in a four-stroke dual-fuel medium-speed marine engine is done by Jensen et al. using thermodynamic zero-dimensional full engine cycle model and considering methane slip contributions from short-circuiting, crevices, and quenched flame. It was found that at low loads, the contribution from quenching was dominant, and at full load, the contribution from crevices [197]. Modeling for reduction of methane slip from a natural gas engine using gas permeation membrane by O₂ concentration control [198] and using premixed micro pilot in a dual-fuel engine in an experimental setup [199] are also conducted; however, non of the studies considered a lean burn gas engine response for transient condition, and the potential influence of time-varying load on methane slip quantity and sources

contribution is not addressed until now.

For this purpose, two numerical models are developed to predict methane slip in the natural gas engine. The first numerical model, Model 1, is part of the engine model and uses the flame speed of the main combustion rate, crevice volume and gas temperature. The second model, Model 2, simulates the amount of unburned fuel leaving the engine by a developed single-cylinder model.

The calculation procedure for both methods is based on the zones and volumes presented in Fig. 4.3. The UHC emissions are solved as scalars, incorporating a one-step post-oxidation model.

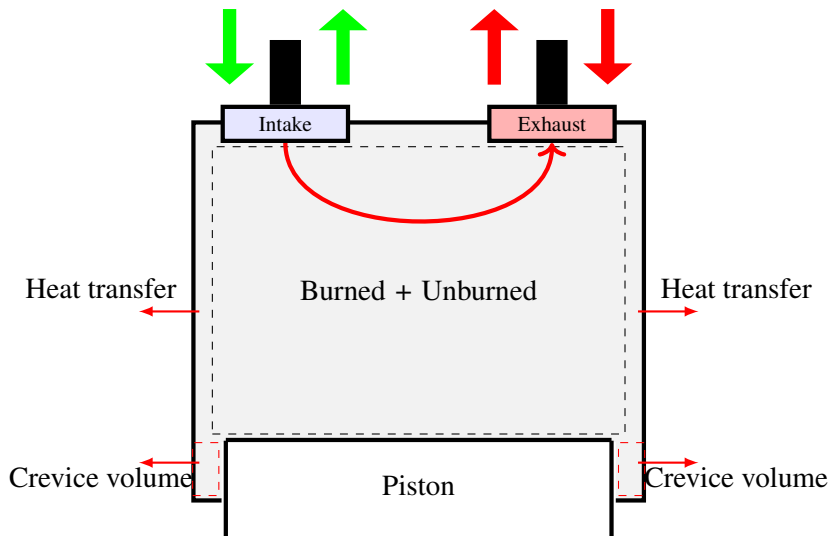


Figure 4.3: Post-combustion zones. The burned and unburned mixtures are combined into a single mixture. The crevice volume is assumed to be constant. Gas exchange only occurs when both of the valves are open.

4.3.1 Model 1

Based on the second criterion proposed by Williams [200], a flame extinguishes when it crosses through a narrow passage. This phenomenon can be explained by:

- The rate of liberation of heat by chemical reactions inside the slab must approximately balance the heat loss rate from the slab by thermal conduction.

The volume bounded by the piston, cylinder liner, top piston ring, and top piston surface is assumed as crevice volume. Besides, there is always a necessity to keep the oil temperature below 170 degrees Celsius. Thus, a flame quenching near the wall, especially between the piston and the liner, is necessary [186].

For calculating the amount of UHC by this model, two following assumptions are considered:

- The engine always follows the thumb rule to stay below the maximum allowed temperature for the oil layer,
- The crevice volume is constant, and all the fuel seized in the crevice volume remains unburned.

Equations of state determine the trapped mass inside the crevice volume in each time-step. During the compression stroke, part of the mixture enters into this volume and remains there until the maximum pressure occurs. Due to pressure reduction during the expansion stroke, the mixture starts returning to the main chamber. This return is associated with two periods. The first step is the time that the main combustion is progressing. Thus, the returned mass of fuel burns with the main combustion rate, and the energy released by the fuel contributes to the engine torque, as discussed in Chapter 3.

Any fuel left after the main combustion, including the quenched flame and the mass trapped at the crevice volume, will undergo the second step. This step is implementing a post-oxidation, which was proposed by Lavoie [201]. In his method, the heat release rate was related to the heat loss by a non-dimensional Peclet number, for two plate quenching by:

$$Pe_2 = \frac{\rho S_L c_{p,f} d_{q2}}{k_f} \quad (4.1)$$

Where ρ , S_L , $c_{p,f}$, d_{q2} and k_f are the density, laminar flame speed, specific heat at constant pressure, two plate quench distance, and thermal conductivity, respectively. With finding a relation between Peclet number and a range of pressure, he proposed the two and single plate quenching distance with a constant proportion:

$$\frac{dq_1}{dq_2} = \frac{Pe_{1,u}}{Pe_{2,u}} = 0.20 \quad (4.2)$$

And then proposed the post oxidation of Equation (4.3) for the integrated mass by an experimental expression:

$$\frac{d(HC)}{dt} = -6.7 \times 10^{15} e^{-\frac{37230}{RT}} f_{HC} f_{O_2} \left(\frac{P}{RT}\right)^2 \quad (4.3)$$

In the modeling of this work, for improving computational performance, the equation was updated into Equation (4.4),

$$R_K = A \times 2000 \times R_S e^{-\frac{1600K \times B}{T}} [f_{HC}] [f_{O_2}] \quad (4.4)$$

Where A and B are multiplier, and T is the mass-averaged overall temperature, and R_S is the burn rate calculated by the combustion model. And total UHC quantity is calculated by:

$$UHC_{total} = \int_{IVO}^{IVC} \dot{m}_f - \int_{comb} \dot{m}_f - \int_{post-comb} \dot{m}_f \quad (4.5)$$

The reported value for UHC is calculated by:

$$UHC_{BS} = \left[\frac{\sum_{i=1}^{no.cyl} (RC \cdot UHC_{total})}{Power_{brake}} \right] \left[\frac{6000 \cdot rpm_{avg}}{n_r} \right] \quad (4.6)$$

where n_r is revolutions per cycle, 2 for a 4-stroke engine. and RC is:

$$RC = 1 - \frac{m_b}{m_{total}} \quad (4.7)$$

Where m_b is the mass of burned species in cylinder i at the start of the cycle and m_{total} is the total mass of all species in cylinder i when the first exhaust valve opens.

4.3.2 Model 2

Model 1 is coupled to the output of the burning rate of the engine model and totally has four shortcomings:

1. The sources are not distinguishable,
2. The reaction rate is originally for propane, and the updated equation is based on flame burn rate,
3. The post temperature is the overall burned mixture temperature,

4. The gas exchange is not a source of UHC.

Then, Model 2 is proposed to make up for the weaknesses of Model 1. The model is initiated in [52] and [197]. The model estimates the total methane slip contribution from three sources: crevice volumes, quenched flame, and short-circuiting due to valve overlap. This model is developed in a single-cylinder rather than the entire engine with nine cylinders. A MATLAB program was developed in this context. Moreover, since the methane content in marine LNG storage is typically above 90%, the specification of pure methane is used as the fuel in this model.

For modeling, the output of the engine simulation is linked to the input of the cylinder model. This ensures that the two models (Model 1 and Model 2) simulate the same engine operating state. The contributions to the total unburned hydrocarbon emissions from different sources are then obtained from Model 2. The schematic of the model coupling is shown in Fig. 4.4. The developed model inputs are inlet and outlet pressure, inlet temperature, lambda (λ), the total energy released by the injected gaseous fuel, and the combustion coefficients. All the data are available in each cycle during the time-varying load. For instance, one minute of simulation for the engine speed of 750 rpm requires 375 interconnections between the two models.

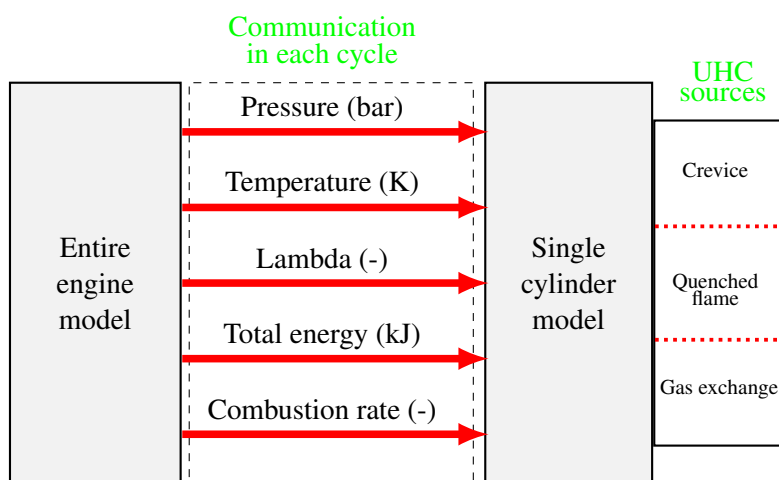
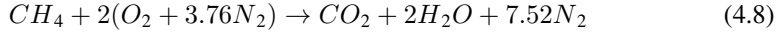


Figure 4.4: Connecting the engine model to Model 2 for determining UHC source contribution.

The procedure for one cycle of the model consists of four courses: gas exchange, compression, combustion, and expansion.

All the species are following Equation (4.8) of chemical equilibrium:



The general form of energy and the mass balance consisting of Equation(4.9) and (4.10) for the energy release and (4.11) for the mass balance provide the fraction of all species determined in the modeling.

$$\frac{dm_b}{d\theta} = \frac{\dot{Q}_c}{\sum_{i=1}^n h_{f,i}(y_{R,i} - y_{P,i})} \quad (4.9)$$

where \dot{Q}_c , the rate of heat release is modeled using the Wiebe function, by Equation(4.10) and the coefficients available from the flame burning rate during time-varying load:

$$\dot{Q}_c = Q_c \left(\frac{a(m+1)}{\theta_d} \right) \left(\frac{\theta - \theta_s}{\theta_d} \right) \exp \left(-a \left(\frac{\theta - \theta_s}{\theta_d} \right)^{m+1} \right) \quad (4.10)$$

$$\frac{dm_i}{d\theta} = \sum \dot{m}y_i + S_i \quad (4.11)$$

S_i , as $\dot{m}_{f,oxidation}$, is a source term in the mass balance of the burned+unburned mixture. With V , the volume of the zones for post oxidation, which is the total volume of the combustion chamber, and M as the molar mass, with calculating the rate of production of species using a global reaction rate proposed by Westbrook and Dyer [202], the potential of post-oxidation can be estimated as:

$$S_i = V_{cy} M_f \dot{\omega}_{f,por} \quad (4.12)$$

and the reaction rate,

$$\frac{d[HC]}{dt} = 1 \times 10^{13} e^{\frac{-48400}{RT}} [HC]^{0.7} [O_2]^{0.8} \quad (4.13)$$

It is assumed that the fuel undergoing post-oxidation is present in the cylinder wall vicinity because the fuel from the wall quench layer and fuel coming out of

the crevices are the major contribution of the post-oxidation. Hence the wall film temperature $T_f = \frac{1}{2}(T_g + T_w)$ is used in the post-oxidation evaluation.

The relative contributions from crevices, $y_{f,out}^{cr}$, short-circuiting, $y_{f,out}^{sc}$, and quenched flame, $y_{f,out}^{qu}$, to the total hydrocarbon emissions are obtained as:

$$y_{f,out}^{cr} = \frac{m_{f,out}^{cr}}{m_{f,out}} \quad (4.14)$$

$$y_{f,out}^{sc} = \frac{m_{f,out}^{sc}}{m_{f,out}} \quad (4.15)$$

$$y_{f,out}^{qu} = 1 - y_{f,out}^{cr} - y_{f,out}^{sc} \quad (4.16)$$

$m_{f,out}$ is the total unburned fuel or methane slip from the engine and can be determined by:

$$m_{f,out} = \int_{ex} \dot{m}_{out} y_{f,cy} \quad (4.17)$$

\dot{m}_{out} of the exhaust port is calculated by one-dimensional quasi-steady compressible flow. The detail is presented in Equation (3.41).

The contribution from short-circuiting to the unburned hydrocarbon emissions is obtained by integrating the product of $y_{f,cy}^{sc}$ and \dot{m}_{out} :

$$m_{f,out}^{sc} = \int_{ex} \dot{m}_{out} y_{f,cy}^{sc} \quad (4.18)$$

Where $y_{f,cy}^{sc}$ is the mass fraction of fuel inside the cylinder from the gas exchange and is defined by the mass balance equation during the gas exchange process as Equation (4.19):

$$\frac{dm_{f,cy}^{sc}}{d\theta} = \dot{m}_{in} y_{f,in}^{sc} - \dot{m}_{out} y_{f,cy}^{sc} - \dot{m}_{cr} y_{f,cy}^{sc} \quad (4.19)$$

The instantaneous in-cylinder mass fraction of fuel from the crevices $y_{f,cy}^{cr}$ is also calculated from the mass balance equation:

$$\frac{dm_{f,cy}^{cr}}{d\theta} = -\dot{m}_{cr}y_{f,cy}^{cr} - \frac{dm_b}{d\theta}y_{f,ubg}^{cr} - (\dot{m}_{out} - \dot{m}_{in})y_{f,cy}^{cr} + S_i \frac{m_{f,cy}^{cr}}{m_{f,cy}} \quad (4.20)$$

The contribution to the total unburned hydrocarbon emissions from the crevices $m_{f,out}^{cr}$ is then determined by integrating the product of $y_{f,cy}^{cr}$ and the total mass flow rate out of the engine, \dot{m}_{out} , over the exhaust phase of the engine cycle:

$$m_{f,out}^{cr} = \int_{ex} \dot{m}_{out} y_{f,cy}^{cr} \quad (4.21)$$

A separate mass balance equation for the total fuel mass in the cylinder is used to determine the instantaneous in-cylinder fuel mass fraction $y_{f,cy}$.

and, \dot{m}_{cr} in Equation(4.20) is determined by differentiation of the ideal gas law applied for the crevice volume:

$$\dot{m}_{cr} = \frac{V_{cr}}{R_{cr}T_{cr}} \frac{dP}{d\theta} \quad (4.22)$$

$y_{f,out}^{qu}$ is the relative contribution to the total hydrocarbon emissions from quenched flame. As seen from the calculation of $y_{f,out}^{qu}$, it is assumed in the model that unburned hydrocarbon emissions are not due to crevices and short-circuiting, is from quenched flame.

Chapter 5

Results and Discussion

This chapter summarizes the simulation results and answers to the objectives motivated and addressed by the research questions.

Most of the results are also presented in papers attached in Appendix A. The motivations of the research addressed in chapter 1 are repeated here as follows:

Research objective 1

What are the primary sources of methane slip in lean burn spark-ignition engines, especially during transient conditions?

Research objective 2

What is the influence of wave characteristics on transient loads and marine gas engine response in terms of combustion efficiency and emissions?

Research objective 3

How to stabilize the engine during transient conditions and improve the combustion?

Research objective 4

How is the engine response concerning sea transient conditions in part-loads?

5.1 Research objective 1 (Paper 1 and Paper 4)

This section identifies the influence of a time-varying load on the quantity of methane slip and the contribution of each source on total methane slip. In two individual cases, the quantity and sources' contribution are discussed.

A regular-sinusoidal torque is used for the first part of modeling, as shown in Fig. 5.1. With assuming a constant frequency for the load, four cases, with 5, 10, 15,

and 20% of the load variation are considered. 20% load variation means $\pm 10\%$ around the nominal value. The mean value is 50000 Nm, which is the nominal torque of the engine at 750 rpm. Thus, the load is always between 90% and 110% of nominal torque and can be classified as a full load condition.

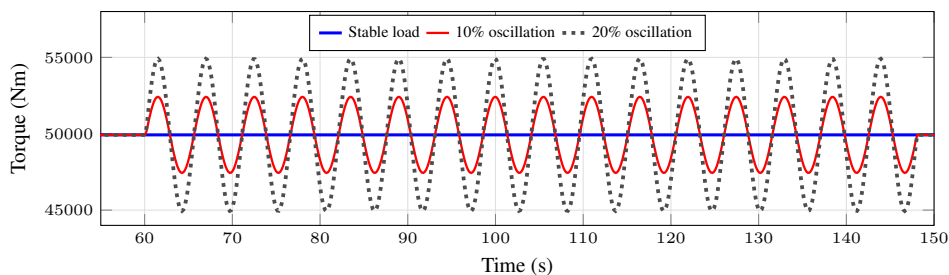


Figure 5.1: Regular harmonic, sinusoidal torques around the full load.

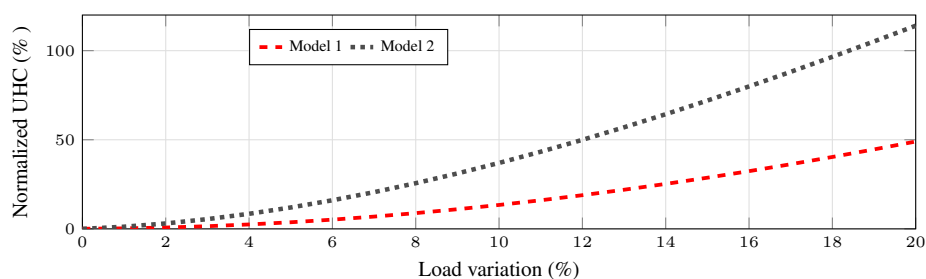


Figure 5.2: Increase of methane slip with load fluctuation.

Fig. 5.2 shows the increasing percentage of the methane slip with the load variation in both models, Model 1 and Model 2, (models are discussed in Chapter 4). The X-axis gives the load variation percentage, and the Y-axis is the normalized UHC value. The normalization factor is the measured value in the full load. 100% means a double quantity of UHC compared to steady-state. As can be seen, both the models presented a non-linearized increment of UHC with higher load fluctuation. 20% of the load change resulted in almost 50% and 115% extra UHC with Model 1 and Model 2, respectively. The gap between the two models is consistent in each load variation percentage, and two reasons can interpret it:

1. Model 1 does not consider the source of gas exchange methane slip,
2. The post-oxidation process in Model 2 is lighter than in Model 1 due to the lower average temperature considered for Model 2.

Fig. 5.3 presents how the source contribution in total UHC changes when the amplitude of the sinusoidal load increases. With zero on the X-axis, the result is presenting a steady condition. As shown, crevice volume has the most contribution of total UHC with 74%. Quenched flame and gas exchanges are 23% and 3% of the total quantity, respectively. During all load oscillation, the crevice volume still showed the highest fraction but with a negative slope. This output confirms that with more load fluctuation, crevice volume may not be the primary source of methane slip and is substituted with the UHC of quenched flame. The percentage of quenched flame changed from 20% in stable loading to 40% in maximum oscillation. The gas exchange process contribution was 3% in all of the conditions, and stayed unchanged with load variation. The reason is the dependency of the gas exchange process to the inlet boost pressure, scavenging process, exhaust pressure, and valve discharge coefficients. The load variation had no impact on these parameters, and the UHC quantity of this source remains unchanged. Fig. 5.4 presents the normalized mass of methane slip for each source for the maximum studied load fluctuation, 20%, to show the sources variation. It must be noted that the mass of each source is normalized with its own value in the steady-state. As demonstrated, the difference in the mass of crevice volume and gas exchanges compared with the steady-state is negligible, but the quenched normalized mass increases to 17 and reduces to zero. The increase occurs when the load reduces, and there is an extra air ratio in the main chamber, as shown in Fig. 5.5. The value of zero occurs when the load increases and the mixture is rich. The lean mixture weakens the flame propagation during the main combustion and reduces the mixture temperature for post-oxidation. Therefore, the gap between the curves is strongly relevant to the post-oxidation, not the gas exchange source.

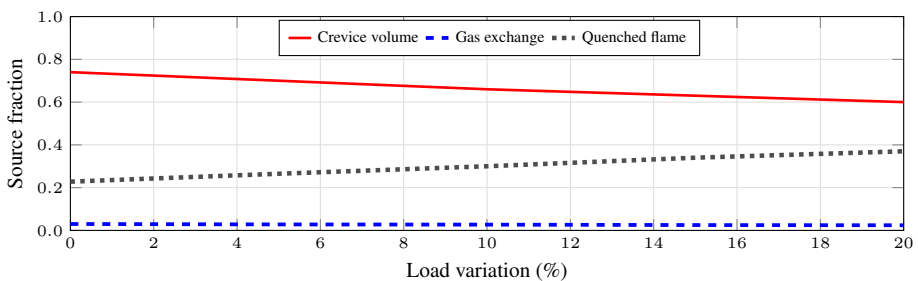


Figure 5.3: Methane slip source contribution during load fluctuation.

The second sinusoidal load implemented on the engine with different wave frequencies and amplitude is shown in Fig. 5.6. It is immediately apparent that there are two differences between the imposed torques. The new imposed torque has a lower load during a steady-state. The torque is 36000 Nm for the time

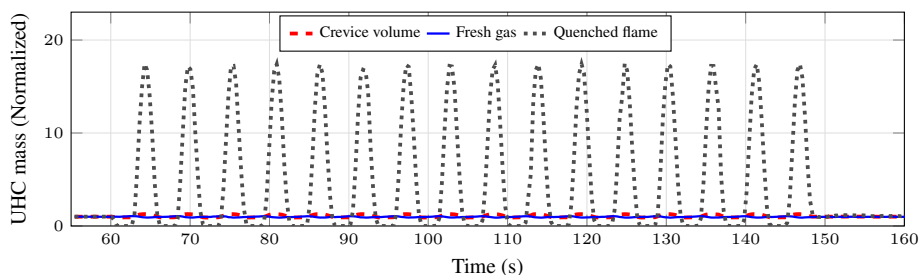


Figure 5.4: Quenched flame has the most variation during time-varying load.

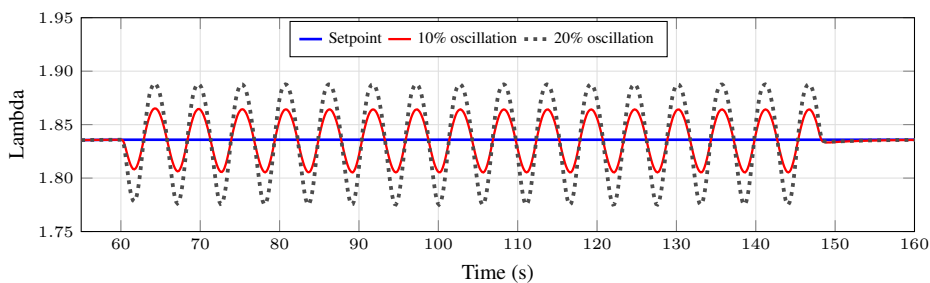


Figure 5.5: Variation of excess air ratio due to engine response delay during propeller load fluctuation.

before 160 seconds. Next is the frequency of the torque, which is lower than in the previous case. The torque period is now more extended, and as a consequence, the engine has more time to respond to the variation. The load changes between 46000 Nm as the maximum and 28000 Nm as the minimum. Fig. 5.7(a)-5.7(c) presents the significance of each source for the implemented time-varying load. Crevice volume and quenched flame have played almost the same role with around 50% of total UHC, while the gas exchange is less than 2%. As expected, the change of gas exchange source is only due to the variation of total UHC mass-produced by other sources. When the torque increases, both the crevice volume and gas exchange percentage increase, but the quenched flame reduces almost to zero. An opposite trend occurs for load reduction.

All in all, the torque mean value throughout the load implementation and fluctuation amplitude play a remarkable role in total UHC value, and among the sources, the quenched flame has by far the most contribution and variation during the transient condition.

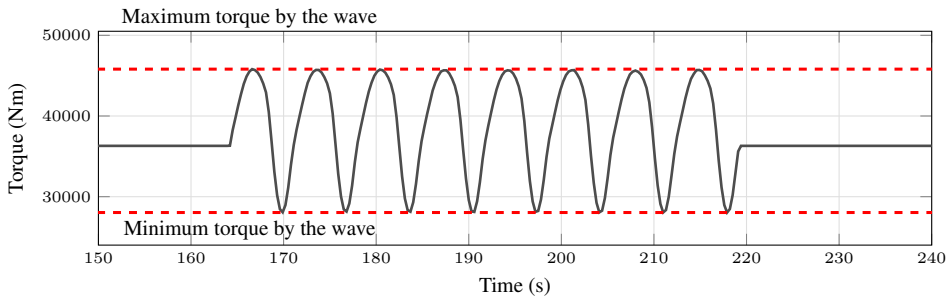


Figure 5.6: A medium harmonic torque. The mean value is 70% nominal torque at 750 rpm.

5.2 Research objective 2 (Paper 2 and Paper 3)

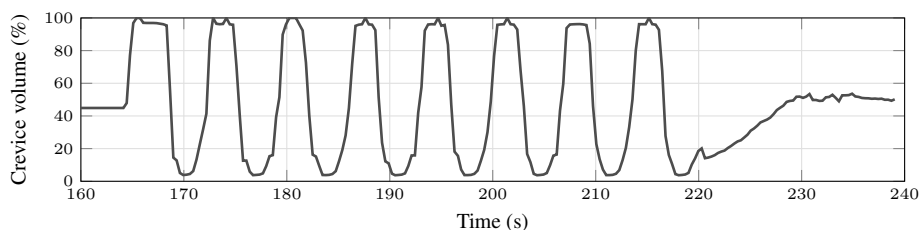
This section identifies the response of the engine and propulsion system in a range of wave characteristics.

A ship travel encounters a domain of wave amplitude and frequency. Changes in the flow field cause fluctuations in propeller thrust and torque. Moreover, the wave causes a periodic change in propeller due to heave and pitch, resulting in a fluctuating load on the engine. In order to consider the engine response regarding all the load variations, a co-simulation was performed. The engine-propeller model simulated sixty-four regular waves. This number is obtained by combining four wave amplitudes, wave directions, and wavelengths. The wave direction is relative to the ship, and 180° is considered as a head wave. Wave characteristics are shown in Table 5.1.

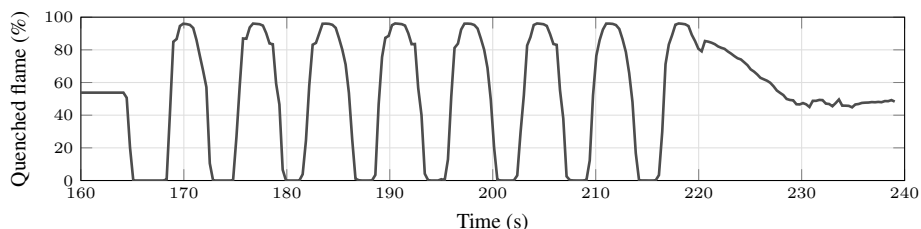
Fig. 5.8 presents the amplitude and frequency of the torques estimated by the propeller model in various wavelengths, wave direction, and wave amplitude. By keeping the ship speed constant, the highest propeller thrust occurs with $\frac{\lambda}{L_{PP}} = 1$, where the added resistance is maximum. However, the highest variation occurs with θ between 60 - 120 and $\frac{\lambda}{L_{PP}} = 1.2$, where the propeller operates in proximity or above the water surface.

Table 5.1: Periodic waves characteristics

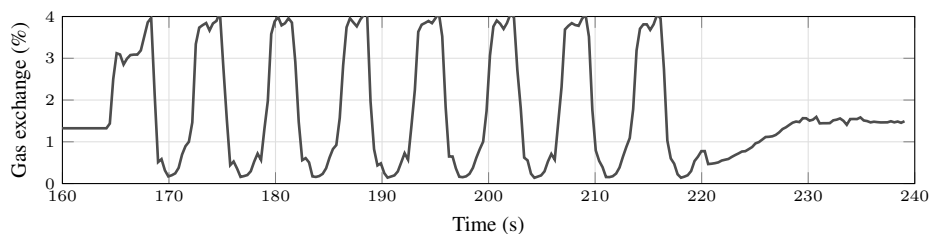
Length (λ/L_{PP})	Amplitude (m)	Direction (θ)
0.6	0.5	0
0.8	1	60
1	1.5	120
1.2	2	180



(a) The UHC percentage produced by the crevice volume reduces if the load declines from full load to 70%.



(b) Quenched flame as the main influential source of variation of total UHC during transient conditions when the load in steady-state is 70% of nominal torque.

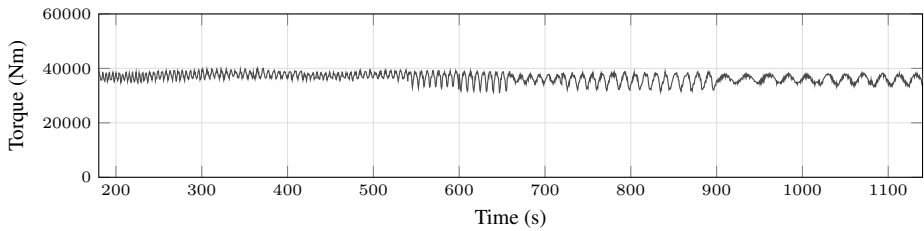


(c) The gas exchange process has a minimum impact on total UHC even in lower loads.

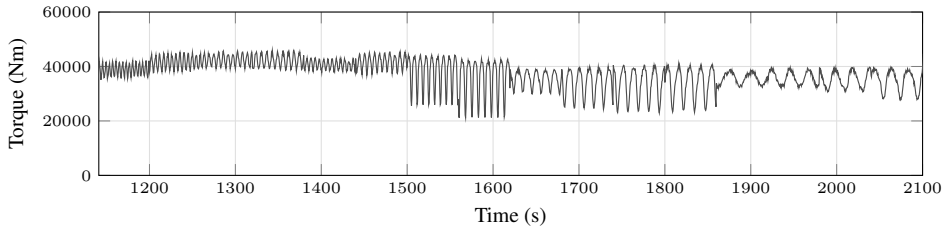
Figure 5.7: The sources of UHC. The UHC percentage of crevice volume and quenched flame are contrasted during the time, while part of the variation on crevice contribution is due to remarkable change of quenched flame source.

The analysis of the results of engine performance in various wave frequencies and amplitude is performed. During the time-varying torque, the engine speed is consistently fluctuating around 750 rpm. This stability is indebted to the high mass moment of inertia of the flywheel, connecting shaft, the water, and the satisfactory performance of the fuel control system.

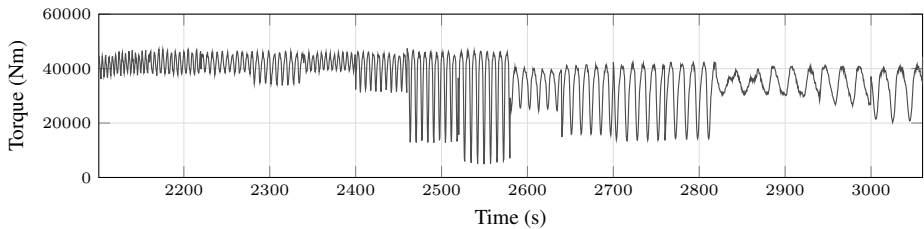
Even the fuel system reacted rapidly to the load variation and kept the engine speed close to the desired value; the specific fuel consumption increased significantly. Fig. 5.9(a) confirm that with only $A=0.5$ and $A=1.0$ meter, there is no notable extra BSFC. With $A=1.5$ and 2 meters, almost all the wavelengths and wave directions resulted in a higher amount of specific fuel consumption. While part of this extra BSFC is due to lower mean load, the analysis shows that this rise is also due



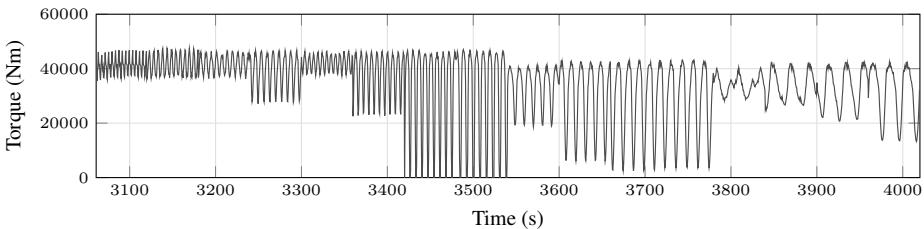
(a) Calculated torque in co-simulation based on regular waves with a wave amplitude of 0.5 meters.



(b) Calculated torque in co-simulation based on regular waves with a wave amplitude of 1.0 meter.



(c) Calculated torque in co-simulation based on regular waves with a wave amplitude of 1.5 meters.



(d) Calculated torque in co-simulation based on regular waves with a wave amplitude of 2.0 meters.

Figure 5.8: The calculated torque by the propeller modeling, which is an input to the engine model.

to combustion efficiency reduction. Since the flame is not propagated steadily during the time-varying load, part of the fuel mixture, particularly close to the wall, remains unburned, and the combustion efficiency reduces. This phenomenon is extremely relevant to the excess air ratio, where any small variation in too lean mixture causes flame extinguishing.

The unstable excess air ratio and incomplete combustion influence the emission formation because the UHC and NO_x are highly sensitive to the extra air and combustion maximum temperature, respectively. UHC distribution is shown in Fig. 5.9(b). As expected, it obeys the same tendency as the BSFC distribution. Any additional air resulted in the higher unburned fuel, which does not participate in the main combustion, and the additional air also resulted in lower temperature during post-combustion. In contrast, there is also a slightly higher amount of NO_x in the contour, as shown in Fig. 5.9(c). This extra NO_x confirms the importance of the load rise and rich mixture impact in transient conditions. The NO_x quantity may reduce during the load reduction to even a half value, but it also increases several times when the load suddenly increases. Therefore, the average gives almost three times more when the wavelength is 1-1.2, and wave direction is between 60-120.

Moreover, engine knock analysis confirms that with A=1.5 m and higher, there is the possibility of knock in main cylinders. This must be highlighted that the model and the outputs for the knock are not validated by the measured data, and the outputs are a rough estimation based on expected results in stable condition. Regarding this output, knock only may occur when there is a significant fluctuation in the engine load.

5.3 Research objective 3 (Paper 4, Paper 5 and Paper 7)

This section identifies how to stabilize the engine and improve combustion during transient conditions.

The previous sections demonstrated the importance of transient conditions and disparity with the steady condition on the engine. The results confirmed that the differences stem from the response delay of the engine on the airflow. This section examined several methods to find a practical solution for improving this delay, focusing on methane slip reduction. During the transient condition, the mechanical delay of the turbocharger, the control system delay of PID controllers, and the dynamic delay of the fluid flow in the intake manifold have been assigned as the main elements.

The results are split into four divisions.

Part 1:

In order to examine the mechanical delay by the turbocharger, five turbocharger shaft moment of inertia is replaced by the initial inertia. The new shafts have less and more mass of moment inertia, respectively. If the base is assumed a coefficient of one, Lag 1 to Lag 5 represents 0.5, 0.75, 1.25, 1.50, and 2.0. Fig. 5.10 is the imposed torque on the engine modeling for turbocharger shaft moment of inertia

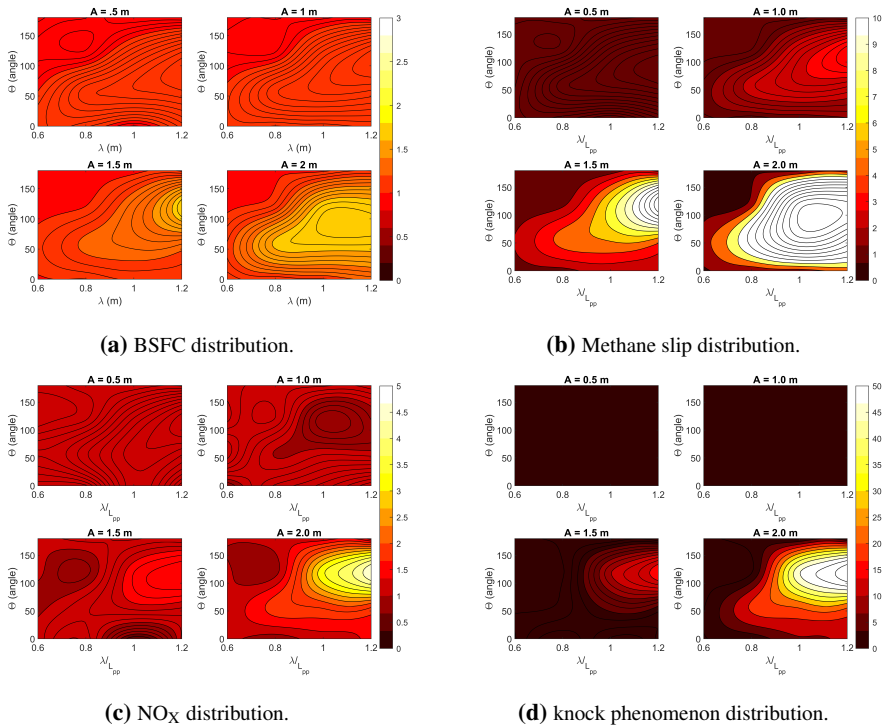


Figure 5.9: The contour representation of the mean values of the model output with various wave characteristics.

assessment. Fig. 5.11 and Fig. 5.12 show the results by applying the new shaft inertia. The higher shaft inertia has the same variation as the lower shaft inertia. Except for the difference on small time scales oscillation for UHC quantity, the mean value for all of the cases is almost equal. This illustrates that the global fluctuation is mainly pertinent to the imposed torque frequency and amplitude on the entire engine, and the turbocharger inertia has an insignificant impact on engine total response. In contrast, the response of the engine with higher shaft inertia got even slower, and the less flexibility in the engine during higher loads resulted in higher NO_x during load rise.

Part 2:

The effect of the control system and dynamic delay are performed together since the placement of the controller to adjust the air ratio subsequently influences the fluid dynamic. The engine was already equipped with a VTG controller to regulate the excess air ratio. The result of this controller is presented together with seven practical concepts for comparison. Thus, a total of eight controlling methods are

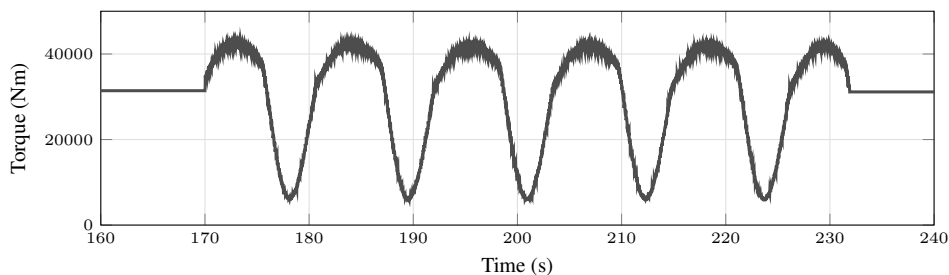


Figure 5.10: The imposed torque for investigation of turbocharger shaft moment of inertia on engine response.

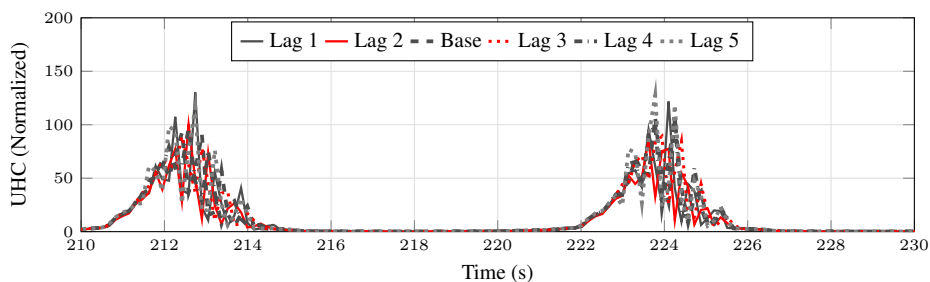


Figure 5.11: Increasing the mass moment of inertia from Lag 1 to Lag 6 with Base as the inertia of the original shaft has negligible influence on methane slip.

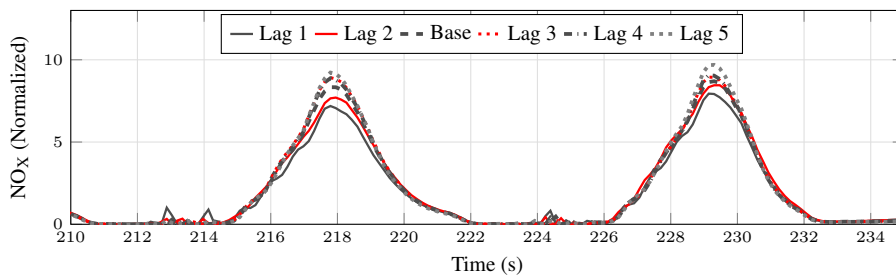


Figure 5.12: Total NO_x value is higher with a higher mass moment of inertia due to the slower response of the turbocharger.

discussed with an imposed torque of Fig. 5.6. These controllers follow either a closed-loop PID algorithm, an open-loop system, or model predictive controller. They are listed as follows:

1. Variable turbine geometry (VTG)

2. Wastegate controller
3. Throttle controller
4. Over-boost adjuster
5. Ignition timing
6. PREPID method
7. Model predictive control (MPC)
8. Solenoid method

The schematic of the implemented controllers is shown for the throttle controller in Fig. 5.13(a) and the PREPID method in Fig. 5.13(b). More details of the schematics and concepts are presented in Paper 4. The controllers are employed to mitigate the sudden excess air ratio variation and reduce the UHC formation.

The VTG includes a compressor, a connecting shaft, and an adjustable turbine. The controller regulates the cross-section area of the turbine inlet based upon the ratio setpoint. This setpoint is usually a function of the load in CI engines and the air-fuel ratio in SI engines. In this study, the adjustable turbine or rack position was actuated among eight different input maps from the manufacturer.

The wastegate controller restricts the amount of exhaust gas through the turbine by bleeding out the extra gas into the atmosphere. It acts as a pressure relief valve that controls the boost pressure in the outlet of the compressor, diverting excess exhaust gases away from the turbine wheel.

The mechanisms considered for the throttle and over-boost adjuster are identical. The throttle controller is located before the intake manifold to restrict the extra airflow, and the over-boost adjuster is located at the end of the intake manifold. This will show the significance of the dynamic of the flow of intake manifold on the total response. Moreover, with a partially opened throttle, there is a pressure drop between turbocharger output and cylinder input, which may influence the total fluid flow, but with an over-boost adjuster, this drawback is eliminated.

While the mentioned controllers followed the closed-loop PID controlling method, spark-timing and PREPID methods are assumed as open-loop controllers. The flame in the lean burn spark-ignition gas engines can not ideally propagate with a direct spark plug. In order to guarantee stable combustion, the flame ignites with a rich mixture in the pre-chamber. In the modeling, a large size spark plug was replaced to produce an equal flame status. In the previous sections, the ignition

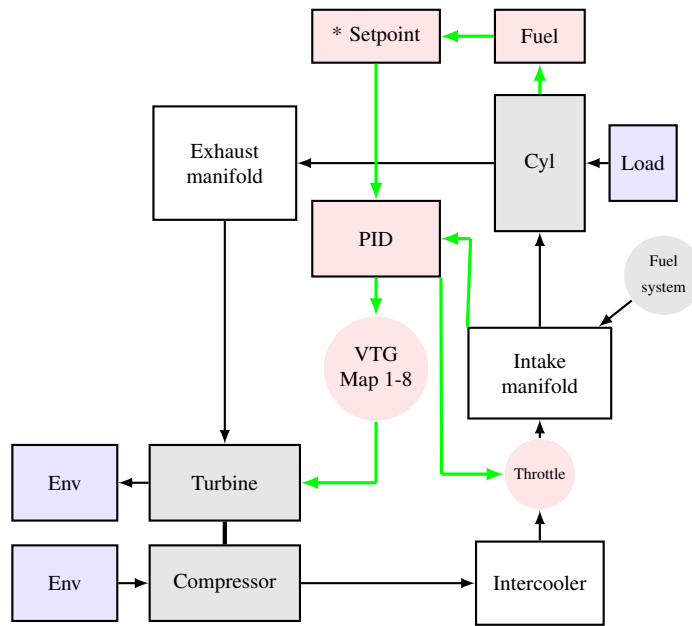
timing was constant during the load variation. With the remarkable oscillation on the air-fuel ratio, as shown in Fig. 5.14, new sets of spark-timing are proposed. The ignition timing is changing based on the air-fuel ratio between 28-34. For instance, in Case 1, the richest mixture with a ratio of 28 will be ignited at 11 CA BTDC, while the leanest mixture with a ratio of 34 is ignited at 15 BTDC. The rest of the ratio will be interpolated.

In addition, a new method, called PREPID, is proposed. In this method, the turbocharger feedback to the load change with the VTG controller was used as a lookup table a few milliseconds in advance. A perfect prediction of the torque is assumed for implementing the table. The closed-loop controller is active until the engine model reaches stability. Afterward, the PREPID provides the input to the turbocharge vane position.

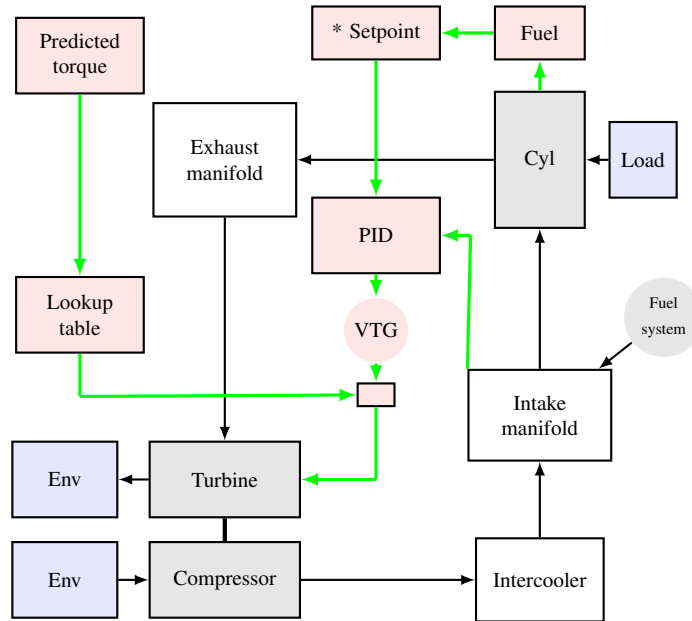
An MPC can anticipate future events to control the actuators accordingly. Using the dynamic equations, an MPC compensates the engine response and minimizes the error between the setpoint and the model output. The main challenge with the MPC is finding a linearized model. Providing a simple linearized equation as a replacement for the entire engine model is scarcely feasible. The idea was to predict the response of the turbocharger based on the exhaust pressure. Therefore, the simplified equation of state is performed for the exhaust pressure, and the output of the MPC box, MV, is calculated by the thermodynamic equations.

Finally, the solenoid method is innovated to eliminate the turbocharger time-lag without the problems of closed-loop controllers response time and dependence on MPC and PREPID method predictability. For this purpose, a solenoid valve that operates electromechanically and allows the fluid to flow when it is electrically energized is installed at the end of the intake manifold to provide the fastest reaction against excess air. During the steady-state conditions, the plug of the valve is closed and does not influence engine performance. Whenever the air-fuel ratio exceeded the setpoint during the transient state, it fully opened within a response time of around 30 ms and fewer. This quick response has a positive impact on controlling the higher excess air ratio, but it may also cause a rapid decline in the excess air rate when the load increases and result in a rich mixture. Therefore, selecting the correct diameter for the solenoid valve is crucial. Several diameters were imposed to find a suitable diameter for this engine and a diameter of 50 mm was chosen for the final state.

A comparison of the results is presented in Table 5.2. This table presents the effect of the implemented methods on the BSFC, UHC, and NO_x formation on the transient condition normalized by the steady-state quantity. The results confirm that there was always a trade-off between the emission compounds. It must be



(a) Schematic of controlling the airflow using an active throttle.



(b) Schematic of controlling the airflow using the PREPID method.

Figure 5.13: Schematic of two of the controlling methods.

noted that the VTG, wastegate, MPC and PREPID are using one controller to adjust the excess air ratio, while the rest of the methods use the VTG controller as a supportive controller as well. Table 5.2 shows that using VTG results in a 119% rise in UHC while wastegate caused a 56% increase. Although wastegate delivered less UHC, it resulted in almost double NO_x quantity. Any further change in the diameter of a wastegate did not improve the UHC formation but increased the NO_x to even further value. In contrast, any attempt at reducing the NO_x by tuning the controller system increased the UHC quantity.

Both the throttle and over-boost adjuster contributed to almost the same fuel consumption and emission formation. Ignition timing focusing on UHC reduction with advance the spark timing showed no enhancement on UHC total value. PREPID method produced almost the same results as the wastegate controller. Advancing or retarding the implemented PREPID lookup table has shown the least improvement. In comparison with the wastegate method, with the PREPID, the method suffers from two defects:

1. Providing a comprehensive lookup table for all of the transient conditions
2. Controlling the engine when the unexpected variation occurs

The primary outputs of the modeling with MPC showed that the implemented plant and created MPC could not predict the required input to the engine model during rapid transient load. Though, the simplification of the model caused an incorrect output for the VTG command.

With applying the solenoid valve, if the ratio increases to more than the setpoint, the valve opens, and the excess ratio discharges into the atmosphere. The results clearly revealed that the solenoid method is extremely applicable for the UHC reduction, where the average quantity is subtracted from 2.19 to almost one. The quantity of one means no disparity compared with the steady-state. However, the increase of NO_x is remarkable. This compound increased by almost 95%. It must be highlighted that the harmonic load implemented during transient conditions had an average of 38500 Nm, while the load during stationary was 36300 Nm. Thus, engine loading increased by 6%. Based on the measured data, this load increment results in an almost 5% increase in NO_x.

Since the ignition timing improves the NO_x formation, four additional ignition timing have been set, as shown in Fig. 5.15. In each case, the focus is retarding the ignition timing during the lower excess ratio. This range contrasts with the ignition timing domain of Fig. 5.14, where it was focused on the higher excess ratio. The timing was retarded several times with maximum retardation to TDC,

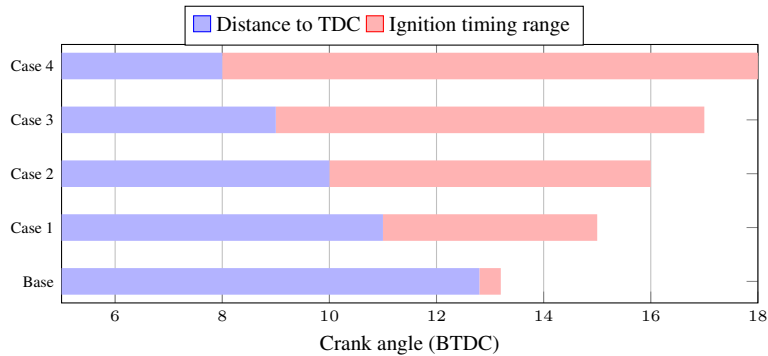


Figure 5.14: Spark ignition timing for promoting flame propagation and reducing the UHC formation. The red section shows the spark timing as a function of excess air ratio, and the blue section shows the distance to the top dead center.

Table 5.2: Performance and emission of the engine after applying the UHC reduction methods.

Method	BSFC	UHC	NO _x
Steady-state	1.0	1.0	1.0
VTG	1.068	2.193	1.017
Wastegate	1.044	1.568	1.742
Throttle	1.058	1.930	1.124
Adjuster	1.056	1.899	1.237
Ignition timing	1.058	2.056	1.002
PREPID	1.043	1.636	1.479
MPC	fail	fail	fail
Solenoid	1.014	1.023	1.944

and the results are shown in Table 5.3. As can be seen, with retarding the ignition timing, the NO_x reduced remarkably from 1.94 to 1.129, which means an 80% reduction, with a slight drawback on UHC and BSFC.

In conclusion, using the solenoid method and retarding the ignition timing contributed to only 2% more BSFC, 6% more UHC, and 13% more in NO_x in the transient condition compared with steady-state.

Part 3:

The engine operating on the ship is already equipped with a throttle controller to adjust the flow rate for loads lower than 30% of the nominal value. This throttle restricts the extra air when the minimum turbocharger flow is still higher than the

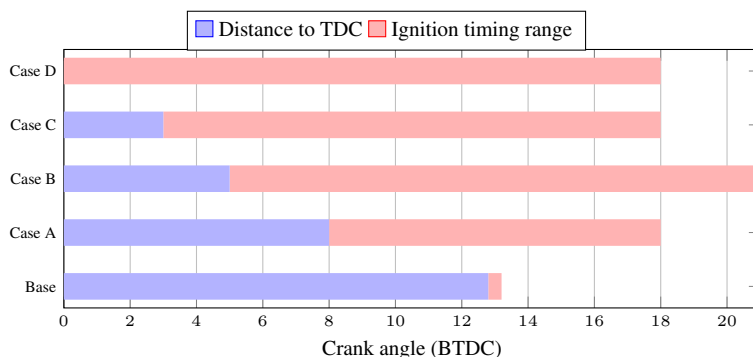


Figure 5.15: A new set of spark ignition timing for reducing NO_x . The timing is imposed based on the air-fuel ratio between 28 to 34 (to cover all lambda variation between 1.6 to 2.0).

Table 5.3: Performance and emission of the engine after retarding the spark ignition timing.

Method	BSFC	UHC	NO_x
Solenoid + Ignition timing base	1.014	1.023	1.944
Solenoid + Case A	1.015	1.016	1.596
Solenoid + Case B	1.016	1.019	1.417
Solenoid + Case C	1.018	1.042	1.284
Solenoid + Case D	1.022	1.067	1.129

demanded flow. But, it was shown in Table 5.2, the throttle did not present any improvement on engine response during the transient condition. For this purpose, and to examine how the throttle will react during lower loads of transient condition, a load from a severe case is chosen as shown in Fig. 5.16, where the brake torque varies between 48000 Nm and 0 Nm. For a better comparison, the steady-state is also modeled, and the load changes from full load to 5% nominal load, including 100%, 75%, 50%, 25%, 20%, 15%, 10%, and 5%. Therefore, for steady-state, the modeling simulated eight steps with 700 seconds duration. This provided sufficient time in each step to cover the numerical error and defines the steady-state. When the load was reduced to 25%, the throttle got active and restricted the additional air.

The results of using a throttle compared with eliminating the throttle for the loads lower than 30% of nominal torque are shown in Fig. 5.17. Fig. 5.17(a) shows that the engine is stabilized with the throttle valve during steady-state, and the UHC formation never rises significantly. But, without the throttle, the

UHC value reached 80, meaning a flame quenching or even the possibility of misfiring. On the contrary, due to the throttle delay, the engine output with and without throttle shows the least discrepancy during the transient condition, shown in Fig. 5.17(b), and the UHC formation with and without throttle is about the same. This demonstrates that the load changes faster than the throttle response in this frequency.

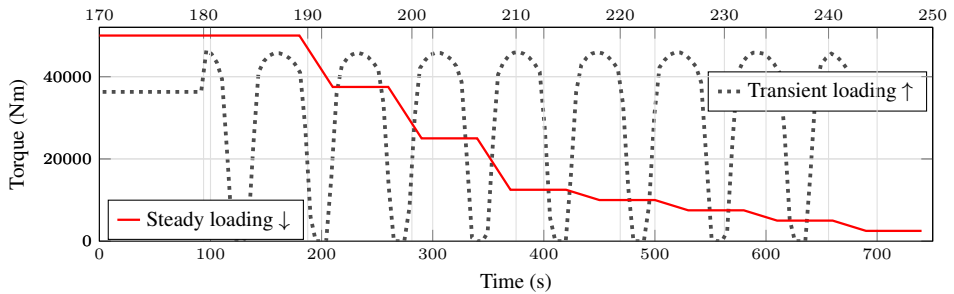
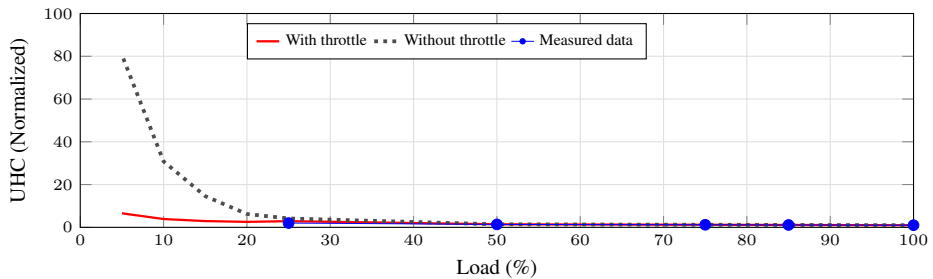
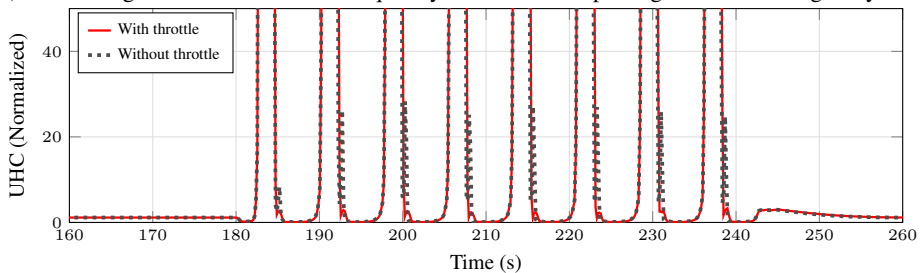


Figure 5.16: The implemented steady loading and a severe transient torque for comparing the response of the engine with and without a throttle during the lower loads.



(a) Controlling the excess air and consequently the methane slip using a throttle during steady-state.



(b) An air throttle showed the least influence on controlling the combustion during transient condition.

Figure 5.17: The influence of the air throttle in both steady-state and transient conditions.

Part 4:

One way to enhance the engine response is to integrate mechanical and electrical drive components on the propeller shaft. This is called a hybrid propulsion system. The main objective of this combination is to reduce fuel consumption and emission formation by approaching the optimum operating curve of the main engine. This integrated propulsion system improves engine performance during low-load and high-load situations. The hybrid concept initiates by compensating part of the required load by an electrified section stored in the Energy Storage System, and the engine is sized and designed based on the mean peak load demands. In the hybrid concept, the electric motor operates as a **PTI** that can drive the propeller shaft in low loads, while during the high-load condition, the electric motor provides part of the required torques. The configuration is shown in Fig. 5.18.

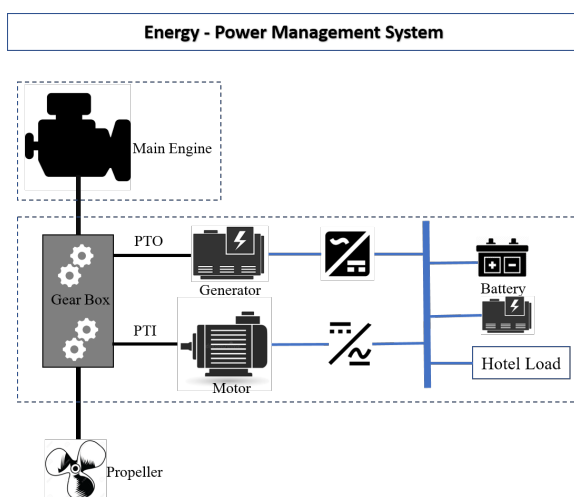


Figure 5.18: Hybrid propulsion system configuration.

Considering the hybrid concept, the dynamic loading calculated by a wave amplitude of two meters can be smoothed to a new loading, as shown in Fig. 5.19.

Fig. 5.20 presents that the hybrid propulsion installment controlled the methane slip overshoot during the transient condition. It is also found that the relative deviation of the methane slip with and without the hybrid system is negligible during load increment, when the **UHC** value is less than one.

Activating the hybrid system during higher loads and reducing the engine maximum power generation, the rich mixture zone mitigates and a more balanced excess air ratio area is achievable. This area has a lower maximum temperature than the normal operating condition, and thus, as can be seen in Fig. 5.21, a

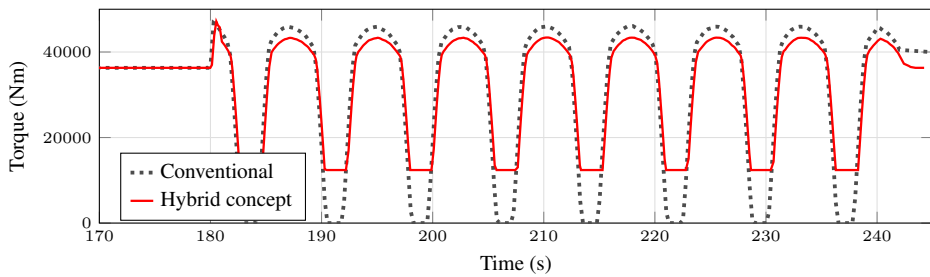


Figure 5.19: Smoothed load using a hybrid configuration.

remarkable reduction of NO_x compound is obtained. The average value during the transient condition is also added to the figure. With supposing the average NO_x quantity for the stable condition to one, the mean value for the entire transient condition without a hybrid propulsion system showed a 340% increment. NO_x formation with the hybrid propulsion system, however, confirmed a 214% rise. This means that the NO_x with the implemented hybrid system reduced up to almost 40%. This reduction is only during the higher loads, where the peak of NO_x output is reduced from the maximum value of 15 to 8.

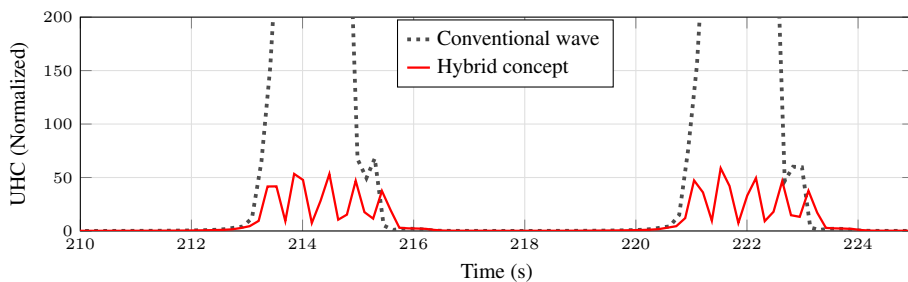


Figure 5.20: The amount of unburned hydrocarbon reduced considerably with the hybrid propulsion concept.

5.4 Research objective 4 (Paper 6)

This section identifies the performance and emission of the natural gas engine in the lower operational load.

Since the engine does not entirely operate in full loads in each voyage, considering maneuvering conditions or warm-up loads, modeling and analyzing the engine response for the part-load is necessary. In the previous sections, the lower loads were only examined during a harmonic wave.

The data from the ship voyage is available for one month and illustrates that

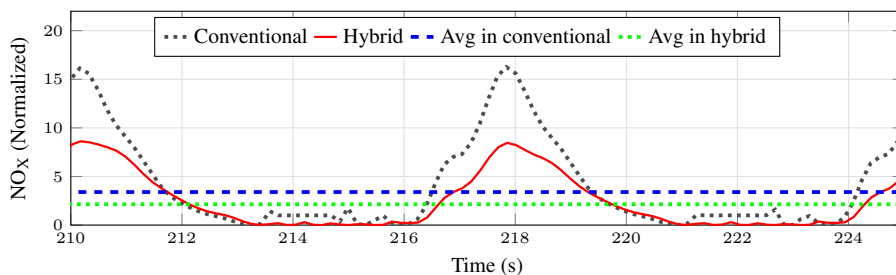
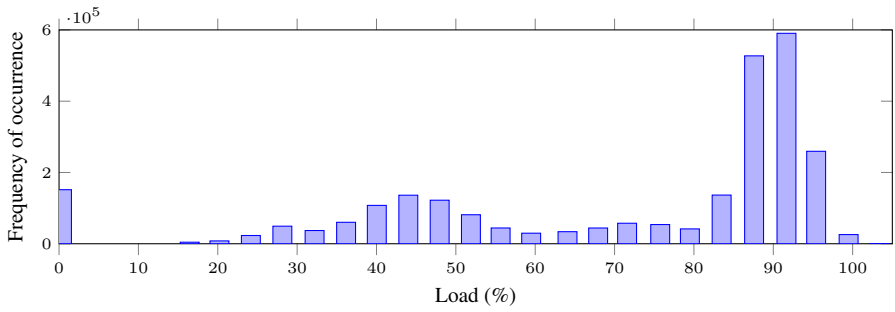


Figure 5.21: Notable reduction of NO_x during load increase with the hybrid implementation.

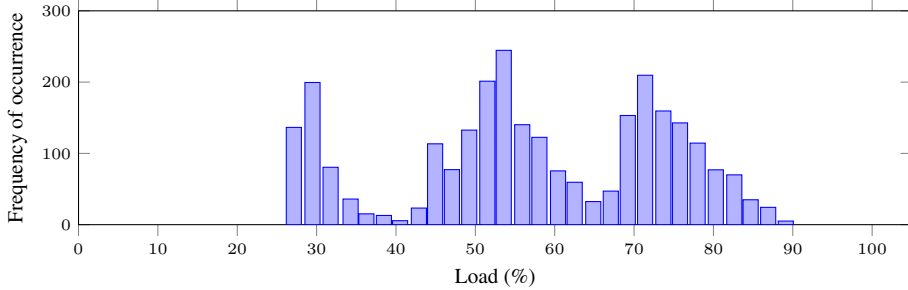
the engine usually works in two operating conditions: between 30 to 55 % and between 80-95% load, shown in Fig. 5.22(a). Therefore, this section is considered with an irregular transient condition for covering all of the loads between 30 and 90%. Since one-month simulation is not possible due to computational time, 50 minutes of the operational load is considered, with a frequency of occurrence as shown in Fig. 5.22(b). The torque and engine speed variations are shown in Fig. 5.23. As can be seen, the irregular speed changes from 500 to 720 rpm and the irregular load varies between 6000Nm and 30000Nm.

For the lower loads, when the turbine geometry can not prevent additional airflow, the throttle is active and restricts the higher air-fuel ratio. Previous results mostly focused on the amplitude of the torque on the engine response, and it was shown that the flame quench plays a dominant role in UHC increasing when the load variation increases. However, the new implementation with a small amplitude and a high frequency shows that the engine is not sensitive to the small variations during higher loads. Fig. 5.24 and Fig. 5.25 confirm that the engine emission increases if the load is less than 70%. Comparing these two figures with the implemented torque and speed illustrates the importance of operating load with small variation and a high frequency. Respecting the time between 500 to 2000, if one or both of the torque and speed are high, methane slip change is small. The time between 1000 to 1500, where both variables are high, NO_x quantity is also small, and fluctuation occurs only with tiny deviation.

An average-based output for a better presentation of the results shows how the transient condition influences the emission formation during part-loads. As can be seen in Fig. 5.26, there is a big gap between the available measured data of steady-state and the modeling output. With load reduction and a higher possibility of flame quenching, the UHC increases to almost double quantity in steady-state. However, during the transient condition, any slight variation of the load with the high frequency results in a deviation in air-fuel ratio, and consequently, a



(a) The number of occurrences (logged data) of the torque percentage for 31 days of vessel operation.



(b) The number of occurrences (logged data) of the torque percentage for 50 minutes of vessel operation.

Figure 5.22: The frequency of occurrence of the torque percentage of the vessel.

significant part of the fuel remains unburned at each cycle. Therefore, methane slip increases to even eight times higher quantity. There is no difference between a transient condition and a steady-state when the load is higher than 80% of nominal torque. This output confirms how the methane slip changes with even a tiny fluctuation of the engine load. Thus, working in an area close to the power curve plays an essential role in reducing the contaminant compounds of the engine.

Almost the same trend is achieved for NO_x . While in steady-state, the lower load showed a lower amount of NO_x , demonstrated in Fig. 5.27, the volume doubled compared with available measured data in transient condition.

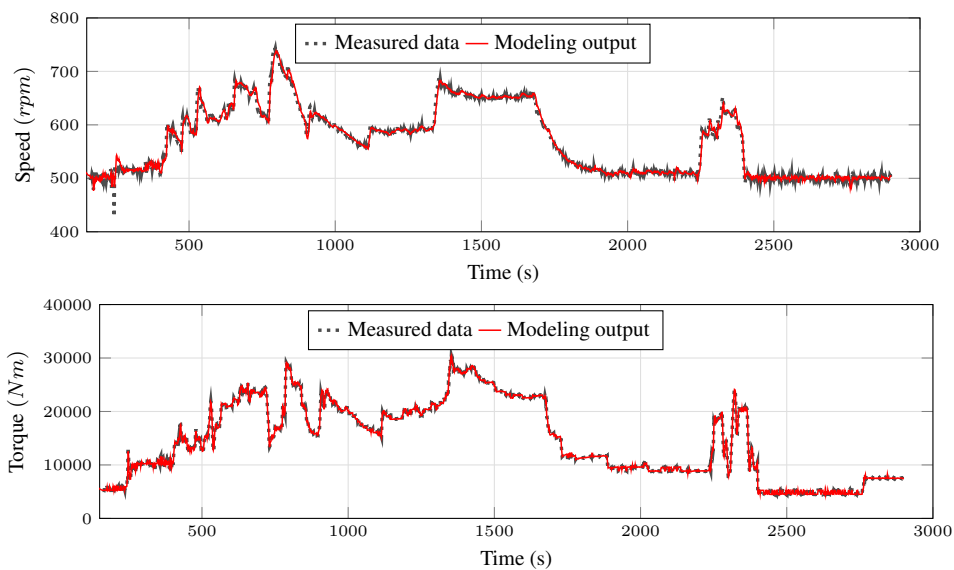


Figure 5.23: Target torque and speed based on the real imposed data of the ship.

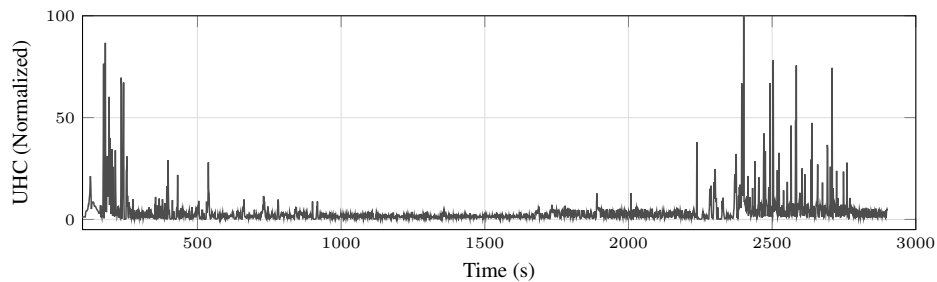


Figure 5.24: UHC formation during the real operational condition in sea state.

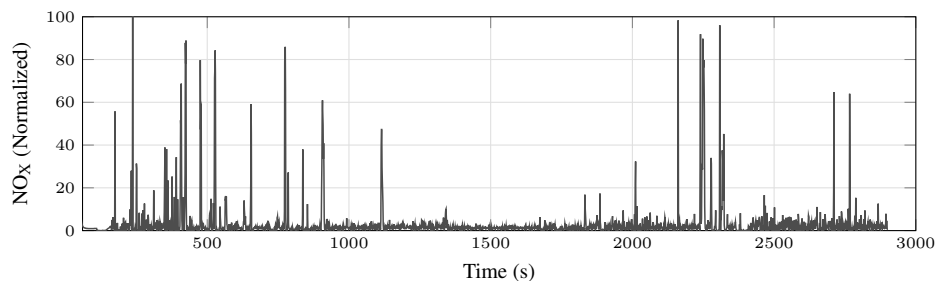


Figure 5.25: NO_x compound during the real operational condition in sea state.

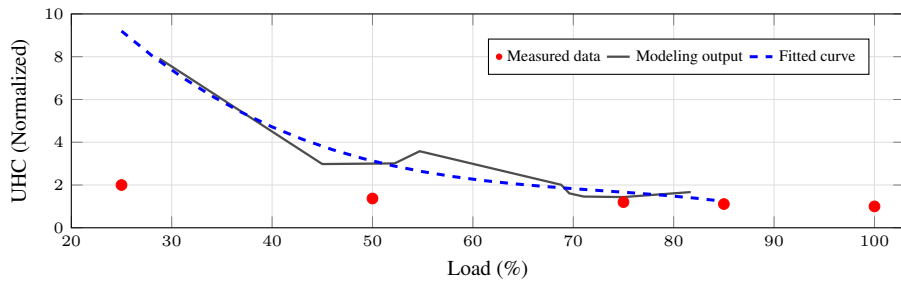


Figure 5.26: Average values of UHC- A comparison of steady-state and transient conditions. There is a big gap between the two states during the lower load operation.

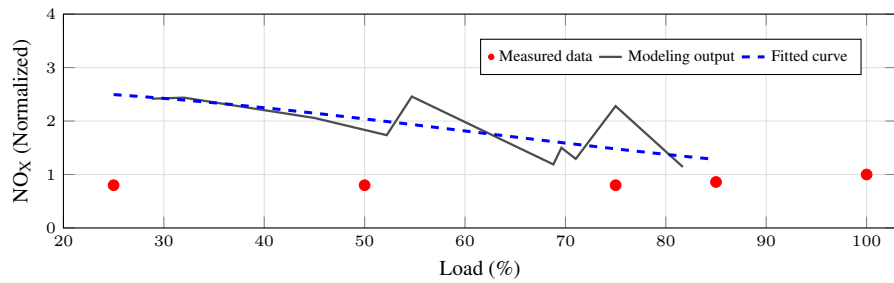


Figure 5.27: Average values of NO_x - A comparison of steady-state and transient conditions.

Chapter 6

Conclusion and Recommendations

6.1 Summary and conclusions

This research work was initiated to develop a detailed predicting response of a lean burn gas engine in a marine propulsion system. Of particular interest was to predict the methane slip during the transient condition. Therefore, the main contribution of the thesis can be summarized as follows:

- ① A detailed engine model with all essential components was developed. The components are inlet and outlet boundary condition, turbine, compressor and shaft data, intercooler, throttle valve, intake and exhaust manifold, gas fuel system, intake and exhaust valves, combustion chamber, and ignition system.
- ② The model was validated both in steady-state from 25% to 100% nominal torque and for the transient condition by real irregular operational waves.
- ③ Two models for the methane slip were developed. The models were a function of burning rate and post oxidation rate, and they had the potential to predict the quantity in steady-state and transient conditions. The first model provided a total quantity for methane slip, and the second model was developed in MATLAB programming to determine the sources contribution.
- ④ A marine power train model, including the engine, propeller, and transmission system, was developed. An engine model with the shaft inertia was coupled to the propeller in the SIMULINK. A discrete-event-based co-simulation was chosen to exchange data between the sub-models, while each sub-model was

solved independently by their internal solver, using their own fixed and non-fixed time-step for the propeller and engine, respectively.

⑤ Several controlling approaches were examined. The concept was to recognize the influence of each component on engine response and methane slip formation.

⑥ Analyzing the long-term voyage of the vessel was performed, and the load distribution around the full load and part-load were shown. Due to the significance of the engine part-load operation and the discrepancy of the methane slip in part-load rather than full load, a separate study was performed for part-loads.

According to the contribution of this study and the raised question of the project, the highlights of the main findings are as follows:

- The engine model accurately predicted the dynamic response of the engines during transient conditions. The fuel consumption and turbocharger system followed according to the available measured data of the vessel, and the model outputs were verified acceptably.
- The methane slip increases if the load oscillates in sea waves. Excess air-fuel ratio deviation from the optimum setpoint during the load reduction plays the most significant role in methane slip due to the flame quenching in very lean combustion.
- Although the quenched flame showed the most variation, the contribution of crevice volume on total methane slip is remarkable in all loads. During the transient condition, it also increases slightly due to a less robust post-oxidation process.
- Examining several practical methods to stabilize the excess ratio deviation showed that the flow dynamic, intake and exhaust capacity, and the types of controllers are the least influential factors. There is an almost one-second delay in engine response, and this delay is due to the turbocharger shaft moment of inertia and other dynamic components of the transmission system.
- Different new inertia of the turbocharger shaft was replaced with the initial shaft. The results confirmed that the implemented change on the mass moment of inertia was important in short time scales, while the general response of the engine was following the magnitude and frequency of the imposed torque from the propeller and wave.
- In order to recover the engine response in transient condition, a rapid solenoid method with a response time of 30ms reduced the methane slip

significantly, and the extra NO_x was eliminated by retarding the spark ignition timing.

- A valve throttle may appropriately provide a restriction on airflow during steady-state; during the transient condition, the throttle response time scale is longer than the load frequency. Thus, the influence of the throttle valve on methane slip and fuel consumption is little for the transient condition.
- During the part-load operation, any small change of load may result in a higher quantity of methane slip. Then, the engine response in part-loads is not only sensitive to the wave amplitude but the wave frequency.

6.2 Recommendations for future work

- *Further development and validation of engine modeling for direct coupling to the methane slip Model 2,*

This is a big step to provide a separated methane slip output with the sources from the engine modeling without a need to couple to the MATLAB developed program. The main issue is the run time of the modeling.

- *Considering variable wall temperature to track influences on flame quenching,*

Flame quenching is very sensitive to the wall temperature. While it was divided into three constant temperature zones in this study, developing the wall temperature calculation code may provide a more accurate result for flame quenching and total methane slip.

- *Detailed data analysis to categorize the load variation in each load condition,*

It is essential to know how critical is each wave condition and how much time is an engine in calm weather, in severe conditions, or in between. The magnitude of load variation in each condition, is crucial for further assessment of natural gas engines for marine application.

- *Assessing cyclic variation on total methane slip in transient conditions,*

The available cyclic of variation methods are suitable for a steady-state. It is essential to develop the transient condition models where the input data for the cyclic of variation model changes in each cycle.

- *Examining fuel quality on methane slip,*

Fuel quality is a controversial challenge in marine applications. The methane number of natural gas fuels plays a remarkable role in combustion.

Therefore, to recognize the methane slip for a wide range of engines worldwide, examining the fuel properties is recommended.

- *Catalytic modeling and examination for methane slip reduction,*
Employing and modeling a monolith catalyst to oxidize the unburned fuel into the H_2O , with a specific focus on temperature variation during the transient condition is recommended.

Bibliography

- [1] P. Ni, X. Wang, and H. Li, “A review on regulations, current status, effects and reduction strategies of emissions for marine diesel engines,” *Fuel*, vol. 279, p. 118477, 2020.
- [2] “Comparison of alternative marine fuels,” Tech. Rep. 2019-0567, Rev. 3, DNV GL AS Maritime, Norway, 2019.
- [3] N. Pavlenko, B. Comer, Y. Zhou, N. Clark, and D. Rutherford, “The climate implications of using LNG as a marine fuel,” *2020 International Council on Clean Transportation*, vol. WORKING PAPER 2020-02, 2020.
- [4] “Review of maritime transport 2017,” Tech. Rep. UNCTAD/RMT/2017), United Nations Conference on Trade and Development, 2017.
- [5] YANMAR Technical Review, “Dual-fuel marine engine (highly reliable environmentally friendly engine).” https://www.yanmar.com/th/technology/technical_review/2015/0727_2.html.
- [6] V. Krivopolianskii, I. Valberg, D. Stenersen, S. Ushakov, and V. Æsøy, “Control of the combustion process and emission formation in marine gas engines,” *Journal of Marine Science and Technology*, vol. 24, no. 2, pp. 593–611, 2019.
- [7] S. Ushakov, D. Stenersen, and P. M. Einang, “Methane slip from gas fuelled ships: a comprehensive summary based on measurement data,” *Journal of Marine Science and Technology*, vol. 24, no. 4, pp. 1308–1325, 2019.
- [8] C. D. Rakopoulos and E. G. Giakoumis, “Review of thermodynamic diesel engine simulations under transient operating conditions,” in *SAE 2006 World Congress & Exhibition*, SAE International, april 2006.

- [9] S. Turns, *An Introduction to Combustion: Concepts and Applications*. McGraw-Hill series in mechanical engineering, McGraw-Hill, 2012.
- [10] W. K. Cheng, D. Hamrin, J. B. Heywood, S. Hochgreb, K. Min, and M. Norris, “An overview of hydrocarbon emissions mechanisms in spark-ignition engines,” in *International Fuels & Lubricants Meeting & Exposition*, SAE International, oct 1993.
- [11] B. Pundir, *IC Engines: Combustion and Emissions*. Alpha Science International Limited, 2010.
- [12] Wikipedia contributors, “Étienne lenoir — Wikipedia, the free encyclopedia,” 2020.
- [13] Wikipedia contributors, “Nicolaus otto — Wikipedia, the free encyclopedia,” 2020.
- [14] United States Environmental Protection Agency (EPA), “Clean air act overview.” www.epa.gov/clean-air-act-overview/clean-air-act-requirements-and-history.
- [15] World Health Organization (WHO) , “Global health observatory data repository.” www.apps.who.int/gho/data/node.main.A995.
- [16] World Health Organization (WHO) , “Air pollution.” www.who.int/health-topics/air-pollution#tab=tab_2.
- [17] J. J. Corbett, J. J. Winebrake, E. H. Green, P. Kasibhatla, V. Eyring, and A. Lauer, “Mortality from ship emissions: A global assessment,” *Environmental Science & Technology*, vol. 41, no. 24, pp. 8512–8518, 2007. PMID: 18200887.
- [18] V. Eyring, H. W. Köhler, J. van Aardenne, and A. Lauer, “Emissions from international shipping: 1. the last 50 years,” *Journal of Geophysical Research: Atmospheres*, vol. 110, no. D17, 2005.
- [19] C. Mohd Noor, M. Noor, and R. Mamat, “Biodiesel as alternative fuel for marine diesel engine applications: A review,” *Renewable and Sustainable Energy Reviews*, vol. 94, pp. 127 – 142, 2018.
- [20] “2019 guidelines for consistent implementation of the 0.50% sulphur limit under marpol annex vi,” tech. rep., International Maritime Organization (IMO), 2019.

-
- [21] RESOLUTION MEPC.176(58), “Revised marpol annex vi: Chapter 3: Requirements for control of emissions from ships,” tech. rep., International Maritime Organization (IMO), October 2008.
- [22] RESOLUTION MEPC 304(72), “Annex 11: Initial imo strategy on reduction of GHG emissions from ships,” tech. rep., International Maritime Organization (IMO), 2018.
- [23] MEPC 70/18/Add 1, “Annex 11: Roadmap for developing a comprehensive imo strategy on reduction of GHG emissions from ships,” tech. rep., International Maritime Organization (IMO).
- [24] J. Gao, G. Tian, A. Sornioti, A. E. Karci, and R. Di Palo, “Review of thermal management of catalytic converters to decrease engine emissions during cold start and warm up,” *Applied Thermal Engineering*, vol. 147, pp. 177 – 187, 2019.
- [25] S. Bengtsson, K. Andersson, and E. Fridell, “A comparative life cycle assessment of marine fuels: liquefied natural gas and three other fossil fuels,” *Journal of Engineering for the Maritime Environment*, no. 225, pp. 97–110, 2011.
- [26] P. C. Spurk, M. Pfeifer, F.-W. Schütze, and T. Kreuzer, “Challenges for the future diesel engines exhaust gas aftertreatment system,” in *2007 Fuels and Emissions Conference*, SAE International, jan 2007.
- [27] T. Pauly, S. Franoschek, R. Hoyer, and S. Eckhoff, “Cost and fuel economy driven aftertreatment solutions -for lean gdi-,” in *SAE 2010 World Congress & Exhibition*, SAE International, april 2010.
- [28] G. Zheng, A. Kotrba, M. Golin, T. Gardner, and A. Wang, “Overview of large diesel engine aftertreatment system development,” in *SAE 2012 Commercial Vehicle Engineering Congress*, SAE International, sep 2012.
- [29] R. Banerjee, S. Roy, and P. K. Bose, “Hydrogen-egr synergy as a promising pathway to meet the pm–nox–bsfc trade-off contingencies of the diesel engine: A comprehensive review,” *International Journal of Hydrogen Energy*, vol. 40, no. 37, pp. 12824–12847, 2015.
- [30] L. Chybowski, R. Laskowski, and K. Gawdzińska, “An overview of systems supplying water into the combustion chamber of diesel engines to decrease the amount of nitrogen oxides in exhaust gas,” *Journal of Marine Science and Technology*, vol. 20, 2015.

- [31] F. Burel, R. Taccani, and N. Zuliani, "Improving sustainability of maritime transport through utilization of liquefied natural gas (LNG) for propulsion," *Energy*, no. 57, pp. 412–420, 2013.
- [32] S. Brynolf, M. Magnusson, E. Fridell, and K. Andersson, "Compliance possibilities for the future eca regulations through the use of abatement technologies or change of fuels," *Transportation Research Part D*, no. 28, pp. 6–18, 2014.
- [33] C. N. L. Fevre, "A review of demand prospects for LNG as a marine transport fuel," Tech. Rep. OIES PAPER: NG 133, The Oxford Institute for Energy Studies, June 2018.
- [34] D. Nikolic, N. . Marstijepović, S. Cvrk, R. Gagić, and I. Filipović, "Evaluation of pollutant emissions from two-stroke marine diesel engine fueled with biodiesel produced from various waste oils and diesel blends," *Brodogradnja*, vol. 67, pp. 81–90, 2016.
- [35] Z. Chen, Y. Ai, T. Qin, and F. Luo, "Quantitative evaluation of n-butane concentration on knock severity of a natural gas heavy-duty SI engine," *Energy*, vol. 189, p. 116244, 2019.
- [36] Z. Wang, G. Du, Z. Li, X. Wang, and D. Wang, "Study on the combustion characteristics of a high compression ratio HCCI engine fueled with natural gas," *Fuel*, vol. 255, p. 115701, 2019.
- [37] S. Lochner and H. Wang-Helmreich, "The potential of natural gas as a bridging technology in low-emission road transportation in germany," *Thermal Science*, vol. 16, pp. 729–746, 2012.
- [38] R. Mikalsen, Y. Wang, and A. Roskilly, "A comparison of miller and otto cycle natural gas engines for small scale CHP applications," *Applied Energy*, vol. 86, no. 6, pp. 922 – 927, 2009.
- [39] H. Thomson, J. J. Corbett, and J. J. Winebrake, "Natural gas as a marine fuel," *Energy Policy*, vol. 87, pp. 153 – 167, 2015.
- [40] R. A. B. Semin, "A technical review of compressed natural gas as an alternative fuel for internal combustion engines," *American J. of Engineering and Applied Sciences*, pp. 302–311, 2008.
- [41] P. Forster and V. Ramaswamy, "Changes in atmospheric constituents and in radiative forcing," Tech. Rep. Chapter 2, The Intergovernmental Panel on Climate Change (IPCC), 2018.

- [42] M. I. Khan, T. Yasmin, and A. Shakoor, "Technical overview of compressed natural gas (CNG) as a transportation fuel," *Renewable and Sustainable Energy Reviews*, vol. 51, pp. 785 – 797, 2015.
- [43] V. Æsøy, P. Magne Einang, D. Stenersen, E. Hennie, and I. Valberg, "LNG-fuelled engines and fuel systems for medium-speed engines in maritime applications," in *SAE International Powertrains, Fuels and Lubricants Meeting*, SAE International, aug 2011.
- [44] P. M. Einang and K. M. Haavik, "The norwegian LNG ferry," *Paper A-095 NGV 2000 YOKOHAMA*, 2000.
- [45] D. Stenersen and O. Thonstad, "GHG and NO_x emissions from gas fuelled engines," Tech. Rep. OC2017 F-108 - Unrestricted, SINTEF, SINTEF Ocean AS, Maritim, 2017.
- [46] S. Brynolf, E. Fridell, and K. Andersson, "Environmental assessment of marine fuels: liquefied natural gas, liquefied biogas, methanol and bio-methanol," *Journal of Cleaner Production*, vol. 74, pp. 86 – 95, 2014.
- [47] M. Y. Selim, "Sensitivity of dual fuel engine combustion and knocking limits to gaseous fuel composition," *Energy Conversion and Management*, vol. 45, no. 3, pp. 411 – 425, 2004.
- [48] G. A. Karim, *Dual-Fuel Diesel Engines*. Boca Raton, 2015.
- [49] D. Woodyard in *Pounders Marine Diesel Engines and Gas Turbines (Ninth Edition)*, Oxford: Butterworth-Heinemann, ninth edition ed., 2009.
- [50] C. S. Weaver and S. H. Turner, "Dual fuel natural gas/diesel engines: Technology, performance, and emissions," in *International Congress & Exposition*, SAE International, mar 1994.
- [51] M. Olofsson, L. Erlandsson, and K. Willner, "Enhanced emission performance and fuel efficiency for HD methane engines," Tech. Rep. AVL MTC Report OMT 1032, International Energy Agency– Advanced Motor Fuels, 2014.
- [52] J. Schramm, "IEA AMF annex 51: Methane emission control," tech. rep., IEA Advanced Motor Fuels, 2019.
- [53] K. Saikaly, O. Le Corre, C. Rahmouni, and L. Truffet, "Preventive knock protection technique for stationary SI engines fuelled by natural gas," *Fuel Processing Technology*, vol. 91, no. 6, pp. 641 – 652, 2010.

- [54] J. Król and P. Ocloń, “Economic analysis of heat and electricity production in combined heat and power plant equipped with steam and water boilers and natural gas engines,” *Energy Conversion and Management*, vol. 176, pp. 11 – 29, 2018.
- [55] L.-P. Yang, E.-Z. Song, S.-L. Ding, R. J. Brown, N. Marwan, and X.-Z. Ma, “Analysis of the dynamic characteristics of combustion instabilities in a pre-mixed lean-burn natural gas engine,” *Applied Energy*, vol. 183, pp. 746 – 759, 2016.
- [56] CIMAC WORKING GROUP “GAS ENGINES”, “Transient response behaviour of gas engines,” *International Council On Combustion Engines*, April 2011.
- [57] Q. Zhang, M. Li, G. Li, S. Shao, and P. Li, “Transient emission characteristics of a heavy-duty natural gas engine at stoichiometric operation with EGR and TWC,” *Energy*, vol. 132, pp. 225 – 237, 2017.
- [58] K. K. Yum, B. Taskar, E. Pedersen, and S. Steen, “Simulation of a two-stroke diesel engine for propulsion in waves,” *International Journal of Naval Architecture and Ocean Engineering*, vol. 9, no. 4, pp. 351 – 372, 2017.
- [59] N. P. Kyrtatos, P. Theodossopoulos, G. Theotokatos, and N. Xiros, “Simulation of the overall ship propulsion plant for performance prediction and control,” *MarPower99 Conference*, 1999.
- [60] U. Campora and M. Figari, “Numerical simulation of ship propulsion transients and full-scale validation,” *Proceedings of the Institution of Mechanical Engineers, Part M: Journal of Engineering for the Maritime Environment*, vol. 217, no. 1, pp. 41–52, 2003.
- [61] J. Neilson and R. Tarbet, “Propulsion system simulations: Making the right choice for the application,” *Naval engineers journal*, vol. 109, no. 5, pp. 83–98, 1997.
- [62] B. Taskar, K. K. Yum, S. Steen, and E. Pedersen, “The effect of waves on engine-propeller dynamics and propulsion performance of ships,” *Ocean Engineering*, vol. 122, pp. 262 – 277, 2016.
- [63] M. Altosole, U. Campora, M. Figari, M. Laviola, and M. Martelli, “A diesel engine modelling approach for ship propulsion real-time simulators,” *Journal of Marine Science and Engineering*, vol. 7, no. 5, 2019.

- [64] O. el Moctar, U. Lantermann, P. Mucha, J. Höpken, and T. E. Schellin, "Rans-based simulated ship maneuvering accounting for hull-propulsor-engine interaction," *Ship Technology Research*, vol. 61, no. 3, pp. 142–161, 2014.
- [65] J. Liu and C. E. Dumitrescu, "Flame development analysis in a diesel optical engine converted to spark ignition natural gas operation," *Applied Energy*, vol. 230, pp. 1205 – 1217, 2018.
- [66] J. Liu and C. E. Dumitrescu, "3D CFD simulation of a CI engine converted to SI natural gas operation using the g-equation," *Fuel*, vol. 232, pp. 833 – 844, 2018.
- [67] M. A. Jemni, G. Kantchev, and M. S. Abid, "Influence of intake manifold design on in-cylinder flow and engine performances in a bus diesel engine converted to LPG gas fuelled, using CFD analyses and experimental investigations," *Energy*, vol. 36, no. 5, pp. 2701 – 2715, 2011.
- [68] Horiba Automotive Test Systems, "Compact and affordable heated THC measurement system." https://www.horiba.com/en_en/products/detail/action/show/Product/mexa-1170hfid-108/.
- [69] K. Kuppa, H. Nguyen, A. Goldmann, B. Korb, G. Wachtmeister, and F. Dinkelacker, "Numerical modelling of unburned hydrocarbon emissions in gas engines with varied fuels," *Fuel*, vol. 254, p. 115532, 2019.
- [70] A. C. Alkidas, R. J. Drews, and W. F. Miller, "Effects of piston crevice geometry on the steady-state engine-out hydrocarbons emissions of a S.I. engine," in *1995 SAE International Fall Fuels and Lubricants Meeting and Exhibition*, SAE International, oct 1995.
- [71] P. R. Meernik and A. C. Alkidas, "Impact of exhaust valve leakage on engine-out hydrocarbons," in *International Fuels & Lubricants Meeting & Exposition*, SAE International, oct 1993.
- [72] T. Kato, K. Saeki, H. Nishide, and T. Yamada, "Development of CNG fueled engine with lean burn for small size commercial van," *JSAE Review*, vol. 22, no. 3, pp. 365 – 368, 2001.
- [73] R. Tilagone and S. Venturi, "Development of natural gas demonstrator based on an urban vehicle with a down-sized turbocharged engine," *Oil & Gas Science and Technology-revue De L Institut Francais Du Petrole*, vol. 59, pp. 581–591, 2004.

- [74] Y. Kitagawa, O. Bondarenko, and Y. Tsukada, "An experimental method to identify a component of wave orbital motion in propeller effective inflow velocity and its effects on load fluctuations of a ship main engine in waves," *Applied Ocean Research*, vol. 92, p. 101922, 2019.
- [75] F. Ma, Y. Wang, H. Liu, Y. Li, J. Wang, and S. Ding, "Effects of hydrogen addition on cycle-by-cycle variations in a lean burn natural gas spark-ignition engine," *International Journal of Hydrogen Energy*, vol. 33, no. 2, pp. 823 – 831, 2008.
- [76] P. Tunestål, M. Christensen, P. Einewall, T. Andersson, B. Johansson, and O. Jönsson, "Hydrogen addition for improved lean burn capability of slow and fast burning natural gas combustion chambers," in *SAE Powertrain & Fluid Systems Conference & Exhibition*, SAE International, oct 2002.
- [77] A. K. Sen, J. Zheng, and Z. Huang, "Dynamics of cycle-to-cycle variations in a natural gas direct-injection spark-ignition engine," *Applied Energy*, vol. 88, no. 7, pp. 2324 – 2334, 2011.
- [78] A. E. Hassaneen, K. S. Varde, A. H. Bawady, and A.-A. Morgan, "A study of the flame development and rapid burn durations in a lean-burn fuel injected natural gas S.I. engine," in *International Fuels & Lubricants Meeting & Exposition*, SAE International, may 1998.
- [79] K. Yoshimura, Y. Tokunaga, D. Hashimoto, and H. Sakurai, "Knock and misfire detection using ion current measurement for ultra lean burn medium speed gas engine," in *JSAE/SAE International Fuels & Lubricants Meeting*, SAE International, jul 2007.
- [80] O. A. Kutlar, H. Arslan, and A. T. Calik, "Methods to improve efficiency of four stroke, spark ignition engines at part load," *Energy Conversion and Management*, vol. 46, no. 20, pp. 3202 – 3220, 2005.
- [81] S. Simsek and S. Uslu, "Investigation of the impacts of gasoline, biogas and LPG fuels on engine performance and exhaust emissions in different throttle positions on SI engine," *Fuel*, vol. 279, p. 118528, 2020.
- [82] H. Guo, B. Liko, L. Luque, and J. Littlejohns, "Combustion Performance and Unburned Hydrocarbon Emissions of a Natural Gas–Diesel Dual Fuel Engine at a Low Load Condition," *Journal of Engineering for Gas Turbines and Power*, vol. 140, 06 2018. 112801.
- [83] A. Yousefi, H. Guo, M. Birouk, and B. Liko, "On greenhouse gas emissions and thermal efficiency of natural gas/diesel dual-fuel engine at low load

- conditions: Coupled effect of injector rail pressure and split injection,” *Applied Energy*, vol. 242, pp. 216 – 231, 2019.
- [84] J. Naber, D. Siebers, S. Di Julio, and C. Westbrook, “Effects of natural gas composition on ignition delay under diesel conditions,” *Combustion and Flame*, vol. 99, no. 2, pp. 192 – 200, 1994. 25th Symposium (International) on Combustion Papers.
- [85] W. W. A. Bakar and R. Ali, *Natural Gas*. London, UK: <https://www.intechopen.com/books/natural-gas/natural-gas>, 2010.
- [86] S. Yeh, “An empirical analysis on the adoption of alternative fuel vehicles: The case of natural gas vehicles,” *Energy Policy*, vol. 35, no. 11, pp. 5865 – 5875, 2007.
- [87] BP2019, “Statistical review of world energy,” Tech. Rep. 68th edition, bp, 2019.
- [88] NGV Global, “Current natural gas vehicle statistics.” www.iangv.org/current-ngv-stats/.
- [89] T. Korakianitis, A. Namasivayam, and R. Crookes, “Natural-gas fueled spark-ignition (SI) and compression-ignition (CI) engine performance and emissions,” *Progress in Energy and Combustion Science*, vol. 37, pp. 89–112, 2011.
- [90] E. Hu, Z. Huang, B. Liu, J. Zheng, and X. Gu, “Experimental study on combustion characteristics of a spark-ignition engine fueled with natural gas–hydrogen blends combining with EGR,” *international journal of hydrogen energy*, no. 34, pp. 1035–1044, 2009.
- [91] S. Di Iorio, P. Sementa, and B. M. Vaglieco, “Experimental investigation on the combustion process in a spark ignition optically accessible engine fueled with methane/hydrogen blends,” *International Journal of Hydrogen Energy*, vol. 39, no. 18, pp. 9809 – 9823, 2014.
- [92] L. Ben, N. Raud-Ducros, R. Truquet, and G. Charnay, “Influence of air/fuel ratio on cyclic variation and exhaust emission in natural gas SI engine,” in *Future Transportation Technology Conference & Exposition*, SAE International, aug 1999.
- [93] M. D. Feist, M. Landau, and E. Harte, “The effect of fuel composition on performance and emissions of a variety of natural gas engines,” may 2010.

- [94] I. Saanum, M. Bysveen, P. Tunestål, and B. Johansson, “Lean burn versus stoichiometric operation with EGR and 3-way catalyst of an engine fueled with natural gas and hydrogen enriched natural gas,” in *2007 Fuels and Emissions Conference*, SAE International, jan 2007.
- [95] J. A. Smith and G. J. J. Bartley, “Stoichiometric Operation of a Gas Engine Utilizing Synthesis Gas and EGR for NO_x Control ,” *Journal of Engineering for Gas Turbines and Power*, vol. 122, pp. 617–623, 04 2000.
- [96] H. Li, T. Gatts, S. Liu, S. Wayne, N. Clark, and D. Mather, “An Experimental Investigation on the Combustion Process of a Simulated Turbocharged Spark Ignition Natural Gas Engine Operated on Stoichiometric Mixture,” *Journal of Engineering for Gas Turbines and Power*, vol. 140, 06 2018. 091504.
- [97] P. Einewall, P. Tunestål, and B. Johansson, “Lean burn natural gas operation vs. stoichiometric operation with EGR and a three way catalyst,” in *SAE 2005 World Congress & Exhibition*, SAE International, april 2005.
- [98] F. Alasfour, “NO_x emission from a spark ignition engine using 30% iso-butanol–gasoline blend: Part 2—ignition timing,” *Applied Thermal Engineering*, vol. 18, no. 8, pp. 609 – 618, 1998.
- [99] Q. Zhang, M. Li, S. Shao, and G. Li, “Ammonia emissions of a natural gas engine at the stoichiometric operation with TWC,” *Applied Thermal Engineering*, vol. 130, pp. 1363 – 1372, 2018.
- [100] S. Onishi, S. H. Jo, K. Shoda, P. D. Jo, and S. Kato, “Active thermo-atmosphere combustion (ATAC) - a new combustion process for internal combustion engines,” in *1979 Automotive Engineering Congress and Exposition*, SAE International, feb 1979.
- [101] D. Yap, S. Peucheret, A. Megaritis, M. Wyszynski, and H. Xu, “Natural gas HCCI engine operation with exhaust gas fuel reforming,” *International Journal of Hydrogen Energy*, vol. 31, no. 5, pp. 587 – 595, 2006.
- [102] M. Yao, Z. Zheng, and H. Liu, “Progress and recent trends in homogeneous charge compression ignition (HCCI) engines,” *Progress in Energy and Combustion Science*, vol. 35, no. 5, pp. 398 – 437, 2009.
- [103] G. J. Hampson, “Heat release design method for HCCI in diesel engines,” in *Powertrain & Fluid Systems Conference & Exhibition*, SAE International, oct 2005.

- [104] V. Hosseini and M. D. Checkel, "Using reformer gas to enhance HCCI combustion of CNG in a CFR engine," in *Powertrain & Fluid Systems Conference and Exhibition*, SAE International, oct 2006.
- [105] M. Fathi, R. K. Saray, and M. D. Checkel, "The influence of exhaust gas recirculation (EGR) on combustion and emissions of n-heptane/natural gas fueled homogeneous charge compression ignition (HCCI) engines," *Applied Energy*, vol. 88, no. 12, pp. 4719 – 4724, 2011.
- [106] H. Zhao, Z. Peng, and N. Ladommatos, "Understanding of controlled autoignition combustion in a four-stroke gasoline engine," *Proceedings of the Institution of Mechanical Engineers, Part D: Journal of Automobile Engineering*, vol. 215, no. 12, pp. 1297–1310, 2001.
- [107] A. Agarwal and D. N. Assanis, "Multi-dimensional modeling of ignition, combustion and nitric oxide formation in direct injection natural gas engines," in *CEC/SAE Spring Fuels & Lubricants Meeting & Exposition*, SAE International, jun 2000.
- [108] S. R. King, "The impact of natural gas composition on fuel metering and engine operational characteristics," in *International Congress & Exposition*, SAE International, feb 1992.
- [109] J. B. Heywood, *Internal Combustion Engine Fundamentals, Second Edition*. McGraw-Hill series in mechanical engineering, McGraw-Hill Education, 2018.
- [110] P. Flynn, G. Hunter, L. Farrel, R. Durrett, O. Akinyemi, A. Zur Loye, C. Westbrook, and W. Pitz, "The inevitability of engine-out NO_x emissions from spark-ignited and diesel engines," *Proceedings of the Combustion Institute*, vol. 28, no. 1, pp. 1211 – 1218, 2000.
- [111] M. Watfa and H. Daneshyar, "Formation of nitric oxide (NO), carbon monoxide (CO) and unburnt hydrocarbons, (HC) in spark ignition engines," *IN: Conf. Combust. Eng.; Cranfield, Beds.; 1975; London; Inst. Mech. Eng.; DA. 1975; PP. 165-183; BIBL. 18 REF.*, 1975.
- [112] F. Alasfour, "NO_x emission from a spark ignition engine using 30% iso-butanol–gasoline blend: Part 2—ignition timing," *Applied Thermal Engineering*, vol. 18, no. 8, pp. 609 – 618, 1998.
- [113] D. S.-K. Ting and M. D. Checkel, "The effects of turbulence of spark-ignited, ultra lean, premixed methane-air flame growth in a

- combustion chamber,” in *1995 SAE International Fall Fuels and Lubricants Meeting and Exhibition*, SAE International, oct 1995.
- [114] R. Scarcelli, N. Matthias, and T. Wallner, “Numerical investigation of combustion in a lean burn gasoline engine,” in *11th International Conference on Engines & Vehicles*, SAE International, sep 2013.
- [115] C. C. O. B. Reynolds and R. L. Evans, “Improving emissions and performance characteristics of lean burn natural gas engines through partial stratification,” *International Journal of Engine Research*, vol. 5, no. 1, pp. 105–114, 2004.
- [116] H. Reddy and J. Abraham, “Ignition kernel development studies relevant to lean-burn natural-gas engines,” *Fuel*, vol. 89, no. 11, pp. 3262 – 3271, 2010.
- [117] Z. Liu and G. A. Karim, “Simulation of combustion processes in gas-fuelled diesel engines,” *Proceedings of the Institution of Mechanical Engineers, Part A: Journal of Power and Energy*, vol. 211, no. 2, p. 159–169, 1997.
- [118] R. Papagiannakis and D. Hountalas, “Combustion and exhaust emission characteristics of a dual fuel compression ignition engine operated with pilot diesel fuel and natural gas,” *Energy Conversion and Management*, vol. 45, no. 18, pp. 2971 – 2987, 2004.
- [119] B. Sahoo, N. Sahoo, and U. Saha, “Effect of engine parameters and type of gaseous fuel on the performance of dual-fuel gas diesel engines—a critical review,” *Renewable and Sustainable Energy Reviews*, vol. 13, no. 6, pp. 1151 – 1184, 2009.
- [120] S. Mahla, A. Dhir, K. J. Gill, H. M. Cho, H. C. Lim, and B. S. Chauhan, “Influence of EGR on the simultaneous reduction of NO_x-smoke emissions trade-off under CNG-biodiesel dual fuel engine,” *Energy*, vol. 152, pp. 303 – 312, 2018.
- [121] S. Nag, P. Sharma, A. Gupta, and A. Dhar, “Experimental study of engine performance and emissions for hydrogen diesel dual fuel engine with exhaust gas recirculation,” *International Journal of Hydrogen Energy*, vol. 44, no. 23, pp. 12163 – 12175, 2019.
- [122] R. W. Bittner and F. W. Aboujaoude, “Catalytic Control of NO_x, CO, and NMHC Emissions From Stationary Diesel and Dual-Fuel Engines,” *Journal of Engineering for Gas Turbines and Power*, vol. 114, pp. 597–601, 07 1992.

-
- [123] M. Dahodwala, S. Joshi, E. Koehler, M. Franke, and D. Tomazic, "Experimental and computational analysis of diesel-natural gas RCCI combustion in heavy-duty engines," in *SAE 2015 World Congress & Exhibition*, SAE International, april 2015.
- [124] S. Imtenan, M. Varman, H. Masjuki, M. Kalam, H. Sajjad, M. Arbab, and I. R. Fattah, "Impact of low temperature combustion attaining strategies on diesel engine emissions for diesel and biodiesels: A review," *Energy Conversion and Management*, vol. 80, pp. 329 – 356, 2014.
- [125] D. E. Nieman, A. B. Dempsey, and R. D. Reitz, "Heavy-duty rcci operation using natural gas and diesel," *SAE International Journal of Engines*, vol. 5, pp. 270–285, apr 2012.
- [126] M. Wissink and R. D. Reitz, "Direct dual fuel stratification, a path to combine the benefits of rcci and ppc," *SAE International Journal of Engines*, vol. 8, no. 2, pp. 878–889, 2015.
- [127] J. Li, W. Yang, and D. Zhou, "Review on the management of rcci engines," *Renewable and Sustainable Energy Reviews*, vol. 69, pp. 65–79, 2017.
- [128] F. Payri, J. Benajes, and M. Reyes, "Modelling of supercharger turbines in internal-combustion engines," *International Journal of Mechanical Sciences*, vol. 38, no. 8, pp. 853 – 869, 1996.
- [129] D. Dowson, C. Taylor, and L. Yang, "Friction modelling for internal combustion engines," in *The Third Body Concept Interpretation of Tribological Phenomena* (D. Dowson, C. Taylor, T. Childs, G. Dalmaz, Y. Berthier, L. Flamand, J.-M. Georges, and A. Lubrecht, eds.), vol. 31 of *Tribology Series*, pp. 301 – 318, Elsevier, 1996.
- [130] D. Zhang and S. H. Frankel, "A numerical study of natural gas combustion in a lean burn engine," *Fuel*, vol. 77, no. 12, pp. 1339 – 1347, 1998.
- [131] M. Kraft, P. Maigaard, F. Mauss, M. Christensen, and B. Johansson, "Investigation of combustion emissions in a homogeneous charge compression injection engine: Measurements and a new computational model," *Proceedings of the Combustion Institute*, vol. 28, no. 1, pp. 1195 – 1201, 2000.
- [132] D. Hrovat and J. Sun, "Methodologies for IC engine idle speed control design," *IFAC Proceedings Volumes*, vol. 29, no. 1, pp. 7939 – 7944, 1996. 13th World Congress of IFAC, 1996, San Francisco USA, 30 June - 5 July.

- [133] M. Larmi, "Transient response model of low-speed diesel engine in ice-breaking cargo vessels," 1993.
- [134] N. Watson, "Dynamic turbocharged diesel engine simulator for electronic control system development," *ASME Transactions, Journal of Dynamic Systems Measurement and Control*, vol. 106, no. 1, pp. 27–45, 1984.
- [135] D. Winterbone, R. Benson, G. Closs, and A. Mortimer, "A comparison between experimental and analytical transient test results for a turbocharged diesel engine," *Proceedings of the Institution of Mechanical Engineers*, vol. 190, no. 1, pp. 267–276, 1976.
- [136] K. Qi, L. Feng, X. Leng, B. Du, and W. Long, "Simulation of quasi-dimensional combustion model for predicting diesel engine performance," *Applied Mathematical Modelling*, vol. 35, no. 2, pp. 930 – 940, 2011.
- [137] K. Allmendinger, L. Guzzella, A. Seiler, and O. Loffeld, "A method to reduce the calculation time for an internal combustion engine model," in *SAE 2001 World Congress*, SAE International, mar 2001.
- [138] M. Ayebe, D. Lichtenthaler, T. Winsel, and H. J. Theuerkauf, "SI engine modeling using neural networks," in *International Congress & Exposition*, SAE International, feb 1998.
- [139] R. Stone, *Introduction to Internal Combustion Engines*. London: Macmillan Education, Limited, third edition. ed., 1999.
- [140] Albrecht, A., Grondin, O., Le Berr, F., and Le Sollicc, G., "Towards a stronger simulation support for engine control design: a methodological point of view," *Oil & Gas Science and Technology - Rev. IFP*, vol. 62, no. 4, pp. 437–456, 2007.
- [141] G. Pacitti, S. Amphlett, P. Miller, R. Norris, and A. Truscott, "Real-time crank-resolved engine simulation for testing new engine management systems," april 2008.
- [142] C. Fyhr and O. Dahlberg, "Complete engine modeling using CFD," in *SAE 2004 World Congress & Exhibition*, SAE International, mar 2004.
- [143] R. Reitz and C. Rutland, "Development and testing of diesel engine CFD models," *Progress in Energy and Combustion Science*, vol. 21, no. 2, pp. 173 – 196, 1995.

- [144] J. Benajes, J. M. Lujan, V. Bermudez, and J. R. Serrano, "Modelling of turbocharged diesel engines in transient operation. part 1: Insight into the relevant physical phenomena," *Proceedings of the Institution of Mechanical Engineers, Part D: Journal of Automobile Engineering*, vol. 216, no. 5, pp. 431–441, 2002.
- [145] D. N. Malkhede, B. Seth, and H. Dhariwal, "Mean value model and control of a marine turbocharged diesel engine," in *Powertrain & Fluid Systems Conference & Exhibition*, SAE International, oct 2005.
- [146] C. Rakopoulos, A. Dimaratos, E. Giakoumis, and D. Rakopoulos, "Evaluation of the effect of engine, load and turbocharger parameters on transient emissions of diesel engine," *Energy Conversion and Management*, vol. 50, no. 9, pp. 2381 – 2393, 2009.
- [147] G. Woschni, "A universally applicable equation for the instantaneous heat transfer coefficient in the internal combustion engine," in *National Fuels and Lubricants, Powerplants, Transportation Meetings*, SAE International, feb 1967.
- [148] Wikipedia, "Stefan-boltzmanns lov — wikipedia,," 2018.
- [149] J. J. Hernandez, M. Lapuerta, C. Serrano, and A. Melgar, "Estimation of the laminar flame speed of producer gas from biomass gasification," *Energy & Fuels*, vol. 19, no. 5, pp. 2172–2178, 2005.
- [150] N. C. Blizard and J. C. Keck, "Experimental and theoretical investigation of turbulent burning model for internal combustion engines," in *1974 Automotive Engineering Congress and Exposition*, SAE International, feb 1974.
- [151] C. Olikara and G. L. Borman, "A computer program for calculating properties of equilibrium combustion products with some applications to I.C. engines," in *1975 Automotive Engineering Congress and Exposition*, SAE International, feb 1975.
- [152] T. Morel and R. Keribar, "A model for predicting spatially and time resolved convective heat transfer in bowl-in-piston combustion chambers," in *SAE International Congress and Exposition*, SAE International, feb 1985.
- [153] H. M. Cho and B.-Q. He, "Spark ignition natural gas engines—a review," *Energy Conversion and Management*, vol. 48, no. 2, pp. 608 – 618, 2007.

- [154] J. Warnatz, U. Maas, and R. W. Dibble, *Physical and Chemical Fundamentals, Modeling and Simulation, Experiments, Pollutant Formation*. Springer-Verlag Berlin Heidelberg, 2006.
- [155] K. Varde, N. Patro, and K. Drouillard, “Lean burn natural gas fueled S.I. engine and exhaust emissions,” in *1995 SAE International Fall Fuels and Lubricants Meeting and Exhibition*, SAE International, oct 1995.
- [156] S. Rousseau, B. Lemoult, and M. Tazerout, “Combustion characterization of natural gas in a lean burn spark-ignition engine,” *Proceedings of the Institution of Mechanical Engineers, Part D: Journal of Automobile Engineering*, vol. 213, no. 5, pp. 481–489, 1999.
- [157] GT-SUITE, “Flow theory manual,” tech. rep., Gamma Technologies, 2017.
- [158] E. Ranzi, A. Frassoldati, R. Grana, A. Cuoci, T. Faravelli, A. Kelley, and C. Law, “Hierarchical and comparative kinetic modeling of laminar flame speeds of hydrocarbon and oxygenated fuels,” *Progress in Energy and Combustion Science*, vol. 38, no. 4, pp. 468 – 501, 2012.
- [159] Y. Zhang, X. Zhang, T. Qian, and R. Hu, “Modeling and simulation of a passive variable inertia flywheel for diesel generator,” *Energy Reports*, 2020.
- [160] C. D. Rakopoulos, E. G. Giakoumis, and A. M. Dimaratos, “Evaluation of various dynamic issues during transient operation of turbocharged diesel engine with special reference to friction development,” in *SAE World Congress & Exhibition*, SAE International, april 2007.
- [161] C. H. Mayr, N. Euler-Rolle, M. Kozek, C. Hametner, and S. Jakubek, “Engine control unit pid controller calibration by means of local model networks,” *Control Engineering Practice*, vol. 33, pp. 125 – 135, 2014.
- [162] M. Howell and M. Best, “On-line pid tuning for engine idle-speed control using continuous action reinforcement learning automata,” *Control Engineering Practice*, vol. 8, no. 2, pp. 147 – 154, 2000.
- [163] A. P. Colburn, “A method of correlating forced convection heat-transfer data and a comparison with fluid friction,” *International Journal of Heat and Mass Transfer*, vol. 7, no. 12, pp. 1359 – 1384, 1964.
- [164] A. Sidorow and R. Isermann, “Physical and experimental modeling of turbochargers with thermodynamic approach for calculation of virtual sensors,” *IFAC Proceedings Volumes*, vol. 45, no. 30, pp. 247 – 254, 2012.

- 3rd IFAC Workshop on Engine and Powertrain Control, Simulation and Modeling.
- [165] N. Pedersen, J. Madsen, and M. Vejlggaard-Laursen, "Co-simulation of distributed engine control system and network model using fmi & scsl," *IFAC-PapersOnLine*, vol. 48, no. 16, pp. 261 – 266, 2015. 10th IFAC Conference on Manoeuvring and Control of Marine Craft MCMC 2015.
- [166] C. Gomes, C. Thule, D. Broman, P. Gorm Larsen, and H. Vangheluwe, "Co-simulation: State of the art," *arXiv e-prints*, p. arXiv:1702.00686, Feb. 2017.
- [167] J. G. Speight, "Chapter 1 - chemistry and chemical technology," in *Handbook of Industrial Hydrocarbon Processes* (J. G. Speight, ed.), pp. 1 – 41, Boston: Gulf Professional Publishing, 2011.
- [168] T. Lachaux and M. P. Musculus, "In-cylinder unburned hydrocarbon visualization during low-temperature compression-ignition engine combustion using formaldehyde plif," *Proceedings of the Combustion Institute*, vol. 31, no. 2, pp. 2921 – 2929, 2007.
- [169] S. A. Lewis, J. M. E. Storey, B. Bunting, and J. P. Szybist, "Partial oxidation products and other hydrocarbon species in diesel HCCI exhaust," in *Powertrain & Fluid Systems Conference & Exhibition*, SAE International, oct 2005.
- [170] K. Liu, L. T. Biegler, B. Zhang, and Q. Chen, "Dynamic optimization of natural gas pipeline networks with demand and composition uncertainty," *Chemical Engineering Science*, vol. 215, p. 115449, 2020.
- [171] D. Y. Chang and J. H. Van Gerpen, "Determination of particulate and unburned hydrocarbon emissions from diesel engines fueled with biodiesel," in *International Fall Fuels and Lubricants Meeting and Exposition*, SAE International, oct 1998.
- [172] P. Lakshminarayanan and Y. V. Aghav, *Hydrocarbons from DI Diesel Engines*. Mechanical Engineering Series. Springer, Dordrecht, 2010.
- [173] S. Mendez, J. T. Kashdan, G. Bruneaux, B. Thirouard, and F. Vangraefschep, "Formation of unburned hydrocarbons in low temperature diesel combustion," nov 2009.
- [174] J. T. Kashdan, S. Mendez, and G. Bruneaux, "On the origin of unburned hydrocarbon emissions in a wall guided, low NOx diesel combustion

- system,” in *JSAE/SAE International Fuels & Lubricants Meeting*, SAE International, jul 2007.
- [175] J. T. Kashdan, N. Docquier, and G. Bruneaux, “Mixture preparation and combustion via LIEF and LIF of combustion radicals in a direct-injection, HCCI diesel engine,” in *2004 Powertrain & Fluid Systems Conference & Exhibition*, SAE International, oct 2004.
- [176] M. Abdelaal and A. Hegab, “Combustion and emission characteristics of a natural gas-fueled diesel engine with EGR,” *Energy Conversion and Management*, vol. 64, pp. 301 – 312, 2012. IREC 2011, The International Renewable Energy Congress.
- [177] V. Chintala, “Influence of flame quenching and crevice gas on hydrocarbon emission formation in an enriched biogas dual-fuel engine – an experimental and theoretical investigation,” *Fuel*, vol. 277, p. 118084, 2020.
- [178] F. Königsson, J. Kuyper, P. Stalhammar, and H.-E. Angstrom, “The influence of crevices on hydrocarbon emissions from a diesel-methane dual fuel engine,” april 2013.
- [179] J. A. Robison and W. M. Brehob, “The influence of improved mixture quality on engine exhaust emissions and performance,” *Journal of the Air Pollution Control Association*, vol. 17, no. 7, pp. 446–453, 1967. PMID: 4167147.
- [180] K. Kato, K. Igarashi, M. Masuda, K. Otsubo, A. Yasuda, K. Takeda, and T. Sato, “Development of engine for natural gas vehicle,” in *International Congress & Exposition*, SAE International, mar 1999.
- [181] D. J. Boam, I. C. Finlay, T. W. Biddulph, T. A. Ma, R. Lee, S. H. Richardson, J. Bloomfield, J. A. Green, S. Wallace, W. A. Woods, and P. Brown, “The sources of unburnt hydrocarbon emissions from spark ignition engines during cold starts and warm-up,” *Proceedings of the Institution of Mechanical Engineers, Part D: Journal of Automobile Engineering*, vol. 208, no. 1, pp. 1–11, 1994.
- [182] G. B. Landsberg, J. B. Heywood, and W. K. Cheng, “Contribution of liquid fuel to hydrocarbon emissions in spark ignition engines,” in *Spring Fuels & Lubricants Meeting & Exhibition*, SAE International, sep 2001.
- [183] J. Hilditch, Z. Han, and T. Chea, “Unburned hydrocarbon emissions from stratified charge direct injection engines,” in *SAE Powertrain & Fluid Systems Conference & Exhibition*, SAE International, oct 2003.

-
- [184] W. Zeng and M. Xie, "A novel approach to reduce hydrocarbon emissions from the HCCI engine," *Chemical Engineering Journal*, vol. 139, no. 2, pp. 380–389, 2008.
- [185] M. Christensen, B. Johansson, and A. Hultqvist, "The effect of piston topland geometry on emissions of unburned hydrocarbons from a homogeneous charge compression ignition (HCCI) engine," in *International Spring Fuels & Lubricants Meeting*, SAE International, may 2001.
- [186] M. de Zwart, G. van Dijk, and J. Klimstra, "Methane emissions from gas engines driving combined heat and power installations," *Journal of Integrative Environmental Sciences*, vol. 9, no. sup1, pp. 113–125, 2012.
- [187] L. Dondero and J. Goldemberg, "Environmental implications of converting light gas vehicles: the Brazilian experience," *Energy Policy*, vol. 33, pp. 1703–1708, September 2005.
- [188] J. T. Wentworth, "Piston and ring variables affect exhaust hydrocarbon emissions," in *1968 Automotive Engineering Congress and Exposition*, SAE International, feb 1968.
- [189] Z. Hu and N. Ladommatos, "Reduction of unburnt hydrocarbon emissions from spark ignition engines using in-cylinder catalysts," *Proceedings of the Institution of Mechanical Engineers, Part D: Journal of Automobile Engineering*, vol. 210, no. 2, pp. 123–129, 1996.
- [190] J. Schramm and S. C. Sorenson, "A model for hydrocarbon emissions from SI engines," in *International Fuels & Lubricants Meeting & Exposition*, SAE International, oct 1990.
- [191] G. T. Kalghatgi, "Combustion chamber deposits in spark-ignition engines: A literature review," in *1995 SAE International Fall Fuels and Lubricants Meeting and Exhibition*, SAE International, oct 1995.
- [192] M. E. Biancolini, S. Cordiner, M. Gambino, and V. Rocco, "Valve timing optimisation to reduce HC emissions for a heavy duty CNG fueled turbocharged engine," (Barcelona, Spain), Conference: European Automotive Congress Barcelona 1999 on Vehicle Systems Technology for the Next Century, 7 1999.
- [193] B. Torkashvand, P. Lott, D. Zengel, L. Maier, M. Hettel, J.-D. Grunwaldt, and O. Deutschmann, "Homogeneous oxidation of light alkanes in the exhaust of turbocharged lean-burn gas engines," *Chemical Engineering*

- Journal*, vol. 377, p. 119800, 2019. ISCRE 25 Special Issue: Bridging Science and Technology.
- [194] K. Persson, L. D. Pfefferle, W. Schwartz, A. Ersson, and S. G. Järås, “Stability of palladium-based catalysts during catalytic combustion of methane: The influence of water,” *Applied Catalysis B: Environmental*, vol. 74, no. 3, pp. 242 – 250, 2007.
- [195] D. Ciuparu, E. Perkins, and L. Pfefferle, “In situ dr-ftir investigation of surface hydroxyls on -Al₂O₃ supported PdO catalysts during methane combustion,” *Applied Catalysis A: General*, vol. 263, no. 2, pp. 145 – 153, 2004.
- [196] H. Korpi, “Emission reduction technologies– towards zero emissions,” tech. rep., WÄRTSILÄ, 12.10.2018.
- [197] M. Jensen, R. Cordtz, and J. Schramm, “Numerical analysis of methane slip source distribution in a four-stroke dual-fuel marine engine,” *Journal of Marine Science and Technology*, 2020.
- [198] H. Tajima, D. Tsuru, H. Tajima, and D. Tsuru, “Reduction of methane slip from gas engines by O₂ concentration control using gas permeation membrane,” in *SAE/KSAE 2013 International Powertrains, Fuels Lubricants Meeting*, SAE International, oct 2013.
- [199] H. C. Wong, S. Whelan, P. Bennicke, I. May, A. Cairns, H. Zhao, and V. Pedrozo, “Reduction of methane slip using premixed micro pilot combustion in a heavy-duty natural gas-diesel engine,” in *JSAE/SAE 2015 International Powertrains, Fuels Lubricants Meeting*, SAE International, sep 2015.
- [200] A. Williams, *Combustion Theory, Second Edition*. Chemical engineering science, 1987.
- [201] G. A. Lavoie, “Correlations of combustion data for s. i. engine calculations - laminar flame speed, quench distance and global reaction rates,” in *SAE Technical Paper*, SAE International, 02 1978.
- [202] C. K. Westbrook and F. L. Dryer, “Simplified reaction mechanisms for the oxidation of hydrocarbon fuels in flames,” *Combustion Science and Technology*, vol. 27, no. 1-2, pp. 31–43, 1981.

Appendix A

Appended Papers

Paper 1

**Unburned Hydrocarbon Formation in a Natural Gas
Engine Under Sea Wave Load Conditions**

**Sadi Tavakoli, Michael Vincent Jensen, Eilif Pedersen, and
Jesper Schramm**



Unburned hydrocarbon formation in a natural gas engine under sea wave load conditions

Sadi Tavakoli^{1,2} · Michael Vincent Jensen² · Eilif Pedersen¹ · Jesper Schramm²

Received: 19 December 2019 / Accepted: 15 April 2020
© The Author(s) 2020

Abstract

Although natural gas is documented as a low-emission fuel compared to the other traditional fossil fuels in internal combustion engines, recent research indicates large amounts of methane emission released by lean burn gas engines and highlights the importance of this emission on global warming. This paper aims at illustrating the main sources of unburned fuel in internal combustion engines with an emphasis on spark ignited natural gas engines. In addition, two unburned hydrocarbon modeling patterns, empirical and thermodynamic, are proposed. Moreover, a verified engine model including all components with an implemented dynamic load based on harmonic sea waves has been set up and coupled to the unburned hydrocarbon formation models. Results show that load variation may contribute to further methane slip and this increment rises sharply when the load amplitude enlarges. The maximum amount of methane slip occurs at reduced loads when the time lag of the control system of the turbocharger causes additional fresh air to flow towards the combustion chamber and brings the flame into the quenching area. As well, inspecting unburned hydrocarbon emission in diverse air–fuel ratios but with the same wave frequency and amplitude uncovers the sensitivity of lean burn gas engines to the dynamic load.

Keywords Natural gas engine · Sea wave · Unburned hydrocarbon · Emission modeling

1 Introduction

The importance of toxic effects and global warming potential of emission compounds from industrial activities in our daily life have been investigated for decades, and environmental legislation is going to be more strict for these applications. International standards such as the Euro norms and the IMO regulations [1, 2] have imposed more strict levels for emission compounds, especially from engines; for instance, Tier III [3] only allows almost one-fifth of NO_x emissions compared to Tier I for marine Diesel engines. The Paris agreement also compelled the authorities to get engaged into the challenge of global warming to keep the overall warming below 2 °C [4]. Acquiring these new emission targets for internal combustion engines would only be applicable if at least one of the following items be taken into account:

- Aftertreatment system.
- Design modification.
- Alternative clean fuels.

Using aftertreatment systems in gasoline and Diesel engines to comply with the emission legislation is a necessity, but these systems not only add costs to the engine, but also need regular maintenance. Design modification has always been an upgrading process to improve engine performance and emission. An example of a work in this fields is the work done by Karthickeyan [5] which showed that piston bowl design boosts swirl and squishes stream lines and the result is a better mixing process of air and fuel. Furthermore, Sadiq and Iyer [6] tried to optimize a small-volume high-speed engine with various fuels and crown geometries, and they concluded that engine behaviour will be enhanced by having a higher turbulent air mixture inside the chamber. Compression ratio optimization, intake and exhaust port modification, fuel system development, exhaust gas recirculation, ignition timing correctness, and accurate control system implementation are other examples of design modifications. Since the customers usually prefer less-complicated less-expensive engines, substituting the conventional fuel with

✉ Sadi Tavakoli
sadi.tavakoli@ntnu.no

¹ Department of Marine Technology, Norwegian University of Science and Technology (NTNU), Trondheim, Norway

² Department of Mechanical Engineering, Technical University of Denmark (DTU), Copenhagen, Denmark

an alternative pure fuel to reach the emission target would be a fair solution. Among all, natural gas in lean burn SI engines or dual fuel engines with a pilot of diesel fuel has got more popular, since application of this fuel contributes to a drastic reduction in emission compounds without additional expenditure for clients. Rosli Semin [7] reported up to 85% NO_x reduction and 30% CO₂ and 95% CO reduction in natural gas engines. Therefore, these engines allow manufacturers to a high extent to meet emission legislations without any fundamental modification on the engine or even using aftertreatment systems [8].

Considering the main purpose of this paper, we mostly describe spark ignition natural gas engine performance and emissions. In contrast to the low aforementioned emission compounds, high amount of methane slip is still a challenge for lean burn gas engines. Although in the initial IMO strategy report, published on April 2018 [9], only considerations to address volatile organic compounds are recommended. It seems that in an early future, a very restricted requirement will be imposed on unburned hydrocarbons, since the global warming potential (GWP) value for methane is 28 times higher than for carbon dioxide on 100 years prospective, based on report by The Intergovernmental Panel on Climate Change (IPCC) [10]. Even a research by Brynolf et al. [11] emphasized that using natural gas in marine applications will not improve the greenhouse gas effect compared to heavy fuel oil because of the methane slip.

In this paper, we present the main sources of methane slip in engines and pay a special attention to natural gas engines. In addition, to recognize the importance of each source on the total unburned hydrocarbon formation during transient conditions which has never been studied before, a developed thermodynamic engine cycle model with an incorporated emission model is considered together with an empirical emission model, and both are coupled to the output of an engine simulation from a commercial software. Since the engine is designed for marine applications, time-based harmonic loads are imposed on the engine.

2 Unburned hydrocarbon formation

2.1 Sources of unburned hydrocarbon

Unburned hydrocarbons (UHC) are typically an output of incomplete combustion due to unfavorable engine design, low fuel quality or failure in the control system. UHC exists in both SI and CI engines, while in the latter one, the HC compounds contain higher molecular weight due to the higher boiling point of the diesel fuel spray [12]. In SI engines, seven classifications can be introduced for sources of UHC:

1. Crevice volume.
2. Wall layer quenching.
3. Pockets of partially reacted mixture.
4. Misfiring.
5. Oil films.
6. Deposits.
7. Valve overlap.

The significance of these sources is highly depended on the engine application whether it is stationary or non-stationary and type of fuel whether it is liquid or gas.

2.1.1 Crevice volume

The regions in the combustion chamber located somewhere between the piston and the liner, the intake and exhaust valve seat gaps, and the injector groove in direct injection engines are all crevice volumes, which account for almost 5% of the trapped and non-reacted mixture in the initial combustion [13]. Wentworth [14] illustrated that his modified piston and top ring minimized the crevice volume, and as a consequence, exhaust hydrocarbons was halved in a wide range of loads and speeds. A restriction of reducing the crevice volume, especially between the piston and the liner, is the existence of an oil layer for lubrication, since the temperature of the oil should not exceed 170 °C. Therefore, having a quenched flame in such area is crucial [15]. Increasing the top land crevice to pass two plate wall quenching as recommended by Huang et al. [16] reduced UHC up to 50%, although a 1–3% fuel consumption increment was also observed.

2.1.2 Wall layer quenching

Liner and piston surfaces are the coldest areas during the combustion phase due to the existence of a water cooling system around the liner and an oil cooling system (not for all engines) on the bottom of the piston. These cooled surfaces transfer energy from the hot gas mixture and create a cold thermal layer close to these regions. This phenomenon ceases the flame propagating and is called flame quenching in the layer adjacent to the wall. Previously, it was assumed that a high percentage of the UHC emission origins from wall quenching, but after developing new technical methods, [17] researchers discovered the impact of post-flame combustion on oxidizing the quenched mixture.

2.1.3 Pockets of partially reacted mixture

Depending on how turbulence influences on the flame, the combustion will be enhanced or quenched. Swirl originating from the intake port and tumble from the piston bowl shape both promote mixing of air and fuel in the combustion

chamber. In case the turbulence increases significantly, the flame front breaks up and leaves pockets of unburned mixture. These pockets are in fact source of unburned hydrocarbon and can exceptionally have a determining function under warming up [18], especially if the target is transferring enthalpy release toward the exhaust port to heat up a catalyst faster in slow combustion [19].

2.1.4 Misfiring

Regardless of reason for misfiring, whether it is due to high dilution with air and exhaust gas, or a fault in the spark plug, or even malfunctioning of the control system [15], the consequences of such an event is that a considerable mass of unburned hydrocarbon is released into the exhaust system. In case of an explosion in the exhaust manifold, turbine, or catalytic converter damages are impending, and otherwise, UHC compounds will be released into the atmosphere. In standard SI gasoline engines, only a defective spark plug and control system may contribute to the misfiring, while in a lean-burn gas engine, high dilution may also result in partial misfiring and cycle-to-cycle variations.

2.1.5 Oil films

Due to solubility of fuel in the oil, a portion of the fuel near the cylinder wall will be absorbed by the lubrication oil film. The quantity of fuel absorbed or desorbed is a parameter sensitive to the oil and fuel specification, oil and fuel temperature, oil film thickness, and time [20]. To confirm this point, a work considering a mass diffusion equation and Henry's constant has been done by Schramm and Sorenson [21]. They revealed that the desorbed hydrocarbons from oil film are extremely dependent on the thickness of the film. This is, however, for a film thickness of up to 2 microns and there would be no shift in thicker films.

2.1.6 Deposits

When oil and fuel burns on the surfaces of the combustion chamber, a sheet of deposits forms on the major part of the surfaces including piston, liner, valve seats, and even crevices [22]. Kalghatgi [23] studied the influence of deposits on the production of NO_x , since he believed that deposits reduce the heat loss to the coolant fluid and, as a consequence, increase the thermal NO_x , while the increase in surface and gas temperature results in less unburned hydrocarbon. Meanwhile, deposits will partly fill the crevices and the UHC created due to crevice volumes reduces. In contrast, these deposits absorb part of the unburned fuel like an oil film. He concluded that there is no solid conclusion about the impact of the combustion chamber deposits. Other studies, however, showed that between 0.5% [13] and 1% [24] of

the injected fuel will be sent out of the combustion chamber unburned due to deposits on the surfaces. Stepien [25] listed the main effects of engine deposit formation and reasoned that the porous nature of deposits in the combustion chamber and the capability of absorbing fuel contributes to a higher amount of UHC emission.

2.1.7 Valve overlap

The valve overlap period is the period where both the intake and exhaust valves are open, and the boost pressure drives the fresh air–fuel mixture directly from the intake port to the exhaust port without taking part in the combustion. This phenomenon arises only in premixed combustion engines where a mixture of air and fuel enters through the intake valves. The wasted mixture is a function of the overlap duration and boost pressure, and could be the source of approximately 5% of UHC [26]. An optimum timing for the inlet and outlet valve openings and their designs relies on several factors such as engine application, engine respiration, speed, EGR, and so on. For instance, camshafts are usually designed based on a trade-off among engine lower speed with least EGR and engine higher speed with the best scavenging and required EGR. Otherwise, a very short overlap contributes to a higher rate of EGR in low load, and this dilution increases the risk of partial burn misfiring [19].

2.2 Difference between the influence of gas and liquid fuel in formation of UHC in SI engines

To explain the importance of state of matter of combustible on UHC product, Landsberg et al. [27] injected liquid and evaporated gasoline fuel inside the combustion chamber and observed that the liquid fuel flow produces between three and seven times greater quantity of UHC in association with the same fuel as vapor, and this rises if this fuel is to be injected directly in to the combustion chamber.

Robison and Brehob [28] used a liquid fuel vaporization carburetor to render a stronger homogeneous mixture of air and fuel. The result shows less UHC emission during warm-up when liquid fuels cannot be vaporized suitably in the port and the cylinder, and regional rich mixtures occur in the combustion chamber. Similar works [29, 30] prove that part of the fuel injected to the intake port will generate wall wetting in the cold start. Tilagone and Venturi [31] changed a gasoline engine of vehicle application to a natural gas engine to evaluate the performance and emission of the engine, and they demonstrated that natural gas contributes to a remarkable decline in emission compound, meaning 50% less UHC compared to a gasoline engine. The main reason for this drop is the limited oil film adsorption–desorption phenomenon. Kato et al. [32] showed that less UHCs released from the same performance gas engine than the gasoline engine is due

to less wall fuel flow in the intake system. Besides, sources of methane slip in the work of Zwart [15] are overlap, misfire, and crevices, and matching with other sources of UHC in typical SI engines, and deposit and oil film are omitted as sources of UHC in SI natural gas engines, if we classify wall quenching as a misfire.

Concerning the literature review, the main causes of UHC in natural gas engines can be interpreted into crevice volume, gas exchange, and flame quenching unburned hydrocarbon. Considering the essence of utilizing natural gas in a very lean burn mixtures, these sources still will produce a substantial volume of UHC in the lean-burn natural gas engines.

3 Unburned hydrocarbon modeling

To determine the disparity of formation of UHC in steady-state and dynamic conditions, a nine-cylinder natural gas engine has been modeled thermodynamically in details with the commercial software, GT Power, and its output is implemented into an empirical UHC modeling within this software. Moreover, a separate thermodynamic engine model has been developed to distinguish the individual sources of UHC formation. The schematic of the procedure of the modeling is shown in Fig. 1. Detailed equations are presented in Sect. 3.1 and 3.2. For simplicity, the empirical UHC model is named Type E, and the thermodynamic UHC model is named Type T.

3.1 Empirical modeling of UHC formation: Type E

The Quench layer is normally the layer at the end of the flame, i.e., near the walls, while the flame itself is normal, parallel or at an angle to the wall. The flame quenching process occurs based on the second rule of thumb criteria by William [33]: The rate of liberation of heat by a chemical reaction inside the flame segment must approximately balance the rate of heat loss from the segment by thermal conduction. Relating the heat release to the heat loss can be done by a non-dimensional Peclet number, which is relatively constant in a wide range of geometrical configurations. For two plate quenching, the Peclet number is determined by:

$$Pe_2 = \frac{\rho S_L c_{p,f} d_{q2}}{k_f}, \tag{1}$$

where ρ , S_L , $c_{p,f}$, d_{q2} , and k_f are the density, laminar flame speed, specific heat at constant pressure, two-plate quench distance, and thermal conductivity, respectively. Lavoie [34] developed an empirical correlation for two-plate quench

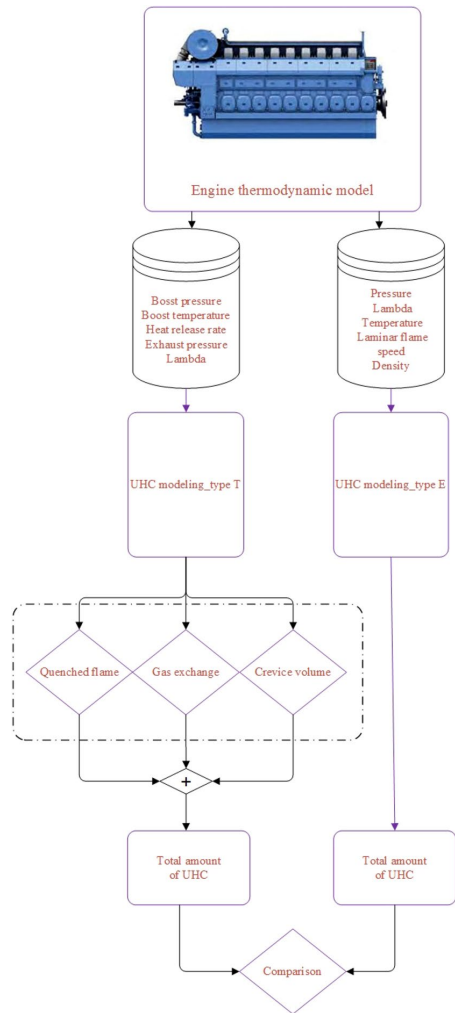


Fig. 1 Emission modeling flowchart

distance which is well fitted for a range of pressure between 3 and 40 bar with:

$$Pe_2 = \frac{9.5}{\phi} \left(\frac{P}{3}\right)^{0.26 \min(1, 1/\phi^2)}, \tag{2}$$

where P is pressure and ϕ is equivalence ratio. Calculating Pe_2 which is Peclet number for two-wall quenching, and laminar flame speed, Eq. (3) gives us the two wall quench distance in Eq. (1):

$$(1 - f)S_L = A(\phi)P^n e^{-E(\phi)/2RT_i}, \tag{3}$$

where f is dilution effect, A is pre-exponential factor, and E is activation energy.

Lavoie then recommended that two- and single-plate quenching distance have the constant proportion in Eq. (4) as shown in Fig. 2 [34]:

$$\frac{dq_1}{dq_2} = \frac{Pe_{1,u}}{Pe_{2,u}} = 0.20. \tag{4}$$

To calculate the amount of fuel captured in the quench layer, it is necessary to integrate the quench layer content; however, Lavoie recommended an experimentally expression for this amount, as:

$$\left(\int_0^\infty \rho z dy \right)_f = \frac{\rho_u dq_2}{22}, \tag{5}$$

where y is perpendicular distance from the wall and the mass fraction of unburned gas is $z = \frac{HC}{HC_0}$, where HC_0 is initial concentration of hydrocarbons in the unburned mixture. The quench layer UHC will undergo post-oxidation according to the new defined mechanisms [34, 35]:

$$\frac{d(HC)}{dt} = -6.7 \times 10^{15} e^{\frac{-37230}{RT}} f_{HC} f_{O_2} \left(\frac{P}{RT} \right)^2. \tag{6}$$

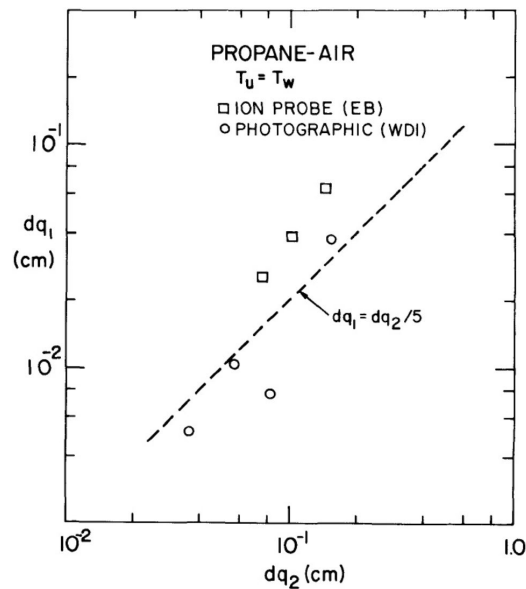


Fig. 2 Single-wall quench versus two-plate wall quench (dq_1 vs dq_2) [34]

If the pressure, temperature, and fuel species fraction stay high enough, a dominant contribution of unburned fuel burns in the post-oxidation process from the end of the main combustion till the end of the cycle.

In this section, two additional sources of the UHC including crevice volume and blown by mixture during the gas-exchange process have been taken into account, as well. Mass of mixture trapped in the crevice volume is calculable by volume and density, and depending on the maximum pressure crank angle, the gas will participate partially in the main combustion and the post-oxidation process. Moreover, the calculation of the gas-exchange UHC source does not need any extra modeling than the quasi-steady modeling.

3.2 Thermodynamic modeling of UHC formation: Type T

The developed thermodynamic engine model is a three-zone full engine cycle model developed with the aim of obtaining information on the source distribution for the unburned hydrocarbon emissions which is not possible in the applied commercial engine simulation software. The model, TECMU, is described in more details in [36]. The model estimates the contribution to the total unburned hydrocarbon emissions from three sources: crevices, wall quenching, and short-circuiting due to valve overlap. To do so, this model is coupled with the output from the commercial engine simulation software. The engine operating condition and calculated outputs are given as input to this model. This ensures that the two models (Type E and Type T) simulate the same engine operating state. The contributions to the total unburned hydrocarbon emissions from different sources are then obtained as an output from the Type-T model.

The procedure of a Type-T simulation is: the estimation of the contribution from the crevices to the unburned hydrocarbon emissions is based on a mass balance for the cylinder content of fuel from the crevice volume. From the mass balance equation, the instantaneous in-cylinder mass fraction of fuel from the crevices $y_{f,cy}^{cr}$ is calculated. The contribution to the total unburned hydrocarbon emissions from the crevices $m_{f,out}^{cr}$ is then determined by integrating the product of $y_{f,cy}^{cr}$ and the total mass flow rate out of the engine, \dot{m}_{out} , over the exhaust phase of the engine cycle:

$$m_{f,out}^{cr} = \int_{ex} \dot{m}_{out} y_{f,cy}^{cr}. \tag{7}$$

Estimation of the contribution from short-circuiting to the engine out emissions of unburned hydrocarbons is performed similarly and simultaneously. The cylinder content of fuel from the intake manifold is calculated based on a mass balance which enables the instantaneous in-cylinder mass fraction of fuel from the intake manifold, $y_{f,cy}^{sc}$, to be

determined. The contribution from short-circuiting to the unburned hydrocarbon emissions is obtained by integrating the product of $y_{f,cy}^{cr}$ and \dot{m}_{out} :

$$m_{f,out}^{sc} = \int_{ex} \dot{m}_{out} y_{f,cy}^{sc} \quad (8)$$

A separate mass balance equation for the total fuel mass in the cylinder is used to determine the instantaneous in-cylinder fuel mass fraction $y_{f,cy}$. The mass of total hydrocarbon emissions $m_{f,out}$ is then calculated as:

$$m_{f,out} = \int_{ex} \dot{m}_{out} y_{f,cy} \quad (9)$$

The relative contributions from crevices, short-circuiting, and wall quenching to the total hydrocarbon emissions are obtained as:

$$y_{f,out}^{cr} = \frac{m_{f,out}^{cr}}{m_{f,out}} \quad (10)$$

$$y_{f,out}^{sc} = \frac{m_{f,out}^{sc}}{m_{f,out}} \quad (11)$$

$$y_{f,out}^{qu} = 1 - y_{f,out}^{cr} - y_{f,out}^{sc} \quad (12)$$

Here, $y_{f,out}^{qu}$ is the relative contribution to the total hydrocarbon emissions from wall quenching. As seen from the calculation of $y_{f,out}^{qu}$, it is assumed in the model that unburned hydrocarbon emissions which are not due to crevices or short-circuiting are from wall quenching.

Possible post-oxidation of unburned fuel remaining in the cylinder after the main combustion has ended is accounted for in the model based on the expression [37]:

$$\frac{d[HC]}{dt} = 1 \times 10^{13} e^{-\frac{48400}{RT}} [HC]^{0.7} [O_2]^{0.8} \quad (13)$$

It is assumed in the model that the fuel undergoing post-oxidation is present in the vicinity of the cylinder wall, since it is fuel from the wall quench layer and fuel coming out of the crevices. Hence, the wall film temperature $T_f = \frac{1}{2}(T_g + T_w)$ is used in the post-oxidation evaluation.

4 Results and discussion

4.1 Validation

The engine specifications are presented in Table 1. The engine is applied as the propulsion system of a cargo vessel named Kvitbjrn from the Rolls Royce company. It is fueled with natural gas and utilizes two sets of control systems to

Table 1 Engine specification

Item	Unit	Amount
Engine model		B 35:40L9PG
Number of cylinders	–	9
Cylinder bore	mm	350
Cylinder stroke	mm	400
Connecting rod	mm	810
Rated speed	rpm	750
Rated power	kW	3940
Max Torque at rated speed	Nm	50200
Fuel type	–	Natural gas

adjust the stability of the engine: PID control system for setting the speed of the engine, and wastegate control system to regulate the air–fuel ratio. In former controller, the engine speed is defined to be fixed on 750 rpm. Proportional–integral coefficients in a closed loop govern the control process and restore the deviation by fuel injection period adaptation. In latter, observing any abnormality in the air–fuel ratio will be adjusted by wastegate valve using the same approach of PID controller. The valve diameter determines the amount of exhaust gases upstream of the turbine inlet, and the boost pressure provides the required air flow subsequently.

The architecture of the engine modeling is shown in Fig. 3. This structure provides modeling of the turbocharger system, intercooler, intake manifold, intake and exhaust valves, combustion chambers, and exhaust manifold. An imposed torque is implemented on the engine through the crankshaft and large mass inertia, and the output data are exported and stored schematic tank. These data are, in fact, the required input of the Type E and Type T models, as shown in Fig. 1.

The combustion coefficients are tuned based on the measured data, and Fig. 4 demonstrates the comparison of the normalized output of the engine modeling and measurement data with a satisfactory agreement in various loads. Figure 4a, b shows for normalized brake-specific fuel consumption and unburned hydrocarbon, respectively. The normalizing factor for BSFC and UHC has gauged data at 100% load. The other data are measured at 85%, 75%, 50%, and 25%, all at a rated speed of 750 rpm.

To monitor a natural gas engine's response to dynamic load and the greatness of this variation on methane slip, a harmonic load has been imposed. Every individual case has taken a specific pattern of the load amplitude alternation (5, 10, 15, or 20% total deviation from the base load), with a constant frequency domain of 0.18 1/s, adapted from [38]. Figure 5 draws a schematic structure of the loading with 0, 10, and 20% deviation (For instance, 20% deviation means 10% overload and 10% under load). The horizontal axis of this figure shows time (second) versus torque on the

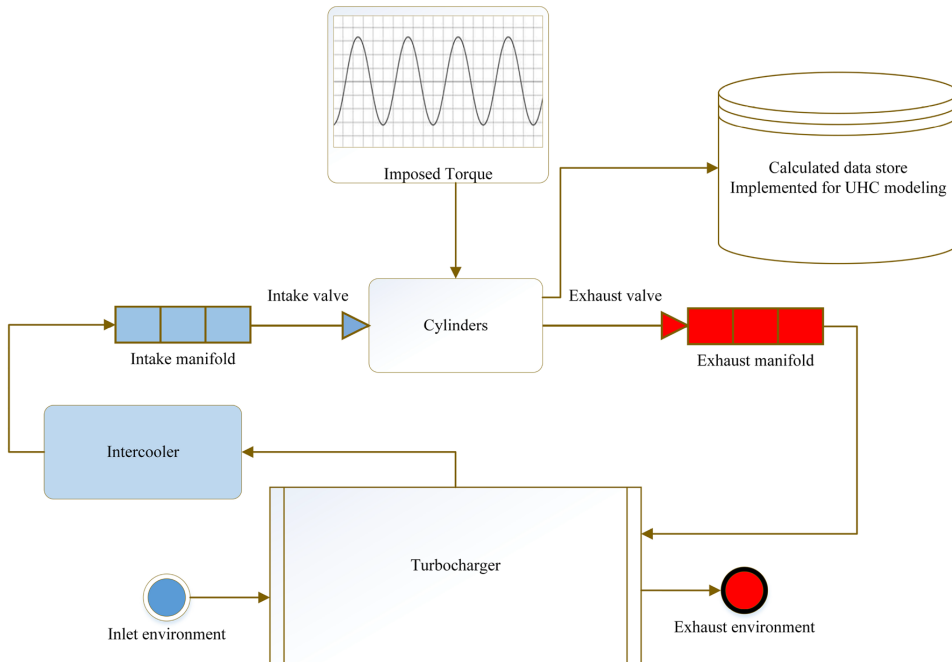


Fig. 3 Engine modeling flowchart

vertical axis. Due to numerical errors of the simulation and for the sake of reaching a stable condition, the modeling of harmonic load was commenced after 60 s of constant load and then proceeded until almost 149 s after start, equals to 16 full-wave cycles. This quantity of cycles ensures the independence of the results from a sudden change in the initial load transition.

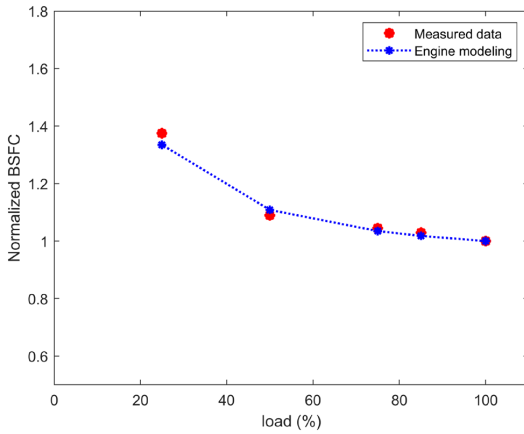
4.2 Unburned hydrocarbon modeling: Type E

Figure 6 illustrates the results of implementing a harmonic sea wave load on the UHC volume from the Type E modeling. The amount of UHC at the commencement of the harmonic load has been viewed as a normalizing factor, so clearly the quantity of UHC before and after the harmonic load corresponds to just 1. As can be seen, there is a notable correlation between load shifting and transition of UHC. Figure 6a shows that with 5% load change, UHC decreases first around 20% during higher load and afterward increases almost 40% during lower load. The average throughout the transient condition presents an entirely 4% UHC addition, given by the red line. Figure 6b–d also displays that the average UHC alternation for 10, 15, and 20% load variation is 13%, 29% and 49%, sequentially. These diagrams indicated that UHC may momentarily increase up to 300% when the

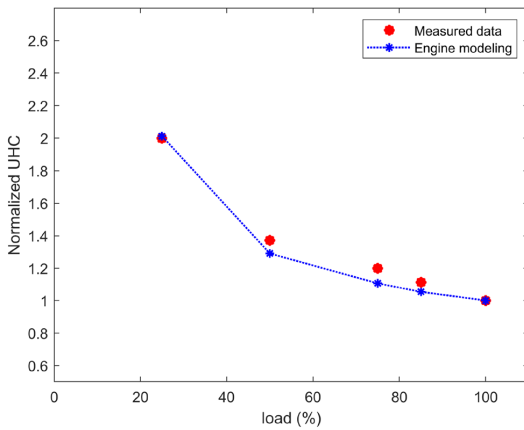
load of the engine lessens in the time scale of sea waves in harsh condition, and may just after decrease due to increasing load, resulting in a more efficient combustion than at nominal rate. The reduction of UHC is around half of the level at the nominal load and speed set point, so overall UHC level in transient conditions rises almost 50% under sinusoidal load in the severe case of 20% load change.

4.3 Unburned hydrocarbon modeling: Type T

Performing simulation with the Type T model, it is possible to classify the unburned fuel emissions as resulting from crevice, gas exchange, and quenched mass fraction. Since the Type T model is an independent single cylinder model which is not included in the applied commercial software, verifying the pressure trace of this model is needed. This verification is done by comparing a normalized pressure trace in rated load and speed. Figure 7 documents that both models are giving the same results during all four phases of compression, combustion, expansion, and gas exchange. In addition, the relative difference of the amount of UHC of these models in the nominal load is almost equivalent and the disparity is less than 3%, which is an acceptable difference.



a Normalized BSFC



b Normalized UHC

Fig. 4 Simulated and measured BSFC and UHC versus load at rated speed

To save the computation time, the Type T model is only applied during the wave load period, and not during the prior constant load period.

The results gained from the preliminary analysis of the Type T model are given in Fig. 8, and the investigation of the outputs reports 12%, 37%, 72%, and 114% more UHC emitted from the engine when the loads vary 5, 10, 15, and 20%, respectively. The UHC level predicted in nominal load is equivalent to the output of Type E and has been used as a normalizing coefficient. In 5% load oscillation, the maximum amount of UHC at lower load is 160%, and at the higher load, it is 80% of that in nominal load, which means a 20% reduction. The time average level is totally

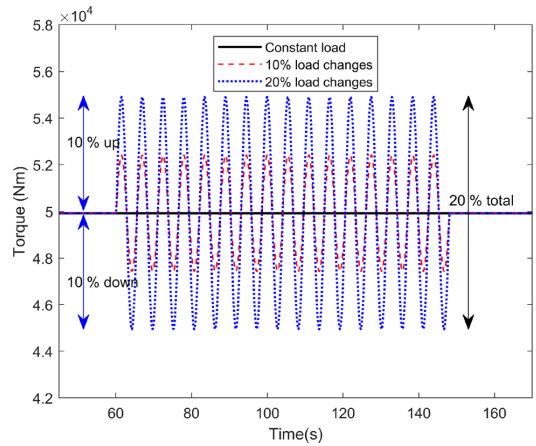


Fig. 5 Imposed dynamic load

12% for under this load shift. With 20% load variation, 500% increase and 45% drop in UHC level are observed.

Comparing the variation predicted by the two models of UHC in Fig. 9 represents a considerable gap between these two models, especially in the higher percentage of the load curve. First reason shows itself up by taking Figs. 6 and 8 into consideration. The UHC amount in Fig. 8 reaches a minimum in higher load, and will not decrease any longer, despite the prediction at the Type E model, where the UHC level even reached 30% of the nominal UHC level at 20% load variation. Moreover, the highest amount of UHC predicted by the Type E model is hardly higher than 300%, while with the Type T model, it goes up to 500%. These differences of UHC formation demonstrate the importance of the post-oxidation process in the combustion chamber and the methodology of computing the mass amount and fraction of unburned fuel. It must be highlighted here that post-oxidation calculation in the Type T model is a function of the average temperature of the wall and the hot gases, while the temperature used in the Type E model for post-oxidation is the burned gas temperature.

Fractional results in Fig. 10a–c from the Type T model are showing that up to 75% of UHC stems from crevice volume, maximum 3% from gas exchange, and around 25% of unburned fuel originates from quenched flame at the nominal load and speed. Therefore, the gas-exchange UHC has the least influence on the UHC level amount, and this is reasonable, because the engine valve timing is redesigned for a natural gas engine application with a very short overlap. In the first few seconds, when the load increases, due to imposing a load shift, crevice is the only source of UHC and the reaction ends around 1, while the fraction of UHC by quenched flame decreases to 0% at

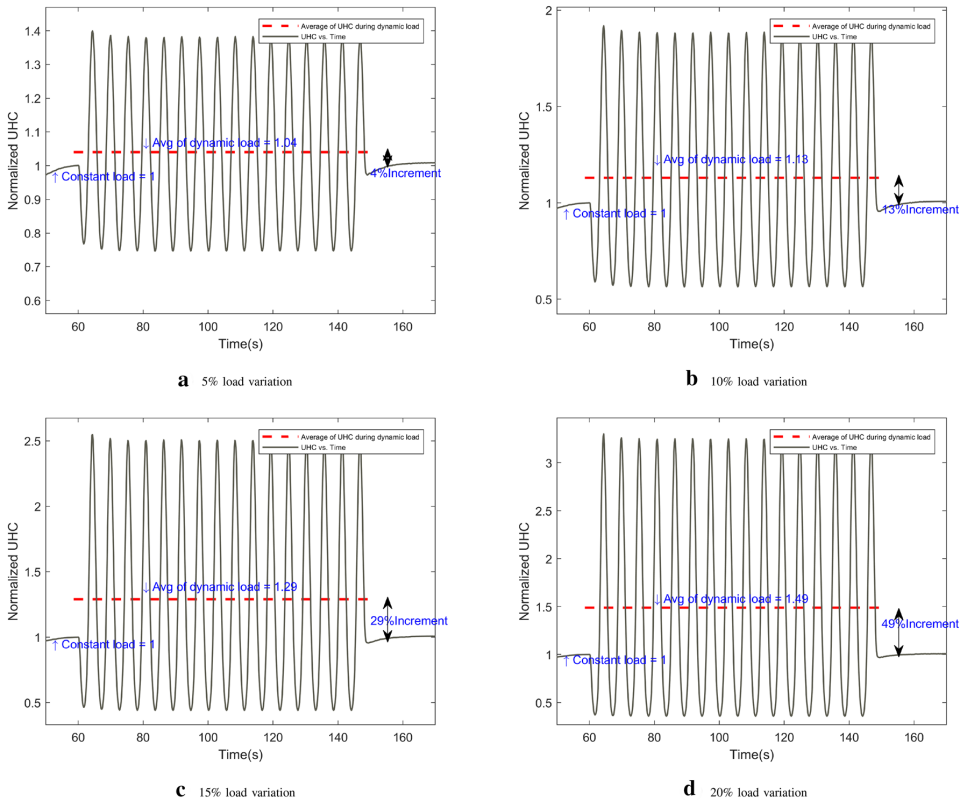


Fig. 6 Unburned hydrocarbon variation (modeling Type E)

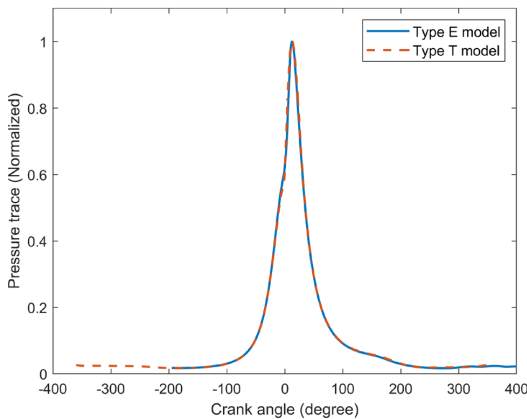


Fig. 7 Comparison of normalized pressure traces

20% load change. This proposes that the flame due to the flame speed and flame quality burns all of the fuel in the main chamber. This addresses the thought that the Type T model predicts a more reasonable output of UHC in the higher load than the Type E model, since as long as there is a crevice volume in the combustion chamber, there is a minimum UHC level as an output of the engine regardless of the load.

The mean lines in Fig. 10a likewise confirm that the UHC fraction due to the crevice volume changes a little, and in contrast, the UHC fraction due to quenched flame, Fig. 10c, changes more significantly when load oscillation increases. Taking Fig. 10b into account, UHC fraction due to the gas-exchange changes almost 15%. However, this variation is a function of variation of the total UHC, and not due to the gas exchange itself, as shown in Fig. 11. It is instantly visible in the figure that quenched flame is nearly the only effective participant of UHC variation in transient marine conditions, as UHC mass due to crevice volume swings slightly around a persistent quantity.

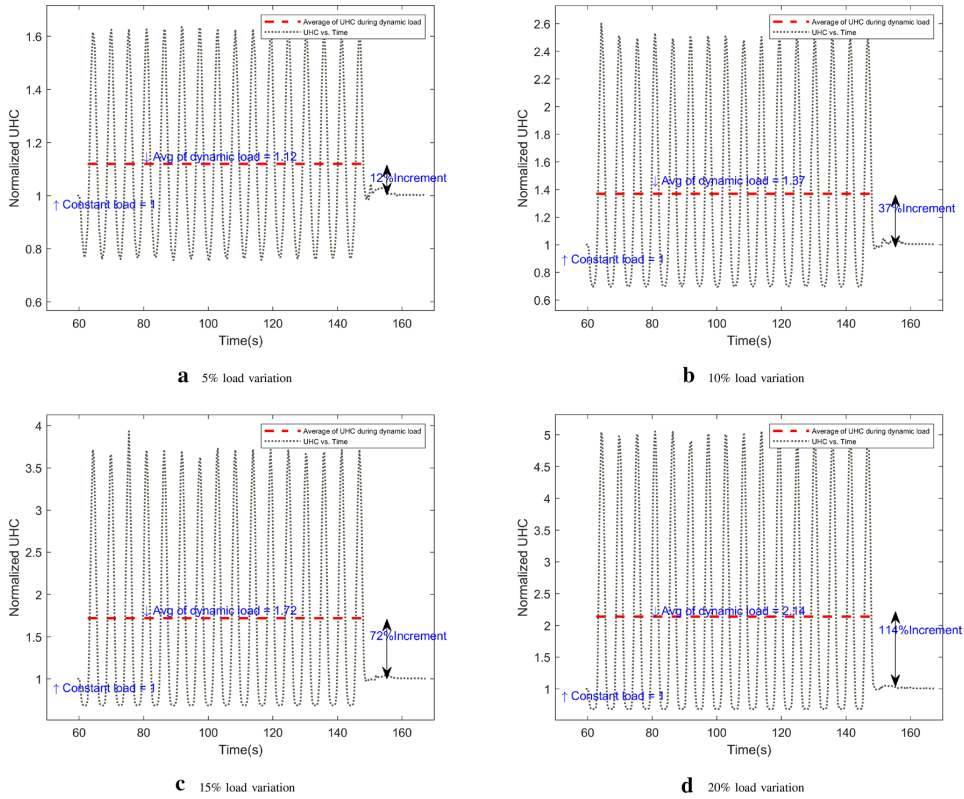


Fig. 8 Unburned hydrocarbon variation (modeling Type T)

4.4 Lean burn mixture sensitivity to dynamic load

Comparing the UHC level with the rate of change of the air–fuel ratio shows that there is a direct correlation between these two parameters. Referring to Fig. 12, it is instantly visible that there are similarities between the variation of lambda during dynamic load period and the imposed variation of torque, as shown in Fig. 5. This indicates a need to understand the various perceptions of the air and fuel system first among all the existing port systems. Primary inspection revealed that load fluctuation ups and downs the required fuel to make up any speed variation deviated from nominal set point. This alternation of fuel flow asks for an equal change of the air flow, and since any command to the controller system to adjust the proper air is going to be done at the end of the exhaust manifold, even with the fastest PID response, there still exists some delay due to the dynamic of the system. Such time lag of the air system drives the engine to work at non-constant lambda.

To figure out how the air–fuel ratio itself influences the amount of UHC, lambda with certain values of 1.73, 1.78,

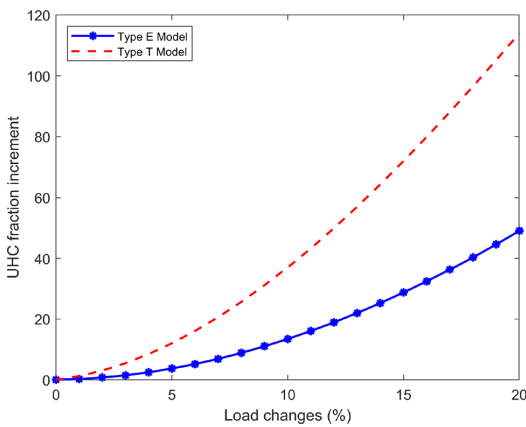


Fig. 9 UHC variation predicted by the two models

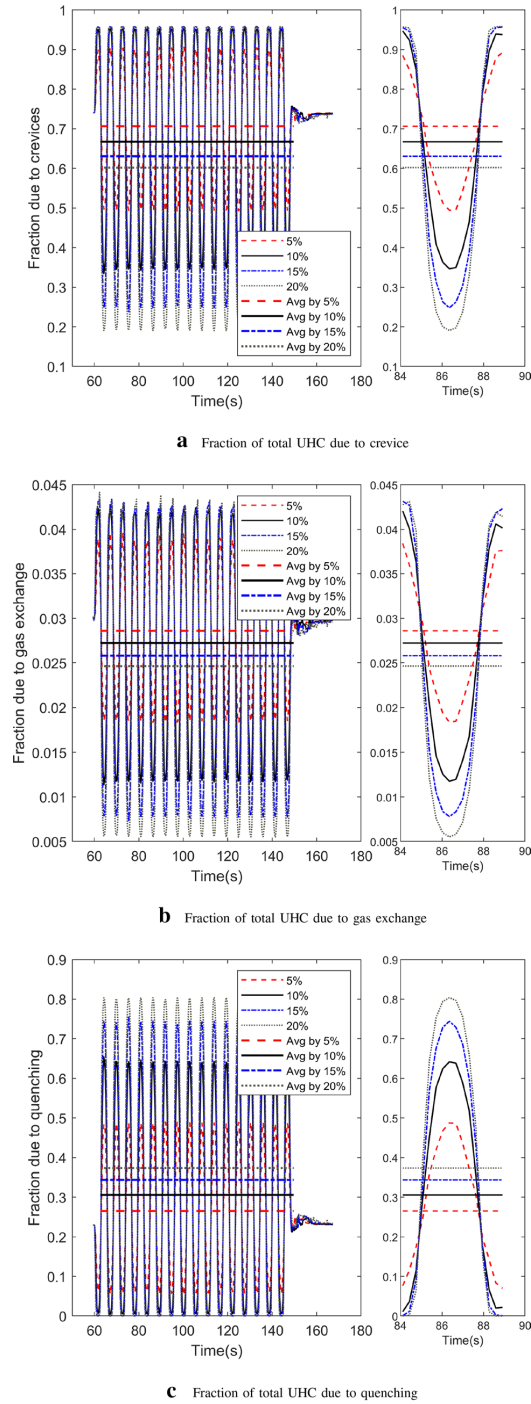


Fig. 10 UHC fraction distribution

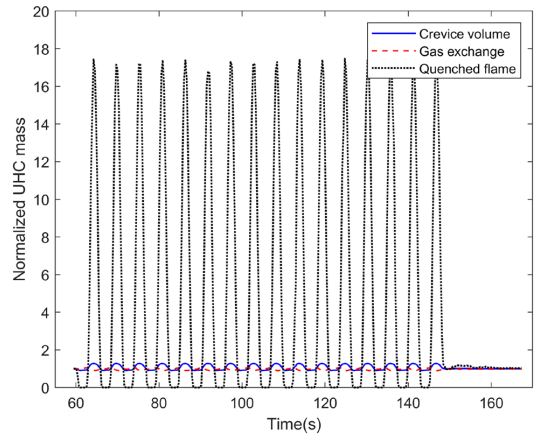


Fig. 11 Normalized mass of UHC sources with 20% load variation

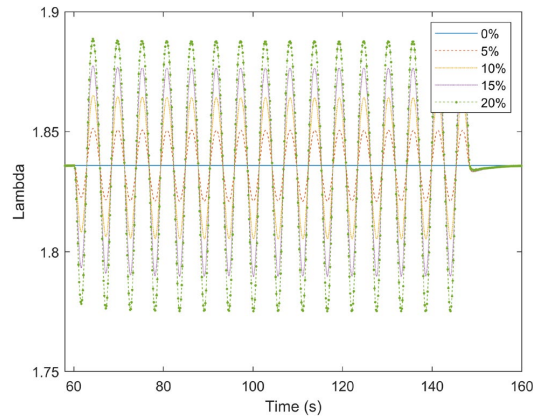


Fig. 12 Air-fuel ratio variation during dynamic load

1.83, and 1.88 has been considered. Lambda equal to 1.83 is our base value of the study, and the target air-fuel ratio corresponding to these lambda values would be 29, 30, 31 (base value) and 32. The findings of the simulations are shown in Fig. 13 and presents similarities between the rate of increasing level of UHC and the trend which appeared in Fig. 9. Lambda boosting multiplies UHC amount in constant load shown by blue columns. This explains to a high extend the significance of providing a firm air-fuel ratio based on the optimal set point.

Furthermore, the results display a contrasting tendency of the UHC pattern in dynamic load, as well. With higher lambda, here 1.88, the engine will produce less UHC in dynamic load. A possible explanation for this fact is that our considered engine is designed on the basis of least UHC

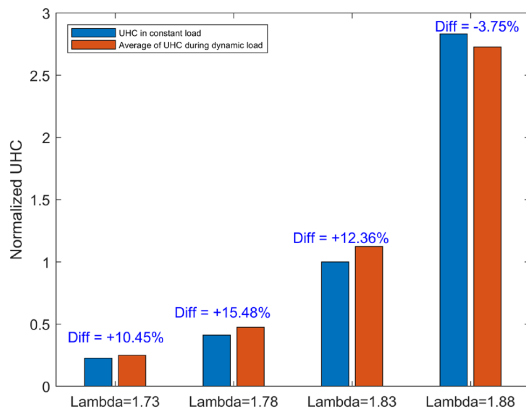


Fig. 13 Effect of air–fuel ratio on UHC level during static and dynamic load

in steady state; therefore, UHC will hardly reduce further in dynamic load, while it may increase quickly. Thus, expecting an increment of UHC during dynamic load is imminent. On the other hand, higher lambda produces higher UHC and both rise and fall of UHC occurs normally for both of the lower and higher load. Therefore, the reduction of UHC in dynamic load can only happen in a very lean or very bad UHC-based designed engine.

5 Conclusion

The amount of UHC in lean burn gas engines has been examined by modeling all subsystems of a marine engine. Two models have been used in the analysis of UHC emissions, with one having the capability of splitting the sources of UHC up. The results show that in stable condition, depending on crevice volume and lambda, UHC formation could be a function of only crevice volume to a high extent. Conversely in transient condition, the time lag in controlling the air–fuel ratio contributes to leaner or richer mixture, and the resulting flame speed slowness and incomplete combustion in leaner mixture areas very close to the wall causes a major part of the fuel being unburned. It was indicated that during 20% of oscillation load, the UHC level may be two times higher compared to a constant load case.

Acknowledgements Open Access funding provided by NTNU Norwegian University of Science and Technology (incl St. Olavs Hospital - Trondheim University Hospital).

Open Access This article is licensed under a Creative Commons Attribution 4.0 International License, which permits use, sharing, adaptation, distribution and reproduction in any medium or format, as long as you give appropriate credit to the original author(s) and the source,

provide a link to the Creative Commons licence, and indicate if changes were made. The images or other third party material in this article are included in the article's Creative Commons licence, unless indicated otherwise in a credit line to the material. If material is not included in the article's Creative Commons licence and your intended use is not permitted by statutory regulation or exceeds the permitted use, you will need to obtain permission directly from the copyright holder. To view a copy of this licence, visit <http://creativecommons.org/licenses/by/4.0/>.

References

1. European emission standards. https://en.wikipedia.org/wiki/European_emission_standards
2. International Maritime Organization. <http://www.imo.org/en/Pages/Default.aspx>
3. United States Environmental Protection Agency. All epa emission standards. <https://www.epa.gov/emission-standards-reference-guide/all-epa-emission-standards> (last updated: 2017)
4. Rogelj J, den Elzen M, Höhne N, Fransen T, Fekete H, Winkler H, Ro Schaeffer, Sha F, Riahi K, Meinshausen M (2016) Paris agreement climate proposals need a boost to keep warming well below 2°C. *Nature* 534:631–639
5. Karthickeyan V (2019) Effect of combustion chamber bowl geometry modification on engine performance, combustion and emission characteristics of biodiesel fuelled diesel engine with its energy and exergy analysis. *Energy*. <https://doi.org/10.1016/j.energy.2019.04.012>
6. Ragadia Sadiq Y, Iyer RC (2019) Experimental investigations on the influence of compression ratio and piston crown geometry on the performance of biogas fuelled small spark ignition engine. *Renew Energy* 146:996–1009
7. Abu Bakar Semin R (2008) A technical review of compressed natural gas as an alternative fuel for internal combustion engines. *Am J Eng Appl Sci* 1:302–311
8. Ushakov S, Stenersen D, Einang PM (2019) Methane slip from gas fuelled ships: a comprehensive summary based on measurement data. *J Mar Sci Technol* 24:1308–1325
9. ANNEX 11: RESOLUTION MEPC.304(72). Initial IMO strategy on reduction of GHG emissions from ships (2018)
10. The Intergovernmental Panel on Climate Change. Global warming potential values, 2016. IPCC Fifth Assessment Report
11. Brynolf S, Fridell E, Andersson K (2014) Environmental assessment of marine fuels: liquefied natural gas, liquefied biogas, methanol and bio-methanol. *J Clean Prod* 74:86–95
12. Heywood JB (1988) *Internal combustion engines fundamental*. McGraw Hill, New York
13. Cheng WK, Hamrin D, Heywood JB, Hochgreb S, Min M, Norris M (1993) An overview of hydrocarbon emissions mechanisms in spark-ignition engines. *SAE* (932708) (1993)
14. Wentworth JT (1968) Piston and ring variables affect exhaust hydrocarbon emission. *SAE* 77(68109):402–416
15. de Zwart M, van Dijk G, Klimstra J (2012) Methane emissions from gas engines driving combined heat and power installations. *J Integr Environ Sci* 9:113–125
16. Huang Z, Pan K, Li J, Zhou L, Jiang D (1996) An investigation on simulation models and reduction methods of unburned hydrocarbon emissions in spark ignition engines. *Combust Sci Technol*. <https://doi.org/10.1080/00102209608935525>
17. Dyer TM (1985) On the source of unburned hydrocarbon emission from lean burn engines. *VDI Ber* 578:17–36
18. Lee S, Tong K, Quay BD, Zello JV, Santavicca DA (2000) Effects of swirl and tumble on mixture preparation during cold start of a gasoline direct-injection engine. *SAE* 109:1783–1796

19. Cedrone KD (2013) Control strategy for hydrocarbon emissions in turbocharged direct injection spark ignition engines during cold-start. PhD thesis, Massachusetts Institute of Technology
20. Yu S, Min K (2002) Effects of the oil and liquid fuel film on hydrocarbon emissions in spark ignition engines. In: Proceedings of the Institution of Mechanical Engineers
21. Schramm J, Sorenson SC (1990) A model for hydrocarbon emission from SI engine. SAE (902169)
22. Abdel Rahman AA (1998) On the emissions from internal-combustion engines: a review. *Int J Energy Res* 22:483–513
23. Kalghatgi GT (1995) Combustion chamber deposits in spark-ignition engines: a literature review. SAE (952443)
24. Haidar HA, Heywood JB (1997) Combustion chamber deposit effects on hydrocarbon emissions from a spark-ignition engine. SAE (972887)
25. Stpień Z (2014) Intake valve and combustion chamber deposits formation—the engine and fuel related factors that impacts their growth. *Nafta-Gaz* 4:236–242
26. Meernik PR, Alkidas AC (1993) Impact of exhaust valve leakage on engine-out hydrocarbons. SAE (932752)
27. Landsberg GB, Heywood JB, Cheng WK (2001) Contribution of liquid fuel to hydrocarbon emissions in spark ignition engines. SAE (2001-01-3587)
28. Robison JA, Brehob WM (1967) The influence of improved mixture quality on engine exhaust emissions and performance. *J Air Pollut Control Assoc* 17:446–453
29. Kato K, Igarash, K, Masuda M, Otsubo K, Yasuda A, Takeda K, Sato T (1999) Development of engine for natural gas vehicle. SAE (01-0574-1999)
30. Cho HM, He B-Q (2007) Spark ignition natural gas engines—a review. *Energy Convers Manag* 48:608–618
31. Tilagone R, Venturi S (2020) Development of natural gas demonstrator based on an urban vehicle with a down-sized turbocharged engine. *Oil Gas Sci Technol* 59:581–591
32. Kato T, Saeki K, Nishideb H, Yamada T (2001) Development of cng fueled engine with lean burn for small size commercial van. *Soc Autom Eng Jpn (JSAE)* 22:365–368
33. Williams FA (1985) *Combustion theory*, 2nd edn. Addison Wesley, Boston
34. Lavoie GA (1978) Correlations of combustion data for SI engine calculation-laminar flame speed, quench distance and global reaction rates. SAE (780229)
35. Gamma Technologies (2019) In-cylinder HC model
36. Schramm J (2019) Methane emission control. IEA Advanced Motor Fuels TCP—Annex 51 report
37. Westbrook CK, Dryer FL (1981) Simplified reaction mechanisms for the oxidation of hydrocarbon fuels in flames. *Combust Sci Technol* 27(1–2):31–43
38. Taskar B, Yum KK, Steen S, Pedersen E (2016) The effect of waves on engine-propeller dynamics and propulsion performance of ships. *Ocean Eng* 122:262–277

Paper 2

The importance of the engine-propeller model accuracy on the performance prediction of a marine propulsion system in the presence of waves

Simone Saettone, Sadi Tavakoli, Bhushan Taskar, Michael Vincent Jensen, Eilif Pedersen, Jesper Schramm, Sverre Steen, and Poul Andersen



The importance of the engine-propeller model accuracy on the performance prediction of a marine propulsion system in the presence of waves

Simone Saettone^{a,*}, Sadi Tavakoli^{a,b}, Bhushan Taskar^a, Michael Vincent Jensen^a, Eilif Pedersen^b, Jesper Schramm^a, Sverre Steen^b, Poul Andersen^a

^a Technical University of Denmark, Kgs. Lyngby, Denmark

^b Norwegian University of Science and Technology, Trondheim, Norway

ARTICLE INFO

Keywords:

Propulsion in waves
Marine propellers
Engine-propeller dynamics

ABSTRACT

The shipping industry is the heart of international trading activities and the global economy. Maritime transport contributes to environmental pollution through the emission of greenhouse gases. New mandatory regulations aim at improving the environmental performance of ships by encouraging power reduction and alternative fuels. These requirements drew attention to the estimation of the ship performance in the presence of waves considering unconventional combustibles. Investigating the effects of waves on untraditional propulsion plants could help to design more environmentally friendly ships. The purpose of this paper is to determine the importance of the time-varying wake field, ship motions, propeller emergence, and engine response on the performance in waves of a marine propulsion system powered by a medium-speed LNG engine. This is performed by comparing the engine-propeller performance estimated by modelling the propulsion plant at three different levels of complexity. The results illustrated the poor prediction accuracy of the propulsion system performance in waves when the time-varying wake field, ship motions, and propeller emergence are neglected. The influence of the engine response on the performance prediction of the engine-propeller system was negligible. The outcomes of this paper demonstrate the importance of considering the effects of the waves on the propulsion system of a ship during the optimization phase.

1. Introduction

Ship transportation is the backbone of the global economy and the international market. Around 80 per cent of the global trade volume and over 70 per cent of the world trade value are carried by sea and are handled by ports worldwide (Hoffmann et al., 2018). On the other hand, the shipping sector is responsible for the annual emission of around 2.5 per cent of global greenhouse gases (GHGs) and about 940 million tonnes of CO₂ (Smith et al., 2015).

Countermeasures against the environmental pollution from ships resulted in new mandatory regulations such as the Initial IMO (International Maritime Organization) Strategy on Reduction of GHG Emissions from Ships and the Energy Efficiency Design Index (EEDI). The former was brought into effect in April 2018 by the International Maritime Organization's Marine Environment Protection Committee (MEPC) to reduce ship emissions and to improve the environmental performance of new and existing vessels. According to the strategy, the total annual global greenhouse gas emissions have to be reduced by at least 50 per cent by 2050 compared to 2008. The latter was introduced

in July 2011 by the IMO for the prevention of air pollution from new vessels. The lower the EEDI, the more energy-efficient is the ship, and the higher its environmental performance. The EEDI formulation encourages the power reduction of the main engine and slow steaming.

These mandatory regulations drew attention to both the estimation of ship performances in waves and the implementation of alternative marine fuels. Liquefied natural gas could be a valid option for the latter. The combustion products for lean burn gas engines contain 25 per cent lower CO₂ and 85 per cent lower NO_x emission values than a marine diesel oil or marine gas oil (Chorowski et al., 2015). It is estimated that the proportion of liquefied natural gas in the global marine fleet will rise from the current 0.3 per cent to over 23 per cent by 2050 (Asariotis et al., 2019). The estimation of ship performances in waves is crucial for two reasons. First, the evaluation of the added resistance caused by waves plays a significant role in the reduction of the main engine size. Second, the presence of waves changes the engine operating point and, as a consequence, modifies the ship emissions. Nevertheless, ships are generally not optimally efficient in realistic sea states. Marine propulsion plants are typically optimized in ideal

* Corresponding author.

E-mail addresses: sisaet@mek.dtu.dk, simonesa@stud.ntnu.no (S. Saettone).

Nomenclature

A	wave amplitude	$Q_{\text{trough}M_2}$	model 2 engine torque amplitude trough relative to model 1
A_E/A_O	blade area ratio	Q_p	propeller torque
B	breadth of the ship	r	fuel consumption
D	propeller diameter	R	propeller radius
g	gravitational acceleration	R_{ADD}	added wave resistance
G_R	gear ratio	t	time
h_p	propeller shaft submergence	T	propeller thrust
J	advance ratio	u	surge velocity
k	wave number	V	ship velocity
K_{Q0}	torque coefficient for a deeply submerged propeller	V_f	fluctuating wake velocity due to waves
$K_{Q\beta}$	torque coefficient for a not deeply submerged propeller	V_m	mean wake velocity due to waves
K_{T0}	thrust coefficient for a deeply submerged propeller	V_t	total wake velocity due to waves
$K_{T\beta}$	thrust coefficient for a not deeply submerged propeller	w	full-scale nominal average wake fraction in waves
L_{PP}	length between perpendiculars	W_{xxx}	sea state identification number
n_e	engine speed	β	thrust diminution factor
n_p	propeller speed	$\eta_{\text{peak}M_2}$	model 2 propeller efficiency peak relative to model 1
\bar{n}	target crankshaft rotation rate	$\eta_{\text{trough}M_2}$	model 2 propeller efficiency trough relative to model 1
P	propeller pitch	η_3	heave motion amplitude
$(P/D)_{D0.7}$	design propeller pitch at 0.7 r/R	η_5	pitch motion amplitude
Q_e	engine torque	$\dot{\eta}_1$	surge velocity amplitude
Q_{eM_1}	engine torque computed by model 1	θ	wave direction (180° is considered as head wave)
Q_{eM_2}	engine torque amplitude computed by model 2	λ	wavelength
$Q_{\text{peak}M_2}$	model 2 engine torque amplitude peak relative to model 1	ρ	water density

conditions where the presence of waves is taken care of by adding a margin to the estimation of the speed-power relationship for a newly built ship in trial conditions. Therefore, it is expected that more energy-efficient ships can be designed if the effect of waves on the propulsion plant is taken into account during the optimization phase.

The effect of waves on the ship propulsion system is a complex physical process resulting from the interaction between the sea environment, vessel performance, and propeller-shaft-engine response. In particular, in case of severe weather conditions, the propeller might come out of the water, causing a drop in the engine torque and, eventually, a drastic increase of propeller rate of revolutions accompanied by intense vibrations. For marine diesel engines, the increased resistance induced by waves might generate what is known as the torque-rich effect. This phenomenon causes the reduction of ship speed, overloading for the main engine, higher fuel consumption, and can lead to the failure of the ship propulsion system (Van Uy, 2016). Therefore, studying the hull-propeller-shaft-engine interaction in realistic conditions is crucial to get a better insight into the overall propulsion system response and to estimate the required engine size accurately.

Full-scale testing is the most accurate method to understand how ship performances are affected by propeller-shaft-engine dynamics. An example of such investigation was carried out by Ogawara et al. (1972), where the dynamic performances of the propulsion system of a container ship were studied. However, full-scale experiments are expensive, time-consuming, and difficult to setup. Numerical computations are a valid alternative, at least in the early phases of the ship propulsion design process. Kyrtatos et al. (1999) predicted the transient response of a large two-stroke marine diesel engine subjected to fluctuating loads obtained from either model tests or the standard propeller law. The main engine was coupled with appended models for the shaft, propeller, ship hull, and the engine speed governor. They demonstrated the overall model reliability to predict the dynamic response of a complete marine power plant system. Campora and Figari (2003) modeled a propulsion plant of a twin shaft arrangement with a controllable-pitch propeller in a MATLAB-SIMULINK environment. The ship propulsion model consisted of separate blocks for the medium-speed diesel engine, governor, hull, controllable-pitch propeller, telegraph, and shaft line. The propeller model was based on either the

propeller open water curves or measurements. Taskar et al. (2016) investigated the effect of waves on the propulsion system of the KVLCC2 tanker along with a method to estimate the propeller wake field in waves. A large two-stroke marine diesel engine model was coupled with the open water data of the KVLCC2 propeller using an inertial shaft model in a MATLAB-SIMULINK environment. The thrust and torque losses due to the propeller emergence were also investigated. This research demonstrated the importance of studying ship performances in waves by utilizing an engine-propeller coupled model. Yum et al. (2017) developed a simulation model of a mechanical propulsion system in waves for the KVLCC2 tanker. The propulsion system included the vessel hull, mechanical shaft, large two-stroke diesel engine, and speed regulator. The shaft was modeled as a single rigid-body with friction, and open water data were used for the propeller model. Simulation results provided a better understanding of the effect of waves on ship performances.

The main goal of this study is to determine the importance of the time-varying wake field, ship motions, propeller emergence and engine response to predict the performance in waves of a marine propulsion system. This is achieved by modelling the propulsion system at three different levels of complexity. The three implementations of the same propulsion system model (steady, unsteady with fixed engine speed, and unsteady with variable engine speed) are compared in terms of estimated engine torque, propeller efficiency, and computation performance. The considered propulsion system is powered by a medium-speed four-stroke natural gas engine with a controllable-pitch propeller. The DTU-developed unsteady low-order boundary-element method ESPPRO (Regener, 2016) is implemented in inhomogeneous inflow for the propeller model. The GT-POWER Engine Simulation Software (Gamma Technologies, 2019a) is used for the engine modelling. The overall propulsion plant model is developed in the MATLAB-SIMULINK co-simulation environment.

2. Case vessel

A full-scale LNG powered vessel is utilized in the present study. The main specifications of the ship, propeller characteristics and engine specifications are shown respectively in Table 1, 2, and 3.

Table 1
Ship main specifications.

Length between perpendiculars	117.6 m
Breadth	20.8 m
Design draft	5.5 m
Design shaft submergence	3.3 m
Service speed	15 kts

Table 2
Propeller main characteristics.

Diameter	4.2 m
Design propeller speed	142 rpm
Number of blades	4
A_E/A_O	0.515
$(P/D)_{D_{0.7}}$	0.975

Table 3
Main engine specifications.

Number of cylinders	9
Cylinder bore	350 mm
Cylinder stroke	400 mm
Rated speed	750 rpm
Rated power	3940 kW

3. Propulsion system model

The MATLAB-SIMULINK co-simulation environment with a fixed-step solver is utilized to design the overall propulsion system model. The data exchange between subsystem blocks is limited to time-discrete communication points. The subsystems are solved separately and independently from each other. The exchanged data between blocks are extrapolated based on the information from the previous time-discrete communication points.

Fig. 1 shows the block diagram of the coupled system. Five main subsystem blocks are implemented to represent the effect of waves on the ship performance:

- **Sea State.** This block represents the state of the sea and provides the wave characteristic to the vessel model.

- **Vessel Model.** The vessel dynamics are implemented in this block. Based on the wave characteristic, propeller thrust, and desired engine speed, the time-invariant propeller pitch and the time-varying ship velocity, wake field and ship motions are computed and given as input to the propeller model.

- **Propeller Model.** The propeller performance is computed in this block. The necessary input are the time-varying propeller speed received from the transmission model and the data provided by the vessel model. The calculated torque is input to the transmission model.

- **Transmission Model.** This block provides speed and torque conversions from the propeller to the engine and vice-versa. The main components of the transmission model are the gearbox, propeller shaft and flywheel.

- **Engine Model.** The engine performance is calculated in this block. In the case of the unsteady implementation with variable rpm, the rotational speed of the engine is computed based on the time-varying torque received from the transmission model, the PID (proportional-integral-derivative) control system, and the inertia of the propulsion system.

3.1. Sea state

Sixty-four regular waves are considered in the present study. This number is obtained by combining four wave amplitudes and directions and wavelengths. The wave direction is relative to the ship, and 180° is considered as head wave. Wave characteristics are shown in Table 4.

3.2. Vessel model

The vessel model computes the data necessary for the calculation of the propeller performances in waves: propeller pitch, average speed loss, and time-varying propeller depth, surge velocity and wake field.

Model tests performed by SINTEF Ocean (former MARINTEK) provide the propeller nominal wake distribution at the design ship speed and the total model resistance, thrust deduction factor, and wake fraction as a function of the ship velocity in calm water conditions.

In this work, the thrust deduction fraction is assumed to be equal to its value in calm water conditions. This assumption is the consequence of two primary reasons. One, open literature provides minimal

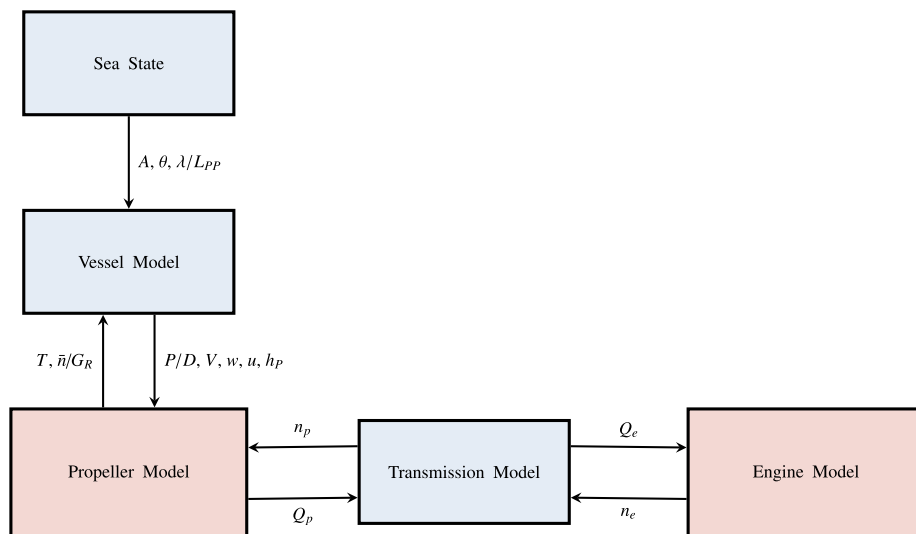


Fig. 1. Block diagram of the propulsion system model.

Table 4
Wave characteristics - Wave W_{214} refers to A_2 , λ/L_{PP1} , and θ_4 .

N_A^2 [-]	A [m]	N_{λ}^2/L_{PP} [-]	λ/L_{PP} [-]	N_{θ}^2 [-]	θ [deg]
A_1	0.5	λ/L_{PP1}	0.6	θ_1	180
A_2	1.0	λ/L_{PP2}	0.8	θ_2	120
A_3	1.5	λ/L_{PP3}	1.0	θ_3	60
A_4	2.0	λ/L_{PP4}	1.2	θ_4	0

knowledge concerning how the thrust deduction fraction changes in waves. Two, performing either expensive model-scale experiments or time-consuming CFD simulations is beyond the scope of the current study.

3.2.1. Propeller pitch and average speed loss

A controllable-pitch propeller with average constant-speed is implemented in the current study. The average propeller rate of revolutions is set equal to the target crankshaft rotation rate \bar{n} (see Section 3.4.6) divided by the gear ratio G_R . The blade pitch is adjusted to maintain the average ship speed in waves equal to its design value if the engine is capable of continuously producing the required power. The propeller pitch is readjusted, and the corresponding average speed loss is computed, if the engine cannot supply the required power. The load limit curve and the propeller law computed for different pitch settings can be seen in Fig. 2.

The propeller pitch and the average speed loss are obtained following the procedure recommended by ITTC (2017b). For simplicity, only wave and added wind resistance are considered in the current study. The added wave resistance is computed in irregular waves even though regular waves are considered for the interaction with the propulsion power plant. This is performed to have realistic values for both the total ship resistance and propeller-engine loads.

The calm water resistance estimated by SINTEF Ocean is converted from model to ship according to ITTC (2017a). The DTU in-house method described by Martinsen (2016) is applied to compute the added resistance in regular waves. Fig. 3 shows the added resistance in regular waves in head sea conditions for different velocities of the ship. The modified Pierson-Moskowitz wave spectrum is applied along with the approach explained in ITTC (2014) to calculate the added resistance in irregular waves. The irregular waves have significant wave heights and peak frequencies equal to the wave heights and frequencies of the considered regular waves.

The added wind resistance is calculated following the procedure described by ITTC (2014).

3.2.2. Ship motions

Heave and pitch transfer functions are obtained using the closed-form expressions of Jensen et al. (2004). The response amplitude operator (RAO) for surge is computed following the method described by Honkanen (1976). The time-varying propeller depth and surge velocity are determined at the computed vessel speed. Heave, pitch and surge velocity RAO in different wave conditions at design ship speed can be seen in Figs. 4, 5 and 6.

3.2.3. Time-varying wake field

The propeller nominal wake distribution is available, at the design ship speed, from model scale experiments performed by SINTEF Ocean. The scaling procedure provided by Sasajima et al. (1966) is applied to obtain the wake field in full scale. The entire wake distribution is contracted to avoid time-consuming calculations. The wake distribution is assumed to be invariant with the ship velocity. The velocity-dependent wake fraction is scaled according to the ITTC (2017a). Fig. 9 shows the full scale nominal wake distribution at the design ship speed.

The method described by Taskar (2017) is applied to determine the

scale factors for the computation of the time-varying wake fields in waves. This approach considers a dimensionless mean increase in propeller inflow V_m and a fluctuating velocity component V_f as follows:

$$V_i = V_f \cdot V_m \quad (1)$$

The fluctuating velocity V_f is calculated including the surge motion effect and the orbital motion of water particles in an attenuated wave at the stern, as described by Ueno et al. (2013). The mean velocity increase V_m is computed assuming the bottom of the ship to be a flat plate that is pitching harmonically, as explained by Faltinsen et al. (1980).

Fig. 7 shows the time-varying inflow averaged over the propeller disk for three representative cases: W_{111} , W_{233} , and W_{344} (see Table 4).

3.3. Propeller model

The main tool for the propeller analysis is the DTU-developed unsteady low-order boundary-element method ESPPRO (Regener, 2016). It is based on potential flow theory where the fluid is assumed to be irrotational and viscosity and compressibility are neglected. Compared to other potential flow numerical methods, the boundary-element method provides a complete representation of the propeller geometry by placing sources and dipoles on the actual propeller surface.

ESPPRO can predict unsteady sheet cavitation and tip vortex cavitation in behind ship conditions. The sheet cavitation model implemented in ESPPRO is described by Regener et al. (2018). Details of the implementation of the tip vortex cavitation model can be found in Mirsadraee (2019). ESPPRO was validated by comparing the predicted propeller performance to both results reported for similar numerical models, such as Vaz and Bosschers (2006) and Vaz et al. (2015), and experimental data, such as Mirsadraee (2019).

In the present work, the propeller blade is discretized into 40 panels in both spanwise and chordwise direction. Equidistant stretching is applied for the former and cosine stretching for the latter. Several blade-wake models are available in ESPPRO (Saettone et al., 2020). The wake model inspired by Hoshino (1993) is selected for the computation of the propeller performance. Fig. 8 shows the comparison between the experimental open water curves and the open water characteristic computed by ESPPRO.

3.3.1. Quasi-steady approach

The propeller performance in waves can be evaluated by using both a quasi-steady and a fully-unsteady approach. The former is a computationally inexpensive method that neglects the time history of the propeller performance related to the time-varying input data, such as wake distribution, propulsion factors, propeller speed fluctuations, and ship motions. The latter provides a complete representation of the

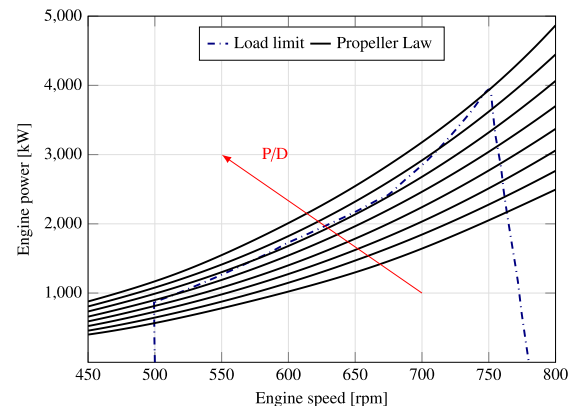


Fig. 2. Load limits.

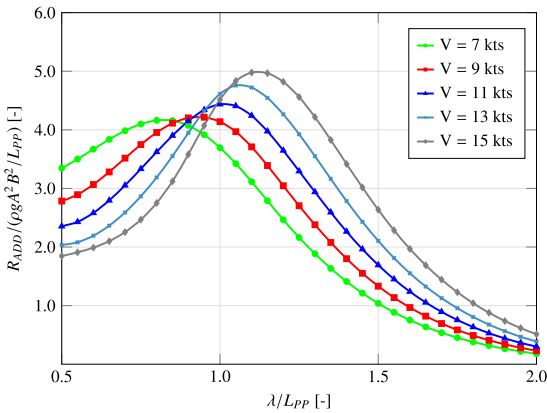


Fig. 3. Added resistance in head regular waves.

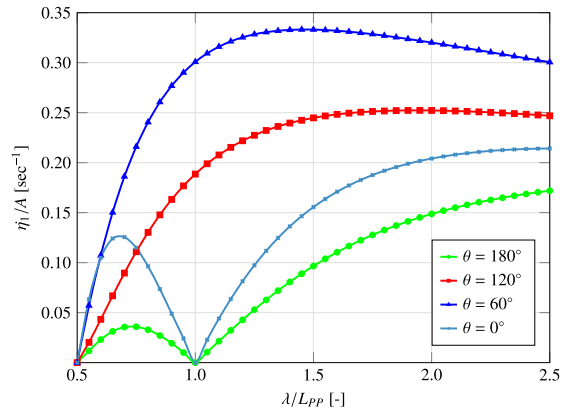


Fig. 6. Surge velocity RAO in different wave conditions at design ship speed.

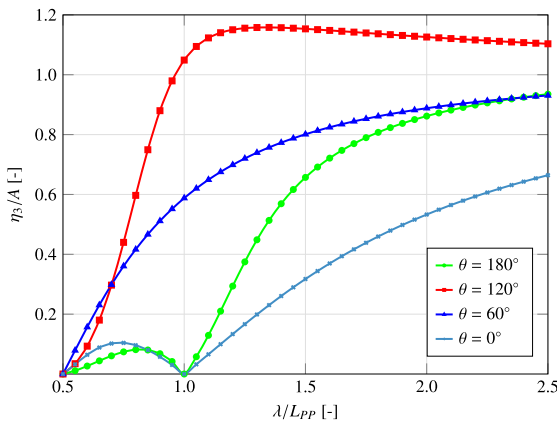


Fig. 4. Heave RAO in different wave conditions at design ship speed.

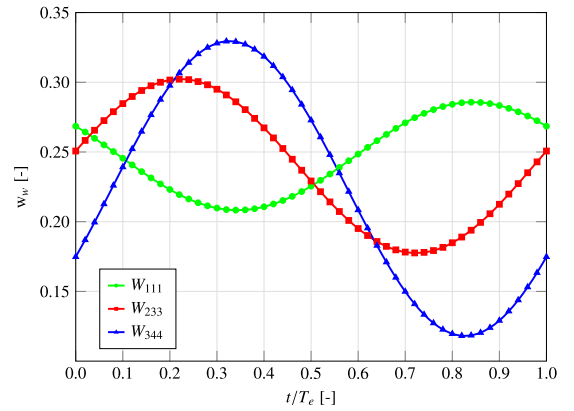


Fig. 7. Time-varying inflow averaged over the propeller disk - W_{111} , W_{233} , and W_{344} .

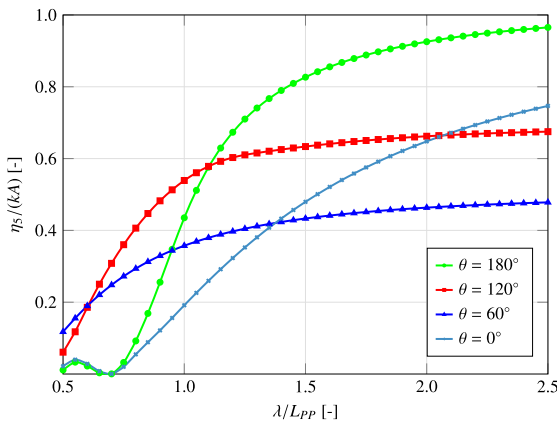


Fig. 5. Pitch RAO in different wave conditions at design ship speed.

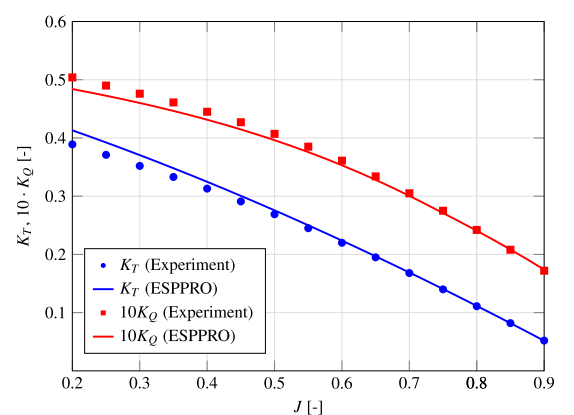


Fig. 8. Open Water Diagram computed by ESPPRO for the design propeller pitch.

propeller dynamics, but it is computationally expensive. Saettone et al. (2020) showed a good agreement between the quasi-steady and the more advanced fully-unsteady approach in the prediction of the propeller performance in waves for the KVLCC2 tanker. As a result, the quasi-steady approach is applied in the current study for the

propeller analysis.

3.3.2. Propeller emergence

The quasi-dynamic approach described by Minsaas et al. (1983) is

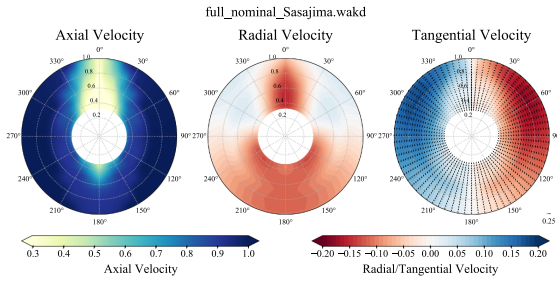


Fig. 9. Full scale nominal wake distribution at the design ship speed.

applied to compute the reduction of thrust and torque caused by wave effects and the propeller emergence. This method implements a thrust diminution factor β for the correction of the performance of a deeply submerged propeller (see Eq. 2). Loss of propeller disc area, wave making by propeller, and Wagner effect are taken into account. The time-varying immersion of the shaft is assumed to be oscillating and periodic. The beta curve proposed by Minsaas et al. (1983) is shown in Eq. 3.

$$K_{T\beta} = \beta \cdot K_{T0} \quad K_{Q\beta} = \beta^{0.8} \cdot K_{Q0} \quad (2)$$

$$\beta = \begin{cases} 1 - 0.675[1 - 0.769(\frac{h_p}{R})]^{1.258} & \frac{h_p}{R} < 1.3 \\ 1 & \frac{h_p}{R} \geq 1.3 \end{cases} \quad (3)$$

3.4. Engine model

A medium-speed four-stroke natural gas engine is considered in the present analysis (see Table 3). The GT-POWER Engine Simulation Software (Gamma Technologies, 2019a) is utilized to setup the engine system simulation model, estimate the engine performance, and model the fundamental components of the engine. Fig. 10 shows the schematic representation of the six main parts of the engine model.

The engine is a spark-ignited lean-burn combustion engine. It is equipped with a variable-geometry charging system to benefit from the power increase offered by the extended knock limit of the lean mixture. The high air temperature produced by the compressor is decreased by an intercooler. The air flow is controlled by the variable turbine geometry. The fuel flow is controlled by mechanical valves before each cylinder.

A load-based approach is implemented for the engine model. In this

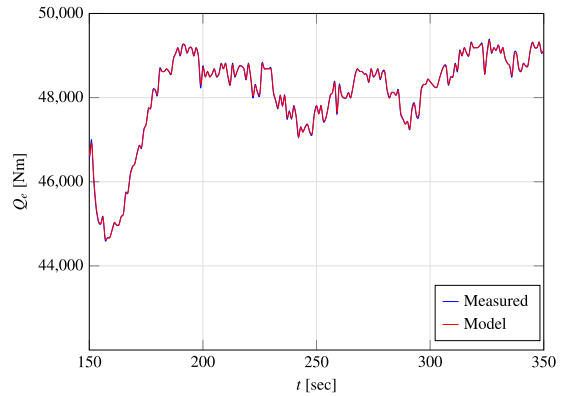


Fig. 11. Engine model - Input engine torque.

methodology, the engine speed is computed based on the torque received from the shaft, the inertia of the propulsion system, and the PID control system. The engine model is validated by comparing the predicted engine performance to measured data. An example of such validation can be seen in Figs. 11 and 12. The good agreement between measured data and predicted engine performance demonstrates the reliability of the engine modelling.

3.4.1. Zone 1: Turbocharger

The turbocharger performance is modeled using maps given in the form of look-up tables. The performance maps contain information about turbine and compressor thermodynamic efficiency as a function of pressure ratio, mass flow rate, and turbocharger speed. The turbine and compressor performance are modeled by following the iterative process described in Gamma Technologies (2019b).

3.4.2. Zone 2: Intercooler

A sea-water-based coolant is utilized for the engine. The intercooler is modeled using the non-predictive approach described in Gamma Technologies (2019b). The fixed outlet temperature is imposed by modelling the intercooler as an infinite sink of heat (multiple pipe object). The heat transfer coefficient is calculated using the Colburn analogy (Colburn, 1964). Measured data are used as the boost temperature during load variations.

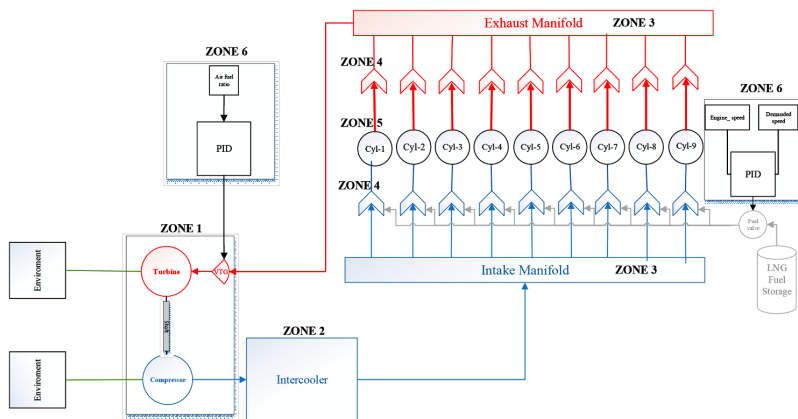


Fig. 10. Schematic of the engine model.

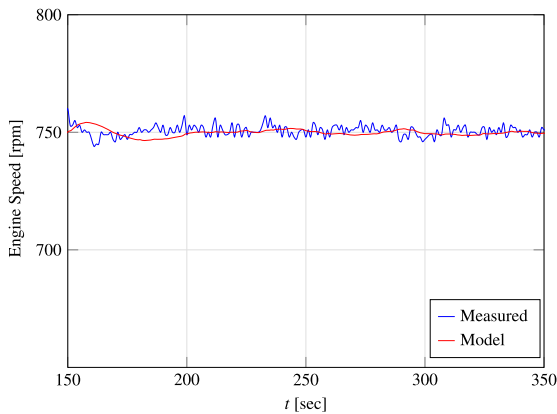


Fig. 12. Engine model - Output engine speed.

3.4.3. Zone 3: Pipe flow

The pipe flow model involves the solution of the Navier-Stokes, conservation of mass, and energy equations. These equations are solved in one dimension, which means that all the quantities are averaged across the flow direction. This approach improves the prediction of the turbocharger working area under dynamic loads.

3.4.4. Zone 4: Intake and exhaust valves

The flow losses across the intake and exhaust valves are modeled to predict the mass flow entering into/leaving the cylinder. The modelling of the flow losses follows the work proposed by Heywood (1988) and the computation of the ratio between the effective and the theoretical flow area (discharge coefficient).

3.4.5. Zone 5: Heat transfer and combustion

The in-cylinder heat transfer and combustion modelling are simultaneously modeled in the cylinder control volume.

The model of Woschni (1968) is implemented to model the convective heat transfer between the gas and the combustion chamber surfaces. Fourier's law of heat conduction is applied to estimate the conductive heat transfer through the cylinder walls. The radiative heat transfer between the gas and the combustion chamber surfaces is modeled by Stefan-Boltzmann law.

The Spark Ignition Turbulent Flame Combustion Model (EngCylCombSI_Turb) (Gamma Technologies, 2019b) is used to predict the burn rate. In-cylinder composition, cylinder temperature and pressure, spark position, spark timing, flame and wall interaction, fuel properties, and in-cylinder flow are taken into account (Gamma Technologies, 2019c). The burn rate is estimated based on the calculation of flame speed and flame kernel development. A thorough explanation of this theory can be found in Blizard and Keck (1974).

3.4.6. Zone 6: PID

The engine speed is regulated by a PID control system installed directly on the fuel valve. The controller's PID algorithm uses the difference between the target crankshaft rotation rate \bar{n} and the measured engine speed to regulate the fuel valve opening and restore the desired speed. The target crankshaft rotation rate is set to be equal to the rated speed of the engine (750 rpm).

The air-fuel ratio is regulated by a PID control system installed on the turbocharger. Accurate control of the mass ratio of air to fuel present in the combustion process is critical for LNG engines. The controller's PID algorithm regulates the amount of air based on the instantaneous fuel flow rate.

3.5. Transmission model

The power transmission system is modeled in GT-POWER (see Section 3.4). It is assumed to be rigid, and it includes a solid mechanical shaft, flange, and gearbox. The resistance to acceleration due to propeller inertia and added water resistance is also taken into account through the engine model. The engine manufacture provides the mass moment of inertia and the mechanical efficiency of the transmission system.

4. Method

The propulsion system performance in waves is usually estimated by avoiding the complexity of creating a unique propulsion system model. Generally, the presence of the engine is neglected, and the propeller performances are computed by ignoring ship motions, propeller emergence, and time-varying propeller speed and wake field. Taskar et al. (2016) showed that these assumptions are not sufficient to study the effect of waves on the propulsion system of the KVLCC2 tanker powered by a large two-stroke diesel engine. Propeller and engine response depend on the ship dimension and shape, engine specifications, and propeller characteristics.

In the current study, the propulsion system is modeled at three different levels of complexity. The three implementations of the same propulsion system model (see Section 3) are referred as Model 1, 2, and 3. The three models are compared in terms of the accuracy of the results and computational performance.

4.1. Model 1: Steady propeller-engine model

This model resembles the traditional way to estimate the propeller-engine performances in waves. The wave effects are taken into account only in terms of added resistance and change of propulsion point. The propeller performances are computed by neglecting ship motions, propeller emergence, and time-varying wake fields. The propeller forces associated with the blade passage frequency are ignored. Therefore, the engine torque and speed are time-invariant.

4.2. Model 2: Unsteady propeller-engine model with fixed engine speed

In this model, the engine speed is assumed to be time-invariant. On the other hand, ship motions, propeller emergence, time-varying wake fields and added resistance are taken into account. The propeller forces associated with the blade passage frequency are computed. As a result, the engine torque is fluctuating, but the propeller speed is time-invariant.

4.3. Model 3: Unsteady propeller-engine model with PID

In this model, the propeller-engine dynamics is taken into account. In addition, time-varying wake fields, ship motions, propeller emergence, and added resistance are considered. The propeller forces associated with the blade passage frequency are also included. The PID control system is activated to regulate the engine speed. Thus, the engine torque and speed are time-variant.

5. Results

5.1. Comparison 1: Model 1 vs Model 2

This comparison is necessary to understand the effect of the time-varying wake field, ship motions, and propeller emergence on the prediction of the propulsion system performance in waves.

The time-varying wake field creates fluctuating engine loads, which may differ considerably from the time-invariant engine torque estimated in steady conditions. Ship motions cause the propeller depth to

Table 5
Comparison among models 1, 2, and 3.

Characteristic	Model 1	Model 2	Model 3
Added Wind Resistance	Yes	Yes	Yes
Added Wave Resistance	Yes	Yes	Yes
Heave Motion	No	Yes	Yes
Pitch Motion	No	Yes	Yes
Surge Motion and Velocity	No	Yes	Yes
Blade Passage Forces	No	Yes	Yes
Propeller Emergence	No	Yes	Yes
Time-Varying Propeller Wake Field	No	Yes	Yes
Time-Varying Engine Speed	No	No	Yes
Propeller Pitch	Same value for all the models		
Average Ship Velocity	Same value for all the models		

change in time, which may lead to a drop in engine torque if the propeller is in proximity or above the water surface. Time-varying engine torque and propeller submergence may also induce a reduction in propeller efficiency compared to the steady analysis.

The computational time of the two approaches and the engine torque and propeller efficiency estimated by models 1 and 2 are com-

pared. For the sake of comparison, the propeller pitch and average speed loss computed for each wave condition are kept constant in both models. Table 5 summarizes the differences between the two models.

5.1.1. Average engine torque

Figs. 13 and 14 show the relative per cent difference between the temporal mean of the engine torque in one encounter wave period estimated by model 2 and the steady torque calculated by model 1. A negative value indicates an overestimation of the propeller load predicted by model 1 compared to model 2. Fig. 13 shows the case of the deeply submerged propeller for four representative examples: ($\beta = 1$): W_{131} , W_{231} , W_{331} , and W_{431} . Fig. 14 illustrates four relevant cases for the propeller either in proximity or above the water surface ($\beta < 1$): W_{341} , W_{342} , W_{343} , and W_{344} . All the cases are displayed in Fig. 28 - Appendix A.

The general trend of the results illustrates a reduction in propeller torque when the time-varying wake field, ship motions, and propeller emergence are taken into account. This outcome is mainly related to both the increase of propeller inflow velocity and the event of propeller emergence. The impact of the former effect can be seen in Fig. 13. The significance of the latter phenomenon is illustrated in Fig. 14. Comparing Fig. 13 and 14 demonstrates that the thrust diminution factor plays a major role in the prediction of the engine performance in waves. Nevertheless, it can also be observed a difference up to 2.5% in engine torque between the two models when the propeller is deeply submerged.

5.1.2. Engine torque amplitude

Figs. 15 and 16 show the amplitude of the engine torque estimated by model 2 as the percentage of the steady torque calculated by model 1. This investigation is necessary to comprehend if it is important to compute the magnitude of the fluctuating torque when estimating the propulsion system performance in waves. Fig. 15 illustrates four relevant cases for the deeply submerged propeller ($\beta = 1$): W_{111} , W_{112} , W_{113} , and W_{114} . In this case, the amplitude is computed as half of the change between the peak and the trough of the time-varying engine torque estimated by model 2. Fig. 16 shows four representative cases for the propeller either in proximity or above the water surface ($\beta < 1$): W_{314} , W_{324} , W_{334} , and W_{344} . In this event, two types of amplitudes are computed: peak and trough amplitude. The former is calculated as the non-negative difference between the peak of the time-varying engine torque and the temporal mean of the engine torque computed by model 2. The latter considers the trough of the engine torque instead of the peak. All the cases are displayed in Fig. 29

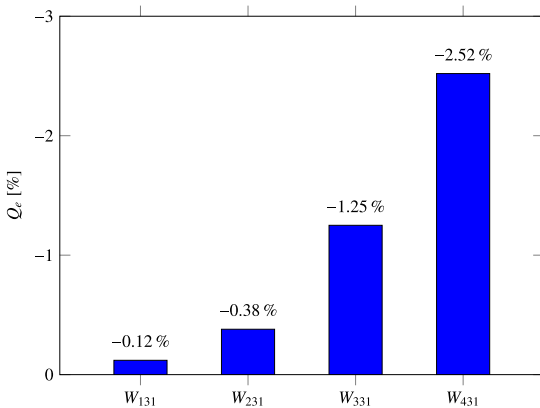


Fig. 13. Relative per cent difference in average engine torque between models 1 and 2 - $\beta = 1$, $A = \{0.5, 1.0, 1.5, 2.0\}$, $\lambda/L_{pp} = 1.0$, $\theta = 180^\circ$.

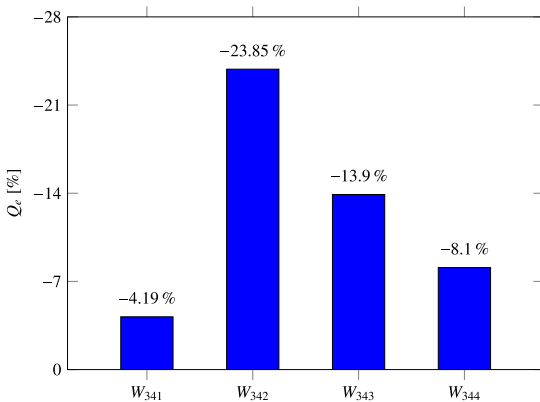


Fig. 14. Relative per cent difference in average engine torque between models 1 and 2 - $\beta < 1$, $A = 1.5$, $\lambda/L_{pp} = 1.2$, $\theta = \{180^\circ, 120^\circ, 60^\circ, 0^\circ\}$.

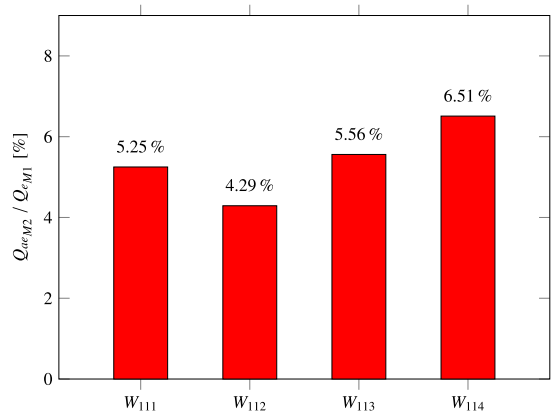


Fig. 15. Torque amplitude estimated by model 2 as a percentage of the torque calculated by model 1 - $\beta = 1$, $A = 0.5$, $\lambda/L_{pp} = 0.6$, $\theta = \{180^\circ, 120^\circ, 60^\circ, 0^\circ\}$.

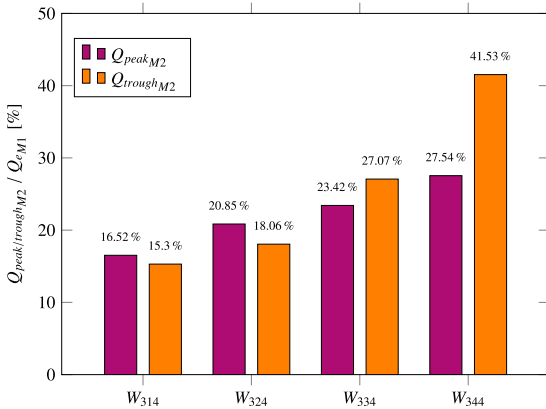


Fig. 16. Torque amplitude (peak and trough) estimated by model 2 as a percentage of the steady torque calculated by model 1 - $\beta < 1$, $A = 1.5$, $\lambda/L_{pp} = \{0.6, 0.8, 1.0, 1.2\}$, $\theta = 0^\circ$.

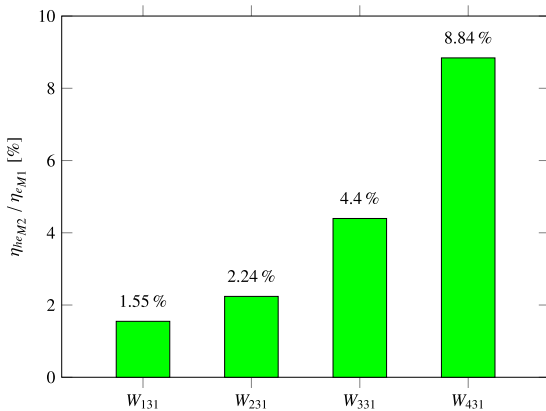


Fig. 17. Propeller efficiency amplitude estimated by model 2 as a percentage of the steady propeller efficiency calculated by model 1 - $\beta = 1$, $A = \{0.5, 1.0, 1.5, 2.0\}$, $\lambda/L_{pp} = 1.0$, $\theta = 180^\circ$.

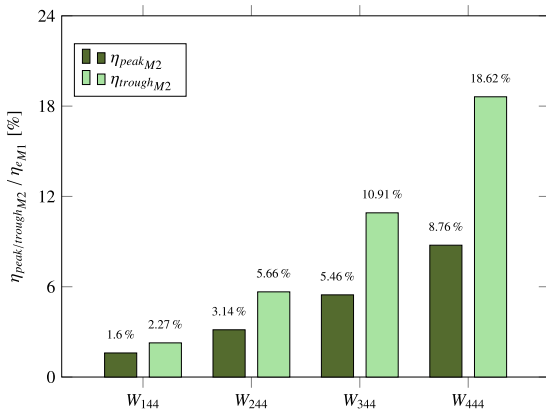


Fig. 18. Propeller efficiency amplitude (peak and trough) estimated by model 2 as a percentage of the propeller efficiency calculated by model 1 - $\beta < 1$, $A = \{0.5, 1.0, 1.5, 2.0\}$, $\lambda/L_{pp} = 1.2$, $\theta = 0^\circ$.

- Appendix A.

The case of the deeply submerged propeller is particularly relevant for this investigation. This is because the relative per cent difference in average engine torque between models 1 and 2 is more pronounced in the event of propeller emergence than when the propeller is far from the water surface (see Section 5.1.1). As a consequence, studying the propeller-engine performance in the case of deeply submerged propeller might be considered unnecessary. However, Fig. 15 illustrates the importance of considering the effect of the time-varying wake field and ship motions on the estimation of the propeller-engine loads even when the propeller is deeply submerged. Therefore, the amplitude of the fluctuating torque due to time-varying wake field and ship motions is not negligible. In the event of the propeller in proximity or above the water surface, it is possible to notice a remarkable value of the torque amplitude estimated by model 2 as a percentage of the steady torque calculated by model 1. This confirms the importance of the thrust diminution factor in the computation of the propulsion system performance in waves.

5.1.3. Propeller efficiency

Figs. 17 and 18 show the amplitude of the propeller efficiency estimated by model 2 as a percentage of the steady propeller efficiency calculated by model 1. Fig. 17 shows the case of the deeply submerged propeller for four representative examples ($\beta = 1$): W_{131} , W_{231} , W_{331} , and W_{431} . Fig. 18 illustrates four relevant cases for the propeller either in proximity or above the water surface ($\beta < 1$): W_{144} , W_{244} , W_{344} , and W_{444} . All the cases are displayed in Fig. 30 - Appendix A. In the case of $\beta = 1$, the amplitude is computed as half of the change between the peak and the trough of the time-varying propeller efficiency estimated by model 2. In the event of $\beta < 1$ (Fig. 18), the amplitude is computed as the difference between the extrema of the time-varying propeller efficiency and the temporal mean of the propeller efficiency estimated by model 2: η_{peakM2} and $\eta_{troughM2}$.

The results show a significant value of the propeller efficiency amplitude estimated by model 2 as a percentage of the propeller efficiency calculated by model 1. Comparing Fig. 17 and 18 demonstrates the major role of the thrust diminution factor in estimation of the propeller efficiency. This is because, in the case of the deeply submerged propeller, the fluctuation of the propeller efficiency is primarily related to the time variation of the advance ratio caused by the time-varying wake fraction. On the other hand, in the event of $\beta < 1$, the thrust decreases more than the torque with the decrease of β . This provides an additional reduction in propeller efficiency.

5.1.4. Computational performance

Model 1 and 2 are compared by evaluating the computation time necessary to simulate all the considered 64 sea states (see Section 3.1). The processing speed of model 1 is around 40 times faster than model 2. The main reason for this outcome is related to the short time-step required for the unsteady simulations. It becomes clear that the shorter the wave encounter period, the smaller the difference in computation time between the two models.

5.2. Comparison 2: Model 2 vs Model 3

This comparison is necessary to evaluate the importance of the engine response on the prediction of the propulsion system performance in waves.

The fluctuation of the propeller speed caused by the presence of the engine may considerably alter the propulsion system loads. This is particularly relevant in the event of propeller emergence, where the engine torque reduces and the engine speed increases. In addition, the amount of engine over-speeding determines if the implemented control-strategy guarantees the safety of the propeller system in harsh weather conditions.

The engine torque calculated by models 2 and 3 and the

computational time of the two approaches are compared. For the sake of comparison, the propeller pitch and average speed loss computed for each wave condition are kept constant in both models. Table 5 summarizes the differences between models 2 and 3.

5.2.1. Engine speed and torque

Figs. 19, 20, 23 and 24 present the engine torque computed by models 2 and 3. The general trend of the results shows a reduction in torque when the engine speed is time-variant. The magnitude of the reduction in engine torque depends on the specific operational condition. These outcomes are primarily related to the combined effect of the propulsion system specifications and PID control system characteristics.

Figs. 19 and 20 show the case of the deeply submerged propeller ($\beta = 1$) for two representative examples: W_{121} and W_{124} . These two sea states are identical apart from the direction of the encountered wave: 180° for W_{121} and 0° for W_{124} . The average velocity of the ship is also the same in these two conditions. Figs. 19 and 20 show a higher average engine torque for W_{121} than W_{124} . This is because of the larger added resistance in the head sea than in following waves. On the other hand, the sea state W_{124} generates a higher value of the engine torque amplitude compared to W_{121} . This is due to the larger variation of the time-varying wake fraction in following sea than in head waves. Figs. 19 and 20 also illustrate a higher reduction in engine torque for W_{124} compared to W_{121} . The relative per cent difference in maximum engine torque between models 2 and 3 is equal to 0.97% for the former and 0.17% for the latter. This is related to both the characteristics of the PID control system, engine stability, and the inertia of the overall system. These effects combined with the different added wave resistance and encounter period induce a higher variation in engine speed and in fuel consumption for W_{124} in comparison to W_{121} (respectively see Figs. 21 and 22).

Figs. 23 and 24 show two representative examples for the case where the propeller is either in proximity or above the water surface ($\beta < 1$): W_{342} and W_{343} . These two sea states have the same wave amplitude and wavelength but different wave direction: $\theta = 120^\circ$ for the former and $\theta = 60^\circ$ for the latter. Both in W_{342} and W_{343} , the engine torque starts decreasing rapidly at the time when the propeller is close enough to the water surface. The PID control system responds to the drop in torque by increasing the engine rotational speed (see Fig. 25). The acceleration of the engine speed is quite gentle because of the characteristics of the PID control system, the fast response of the engine, and the inertia of the propulsion system. Furthermore, it is possible to observe an overshooting in engine torque as soon as the propeller is deeply submerged again. This is due to the variation in propeller depth combined with the action of the PID control system. Comparing Figs. 23 and 24, a higher drop in torque for W_{342} than W_{343} can be notice. This is primarily related to the different ship motions generated in quartering sea compared to bow sea. The difference in torque decrease between W_{342} and W_{343} can also be seen through the different amplitude of the engine speed and the fuel consumption (respectively see Figs. 25 and 26).

It is important to verify the amount of engine overspeeding to guarantee the safety of the propulsion system. An excessive overspeed can result in damage to the crankshaft, broken valve seats, and other dangerous phenomena. Generally, the maximum allowed overspeed is around 110–115% of the maximum continuous speed (MCS). Fig. 27 shows the engine speed fluctuation for the harshest condition analyzed in the present study: W_{432} . The maximum overspeed is lower than 103% of the MCS: this demonstrates the safety of the implemented control-strategy.

It is also relevant to compare the magnitude of the reduction in engine torque to similar studies. For instance, Taskar et al. (2016) investigated the effect of waves on the propulsion system of the KVLCC2 tanker powered by a large two-stroke diesel engine. They observed a higher fluctuation of the propeller speed caused by the presence of the engine than in the present analysis. This is mainly related to the faster

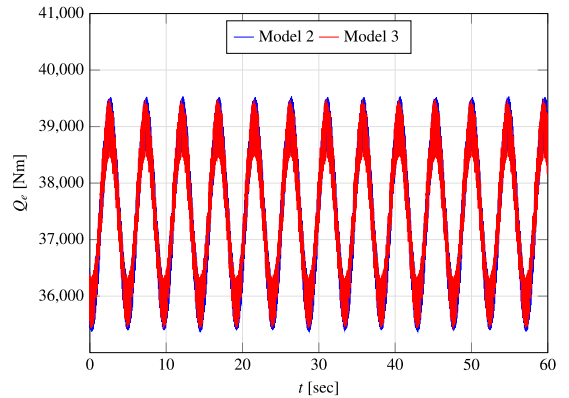


Fig. 19. Engine torque estimated by models 2 and 3 for sea state W_{121} - $A = 0.5$, $\lambda/L_{pp} = 0.8$, $\theta = 180^\circ$.

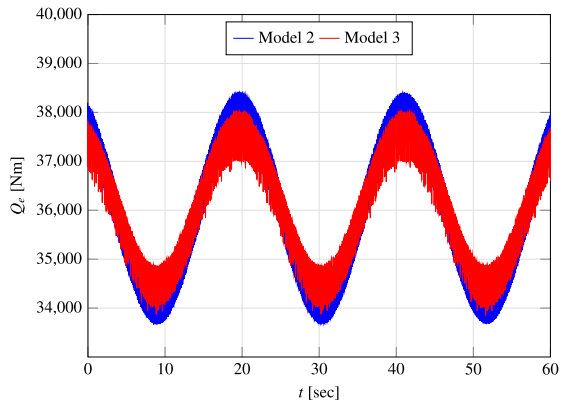


Fig. 20. Engine torque estimated by models 2 and 3 for sea state W_{124} - $A = 0.5$, $\lambda/L_{pp} = 0.8$, $\theta = 0^\circ$.

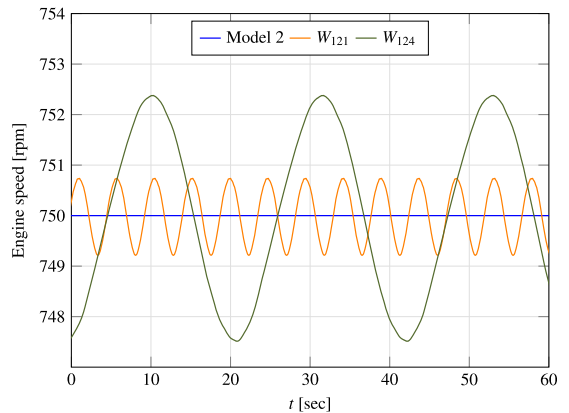


Fig. 21. Engine speed estimated by model 3 for sea state W_{121} and W_{124} - $A = 0.5$, $\lambda/L_{pp} = 0.8$, $\theta = \{0^\circ, 180^\circ\}$.

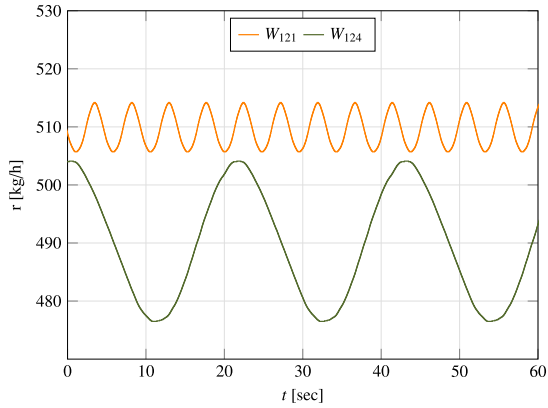


Fig. 22. Fuel consumption estimated by model 3 for sea state W_{121} and W_{124} - $A = 0.5$, $\lambda/L_{pp} = 0.8$, $\theta = \{0^\circ, 180^\circ\}$.

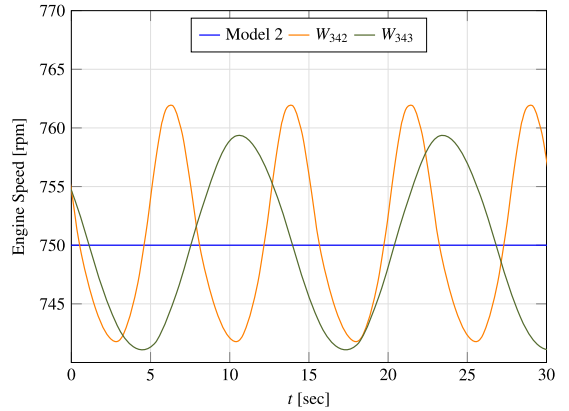


Fig. 25. Engine speed estimated by model 3 for sea state W_{342} and W_{343} - $A = 1.5$, $\lambda/L_{pp} = 1.2$, $\theta = \{60^\circ, 120^\circ\}$.

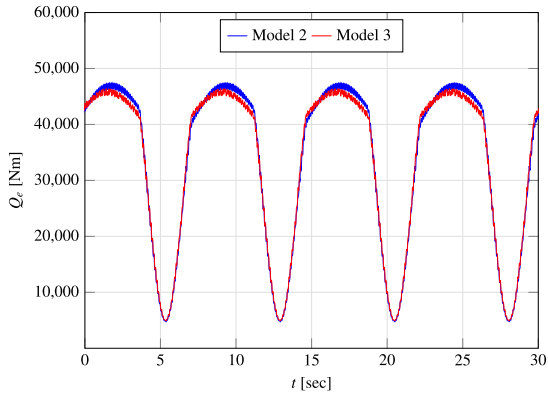


Fig. 23. Engine torque estimated by models 2 and 3 for sea state W_{342} - $A = 1.5$, $\lambda/L_{pp} = 1.2$, $\theta = 120^\circ$.

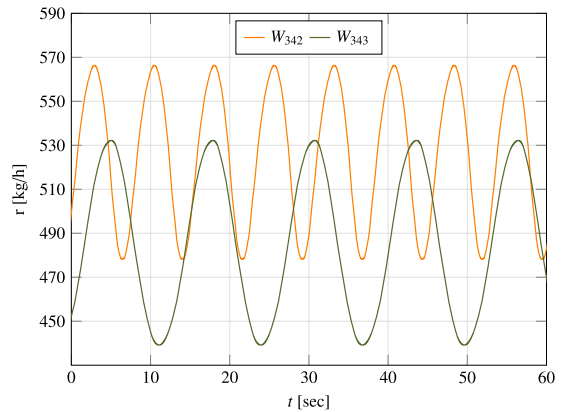


Fig. 26. Fuel consumption estimated by model 3 for sea state W_{342} and W_{343} - $A = 1.5$, $\lambda/L_{pp} = 1.2$, $\theta = \{60^\circ, 120^\circ\}$.

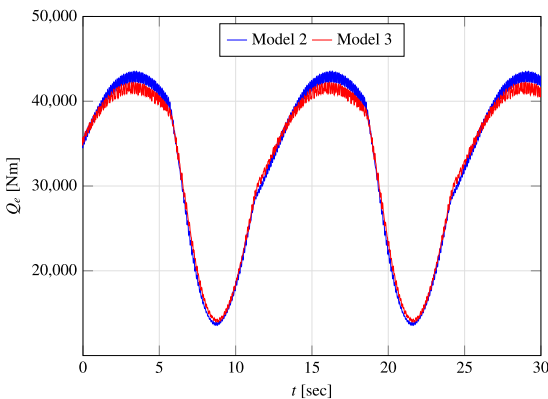


Fig. 24. Engine torque estimated by models 2 and 3 for sea state W_{343} - $A = 1.5$, $\lambda/L_{pp} = 1.2$, $\theta = 60^\circ$.

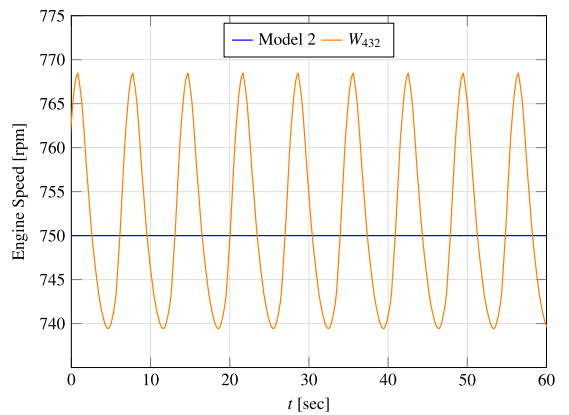


Fig. 27. Engine speed estimated by model 3 for sea state W_{432} - $A = 2.0$, $\lambda/L_{pp} = 1.0$, $\theta = 120^\circ$.

response of the medium-speed LNG engine compared to the large two-stroke diesel engine.

5.2.2. Computational performance

Model 2 and 3 are compared by evaluating the computation time necessary to simulate all the considered 64 sea states (see Section 3.1). The processing speed of model 2 is around 3 times faster than model 3. The primary cause for this result is related to the additional time required by model 3 to achieve time-periodic convergence.

6. Conclusions

The performance of a propulsion system powered by a medium-speed four-stroke LNG engine with a controllable-pitch propeller was computed. This was performed by modelling the marine propulsion system at three different levels of complexity. The three implementations of the same propulsion system model (steady, unsteady with fixed engine speed, and unsteady with PID control system) were compared in terms of estimated engine torque and speed and propeller efficiency. This was necessary to determine the influence of the time-varying wake field, ship motions, propeller emergence and engine response on the performance prediction of the analysed marine propulsion system in the presence of waves.

The results illustrate a significant overestimation of the temporal mean of the engine torque computed by the steady engine-propeller model (up to 35% in average engine torque between the steady and unsteady torque). The torque amplitude estimated by the unsteady engine-propeller models constitutes a significant percentage of the steady torque calculated by neglecting the time-varying wake field, ship motions and propeller emergence (up to 60% in torque amplitude estimated by model 2 as a percentage of the torque calculated by model 1). Similarly, the fluctuation of the time-varying propeller efficiency represents a remarkable portion of the propeller efficiency estimated by the steady engine-propeller model (up to 55% in propeller efficiency amplitude estimated by model 2 as a percentage of the steady propeller efficiency calculated by model 1). The discrepancies between the steady and unsteady models are more pronounced in the case of propeller emergence than when the propeller is deeply submerged. Nevertheless,

Appendix A

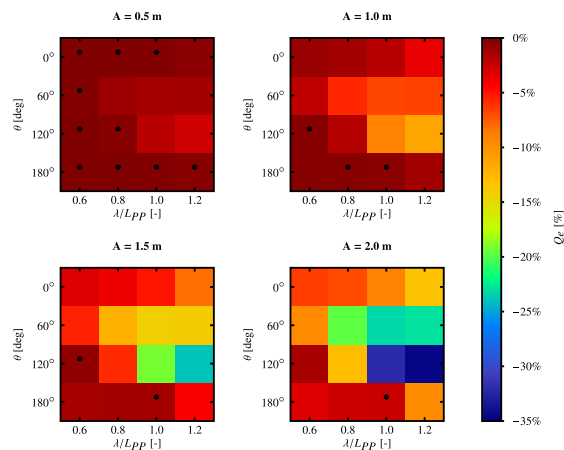


Fig. 28. Relative per cent difference in average engine torque between models 1 and 2 - The dot represents $\beta = 1$.

the results show a considerable difference in engine torque and propeller efficiency between the steady and unsteady models when the propeller is far from the water surface (up to 2.5% in engine torque and up to 9% in propeller efficiency). These outcomes indicate that neglecting time-varying wake field, ship motions and propeller emergence would lead to a poor prediction accuracy of the propulsion system performance in the presence of waves.

The quick response of the engine combined with the characteristic of the PID control system causes a negligible reduction in engine torque compared to the case where the engine speed is time-invariant (up to 5% in relative per cent difference between the torque estimated by model 2 and 3). This makes it possible to investigate the propulsion system performance in waves without modelling the presence of the engine. This outcome is strictly related to the considered hull-propeller-shaft-engine system.

As future work, it would be interesting to evaluate the performance of other types of propulsion systems in waves.

CRedit authorship contribution statement

Simone Saettone: Conceptualization, Methodology, Software, Formal analysis, Writing - original draft, Writing - review & editing, Visualization. **Sadi Tavakoli:** Conceptualization, Methodology, Software, Writing - original draft. **Bhushan Taskar:** Conceptualization, Methodology, Writing - review & editing. **Michael Vincent Jensen:** Conceptualization, Writing - review & editing. **Eilif Pedersen:** Conceptualization, Supervision, Project administration. **Jesper Schramm:** Conceptualization, Supervision, Project administration. **Sverre Steen:** Conceptualization, Supervision, Project administration. **Poul Andersen:** Conceptualization, Supervision, Project administration, Writing - review & editing.

Declaration of Competing Interest

The authors declare that they have no known competing financial interests or personal relationships that could have appeared to influence the work reported in this paper.

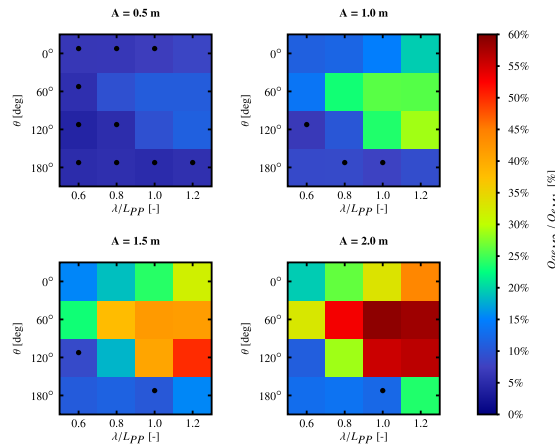


Fig. 29. Torque amplitude estimated by model 2 as a percentage of the torque calculated by model 1 - The dot represents $\beta = 1$.

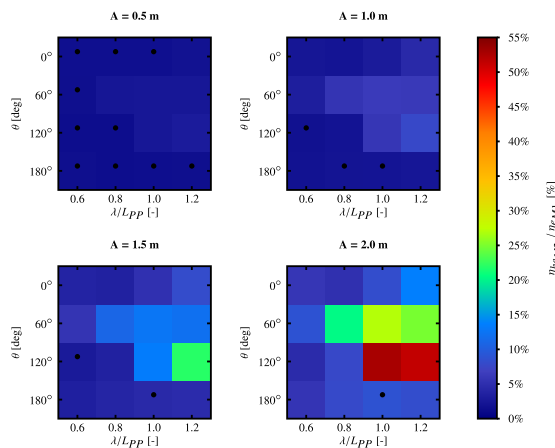


Fig. 30. Propeller efficiency amplitude estimated by model 2 as a percentage of the steady propeller efficiency calculated by model 1 - The dot represents $\beta = 1$.

Supplementary material

Supplementary material associated with this article can be found, in the online version, at [10.1016/j.apor.2020.102320](https://doi.org/10.1016/j.apor.2020.102320)

References

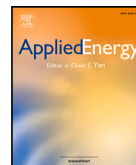
- Asariotis, R., Assaf, M., Ayala, G., Benamara, H., Chantrel, D., Hoffmann, J., Premti, A., Rodriguez, L., Youssef, F., 2019. Review of Maritime Transport, 2019. Technical Report. United Nations.
- Blizard, N.C., Reck, J.C., 1974. Experimental and theoretical investigation of turbulent burning model for internal combustion engines. Technical Report. SAE Technical Paper.
- Campora, U., Figari, M., 2003. Numerical simulation of ship propulsion transients and full-scale validation. *Proceed. Instit. Mech. Eng. Part M* 217 (1), 41–52.
- Chorowski, M., Duda, P., Polinski, J., Skrzypacz, J., 2015. LNG systems for natural gas propelled ships. *IOP Conference Series: Materials Science and Engineering*. 101. IOP Publishing, pp. 012089.
- Colburn, A.P., 1964. A method of correlating forced convection heat-transfer data and a comparison with fluid friction. *Int J Heat Mass Transf* 7 (12), 1359–1384.
- Faltinsen, O.M., 1980. Prediction of resistance and propulsion of a ship in a seaway. *Proceedings of the 13th symposium on naval hydrodynamics*, Tokyo.
- Gamma Technologies, 2019a. GT-POWER - Version 2019.
- Gamma Technologies, 2019b. GT-POWER Flow Theory Manual Version 2019.
- Gamma Technologies, 2019c. GT-SUITE Engine Performance Tutorials Version 7.3.
- Heywood, J.B., 1988. *Internal Combustion Engines Fundamentals*. McGraw-Hill Book Co, NY, pp. 458–470.
- Hoffmann, J., Juan, W., Sirimanne, N.S., 2018. *Review of Maritime Transport 2018*. United Nations Publications.
- Honkanen, M., 1976. On the wave induced motions of ships. Technical Report. The Swedish Academy of Engineering Sciences in Finland.
- Hoshino, T., 1993. Hydrodynamic analysis of propellers in steady flow using a surface panel method. *J. Soc. Naval Archit. Jpn.* 1993 (174), 71–87.
- ITTC, 2014. Recommended Procedures and Guidelines: Speed and Power Trials, Part 2 Analysis of Speed/Power Trial Data. *International Towing Tank Conference*. 7.5-02-01-2.
- ITTC, 2017a. Recommended Procedures and Guidelines: 1978 ITTC Performance Prediction Method. *International Towing Tank Conference*. 7.5-02-03-01.4.
- ITTC, 2017b. Recommended Procedures and Guidelines: Predicting Powering Margins. *International Towing Tank Conference*. 7.5-02-03-01.5.
- Jensen, J.J., Mansour, A.E., Olsen, A.S., 2004. Estimation of ship motions using closed-form expressions. *Ocean Eng.* 31 (1), 61–85.
- Kyratos, N.P., Theodossopoulos, P., Theotokatos, G., Xiros, N., 1999. Simulation of the overall ship propulsion plant for performance prediction and control. *Trans.-Instit. Marine Eng.-Ser. C* 111, 103–114.
- Martinsen, M. A., 2016. An design tool for estimating the added wave resistance of container ships.

- Minsaas, K., Faltinsen, O., Persson, B., 1983. On the importance of added resistance, propeller immersion and propeller ventilation for large ships in a seaway. Proceedings of International Symposium on Practical Design of Ships and other Floating Structures -PRADS'83.
- Mirsadraee, Y., 2019. Development of a Model for Propeller Tip Vortex Cavitation and Analysis of the Radiated Pressure Fluctuations. Technical University of Denmark.
- Ogawara, Y., Iwata, S., Tsujita, T., Sasaki, K., 1972. Governing operation of diesel engine for high-speed ship in rough sea. *Jpn. Shipbuild. Marine Eng.* 6 (4).
- Regener, P.B., 2016. Hull-Propeller Interaction and Its Effect on Propeller Cavitation. Technical University of Denmark.
- Regener, P.B., Mirsadraee, Y., Andersen, P., 2018. Nominal vs. effective wake fields and their influence on propeller cavitation performance. *J. Mar. Sci. Eng.* 6 (2), 34.
- Saettone, S., Taskar, B., Regener, P.B., Steen, S., Andersen, P., 2020. A comparison between fully-unsteady and quasi-steady approach for the prediction of the propeller performance in waves. *Appl. Ocean Res.* 99, 102011. <https://doi.org/10.1016/j.apor.2019.102011>.
- Sasajima, H., Tanaka, I., Suzuki, T., 1966. Wake distribution of full ships. *J. Zosen Kiokai* 1966 (120), 1–9.
- Smith, T. W. P., Jalkanen, J. P., Anderson, B. A., Corbett, J. J., Faber, J., Hanayama, S., O'keeffe, E., Parker, S., Johanasson, L., Aldous, L., et al., 2015. Third IMO GHG Study.
- Taskar, B., 2017. The Effect of Waves on Marine Propellers and Propulsion. Norwegian University of Science and Technology.
- Taskar, B., Yum, K.K., Steen, S., Pedersen, E., 2016. The effect of waves on engine-propeller dynamics and propulsion performance of ships. *Ocean Eng.* 122, 262–277.
- Ueno, M., Tsukada, Y., Tanizawa, K., 2013. Estimation and prediction of effective inflow velocity to propeller in waves. *J. Mar. Sci. Technol.* 18 (3), 339–348. <https://doi.org/10.1007/s00773-013-0211-8>.
- Van Uy, D., 2016. A study on torque rich phenomena in ship operation. *J. Shipp. Ocean Eng.* 6, 154–164.
- Vaz, G., Hally, D., Huuva, T., Bulten, N., Muller, P., Becchi, P., Herrero, J.L., Whitworth, S., Macé, R., Korsström, A., 2015. Cavitating flow calculations for the E779A propeller in open water and behind conditions: code comparison and solution validation. Proceedings of the 4th International Symposium on Marine Propulsors (smp-15), Austin, TX, USA. pp. 330–345.
- Vaz, G.N.V.B., Bosschers, J., 2006. Modelling three dimensional sheet cavitation on marine propellers using a boundary element method. Proceedings of the Sixth International Symposium on Cavitation, Wageningen, The Netherlands. pp. 11–15.
- Woschni, G., 1968. A universally applicable equation for the instantaneous heat transfer coefficient in the internal combustion engine. *SAE Trans.* 3065–3083.
- Yum, K.K., Taskar, B., Pedersen, E., Steen, S., 2017. Simulation of a two-stroke diesel engine for propulsion in waves. *Int. J. Naval Archit. Ocean Eng.* 9 (4), 351–372.

Paper 3

Modeling and Analysis of Performance and Emission of Marine Lean-burn Natural Gas Engine Propulsion in Waves

Sadi Tavakoli, Simone Saettone, Sverre Steen, Poul Andersen,
Jesper Schramm and Eilif Pedersen



Modeling and analysis of performance and emissions of marine lean-burn natural gas engine propulsion in waves

Sadi Tavakoli^{a,b,*}, Simone Saettone^{a,b}, Sverre Steen^a, Poul Andersen^b, Jesper Schramm^b, Eilif Pedersen^a

^a Department of Marine Technology, Norwegian University of Science and Technology, Norway

^b Department of Mechanical Engineering, Technical University of Denmark, Denmark

ARTICLE INFO

Keywords:

Natural gas engine
Dynamic load
Marine propulsion plant
Response time

ABSTRACT

In many vessels, the prime mover is a diesel engine, while the researchers recommended using natural gas as an attractive option to comply with the latest emission legislations. This study aims to analyze the dynamic response of a spark-ignition engine fueled by natural gas. Due to the complexity of power system operation in transient conditions, ship propulsion modeling is performed to assess the environmental impact of dynamic load. A co-simulation modeling in MATLAB- SIMULINK platform was developed to couple the medium-speed, four-stroke, turbocharged, spark-ignition engine to a propeller immersed in seawater. The engine's essential elements were implemented, and the validity of the modeling was evaluated using the manufacturer's data in both steady-state and transient conditions. The main goal was to determine the importance of the transient loads on the engine response, particularly during harsh weather conditions. Hence, simulations of various wave conditions with multiple wave amplitude, wave direction, and wavelength were conducted. Compared with the steady-state, the transient condition resulted in a deterioration of the combustion efficiency. Furthermore, the amount of unburned fuel, NO_x compounds, and brake specific fuel consumption have increased.

1. Introduction

The global trend of employing the marine transportation system has expanded during recent decades [1], and the marine diesel propulsion system has had the widest market in Europe over the last five years, as shown in Fig. 1. The figure shows that internal combustion engines have been extensively used as a power source for the seaborne craft. Thus, they will account for a significant part of marine emission compounds. For instance, Matthias et al. [2] showed that ship emissions might directly result in air pollution in coastal areas by producing NO₂ and SO₂. Much research has looked at the importance of air pollution to global warming, the formation of acid rain and depletion of ozone [3]. For the sake of controlling emissions, international standards set limits according to the application and power scope. For example, IMO [4] limited the total amount of emissions in the year 2000 to 12.1 g/kW h, in 2011 to 9.7 g/kW h and 2016 to 2.4 g/kW h for an engine speed of 720 rpm. Although diesel engines are lean combustion engines with relatively low concentrations of HC and CO [5], they still release a large amount of emission compounds [6]. Emissions legislation has forced manufacturers to redesign their products, which can be fulfilled by engine enhancement, propeller modification, and control system installation. The utilization of natural gas fuel – partly in LPDF or fully

in LBSI – has provided an alternative solution without installing an after-treatment system [7].

Combustion and emission of diesel and gas engines were studied in numerous works, but only a few studies have identified the engine's dynamic response in time-varying load. The elements of ship propulsion include the ship hull, the propeller, and the engine. Traditionally, these three elements have been studied individually and principally in calm water, while a real ship works in waves that cause motions and give a time-varying inflow and load on the propeller that again interacts with the engine. To simulate a ship propulsion system that includes engine model, hull model, propeller model, and control system, Campora and Figari [9] developed a mathematical model that communicated all sub-models using the SIMULINK environment to investigate the system response in harsh and transient conditions. Kyrtatos et al. [10] developed a mathematical model for transient and steady-state modeling by implementing a proportional integration control system in a ship propulsion system. Maneuvering motions have been discussed by Moc-tar et al. [11] in a simulation of the engine propeller model, test scale model, and real scale measurement. The engine modeling was done based on a constant and variable propeller speed in an abrupt change

* Corresponding author at: Department of Marine Technology, Norwegian University of Science and Technology, Norway.
E-mail address: sadi.tavakoli@ntntu.no (S. Tavakoli).

Nomenclature

ρ	Density
A_c	Surface area at flame front
h_c	Convective heat transfer coefficient (W/m ² K)
P_f	Absolute pressure ratio
Pr	Prandtl number
S_T	Turbulent flame speed
T_{cp}	Instantaneous crank pin torque
$\Delta\omega$	Shaft speed
Δt	Simulation time step
\dot{m}	Mass flow
η	Efficiency
γ	Specific heat ratio (1.4 for air at 300 K)
λ	Wave length
τ	Taylor time scale
θ	Wave direction
A	Wave amplitude
A_{eff}	Effective flow area
A_R	Reference area
B	Cylinder Bore (m)
$BMEP$	Brake mean effective pressure
C_D	Discharge coefficient
C_f	Fanning friction of smooth pipe
c_p	Specific heat
EGR	Exhaust gas recirculation
h	Enthalpy
HC	Hydrocarbon
I	Shaft moment of inertia
IVC	Intake valve closure
$LBSI$	Lean burn spark ignition
$LPDF$	Lean partial dual fuel
M	Mass
NO_2	Nitrogen dioxide
P	Pressure
PR	Pressure ratio
R	Gas constant
RAO	Response amplitude operator
S_L	Laminar flame speed
SO_2	Sulfur dioxide
T	Temperature
T_f	Friction torque
U_{eff}	Effective velocity outside boundary layer
UHC	Unburned hydrocarbon
VGT	Variable geometry turbine

of power demand. The model's output showed the impact of engine dynamics on the entire system and the time delay caused by the engine due to the response time. They also investigated three moments of inertia for the propeller and showed that the time delay in reaching the new operating setpoint stretches with a higher moment of inertia. A study by Theotokatos [12] presented a method of coupling a turbocharged two-stroke diesel engine response to the fixed-pitch propeller. He indicated that the mean value model of the engine appropriately calculated the engine response time, while there was a notable gap between the real turbocharger speed and boost pressure with the simulated data. Hence, he proposed multi-zone modeling to predict a precise output; otherwise, the rapid transient condition's accurate modeling is hard to achieve. Real-time modeling was developed by Altosole et al. [13] to improve

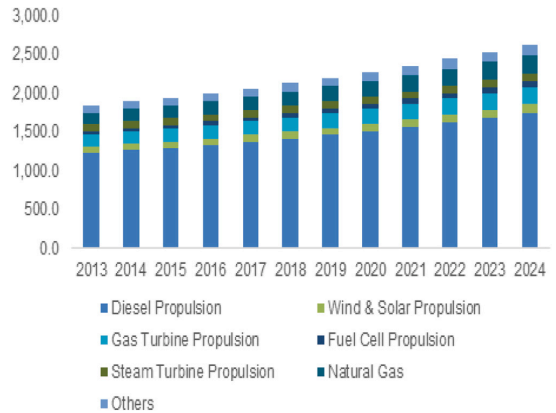


Fig. 1. The number and type of power propulsion system between 2013 and 2024 in Europe. [8].

the ship simulator. Simulation time for the whole propulsion system reached 1% of comparable work done with a fully thermodynamic model by applying a look-up table instead of modeling the cylinders. However, less sensitivity to the boundary conditions such as air pressure and temperature, and providing the look-up table through parallel thermodynamic modeling, are the drawbacks of this work. A ship traveling at sea with the wave and wind resistance was simulated using a co-simulation modeling of a two-stroke diesel engine and propeller by Yum et al. [14]. The model provided dynamic shaft torque and calculated the engine's efficiency during the transient condition. With one constraint installed on the fuel system to limit the maximum smoke, they found the engine encountered some delay in response time because of the turbocharger mass moment of inertia and the high capacitance of the manifold volume. Taskar et al. [15] also explained the influential parameters on a wave in a ship trip and identified the propulsion performance drop. They concluded that re-setting the exhaust valve timing closure and changing the injection timing helped reach more efficient combustion with less brake specific fuel consumption throughout the transient condition. Systematic models of propulsion systems have also been developed in similar studies to uncover the system's challenges, predict possible solutions, and optimize the system with the least experiments [16,17].

The use of natural gas in the shipping industry to fulfill stringent emission legislation was first tried in 2000, and the quantity of the gas engine progressively increased until 2016 [18]. Natural gas is a low carbon fuel since it has high hydrogen to carbon ratio, and it has a higher heating value on a mass basis than fuels such as gasoline [19]. In addition, the specific heat capacity of natural gas reduces the mixture temperature and increases the ignition delay in comparison with the conventional diesel operation [20]. To achieve a high BMEP natural gas equivalent with a diesel engine, without struggling with a high amount of NO_x and knock phenomenon, lean-burn combustion was recommended. However, concerning Fig. 2, there is only a narrow area where the engine works at an optimized setpoint. Einewall et al. [22] recommended an EGR-diluted mixture with stoichiometric combustion and installing a three-way catalyst instead of lean-burn combustion. This method significantly improved the reduction of NO_x and unburned hydrocarbon (UHC) emission, but the drawbacks were higher CO and efficiency drop. In addition, the efficiency gain of lean operation may be ruined due to misfire in incomplete combustion and releasing unburned methane [23]. Therefore, it is always a trade-off between engine combustion efficiency and emission compounds. To optimize this trade-off, the type and quality of ignition and combustion play a dominant role [24].

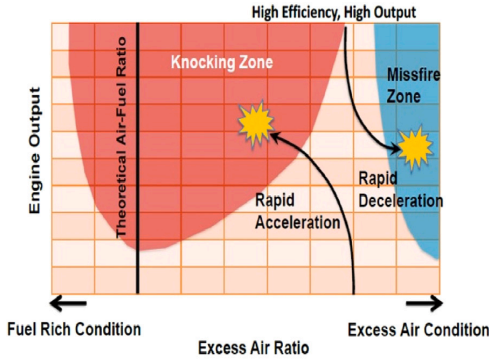


Fig. 2. The narrow working region of a lean-burn gas engine [21]. Any unstable situation leads the engine into the misfire zone or knocking zone.

The briefly reviewed literature above revealed the necessity to know the lean-burn gas engine response in a marine application where the load changes dynamically. A specific marine engine's primary data, such as fuel flow, was available during a long voyage, but the emission quantity and instantaneous response of the engine are not well determined. Therefore, this study's main objective is to predict the engine response by developing a co-simulation platform. Section 2 explained the procedure of modeling the propulsion system using the thermodynamic equations for the engine, a controllable-pitch propeller, and a high-inertia shaft. The available data was used to verify the modeling both during steady-state and transient conditions in Section 3. Section 4 described the importance of time-varying load on the specific fuel consumption, combustion efficiency, knock phenomenon, probability of the turbocharger surge, variation of air-fuel ratio and essential emission compounds with a certain focus on the harsh weather condition. The results were concluded in Section 5.

2. Simulation framework

Ship propulsion efficiency explains engine, propeller, and control system performance. Accordingly, high-fidelity mathematical model-building with detailed equations of all sub-models is influential in the co-simulation. The propulsion setup in this study is a conventional operation mode, as shown in Fig. 3(a), where the clutch is disengaged. In co-simulation, the different subsystems are modeled in a distributed manner, and the subsystems were carried out like a black box. This study consisted of an engine and propeller being connected through a rigid shaft. The engine was modeled thermodynamically, and the propeller was simulated using the boundary-element method (BEM). To properly co-simulate the entire system, an interface was required to solve each subsystem and organize the blocks' connecting input and output. The connection was performed on the MATLAB-SIMULINK platform.

A discrete-event-based co-simulation [25] was chosen to exchange data between the sub-models, while each sub-model was solved independently by their internal solver, using their own fixed and non-fixed time-step for the propeller and engine, respectively. A schematic of the co-simulation is shown in Fig. 3(b).

The decomposition of a typical engine reports a significant number of components on the physical level. A modeling library is a powerful tool to model such a complex system [26] believe that a model library can handle the dictated equations and make them reusable. A model library for the turbocharged diesel engines was also done by Yum and Pedersen [27] and Huang et al. [28]. For this purpose, a model library

was developed and used in this work. Many researchers have used this platform to model their library-based modeling [29–31].

The engine's flow process commenced by air suction from the environment into the compressor, moving within the intercooler, manifold, and intake ports sequentially. The mixture burned inside the cylinders, and burnt gases moved across the exhaust valves, exhaust port, exhaust manifold, turbine, and finally discharged into the atmosphere. The turbine and compressor are connected via a mechanical-rigid shaft. The generated power of the engine was delivered to the propeller through massive inertia and the gearbox. The inertia covered all of the rotating components, including the crankshaft, camshaft, flywheel, connecting shaft, propeller, and seawater. The components split into 11 zones in the modeling process, as shown in the schematic of Fig. 4.

2.1. Zone 1: Environment

The 'sea reference condition' states the free water surface boundary condition on an ocean. A fixed atmospheric pressure, temperature, and zero amplitude were utilized for the compressor's inlet and the outlet of the turbine.

2.2. Zone 2: Turbocharger

In order to model the turbocharger's performance, the information from the compressor and turbine as a function of speed, pressure ratio, mass flow rate, and efficiency were implemented in the format of look-up tables, which were provided by the manufacturer, ABB company. The turbocharger speed and pressure ratio were predicted at each time-step, and two other unknowns were taken from the look-up table [32]. The calculation started with isotropic enthalpy differences of compressor and turbine, which were calculated by Eqs. (1) and (2). By finding the proper thermodynamic efficiency extracted from the look-up table, the enthalpy out of the compressor and turbine could be computed respectively by Eqs. (3) and (4). The computation was repeated until the predicted parameters reached an acceptable convergence.

$$\Delta h_s = c_p T_{\text{total,in}} (PR^{\frac{\gamma-1}{\gamma}} - 1) \quad (1)$$

$$\Delta h_s = c_p T_{\text{total,in}} (1 - PR^{(1-\gamma)/\gamma}) \quad (2)$$

$$h_{\text{out}} = h_{\text{in}} + \frac{\Delta h_s}{\eta_s} \quad (3)$$

$$h_{\text{out}} = h_{\text{in}} - \Delta h_s \eta_s \quad (4)$$

The Eqs. (5) and (6) calculated the turbocharger's shaft speed and power:

$$\Delta \omega = \frac{\Delta t (T_{\text{turbine}} - T_{\text{compressor}} - T_{\text{friction}})}{I} \quad (5)$$

$$P = \dot{m} (h_{\text{in}} - h_{\text{out}}) \quad (6)$$

where subtext script in, out and s stands for inlet, outlet and isotropic, respectively. The thermodynamic table of the fluid estimated the outlet temperature accordingly. T_{total} in the first equations was calculated by Eq. (7):

$$T_{\text{total,in}} = T_{\text{in}} + \frac{u_{\text{in}}^2}{2c_p} \quad (7)$$

where u_{in} is inlet velocity.

2.3. Zone 3: Intercooler

The intercooler was cooled by seawater, and the inlet air temperature was available from the measured data of a long journey. Therefore, a non-predictive approach was adopted for finding the boost temperature. The intercooler was assumed as multiple pipes with infinite heat sink, and the outlet temperature was given as a function of boost pressure in the look-up table. To calculate the amount of heat flux,

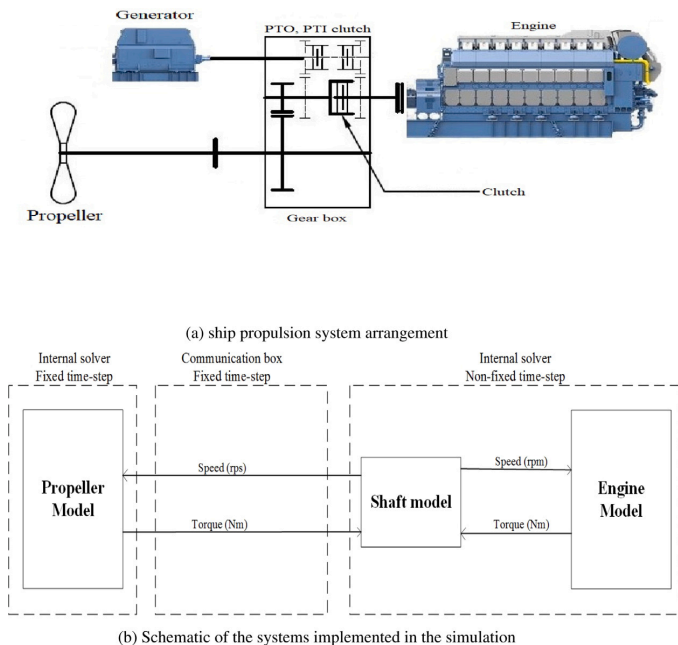


Fig. 3. Propulsion system in test bench and simulation.

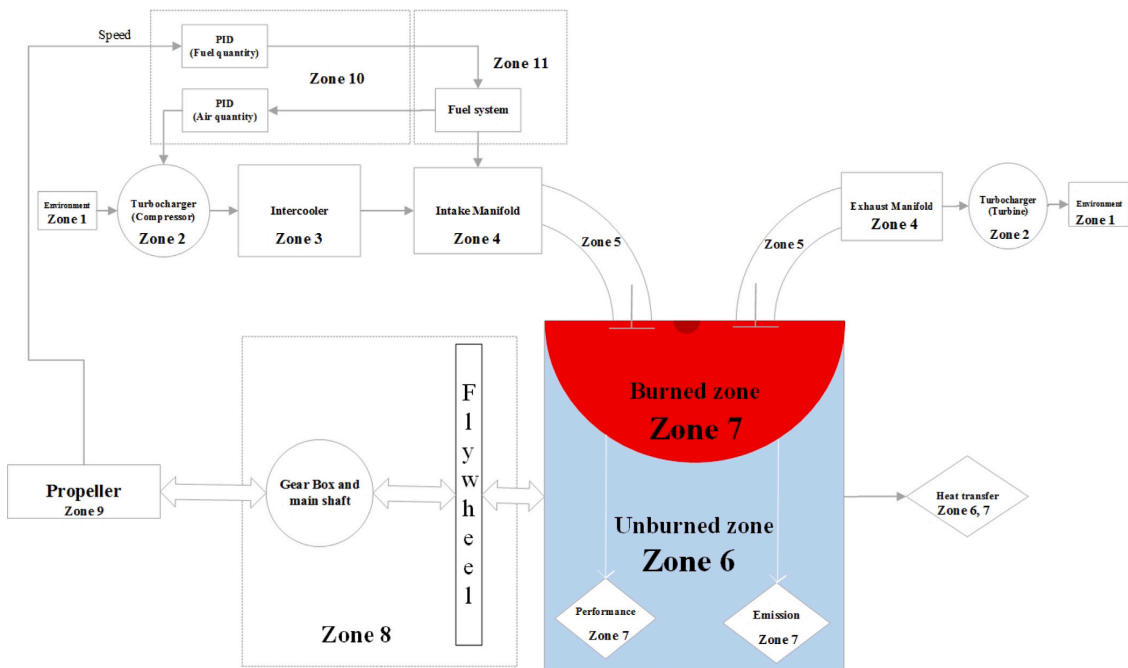


Fig. 4. Modeling zones including the engine, propeller and connecting shaft.

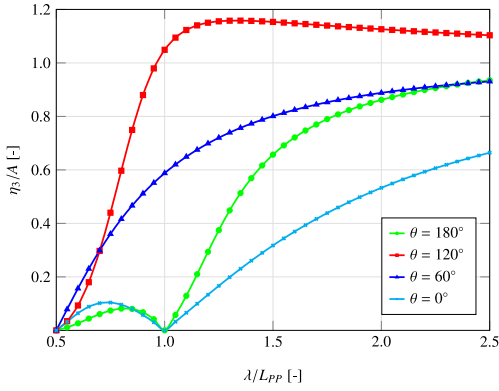


Fig. 5. Heave RAO in different wave conditions at design ship speed.

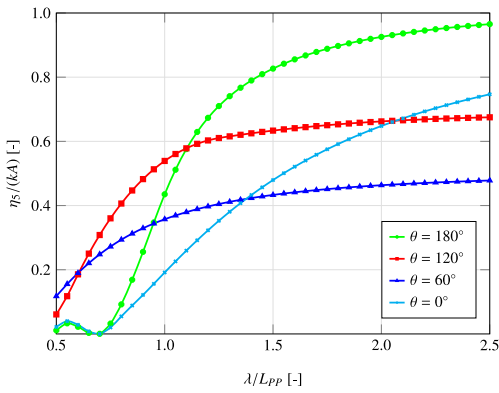


Fig. 6. Pitch RAO in different wave conditions at design ship speed.

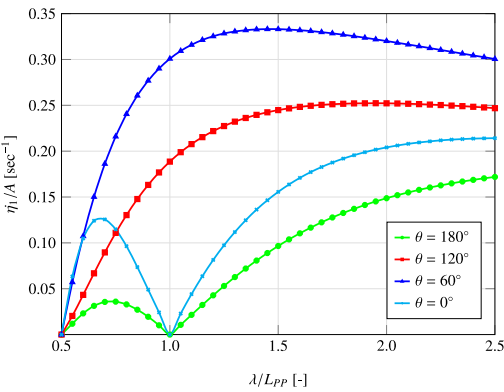


Fig. 7. Surge velocity RAO in different wave conditions at design ship speed.

the Colburn analogy [33] was used, which permits the prediction of an unknown heat transfer coefficient when one of the other coefficients is known, by:

$$h_g = \left(\frac{1}{2}\right) C_f \rho U_{eff} C_p Pr^{(1/3)} \quad (8)$$

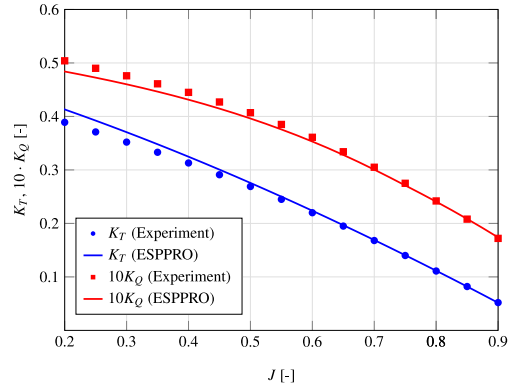


Fig. 8. Open Water Diagram computed by ESPPRO for the design propeller pitch.

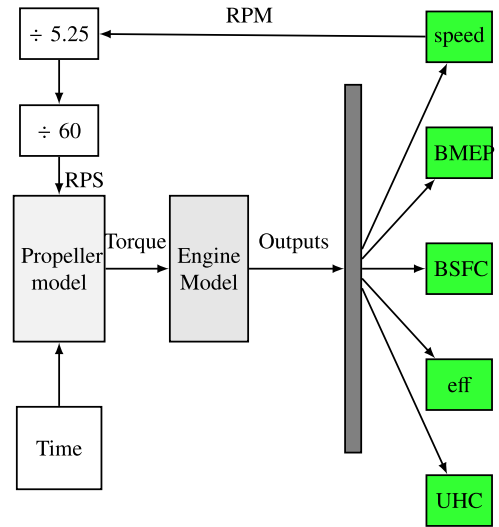


Fig. 9. The implemented blocks connected in MATLAB-SIMULINK with a time step 0.1 s.

and, heat flux is calculated by:

$$q_{convection} = h_g(T_{gas} - T_{wall}) \quad (9)$$

More information is presented in [34].

2.4. Zone 4: Intake and exhaust system

The dimensions of intake and exhaust volume were implemented correctly, as reported in the design drawings. Developing the equation of Navier–Stokes in thermodynamic modeling and implementing in the discretized volume predict the fluid flow across the pipes and provides a correct input to the turbocharger. The input plays a significant role in predicting turbocharger response [35]. Hence, conservation equations of continuity, energy, and momentum presented in Eq. (10), (11) and (12) were implemented for the pipes and manifolds with different discretized length scales for the straight pipes and bends [36].

$$\frac{dm}{dt} = \sum_{boundaries} \dot{m} \quad (10)$$

$$\frac{dme}{dt} = -\rho \frac{dv}{dt} + \sum_{boundaries} (\dot{m}H) - hA_s(T_{fluid} - T_{wall}) \quad (11)$$

$$\frac{d\dot{m}}{dt} = \frac{d\rho A + \sum_{boundaries} (\dot{m}u) - 4C_d \frac{\rho u |u|}{2} \frac{dx A}{D} - K_p (\frac{1}{2} \rho u |u|) A}{dx} \quad (12)$$

2.5. Zone 5: Intake and exhaust valves

The intake and exhaust valves' capacities ultimately restricts the total flow of the engine. Therefore, calculating the mass flow rate passing through the valves was crucial for an accurate engine performance estimate. A feasible approach was the one-dimensional isotropic flow analysis for compressible flow over a flow restriction proposed by Heywood [37]. With a pressure upstream and downstream of the valve, the mass flow rate was determined by the pressure difference:

$$\dot{m} = A_{eff} \rho_{is} U_{is} = C_D A_R \frac{P_u}{\sqrt{RT_u}} \cdot \left(\frac{P_d}{P_u}\right)^{1/\gamma} \sqrt{\left[\frac{2\gamma}{\gamma-1} (1 - P_r)^{\frac{\gamma-1}{\gamma}}\right]} \quad (13)$$

where u is upstream and d is the downstream stagnation point. Here, C_D was an experimentally determined discharge coefficient. For choked flow, the modified equation was applied [37].

2.6. Zone 6: Unburned mixture zones

A mixture of air and fuel with an excess air ratio setpoint of 1.8 was captured in a non-fixed control volume. The mixture was assumed to be perfectly mixed. During the compression stroke, the volume reduces, and the pressure and temperature of compressed mass increases. The heated surfaces of the piston, cylinder head, and liner from the previous cycle warmed the mixture up from IVC to almost the next 100 crank angles. Afterward, it transferred conversely. The wall temperature was assumed to be constant throughout the cycle, though several thermal zones were imposed concerning the cylinder's interior. The maximum motoring pressure and temperature in rated load/speed ended in approximately 85 bar and 850 K.

The exchange of thermal energy between gases and boundaries was called 'heat transfer', which was classified into three main mechanisms of *conduction*, *convection*, and *radiation*. Heat conduction and radiation were calculated using Fourier's law [38] and Stefan-Boltzmann's law [39], respectively. In order to model the in-cylinder heat convection, h , Woschni [40] recommended modeling of this coefficient using Eq. (14):

$$h_{c(Woschni)} = \frac{K_1 P^{-0.8} W^{0.8}}{B^{0.2} T K_2} \quad (14)$$

where K_1 and K_2 are constant and W is average cylinder gas velocity (m/s).

2.7. Zone 7: Burned zone

More sophisticated modeling was necessary for zone 7. The burned zone involved heat transfer modeling and combustion modeling, emission modeling, and knock modeling.

2.7.1. Combustion

The information of cylinder geometry, spark plug timing, spark plug location, and fuel type was available. The 'EngCylCombSITurb' [36] is recommended for flame modeling if the information is available, and calculates the combustion burning rate by a laminar (S_L) and turbulent (S_T) flame speed with a two-zone approach. It assumes that eddies are entrained by the flame front at a turbulent velocity, while the mixture of fuel and air is burning at laminar velocity. The rate of transference of the mixture from the unburned zone to the burned zone was equal to the rate of change of M_b and was calculated by Eq. (15).

$$\frac{dM_b}{dt} = \frac{M_c - M_b}{\tau} \quad (15)$$

where index b symbolizes burned classification, u unburned classification and e entrained classification. M_e is the entrained fuel passing the border of unburned-burned mixture and is calculable by Eq. (16).

$$\frac{dM_e}{dt} = \rho_u A_e (S_T + S_L) \quad (16)$$

Time constant, τ , is a function of Taylor length scale and laminar flame speed:

$$\tau = \frac{\lambda}{S_L} \quad (17)$$

Detailed equations of calculation of surface area at flame front (A_e), turbulent flame speed (S_T) and laminar flame speed (S_L) are presented in [41].

2.7.2. Emission

Natural gas engines produce four main emission compounds throughout the combustion: NO_x , UHC, CO_2 , and CO [42]. Due to the complexity of solving hundreds of reactions of species, emission modeling is essential.

2.7.2.1. NO_x formation. NO_x was calculated using the reduced mechanism described by Zeldovich [43]:



where Eqs. (18) and (19) are thermal NO_x formation and Eq. (20) is particular at near-stoichiometric conditions and in fuel-rich mixtures.

2.7.2.2. Unburned hydrocarbon formation. The word hydrocarbon refers to any compound consisting of carbon and hydrogen. Incorporating of any other atoms disqualifies from being considered as a hydrocarbon [44]. This work has not considered the chemical mechanism and formation of a chain of hydrocarbon in molecular structure. Therefore, any fuel left unburned after post-oxidation at the exhaust valve opening (EVO) is considered as unburned hydrocarbon emission or methane slip. In typical steady-state conditions in the loads close to the nominal loading, almost 80% of the whole methane slip originates from the crevice volume, 15% forms due to quenched flame, and less than 5% from gas exchange process [45]. The percentages change when the load varies during the unsteady state, but the two primary sources are still quenched flame and mass of the crevice volume. Thus, in this study, to estimate the total amount of unburned hydrocarbon, the fuel re-entered from the crevice volume during the main combustion burns by the main reaction rate. The rest of the re-entered mass mixes with the fuel, which is quenched, and the new mixture burns by a new reaction rate of Eq. (21) introduced by Lavoie [46] during the post-oxidation, between the main combustion and EVO. The unburned fuel after the post-oxidation is presented as methane slip.

$$\frac{d(HC)}{dt} = -6.7 \times 10^{15} e^{-\frac{37230}{RT}} f_{[HC]} f_{[O_2]} \left(\frac{P}{RT}\right)^2 \quad (21)$$

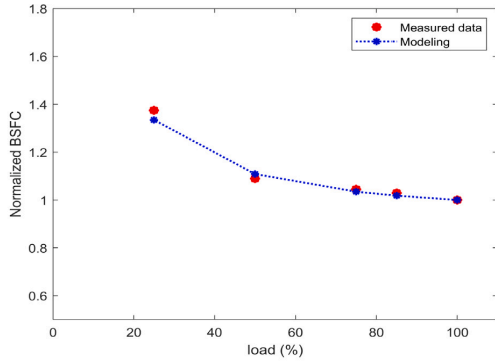
where $f_{[HC]}$ and $f_{[O_2]}$ are the mass fraction of fuel and O_2 .

To improve the computational performance in this study, the equation was modified to:

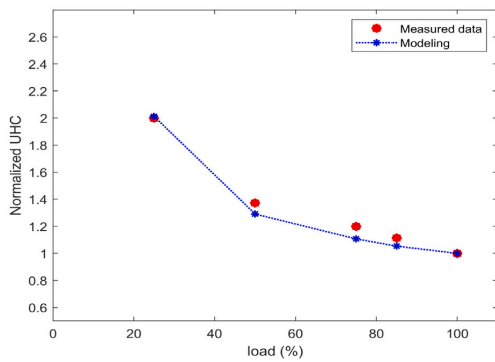
$$R_K = A \times 2000 \times R_S e^{-\frac{1600K \times B}{T}} [f_{HC}] [f_{O_2}] \quad (22)$$

where A and B are multiplier and are constant throughout the load variation, and T is the mass-averaged overall temperature, and R_S is the burn rate calculated by the combustion model.

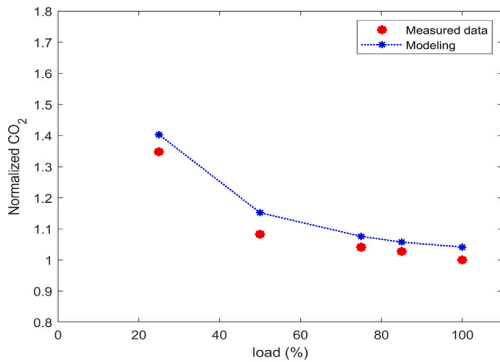
2.7.2.3. CO And CO_2 . Natural gas has a high H/C ratio compared with diesel fuel. As a result, natural gas engines produce less CO_2 , and even up to 20% less than similar gasoline engines [42]. Furthermore, in very lean combustion, a very low level of carbon monoxide (CO) is achievable [47]. Thus, the variation of these two compounds is not presented, except the CO_2 graph for the modeling validation.



(a) Normalized brake specific fuel consumption



(b) Normalized unburned hydrocarbon



(c) Normalized CO₂

Fig. 10. Validation of the combustion modeling and emission formation with constant loads in the steady state.

2.7.3. Knock

There are several methods of modeling and predicting the knock phenomenon. There is also the possibility of directly or indirectly detecting knock by, for example, studying inside cylinder parameters or engine block vibration [48]. The measured data for verification of the knock model does not exist, and this work only used the non-validated modeling method recommended by Gamma Technologies for natural gas engines [34]. This method has a dependence on the air–fuel ratio

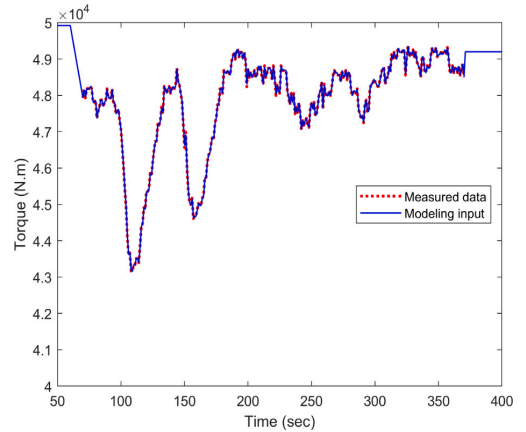


Fig. 11. A time-varying torque adapted from the engine operating loads.

and EGR on the induction time. The knock index is defined by:

$$K_1 = 10000 \cdot M \cdot u(\alpha) \cdot \frac{V_{TDC}}{V(\alpha)} \exp\left(\frac{-6000}{T(\alpha)}\right) \times \max[0, 1 - (1 - \phi(\alpha))^2] \cdot I_{index} \quad (23)$$

where M is a multiplier and can be found during the validation step. For this study, we used M=1, and I_{index} was calculated by Eq. (24):

$$I_{index} = \int \frac{1}{\tau} dt \quad (24)$$

and τ is defined by Eq. (25):

$$\tau = M_1 * 1.9858 - \left[10^{-9} \exp\left(\frac{18659}{M_2 T}\right) \left(\frac{MN}{100}\right)^{0.978} \times (Fuel^{-0.578})(O_2^{-0.28})(Diluent^{0.03}) \right] \quad (25)$$

where MN is the fuel methane number, M_1 and M_2 are equalized to 1, and diluent concentration is the sum of concentrations of N_2 , CO_2 , and H_2O .

2.8. Zone 8: Power transmission

The power transmission model includes the flywheel, crankshaft, main shaft, and gearbox to transmit the power to/from the engine. All the inertia were assumed to be rigid. The inertia concerning water resistance and the propeller were added to this model as well. The entire propulsion shaft was modeled as single and rigid, and the brake torque T_b was calculated by:

$$T_b(t) = T_s(t) - I \cdot \dot{\omega}_{ct}(t) \quad (26)$$

where, $\dot{\omega}_{ct}(t)$ is the instantaneous crank-train acceleration. The shaft torque, T_s , is also calculated by:

$$T_s(t) = T_{cp}(t) + T_a(t) - T_f(cyc) \quad (27)$$

where $T_a(t)$ is the instantaneous torque of any other attachment and equal to 0 in the present work. $T_{cp}(t)$, is the crankpin torque and was calculated by a function of force on the crank in the x- and y-direction.

2.9. Zone 9: Propeller and vessel modeling

A controllable-pitch propeller was used for the current investigation. The blade pitch was modified to maintain the average ship speed

in waves equal to its design value if the engine could not continuously produce the required power.

Model experiments by SINTEF Ocean provided the propeller's nominal wake distribution at the design ship speed, and the thrust deduction factor, wake fraction, and model resistance as a function of the ship velocity in calm water.

Only wind, wave, and added resistance were taken into account. The added wave resistance was computed in irregular waves, even though regular waves were considered. The DTU in-house method described by Martinsen [49] was used to compute the added resistance in regular waves. The approach explained in ITTC [50] was used to calculate the added resistance in irregular waves, which had significant peak frequencies and wave heights equal to the wave frequencies and heights of the studied regular waves. The added wind resistance was computed using the procedure explained by ITTC [50], and the calm water resistance was converted from model to full-scale according to ITTC [51].

The pitch and heave transfer functions were computed using the procedure developed by Jensen et al. [52], while the surge velocity was computed following the method described by Honkanen [53]. Heave, pitch, and surge velocity RAOs are shown respectively in Figs. 5–6–7.

The scaling procedure developed by Sasajima et al. [54] was used to calculate the wakefield on a full scale. The entire wake distribution was contracted to avoid time-consuming calculations. The method described by Taskar [55] was used to obtain the time-varying wakefields in waves.

The primary tool used for the propeller analysis was the DTU-developed unsteady low-order boundary-element method ESPPRO [56], which was based on potential flow theory, where the flow is assumed to be inviscid, incompressible, and irrotational.

Fig. 8 shows the comparison between the experimental open water curves and the open water characteristic computed by ESPPRO. The quasi-steady approach described by Saettone et al. [57] was used for the propeller analysis.

The quasi-dynamic approach described by Minsaas et al. [58] was used to determine the reduction of thrust and torque caused by the propeller emergence. More discussion of the models is presented in [59].

2.10. Zone 10: Controlling system

In this methodology, the propeller supplied the torque, and the speed was computed inside the engine block, according to the schematic presented in Figs. 3(b), and 4, PID block named fuel quantity. The PID controller installed on the fuel valve adapted the engine speed, calculated the speed deviation compared with the setpoint in each time-step, and regulated the fuel valve lift and duration to inject a correct fuel quantity. The speed of the PID system affects engine response and stability. Moreover, to fix the excess ratio, additional PID (air quantity) was installed. This controller identified the fuel volume and actuated the turbine's VGT to provide the proper amount of air.

2.11. Zone 11: Fuel system

The fuel, natural gas, was injected into the air — just upstream of the intake valves. The fuel tank's exit to the entrance of the intake port was defined as the fuel system. To simulate the fuel delivery system's dynamics, all fundamental components of this system, including the fuel tank, orifices, fuel lines, and fuel valves, were assembled. For simplicity, the fuel tank was assumed to be a constant pressure after the pump. The lines, orifices, and valves followed the conservation equations of fluid flow presented in Section 2.4.

Table 1
Engine specification.

Item	Unit	Amount
Number of cylinders	–	9
Cylinder bore	mm	350
Cylinder stroke	mm	400
Connecting rod	mm	810
Maximum power	kW	3940
Rated speed	rpm	750
Fuel type	–	Natural gas

Table 2
Ship main specification.

Length between perpendiculars	117.6 m
Breadth	20.8 m
Design draft	5.5 m
Design shaft submergence	3.3 m
Service speed	15 kts

Table 3
Periodic waves characteristics.

Length (λ/L_{pp})	Amplitude (m)	Direction (θ)
.6	.5	0
.8	1	60
1	1.5	120
1.2	2	180

3. Simulation setup and validation

3.1. Simulation setup

A simulation of a B 35:40L9PG marine gas engine fitted on a cargo ship called Kvitbjørn was performed. The lean-burn gas engine ignites by a spark plug and operates at an excess air ratio of 1.8. In order to achieve stable combustion with this lean mixture, a pre-chamber was connected to the main chamber. In the simulation platform, we replaced a larger initial spark size by the spark plug. The specification of the engine and the vessel are presented in Tables 1 and 2.

The thermodynamic equations of the engine were implemented in GT-SUITE and compiled for the MATLAB-SIMULINK platform. The compiled file was connected with the developed propeller model, as shown in Fig. 9. The communication time-step was 0.1 s.

To estimate the engine response and to examine the engine's performance and emission as the prime mover of the propulsion system, 64 regular waves were imposed with a combination of four-wave amplitude, four-wave direction, and four wavelengths as shown in Table 3.

3.2. Validation

In order to verify the accuracy of the model, a comparison of the measured data and simulation output was performed. This verification is done both in steady-state and transient conditions. Fig. 10 show a slight disagreement in the output of the simulation and the measured data for the steady-state conditions. The engine rotational speed was assumed to be constant at around 750 rpm, and successive increases in the load from 25% to 100% of the nominal load were established. Brake specific fuel consumption in Fig. 10(a) stands for engine performance characteristics and verifies the combustion modeling, and unburned hydrocarbon in Fig. 10(b) together with CO₂ formation in Fig. 10(c) stands for emission characteristics and verify emission modeling. The quantities in 100% load at 750 rpm were used for normalizing the values.

As far as the transient condition was concerned, to increase the model's reliability, a time-varying torque was applied, as shown in Fig. 11. Fig. 12 shows the resemblance of the simulation output and

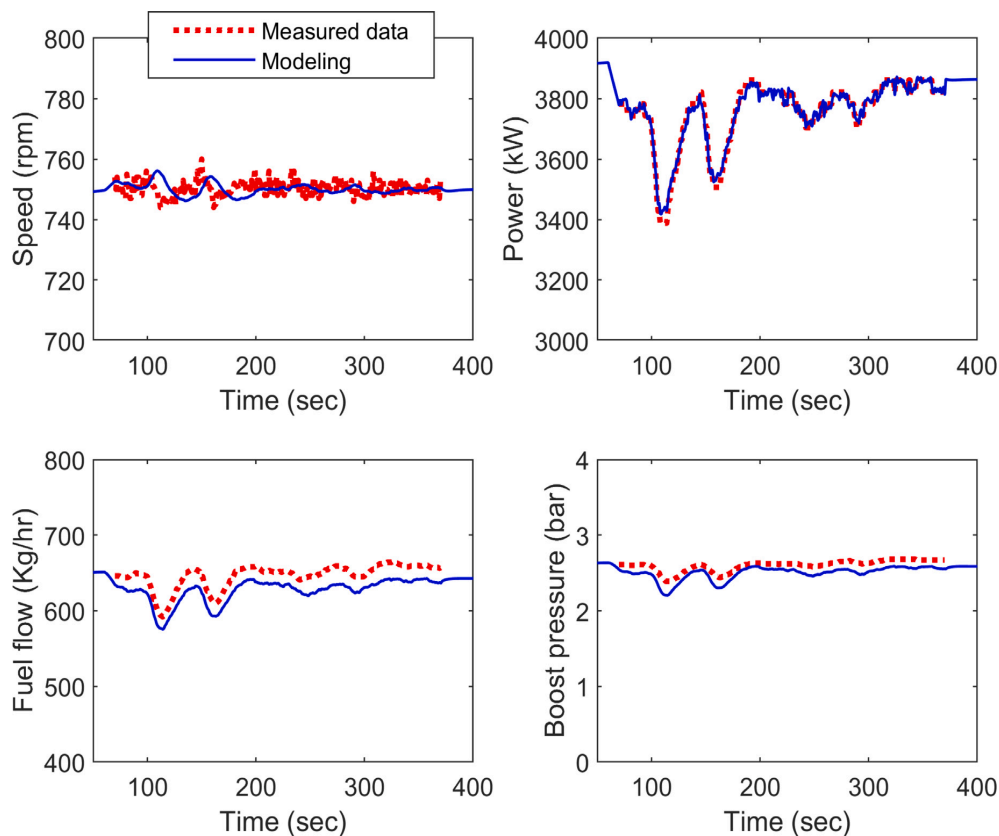


Fig. 12. A comparison of the vessel logged data and modeling output during a transient condition. The modeling's validity is started after 60 s of the simulation with a maximum load to reach the numerical stability.

measured data. The output shows that the data obtained by the simulation is broadly consistent with the major trends of the measured data. Load variation was started at the second 60, to disregard the primary numerical error. As can be seen, the simulation speed hardly fluctuates around 750 rpm, similar to the measured data. Power as a function of torque and speed also provided an acceptable output. The fuel flow graph revealed a satisfactory fuel consumption tendency by the modeling, even though there was a gap between the simulation and measured data. Turbocharger modeling also presented the same preciseness, as shown in the last sub-figure, with the boost pressure data. Thereby, the turbocharger map and thermodynamic equations were executed correctly since the rate of change of boost pressure in simulation is almost identical with the measured values.

4. Results and discussion

In order to assess the response of the natural gas engine in marine applications, all the 64 waves were evaluated in terms of combustion, efficiency, and emission. Fig. 13 shows a decline in the mean brake torque when the wave amplitude increases. The distribution of mean torque with $A=0.5$ is very smooth in all wavelengths and directions. This mean value was computed after using a low-pass filter to eliminate sharp transition effects. For higher amplitude, this figure explains that the amplitude plays a crucial role in the variation of the torque. Regarding the vertical axis, wave directions between 50° and around 100° had the most significant influence and, taking the wavelength

into account, λ/L_{PP} higher than 1 delivered the least mean torque. Less mean torque in these contours means more variation in the torque domain.

A key area of interest for the simulation is finding the engine's speed variation with multiple separated wave frequencies and strengths. The distribution of the average speed is represented in Fig. 14, where the values are hardly distinguishable from the target speed (except for $A = 1.5$ and $A = 2$) and where the average speed may decline to 745. Two main reasons can be found for such stability of engine speed. The first reason is the importance of the shaft inertia in controlling sudden variation of the speed. The second reason is the wave frequency, peculiarly when the frequency is high. During the higher frequencies, the input torque varies in a shorter period, and consequently, each wave compensates a fraction of the speed drop in the lower loads of the wave domain.

The in-cylinder pressure parameter distribution was used for the evaluation of combustion assurance. Fig. 15 presents the maximum engine pressure during the load variation. The range of in-cylinder pressure always changes between a minimum of 90 bar and a maximum of 120 bar. Referring to the steady-state pressure with an almost 106 bar, and a maximum designed pressure 180 bar, the range of change displays an acceptable condition.

As emphasized earlier, the use of natural gas engines for marine transport may result in a substantial drop in emission compounds, but they are also sensitive to the combustion quality. Any deviation from the optimum setpoint can result in a misfire or knock phenomenon. This is presented in Fig. 16, 17 and 18. Fig. 16 shows that there is

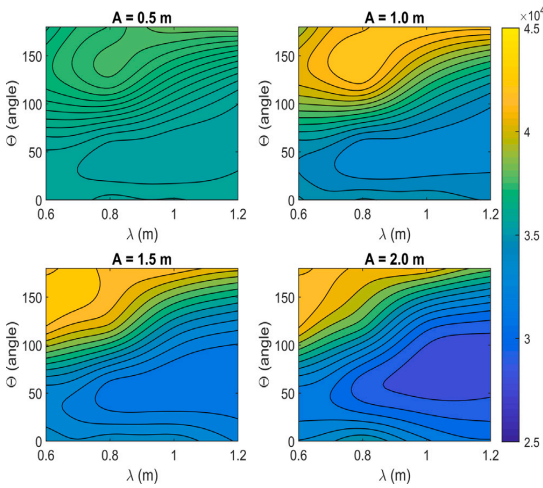


Fig. 13. Mean brake torque contour.

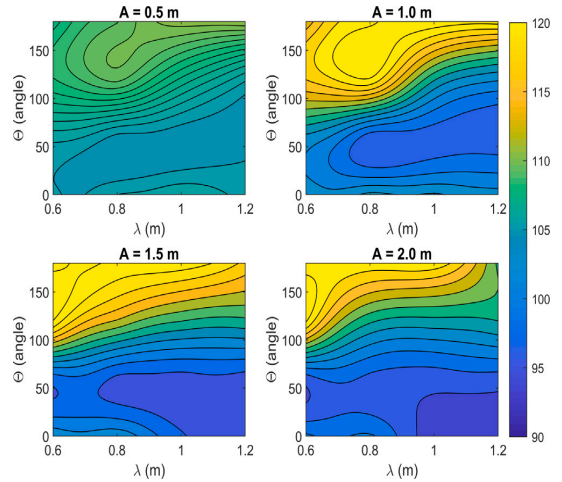


Fig. 15. Mean maximum pressure contour.

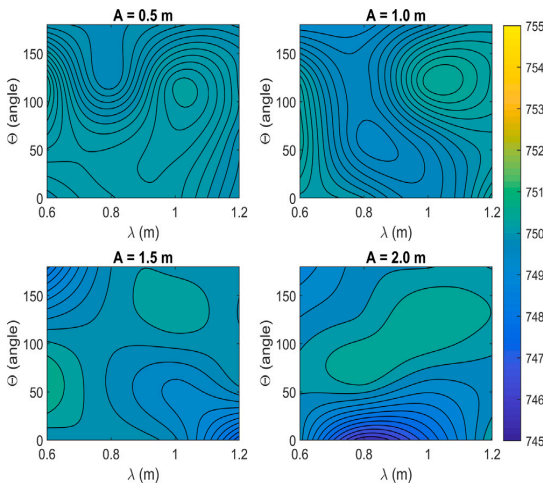


Fig. 14. Mean engine speed contour.

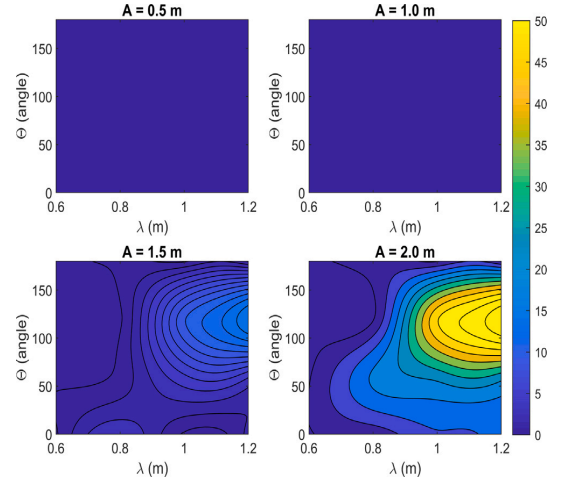


Fig. 16. Knock index contour.

no knock on engine combustion until the wave amplitude is less than 1 meter, and change of frequency, wavelength, and wave direction does not lead to knocking. With $A = 1.5$, a slight potential of knock appears, particularly with a wave direction of 120 and $\lambda/L_{PP} = 1.2$. With $A = 2$, the knock index's output lies in the higher λ/L_{PP} and intermediate wave direction. The next two figures describe almost the same procedures as well. It must be highlighted that the two figures maximum quantity has been limited to 3 and 10 for the sake of presenting infinite values in the contours. Therefore, any value higher than 3 for NO_x in Fig. 17 and 10 for UHC in Fig. 18 corresponds to 3 and 10, respectively. Besides, NO_x and UHC quantities in the steady-state are considered as normalizing coefficients. A comparison between Figs. 17 and 18 verifies that the lean-burn gas engine sensation is very high to the UHC formation. However, the range of contour is wider in Fig. 18, with $A = 1.5$, we have a wider spectral color of UHC rather than NO_x . The value of UHC even furthered with $A = 2$ in both the value and the domain. These two contours provide the significance of the higher waves on emission formation, but there is still a larger value

Table 4
Sample waves for visualization.

Case no.	Amplitude (m)	Wave length (λ/L_{PP})	Direction (θ)
1	0.5	.6	180
2	1.0	0.8	0
3	1.5	1	60
4	2.0	1.2	120

for emission formation when the wave amplitude is low. For instance, with $A = 1.0$ m, NO_x and UHC show a number between 1 and 2 for several waves. The values mean that even with light waves, there is a probability of a rise in the emission amount up to 100%.

Since we have utilized standard waves, all of the simulation output is periodic with a function of wave frequency. For clarity, in the next section, four waves with the highest disparity are presented and discussed. This illustration aims to show the magnitude of the effect of the waves on engine performance. The waves specification are presented in Table 4.

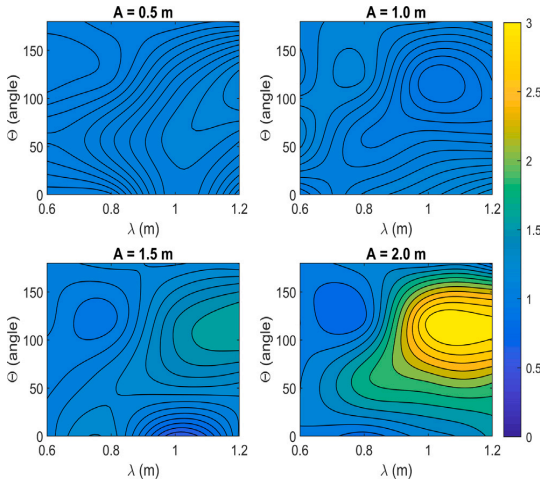


Fig. 17. Mean normalized NO_x contour.

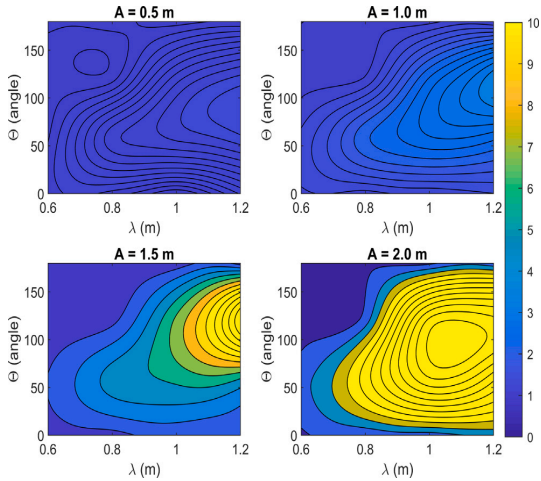


Fig. 18. Mean normalized UHC contour.

Fig. 19 shows the variations in torque from about 0 Nm to over 45000 Nm. Wave no. 1 did not significantly influence the input engine torque, and the variation only fluctuated between 35 000 to 38 000 Nm — an area very close to the demanded load. Wave no. 2 provided a higher and lower torque than Wave no. 1, but the wave frequency was almost one-sixth. The importance of the frequency can be seen when the engine attempts to compensate for the deviations. For wave no. 3, the input torque dropped suddenly to around 15 000 Nm and reached a maximum of 41 000 Nm. This abrupt reduction indicates that the propeller was partly above the water’s surface. Fig. 20 shows β , which is the input of the modeling as an indicator of the position of the propeller inside the water. Any number less than 1 means incomplete immersion of the propeller in the water. The quantity of β for the wave no. 4 reached 0, which implies the propeller was entirely out of the water. Thus, the input shaft torque reached 0 Nm for part of the time in each wave.

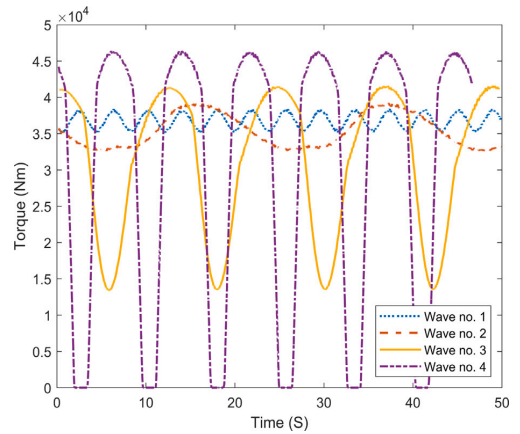


Fig. 19. Instantaneous torque variation of four separate waves with the maximum difference.

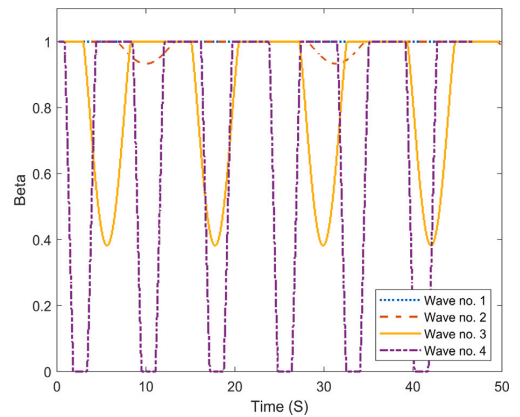


Fig. 20. Beta variation. An index of showing how immerse is the propeller.

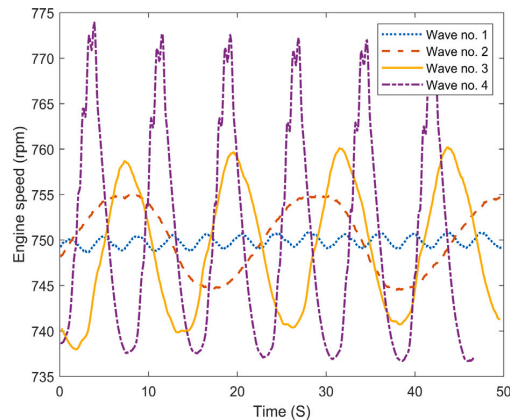


Fig. 21. Engine speed variation around the setpoint with an acceptable stability.

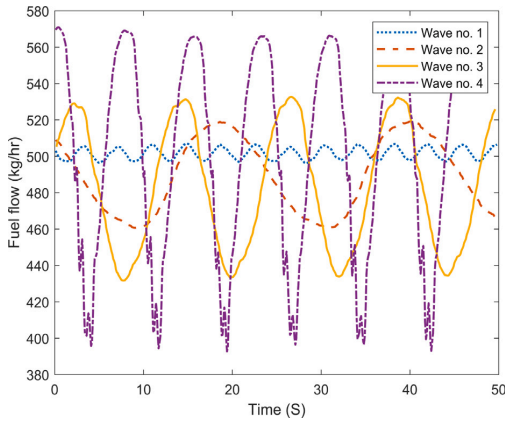


Fig. 22. The rate of natural gas fuel mixed with the intake air to keep the engine speed stable.

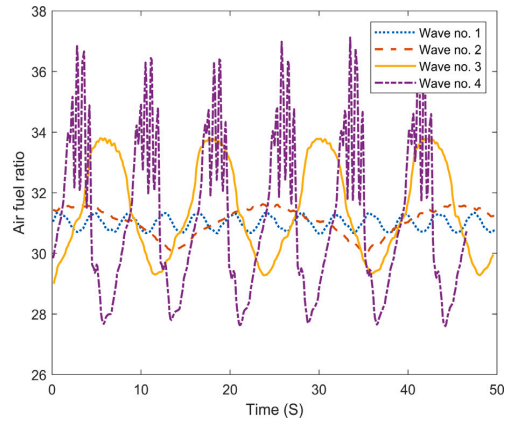


Fig. 25. Air-fuel ratio variation during transient condition with a lot of fluctuation with wave no.4.

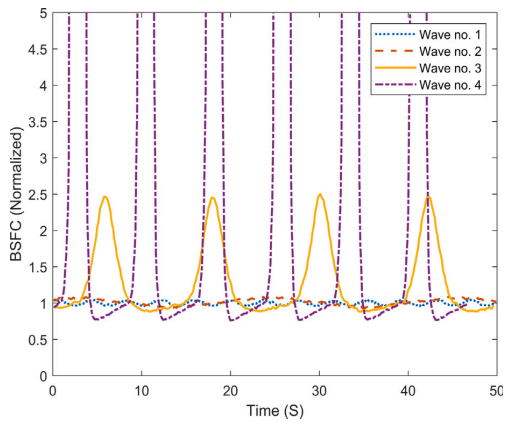


Fig. 23. Normalized BSFC with a sharp rise during load reduction.

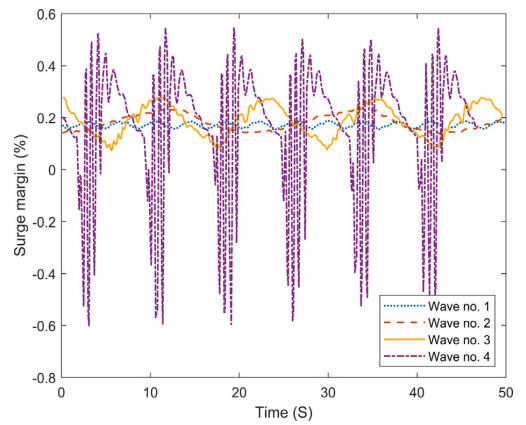


Fig. 26. Surge margin.

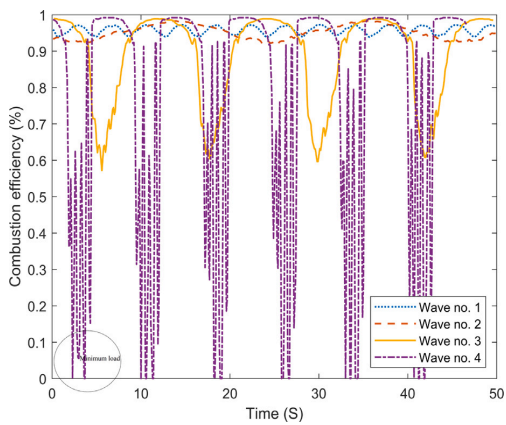


Fig. 24. Combustion efficiency variation and sudden reduction with the load decline.

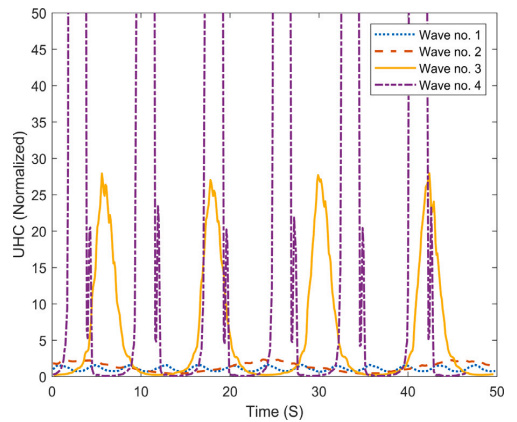


Fig. 27. Normalized UHC.

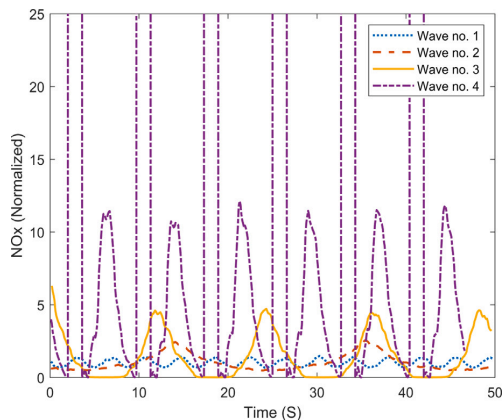


Fig. 28. Normalized NO_x .

Fig. 21 shows that due to the rapid response of the control system and high inertia of the shaft, the engine speed is highly stable with the load variation. After the react of the engine control system, as can be seen in Fig. 22, the fuel flow was significantly reduced in a short time. The fuel flow drop regulated the engine speed immediately and limited the over-speed state. Fig. 22 shows that the volume of fuel flow never reaches 0 to keep the engine running. Besides, the control system's resistance against sudden change contributes to achieving a stable engine in harsh working conditions.

Fig. 23 shows a gradual rise in the fuel consumption unit. During harsh conditions, the increased brake fuel consumption corroborates these earlier findings, where the fuel continued to release into the combustion chamber to prevent a shutdown. This increase in BSFC could also be attributed to combustion efficiency. The decline in the input load resulted in unstable combustion in the combustion chamber, as can be seen in Fig. 24. In the normal working area, combustion efficiency fluctuated around 95%, which is also proved by Heywood [37]. Load variation resulted in unstable combustion as well, which both increased and decreased efficiency. The slight increment of combustion efficiency appears during higher torque, with an almost flat curve. Moreover, the combustion efficiency dropped during the lower load and met a complete misfiring in wave no. 4. Comparing the two results of Figs. 24 and 19, it can be seen that the constant duration with a quantity of 0 is not equal. A good explanation of this phenomenon can be found in Fig. 25, where the air–fuel ratio during stable conditions is 31. This lean combustion helped to reach the minimum emission and maximum achievable combustion efficiency, while the burned mixture's pressure and the temperature never reached a critical point. This feature, however, showed a negative impact during the transient condition. With any sudden change of load, the air–fuel ratio moved away from the optimum border and, a very lean mixture was already in the main chamber. Since there was no connection between the diluted mixture and ignition timing, the spark plug worked based on the previous timing. The initial flame did not provide a stable propagated flame and resulted in misfiring in the worst cases. However, this high volume of air–fuel ratio was not delivered consistently by the turbocharger, and lots of variation around the setpoint between 32 and 36 could occur in each load cycle. For waves no. 1, 2 and, 3, the turbocharger delivered the required air with the least variation. By referring to Fig. 26, for the three first waves, we can see that the turbocharger operated in a safe area with surge margin always more than 0.1. However, for wave no. 4, the surge margin turned negative, meaning that the surge possibility was high. Surge margin shifting in the modeling was highly dependent on the amount of shaft inertia as well. Higher inertia may

have contributed to slowing response to any change, but it also made it stiffer in transient conditions. The graph shows that the engine will never encounter a working region outside the map — except in severe circumstances. It is worthwhile noting that the surge margin was calculated by Eq. (28):

$$\text{Surge margin}_{\text{fraction}} = \frac{\dot{m} - \dot{m}_{\text{Surge line}}}{\dot{m}_{\text{Surge line}}} \quad (28)$$

The importance of the sea waves on the mass of emission compounds is depicted in Figs. 27 and 28. The amount of unburned hydrocarbon from gas-powered ships during steady-state conditions in a well-designed chamber could be around 1 to 2% of fuel consumption. By looking at Fig. 27, we can see that the same proportion applied to the wave no. 1, even though the oscillation of UHC was not negligible. A wider range of variations also occurred for the wave no. 2, with a maximum of more than double the stable output. For waves no. 3 and 4, most of the fuel injected into the atmosphere without combusting and, the average quantity of UHC shows an almost 30 times increment. NO_x showed the same pattern for UHC, but contrasted during the time. However, wave no. 3 still had a normal quantity during the time, and wave no. 4 showed two peaks: a maximum value of 15 and a maximum of infinity. The limited value equal to 15 initiated of the burned mixture's temperature due to rich combustion when the air–fuel ratio became around 28 during the higher load. There was no specific definition for the second peak; however, it is assumed to originate from a numerical error during the communication steps.

In order to clarify the effect of sea waves on engine performance characteristics, the engine response with the highest load variation is displayed in Fig. 29. wave no. 4 was chosen, and a multiple-graph shows the wave torque at the top of the plot, and the engine speed, normalized BSFC, surge margin, air–fuel ratio, and combustion efficiency are presented from top to bottom, respectively. As can be seen, there was a direct correlation between load oscillation and engine performance uncertainty, except the engine speed. Moreover, it can be found that the influential primary part of the waves is the lower section of the waves when the load reduces. Although the higher loads may cause additional fuel consumption and NO_x , the lean-burn gas engines are highly affected by extra air than the setpoint value, and the extra air is only available during the load decrease.

5. Conclusion

This study discussed a validated ship propulsion simulation model, which stems from the need to know the natural gas engine's behavior under transient marine conditions — especially under severe loads. The engine's thermodynamic equations, proportional-integration method for the controller, and boundary-element method for the controllable pitch propeller behind ship conditions were all implemented. The measured data verified the engine model during steady-state and transient conditions. There was a good agreement between the simulated and measured data, which proves the model's accuracy above predicting new imposed waves. Several wavelengths, wave amplitudes, and wave directions were simulated to investigate the marine engine's performance and emission throughout the regular waves' full cycles. The results reported in this paper show that:

1. The input wave's configuration played a crucial role in the gas engine response, and, as a result, fuel consumption, combustion efficiency, and emission compounds are all influenced by sea waves compared with steady-state.
2. The system appropriately controlled the engine's speed, and the deviation from the desired setpoint was always on a minimum.
3. High probability of knock phenomenon and the high possibility of a surge of the turbocharger was determined during harsh conditions.

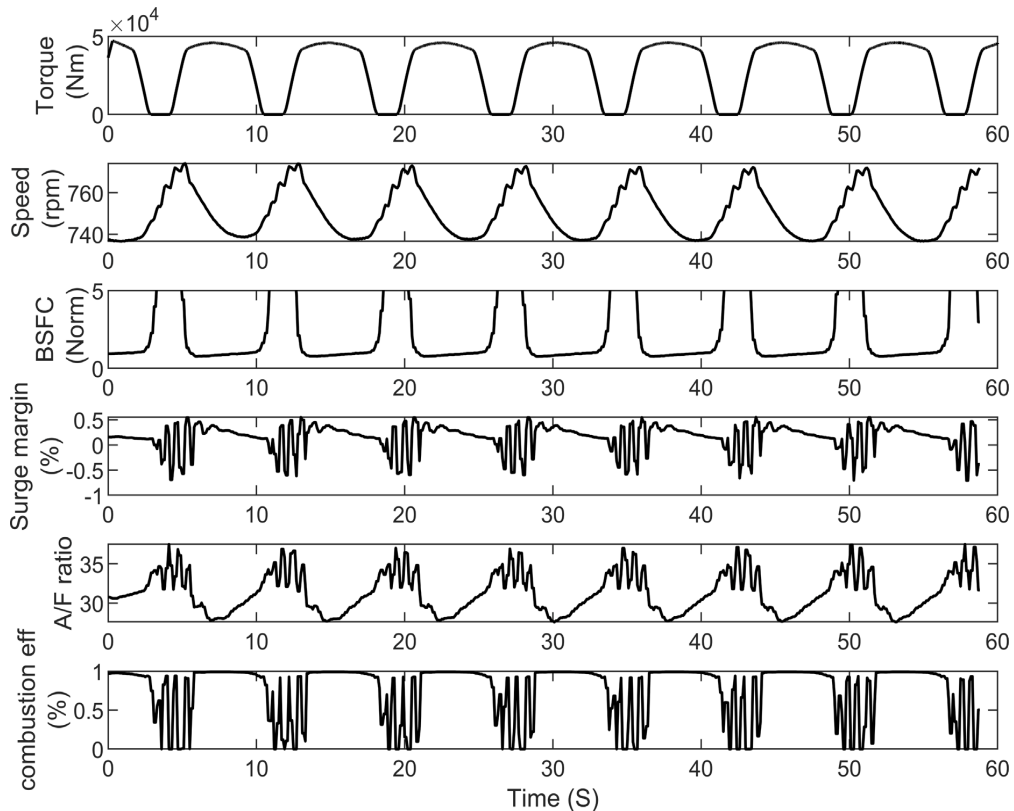


Fig. 29. Engine performance characteristic during highest torque variation.

- The combustion efficiency's reduction highlights that a considerable amount of unburned hydrocarbon emission discharges into the atmosphere due to misfire in many cycles of the severe waves.
- The use of natural gas for ship propulsion may offer a lower emission option than traditional fossil fuels in stationary combustion, but in sizeable oscillating sea waves, lean-burn gas engine stability and emission is debatable.

For improving the combustion stability in transient marine conditions, two practical methodologies are available:

- Utilizing the current technologies such as hybrid propulsion systems of combining the engine to the batteries, fuel cell, and even renewable energy sources for smoothing out the fluctuation of the load and optimizing the propulsion efficiency for the vessel with flexible power demand.
- Developing the available controlling systems to provide the optimum excess air ratio and prevent any misfiring.

Both methods have their pros and cons. A hybrid system usually costs more and requires a redesigning of the arrangement of the operating vessels. Developing the available controlling systems is less expensive and more straightforward, but the rapid response controller's application needs a comprehensive examination.

CRedit authorship contribution statement

Sadi Tavakoli: Conceptualization, Writing - original draft, Writing - review & editing, Formal analysis, Software. **Simone Saettone:** Conceptualization, Writing - original draft, Software. **Sverre Steen:** Conceptualization, Supervision. **Poul Andersen:** Conceptualization, Supervision. **Jesper Schramm:** Conceptualization, Writing - review & editing, Supervision. **Eilif Pedersen:** Conceptualization, Writing - review & editing, Supervision.

Declaration of competing interest

The authors declare that they have no known competing financial interests or personal relationships that could have appeared to influence the work reported in this paper.

References

- United Nations Conference on Trade and Development. *The review of maritime transport 2018*. 2018.
- Matthias Volker, Bewersdorff Ines, Aulinger Armin, Quante Markus. The contribution of ship emissions to air pollution in the North Sea regions. *Environmental Pollution* 2010;158(6):2241 – 2250.
- Ashfaq Ahmad, Sharma Pratiksha. Environmental effects of air pollution and application of engineered methods to combat the problem. *J Ind Pollut Control* 2012. [http://www.icontrolpollution.com/articles/environmental-effects-of-air-pollution-and-application-of-engineered-methods-to-combat-the-problem-
php?aid=45739](http://www.icontrolpollution.com/articles/environmental-effects-of-air-pollution-and-application-of-engineered-methods-to-combat-the-problem-
php?aid=45739).
- International Maritime Organization. [http://www.imo.org/en/OurWork/Environment/PollutionPrevention/AirPollution/Pages/Nitrogen-oxides-\(NOx\)-%E2%80%93-Regulation-13.aspx](http://www.imo.org/en/OurWork/Environment/PollutionPrevention/AirPollution/Pages/Nitrogen-oxides-(NOx)-%E2%80%93-Regulation-13.aspx).

- [5] Majewski W Addy, Khair Magdi K. Diesel emissions and their control. SAE International; 2006, ISBN: 978-0-7680-0674-2.
- [6] Resitoglu Ibrahim Aslan, Altinisik Kemal, Keskin Ali. The pollutant emissions from diesel-engine vehicles and exhaust aftertreatment systems. *Clean Tech Environ Policy* 2015;15-27.
- [7] Ushakov Sergey, Stenersen Dag, Einang Per Magne. Methane slip from gas fuelled ships: a comprehensive summary based on measurement data. *J Mar Sci Technol* 2019.
- [8] Global market insights. <https://www.gminsights.com/industry-analysis/marine-propulsion-engine-market>.
- [9] Campora U, Figari M. Numerical simulation of ship propulsion transients and full-scale validation. *Eng Mar Environ* 2002;217.
- [10] Kyrtatos NP, Theodosopoulos P, Theotokatos G, Xiros N. Simulation of the overall ship propulsion plant for performance prediction and control. 2007.
- [11] el Moctar Ould, Lantermann Udo, Mucha Philipp, Höpken Jens, Schellin Thomas E. RANS-based simulated ship maneuvering accounting for hull-propulsor-engine interaction. *Ship Technol Res* 2015;142-61.
- [12] Theotokatos Gerasimos P. Ship propulsion plant transient response investigation using a mean value engine model. *Int J Energy* 2008;2.
- [13] Altosole Marco, Campora Ugo, Figari Massimo, Laviola Michele, Martelli Michele. A diesel engine modelling approach for ship propulsion real-time simulators. *J Mar Sci Eng* 2019.
- [14] Yum Kevin Koosup, Taskar Bhushan, Pedersen Eilif, Steen Sverre. Simulation of a two-stroke diesel engine for propulsion in waves. *Int J Nav. Archit. Ocean Eng* 2016.
- [15] Taskar Bhushan, Yum Kevin Koosup, Steen Sverre, Pedersen Eilif. The effect of waves on engine-propeller dynamics and propulsion performance. *Ocean Eng* 2016;262-77.
- [16] Vrijdag A, Stapersma D, van Terwisga T. Systematic modelling, verification, calibration and validation of a ship propulsion simulation model. *J Mar Eng Technol* 2014.
- [17] Zhaoa Feiyang, Yanga Wenming, Tana Woei Wan, Choub Siaw Kiang, Yub Wenbin. An overall ship propulsion model for fuel efficiency study. In: *The 7th international conference on applied energy*. 2015, p. 813-18.
- [18] International Maritime Organization. Studies on the feasibility and use of LNG as a fuel for shipping. Technical report, 2016.
- [19] Johnson Derek R, Heltzel Robert, Nix Andrew C, Clark Nigel, Darzi Mahdi. Greenhouse gas emissions and fuel efficiency of in-use high horsepower diesel, dual fuel, and natural gas engines for unconventional well development. *Appl Energy* 2017;206:739-50.
- [20] Yousefi Amin, Birouk Madjid. Investigation of natural gas energy fraction and injection timing on the performance and emissions of a dual-fuel engine with pre-combustion chamber under low engine load. *Appl Energy* 2017;189:492-505.
- [21] YANMAR Technical Review. Dual-Fuel Marine Engine (Highly Reliable Environmentally Friendly Engine). https://www.yanmar.com/th/technology/technical_review/2015/0727_2.html.
- [22] Einewall Patrik, Tunestål Per, Johansson Bengt. Lean burn natural gas operation vs. Stoichiometric operation with EGR and a three way catalyst. *SAE* 2005. 2005-01-0250.
- [23] Chen SK, Beck NJ. Gas engine combustion principles and applications. *SAE* 2001. 2001-01-2489.
- [24] Cho Haeng Muk, He Bang-Quan. Spark ignition natural gas engines—A review. *Energy Convers Manage* 2007;48:608-18.
- [25] Pedersen Nicolai, Madsen Jan, Vejlggaard-Laursen Morten. Co-simulation of distributed engine control system and network model using FMI & SCNSL. In: 10th IFAC conference on manoeuvring and control of marine craft MCMC 2015. *IFAC-PapersOnLine* 2015;48(16):261-6.
- [26] Breunese APJ, Broenink JF, Top JL, Akkermans JM. Libraries of reusable models: theory and application. *Simulation* 1998;7-22.
- [27] Yum Kevin, Pedersen Eilif. Architecture of model libraries for modelling turbocharged diesel engines. *Math Comput Modell Dyn Syst* 2016.
- [28] Huang Lin, Cheng Gang, Zhu Guoqing, Li Dongliang. Development of a bond graph based model library for turbocharged diesel engines. *Energy* 2018;728-43.
- [29] Ciesla Christopher, Keribar Rifat, Morel Thomas. Engine/powertrain/vehicle modeling tool applicable to all stages of the design process. *SAE* 2000.
- [30] Yang Xiaolong, Liao Cheng, Liu Jingping. Harmonic analysis and optimization of the intake system of a gasoline engine using GT-power. *Energy Procedia* 2012;756-62.
- [31] Wei Chaoyi, Chen Mengqi, Jiang Yinjing. Electronic control fuel injection system based on GT-POWER and mototron. *Energy Procedia* 2016;773-9.
- [32] Sidorow Andreas, Isermann Rolf. Physical and experimental modeling of turbocargers with thermodynamic approach for calculation of virtual sensors. *France: Rueil-Malmaison*; 2012.
- [33] Colburn AP. A method of correlating forced convection heat transfer data and a comprasion with liquid frictions. *International Journal of Heat and Mass Transfer* 1964;7(12):1359 - 1384.
- [34] GT-SUITE. Flow theory manual. Technical report, Gamma Technologies; 2017.
- [35] Hiereth Hermann, Prenninger Peter. Charging the internal combustion engine. *Springer-Verlag Wien*; 2007, 1613-6349.
- [36] GT-SUITE. Engine performance. Technical report, Gamma Technology; 2017.
- [37] Heywood John B. Internal combustion engines fundamental. *New York: McGraw-Hill, Inc*; 1988.
- [38] Wikipedia. https://en.wikipedia.org/wiki/Thermal_conduction.
- [39] Wikipedia. https://no.wikipedia.org/wiki/Stefan-Boltzmanns_lov.
- [40] Woschni G. A universally applicable equation for the instantaneous heat transfer coefficient in the internal combustion engine. 1967.
- [41] Blizard Norman C, Keck James C. Experimental and theoretical investigation of turbulent burning model for internal combustion engine. *SAE* 1974;740191.
- [42] Cho Haeng Muk, He Bang-Quan. Spark ignition natural gas engines—A review. *Energy Convers Manage* 2007;608-18.
- [43] Warnatz J, Maas U, Dibble RW. Combustion physical and chemical fundamentals, modeling and simulation, experiments, pollutant formation. *New York: Springer*.
- [44] Speight James G. Chemistry and chemical technology. In: Speight James G, editor. *Handbook of industrial hydrocarbon processes*. Boston: Gulf Professional Publishing; 2011, p. 1-41 [chapter 1].
- [45] Tavakoli Sadi, Jensen Michael Vincent, Pedersen Eilif, Schramm Jesper. Unburned hydrocarbon formation in a natural gas engine under sea wave load conditions. *J Mar Sci Technol* 2020.
- [46] Lavoie GA. Correlations of combustion data for SI engine calculation-laminar flame speed, quench distance and global reaction rates. *SAE* 1978;(780229).
- [47] Kato K, Igarashi K, Masuda M, Otsubo K, Yasuda A, Takeda K, et al. Development of engine for natural gas vehicle. *SAE* 1999. 01-0574.
- [48] Zhen Xudong, Wang Yang, Xu Shuaiqing, Zhu Yongsheng, Tao Chengjun, Xu Tao, et al. The engine knock analysis - An overview. *Appl Energy* 2012;628-36.
- [49] Martinsen MA. An design tool for estimating the added wave resistance of container ships. 2016.
- [50] ITTC. Recommended procedures and guidelines: Speed and power trials, part 2 analysis of speed/power trial data. In: *International towing tank conference*. 2014. 7.5-04-01-01.2.
- [51] ITTC. Recommended procedures and guidelines: 1978 ITTC performance prediction method. In: *International towing tank conference*. 2017. 7.5-02-03-01.4.
- [52] Jensen JJ, Mansour AE, Olsen AS. Estimation of ship motions using closed-form expressions. *Ocean Eng* 2004;31(1):61-85.
- [53] Honkanen M. On the wave induced motions of ships. *The Swedish Academy of Engineering Sciences in Finland*; 1976.
- [54] Sasajima Hideo, Tanaka Ichiro, Suzuki Toshio. Wake distribution of full ships. *J Zosen Kiokai* 1966;1966(120):1-9.
- [55] Taskar B. The effect of waves on marine propellers and propulsion (Ph.D. thesis), Norwegian University of Science and Technology; 2017.
- [56] Regener PB. Hull-propeller interaction and its effect on propeller cavitation (Ph.D. thesis), Technical University of Denmark; 2016.
- [57] Saetone S, Taskar B, Regener PB, Steen S, Andersen P. A comparison between fully-unsteady and quasi-steady approach for the prediction of the propeller performance in waves. *Appl Ocean Res* 2020.
- [58] Minsaas K, Faltinsen O, Persson B. On the importance of added resistance, propeller immersion and propeller ventilation for large ships in a seaway. 1983
- [59] Saetone Simone, Tavakoli Sadi, Taskar Bhushan, Jensen Michael Vincent, Pedersen Eilif, Schramm Jesper, Steen Sverre, Andersen Poul. The importance of the engine-propeller model accuracy on the performance prediction of a marine propulsion system in the presence of waves. *Appl Ocean Res* 2020;103:102320.

Paper 4

Strategies on Methane Slip Mitigation of Spark Ignition Natural Gas Engine During Transient Motion

Sadi Tavakoli, Jesper Schramm and Eilif Pedersen

This paper is not included due to copyright available at
<https://doi.org/10.4271/2021-01-5062>

Paper 5

Influence of Turbocharger Inertia and Air Throttle on Marine Gas Engine Response

Sadi Tavakoli, Jesper Schramm and Eilif Pedersen

Influence of Turbocharger Inertia and Air Throttle on Marine Gas Engine Response

Sadi Tavakoli^{1,2,*}, Jesper Schramm², Eilif Pedersen¹

¹Department of Marine Technology, Norwegian University of Science and Technology
Address, Trondheim, Norway

²Department of Mechanical engineering, Technical University of Denmark
Address, Copenhagen, Denmark

*Sadi.tavakoli@ntnu.no

Abstract - Due to the current emission legislation, improving the marine propulsion system performance has received considerable notice. Employing natural gas as the primary energy source presented remarkable attention in the lean-burn mixture. Lean combustion enhances the thermal efficiency in a steady-state, but the engine in a transient marine condition encounters a time-varying load with high frequency and amplitude. The in-cylinder states during the transient conditions are pretty different from similar steady-state conditions. A significant part of this difference is the response time of the engine components. This study aimed to analyze the influence of the air throttle and the turbocharger mass moment of inertia. The examination was performed on a developed thermodynamics model of a spark-ignition engine. The model was verified with an imposed constant and transient load. The influence of the air throttle is discussed in a comparison of steady-state and transient conditions. The importance of turbocharger inertia is discussed with several coefficients on the mass moment of inertia.

The results show that the air throttle can restrict the extra air if the frequency is low or the engine works in a steady-state. The emission formation is also reduced with the throttle during lower loads of the steady-state, but the throttle has a negligible influence during the rapid transient condition. Moreover, changing the shaft inertia plays a dominant role in the engine mechanical delay and, consequently, the total engine response. Lower and higher inertia proposed on the engine model resulted in more and less variation on engine performance and emission formation, respectively. However, the engine long-term response is more relevant to the wave amplitude and frequency than the turbocharger characteristic.

Keywords: Natural gas engine, Marine propulsion system, Throttle valve, Turbocharger lag, Mechanical delay

© Copyright 2021 Authors - This is an Open Access article published under the Creative Commons Attribution License (<http://creativecommons.org/licenses/by/3.0>). Unrestricted use, distribution, and reproduction in any medium are permitted, provided the original work is properly cited.

Nomenclature

CO ₂	Carbon dioxide
EIVC	Early intake valve closure
NOX	Nitrogen oxides
SOX	Sulphur oxides
CO	Carbon monoxide
EGR	Exhaust gas recirculation
EIVC	Early intake valve closure
f _{mep}	Friction mean effective pressure
LNG	Liquid natural gas
PM	particulate matter
UHC	Unburned hydrocarbon

1. Introduction

In recent years the market has indicated more demand to clean and sustainable alternative fuels, and natural gas has been regarded as a clean fuel with wide availability. Burning natural gas has shown a remarkable reduction in emission compounds, including carbon monoxide (CO), nitrogen oxides (NO_x), and particulate matter (PM). With a higher ratio of Hydrogen to carbon in natural gas properties compared to conventional fossil fuel such as gasoline

and diesel fuel, the engine will produce even 20% less CO₂.

Shipping emissions are currently increasing, and due to the increase of global-scale trade, the trend gets even more in the future [1]. Moreover, the shipping industry's propulsion system plays a notable role in releasing hazardous emissions such as NO_x and SO_x [2,3]. LNG's utilization as the primary fuel of a lean-burn spark-ignition engine is one of the most promising solutions [4]. The lean-burn spark-ignition gas engine is Otto cycle theory working with an excess air ratio in the scale of lambda 2. This excess air reduces the engine components' thermal load during the combustion phenomenon and creates a steep decline in the NO_x compound [5]. In contrast to the lean combustion's earlier advantages, however, the emitted methane from the primary combustion due to incomplete combustion is considerable. This emission formation exposes a global warming potential 28 times higher than CO₂ in 100 years time scale [6].

In the marine propulsion system, the time-varying wakefield creates fluctuating engine loads, which may differ considerably from the time-invariant engine torque estimated in steady conditions. Providing a stable operational condition gets even worse when the engine torques and the thermal load are low. Supplementary control of the airflow by an air throttle to restrict the extra air improves the flame quality. This additional control is performed in the pioneer manufacturers as well [7].

The effect of intake throttling has been studied predominantly on the CI and SI engines [8,9]. The intake-throttling device enhanced EGR injection by reducing the pressure behind the intake valve, and it effectively accelerated the natural gas combustion [10]. In contrast, due to the pumping losses caused by partially opened of the throttle in the air passage, the engine's efficiency decreased during lower loads. Therefore, using early intake valve closure (EIVC) on intake valves was proposed to improve the combustion quality in direct injection gasoline engines. Ojapah et al. [11] developed this idea by testing a single-cylinder engine and concluded that EIVC contributed to combustion efficiency improvement. The drawback was increasing the UHC formation due to slower combustion compared with throttle control. In addition to the requirements to

examine the effect of the air throttle on engine response, the mechanical delay or the turbocharger lag is a notable off-design feature of the turbocharged engines during the transient condition. This feature distinguishes the response of the engine in transient condition with the steady-state. If all the differences are classified in thermal delay, mechanical delay, and dynamic delay, part of the mechanical delay is associated with the turbocharger lag. It is agreed that when the engine is under transient operation, the energy transported by the exhaust gases arrives very quickly at the turbine [12], even with the fastest feedback caused by the fuel system to compensate for the deviation of the torque or demanded speed, the compressor air-supply cannot match this higher fuel-flow instantly [13]. For the lean-burn gas engine, this lag led the mixture to a lower value during load increment and a higher value during load decrement [14]. Since the combustion of the lean-burn spark-ignition engines is critically sensitive to the air excess ratio, this phenomenon reduces the combustion efficiency and increases the NO_x.

This study evaluated the air throttle influence during lower loads in steady-state and transient conditions by returning to the hypothesis posed in this section. Moreover, the turbocharger lag is also modeled and discussed throughout a marine time-varying load. Thus, a thermodynamic engine model was developed to model a marine gas engine. The engine was simulated with an imposed constant torque for the steady-state condition, and two imposed changeable torques for the transient state. In the next sections, the modeling procedure is first presented in Section 2, and the primary output is verified with the engine measured data. The imposed loads are presented in Section 3, and the throttle assessment in lower loads plus the turbocharger lag is discussed in Section 4. The conclusion is expressed in Section 5.

2. Simulation Method

2.1. Implemented Equations

A thermodynamic model was performed by GT-suite 2019 software. This program simulated the dynamic of the inlet and outlet gases, turbocharger performance, and combustion flame characteristics. Depending on the model's type, the simulation could be predictable, semi-predictable, or non-predictable

[15]. The thermodynamic process model commenced from the atmosphere with a boundary inlet temperature and sea level pressure. It was continued to the compressor with an implemented performance map or look-up table from the manufacturer. The converted thermodynamic energy from the turbocharger mechanical shaft provided a high boost pressure and the inlet air temperature. A charge air cooler received the high-temperature air at the entry, and it delivered the low temperature air with some pressure drop. In order to simulate the dynamics of the airflow in the pipes, the equations of momentum were derived together with energy and mass conservation in the discretized volume. To estimate the mass flow rate over the intake and exhaust valves, a one-dimensional isotropic flow analysis for compressible flow through a flow restriction was performed [16].

Combustion was modeled in all the cylinders by implementing the flame propagation model [17], and the emission formation was calculated using the proposed reaction rates for the species estimated in the equilibrium for the essential species, such as N_2 , O_2 , CO_2 . Afterward, the burned gas was passed via the exhaust valves and exhaust ports. The high enthalpy gas of the exhaust carries considerable thermal energy, and it drives the turbine to generate torque to rotate the connecting shaft and compressor. Then, the low enthalpy gas discharges into the atmosphere, and the cycle becomes complete. The specification of the marine engine is presented in Table 1.

Table 1: Engine specification

Item	unit	amount
Number of cylinders	-	9
Cylinder bore	mm	350
Cylinder stroke	mm	400
Connecting rod	mm	810
Maximum power	kW	3940
Rated speed	rpm	750
Maximum Torque at rated speed	Nm	50200
Fuel type	-	Natural gas

A detail of the implemented equations was presented in work by these authors in [18]. The available measured data, such as sea boundary condition, wall temperatures, spark plug locations, and timings were all imposed in the simulation model. A

schematic of the engine modeling and the air throttle position is shown in Fig. 1. Due to the importance of the flow modeling in predicting the dynamic and mechanical delay of the engine response, these two items are developed in this section. Further modeling can be found in [19].

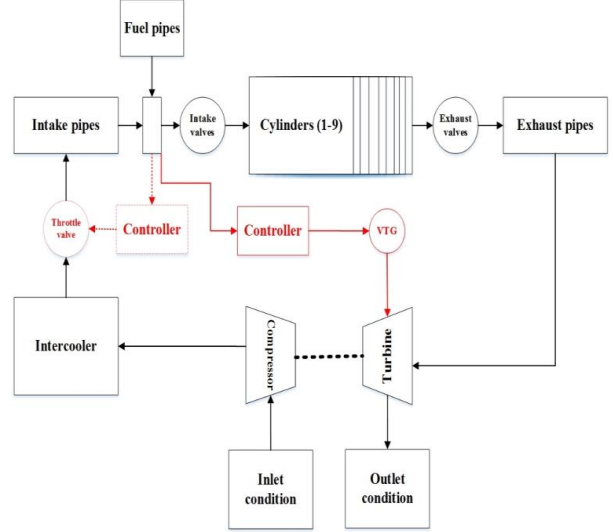


Fig. 2: Decomposition of the engine modelling

To calculate the dynamic delay of the fluid flow and consequently the turbocharger response, the equations of conservation are involved the conservation of momentum as well as Equation (1) and (2) [20].

$$\frac{dm}{dt} = \sum_{boundaries} \dot{m} \quad (1)$$

$$\frac{dme}{dt} = -\rho \frac{dv}{dt} + \sum_{boundaries} (\dot{m} H) - hA_S (T_{fluid} - T_{wall}) \quad (2)$$

$$\frac{d\dot{m}}{dt} = \frac{dPA + \sum_{boundaries} (\dot{m}u) - 4C_f \frac{\rho u |u| dx}{2} - K_p (\frac{1}{2} \rho u |u|) A}{dx} \quad (3)$$

Where m is mass of volume, and \dot{m} is the boundary mass flux. A is the cross-sectional flow area, and A_S is the heat transfer surface area.

In the discretized volume, the Equation (1) and (2) yield the mass and energy in each volume. With the available volume and mass, the density can be calculated. Afterward, the equations of state define

density and energy as a function of pressure and temperature, and the solution will be continued iteratively on pressure and temperature until they satisfy the density and energy already calculated for this time step.

A turbocharger consists of three components: The turbine, the compressor, and the connecting shaft. These components have a mass moment of inertia, which is influential in the turbocharger rotational speed. The higher the moment of inertia, the more time to reach the new stable speed. The rotational speed is a function of pressure ratio, efficiency, and flow rate of compressor and turbine. Thus, a performance map from the manufacturer is imposed on the modeling. Turbocharger speed and pressure ratio are predicted at each time-step, and two other unknowns are taken from the look-up table [21].

The calculation starts with Equation (4) and predicted pressure ratio and calculating total temperature by Equation (5).

$$\Delta h_S = C_p T_{total,in} (PR^{\frac{\gamma-1}{\gamma}} - 1) \quad (4)$$

$$T_{total,in} = T_{in} + \frac{u_{in}^2}{2C_p} \quad (5)$$

where u_{in} is inlet velocity. The outlet enthalpy will be calculated by Equation (6) and the compressor power by Equation (7) provide subsequently the torque of the compressor.

$$h_{out} = h_{in} + \frac{\Delta h_S}{\eta_s} \quad (6)$$

$$P = \dot{m} (h_{in} - h_{out}) \quad (7)$$

where subscript in, out and s stands for inlet, outlet and isotropic, respectively. Using equations (8), the new calculated rotational speed is provided.

$$\Delta \omega = \frac{\Delta t (T_{turbine} - T_{compressor} - T_{friction})}{I} \quad (8)$$

For the turbine, the following equations are employed:

$$\Delta h_S = C_p T_{total,in} (1 - PR^{\frac{1-\gamma}{\gamma}}) \quad (9)$$

$$h_{out} = h_{in} - \eta_s \Delta h_S \quad (10)$$

The computation will be repeated until the predicted parameters reach an acceptable convergence.

2.2. Validation

The model is validated both in steady-state and in transient conditions. Comparing experimental and simulation output verifies that the model could accurately predict the engine performance and emission compounds. Table 2 presents the validation for a steady-state. Normalized BSFC for performance prediction and normalized UHC for emission prediction is given. As can be seen, there is always a negligible difference between the modeling and the measured data. In the worst case, the deviation for UHC in 75% load is 8.3%, and it is still acceptable.

Furthermore, Fig. 2 shows that during the in almost 300 seconds of the load variation of the transient condition, the operating engine tried to maintain on 750 rpm, and the modeling is also showing the same trend with a minor difference. Fig. 3 presented the fuel flow rate. This figure displays an acceptable agreement of the simulation results with the time-varying load. There is a difference between the modeled flow rate and the operational value, but this deviation is almost constant during the time. The main reason for this difference could be the difference in modeling the friction of the components, such as friction in the cylinders as f_{mep} . This friction was assumed to be constant during the time-varying load in the engine modeling.

Table 2: Engine model verification during the steady-state with a comparison of measured and simulated data.

Load (%)	Torque (Nm)	BSFC (Normalized)			UHC (Normalized)		
		Measured	Theory	Deviation (%)	Measured	Theory	Deviation (%)
100	50200	1	1	0	1	1	0
85	42670	1.029	1.018	1	1.11	1.05	5.4
75	37650	1.045	1.034	1	1.20	1.10	8.3
50	25100	1.089	1.108	-1.7	1.37	1.30	5.1
25	12500	1.374	1.334	2.9	2.01	2.01	0.5

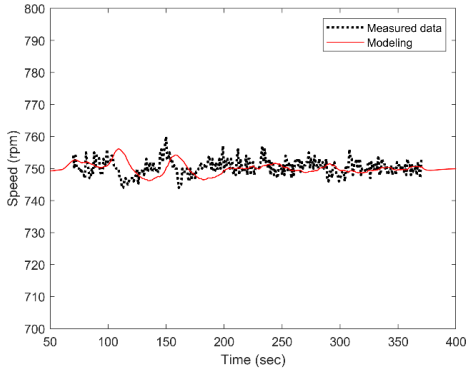


Fig. 2: Engine speed variation on 750 rpm and comparison with the measured data shown by dotted curve.

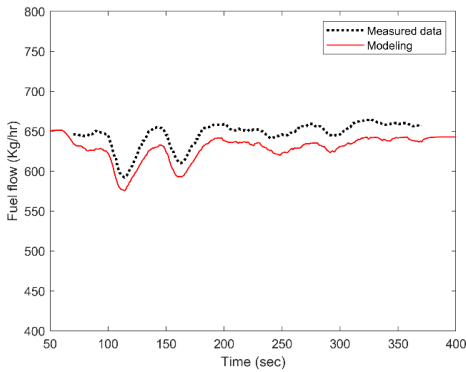


Fig. 3: Fuel flow comparison between measured data and simulated model

3. Implemented Steady and Transient Torque

In order to evaluate the significance of throttle in the lower loads of a lean-burn spark-ignition gas engine, two operating loads were studied, steady-state and unsteady state.

For the steady-state condition, the implemented load reduced from 100% to 50%, 25%, 20%, 15%, 10% and 5%. 100% and 50% mean 50000 and 25000 Nm, and the airflow is regulated with the standard variable turbine geometry (VTG) controller. In the 25% load and less, which are 12500 Nm and less, the throttle also regulated the amount of airflow. The throttle controller consisted of a conventional PID controller with two sensors from air and fuel pipes to calculate the ratio and one actuator to change the

throttle valve degree between 0 to 90. The load-time curve for steady-state is shown in Fig. 4.

An identical controlling pattern of VTG and throttle was utilized for the transient condition. The estimated harmonic load against harsh weather conditions is shown in Fig. 5. A ship traveling in various wavelengths, wave amplitudes, and wave directions influences the wave size and changes the thrust and torque fluctuations. More detail of the wave calculation is presented in [22]. This wave amplitude and frequency satisfied our requirement for modeling the marine engine in a broad spectrum of loading. The brake torque changed from a constant value of 36000 Nm in the second 180 to almost 45000 Nm and then reduced to zero. The wave period was nearly seven seconds, which has around four seconds for the higher loads, and fewer than three seconds for the loads less than 30%, the duration when the throttle is active.

In addition, another wave characteristic was considered for the turbocharger lag assessment. This wave has a lower frequency and amplitude; then, it is more understandable to recognize the mechanical lag caused by the turbocharger. The implemented wave is shown in Fig. 6.

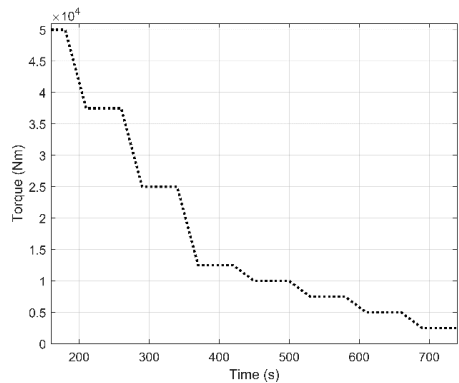


Fig. 4: Implemented steady-state loading for throttle assessment.

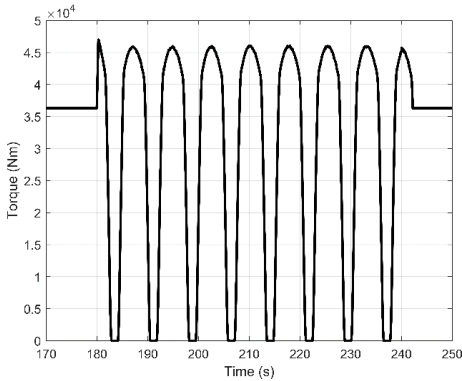


Fig. 5: Implemented dynamic loading calculated by a wave amplitude of two meters for throttle assessment.

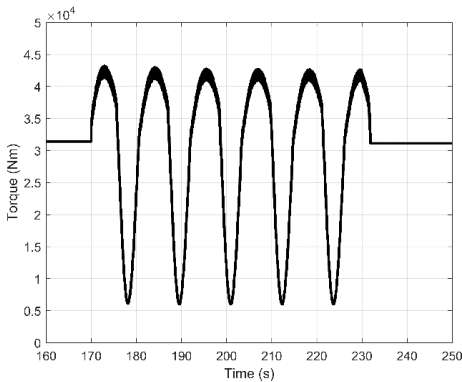


Fig. 6: Implemented dynamic loading for examining the turbocharger lag.

4. Results and Discussion

The nominal engine speed of 750 rpm was chosen for the modeling. The engine speed operated around the constant value by adjusting the fuel rack position with a PID controller. The result section is divided into two parts. First, the impact of the air throttle is discussed during the steady-state and transient conditions. Afterward, the turbocharger lag is presented by considering several inputs to the mass moment of inertia. The inertia's base value is considered one, and the others are relative values with the coefficients of 0.5, 0.75, 1.25, 1.5, and 2.

4.1. Throttle Assessment

Fig. 7 illustrates the air-fuel ratio comparison in a steady-state with and without throttle. A target setpoint, which is a constant quantity of 31, was also shown. As can be seen, during steady-state with a throttle, the air-fuel ratio stayed equal to the setpoint. However, there was an exception with the 25% load. This deviation may stem from numerical error and is negligible. While without the throttle, the ratio grew up to 34 during lower loads. This ratio is extremely lean for stable combustion, and it results in quenching the flame. Fig. 8 shows that the combustion efficiency reduces during the lower load if there was no throttle on the air passage. Besides, with the throttle, combustion efficiency lingered almost constant with load change since the air-fuel ratio was consistent.

In contrast, Fig. 9 shows that using a throttle during the transient load was not adequate for regulating the amount of air. This is indicated in the figure using a circle. Therefore, the excess ratio always exceeded the setpoint with or without throttle. The combustion efficiency also shows the same pattern, as shown in Fig. 10. Referring to the frequency of the waves in Fig. 5 and based on the results, we can conclude that this small time scale is extremely short for the throttle to turn into convergence. Therefore, for such high-frequency waves, a device with a more rapid response is needed to provide acceptable stability.

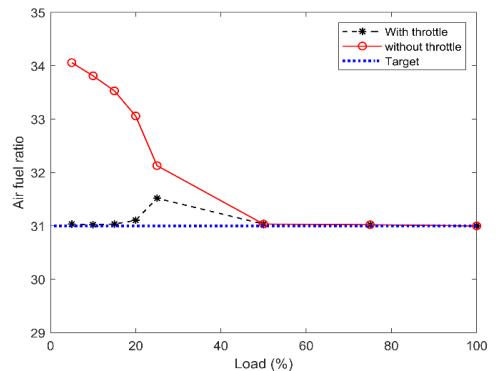


Fig. 7: Air fuel ratio variation during steady-state

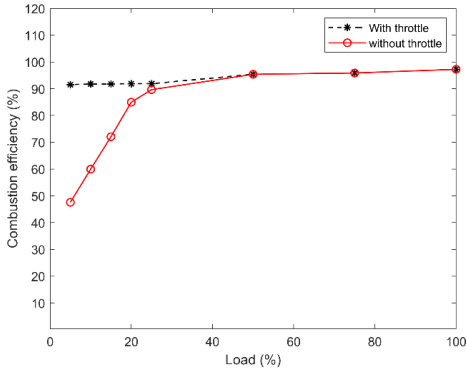


Fig. 8: Combustion efficiency during steady-state

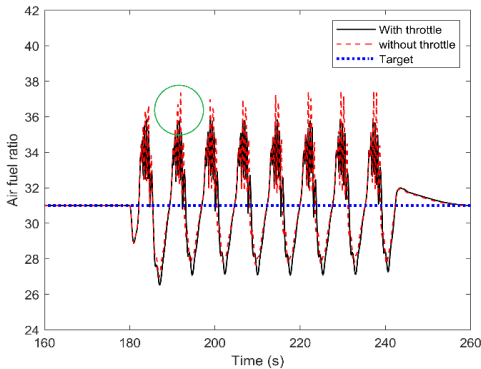


Fig. 9: Air fuel ratio variation during transient condition

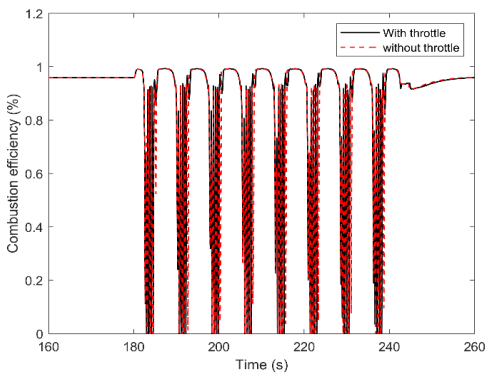


Fig. 10: Comparison of combustion efficiency in the engine with and without throttle during transient condition

The data obtained for the emission formation, NO_x and UHC, are broadly consistent with the performance output's major trends. Fig. 11 and Fig. 12 displayed the variation of unburned hydrocarbon in these two operational modes, with and without throttle. These authors' previous work [14] revealed that the UHC compound directly correlates with the air-fuel ratio, and a higher amount of excess air ratio deteriorated the combustion quality and resulted in the flame quench. Besides, flame quench was one of the three primary UHC sources in lean-burn spark-ignition gas engines together with gas exchange and crevice volume. Therefore, a significant part of the fuel remained unburned when the excess ratio increased to a value more than the setpoint. When the load declines, the fraction of unburned fuel will increase as well. As shown in Table 2, the measure data proved that the UHC quantity in 25% load is doubled compared with 100% load. Following the same trend in Fig. 11 shows seven times UHC increases with a 5% load when the engine is working in steady-state and with the throttle. Skipping the throttle may increase the UHC up to 80 times higher value. This amount of unburned fuel results in almost twice fuel consumption during the lower loads. Hence, the significance of using a throttle during lower loads can be proved in the emission aspect as well, even though it is not beneficial in transient conditions, as shown in Fig. 12.

Furthermore, NO_x showed a contrast procedure compared with the UHC compound, as shown in Fig. 13 and Fig. 14. This emission compound is deeply relevant to the flame temperature [16]. With a higher air-fuel ratio, the combustion chamber's thermal load declined, and the amount of NO_x was reduced. It worth mentioning that in Fig. 13, there is a sudden reduction for the 25% load for the engine output with a throttle. Part of this reduction of NO_x stems from the unexpected higher air-fuel ratio, as was mentioned in Fig. 7.

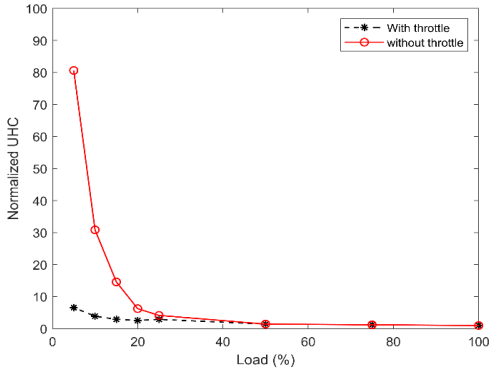


Fig. 11: Normalized unburned hydrocarbon formation during the steady-state.

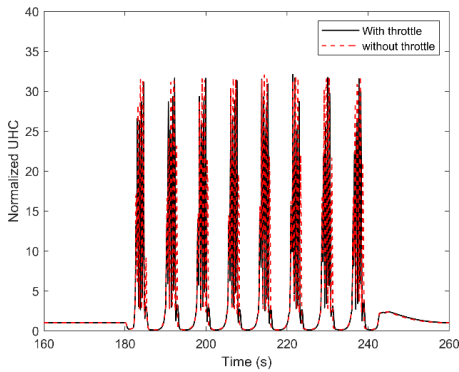


Fig. 12: Normalized unburned hydrocarbon formation during the transient condition.

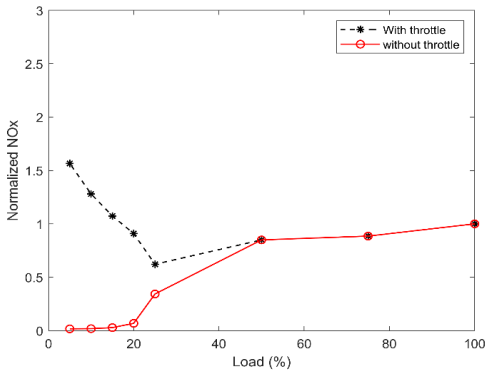


Fig. 13: NO_x formation during steady state

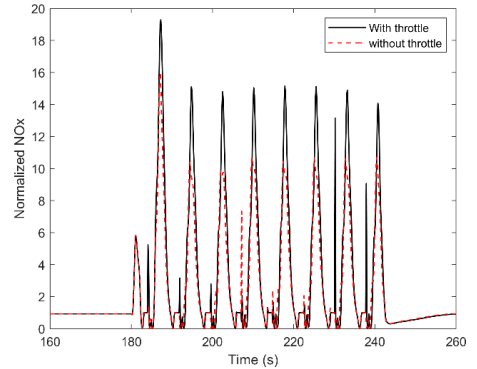


Fig. 14: NO_x formation during transient condition

4.2. Turbocharger Inertia

The previous section about transient engine operation clearly showed the engine mechanical and dynamic delay with the corresponding variation in implemented torque during the transient times. The modeled engine that is the object of this study has input inertia equal to the manufacturer's value. A different value for the inertia is assumed to predict a more accurate evaluation of the turbocharger lag. Both the increment and decrements of the inertia influence the lag of the turbocharger by changing turbocharger speed. The turbocharger rotational speed is shown in Fig. 15.

For clear visibility, part of the wave is presented. During the load variation, the shaft rotational speed varies between 19000 to 23000. This domain is almost constant for all of the inertia. It shows that the other components dynamic and the magnitude of the waves are crucial governors on engine performance when the engine response is on an investigation. However, in a short time scale, the small scale variation occurs when the load decreases. The inertia, with a coefficient of 0.5, has the most considerable oscillation. During the load increment, all of the cases have a smooth response to the load.

The turbocharger with a coefficient of 2.0 has the least oscillation, but the turbo speed is the highest throughout the time. This means that the total speed reduction for the high inertia is the lowest. Almost the same approach is obtainable for the boost pressure in Fig. 16. During the load increment, all the cases have

the same boost pressure, while during the load reduction, more drop and more fluctuation is achieved by low shaft inertia. Moreover, this figure confirms that the available turbocharger shaft inertia, coefficient 1, is chosen correctly. The blue line has the minimum difference with higher inertia but a noticeable distance to the lower inertia. This proves that increasing the shaft inertia will not contribute to a remarkable enhancement of boost pressure.

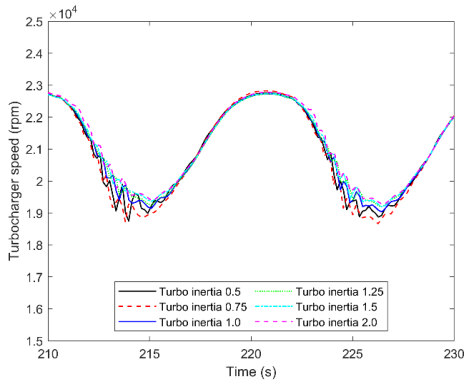


Fig. 15: Turbocharger rotational speed variation with various shaft moment of inertia.

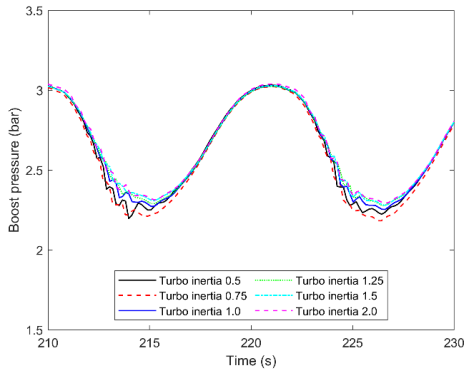


Fig. 16: Boost pressure after intercooler. A higher shaft inertia gives less fluctuation on boost pressure during load reduction.

The oscillation of the turbocharger and its influence on the air-fuel ratio is visible in Fig. 17. The air-fuel ratio is continually reducing during load increment, and there is a negligible difference between

the cases. However, the response is different during lower loads, in this figure for the seconds between 210-216 and 222 to 226. The turbocharger inertia with a coefficient of 0.5 with the black line gives a huge oscillation in the time scale of seconds. With an engine speed of 750 rpm, the different air-fuel ratios in different subsequent cycles are possible. It can be more noticeable if the intake manifold and the fluid dynamic do not distribute the flow equally. As a consequence, there would be lots of variation between the cycles and the cylinders.

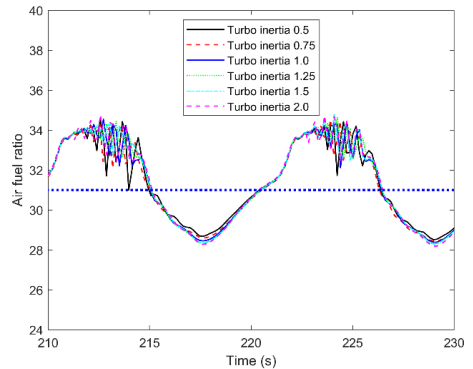


Fig. 17: Air fuel ratio with a striking variation on lower loads. This variation is relevant to the turbocharger stability to prevent any surge phenomenon.

Considering the combustion efficiency in Fig. 18, as the fraction of the burned fuel to the total injected fuel, and thermal efficiency in Fig. 19, as the fraction of brake work to the total injected energy, there are striking variations. With increasing the turbocharger lag, the variation reduces, and the engine moves toward more stable combustion. This output clears how vital is the turbocharger performance on combustion efficiency, thermal efficiency, and stability of the engine during the transient marine condition. However, the total fuel consumption and the fuel flow average are almost constant for all cases. BSFC is shown in Fig. 20, and it is hardly possible to figure out the differences between the simulation cases. The noticeable output from this figure is the variation of the BSFC during the marine wave, where it increased from a normalized value of one to more than 5. The

BSFC of the times before 170, as steady-state, was chosen for normalizing.

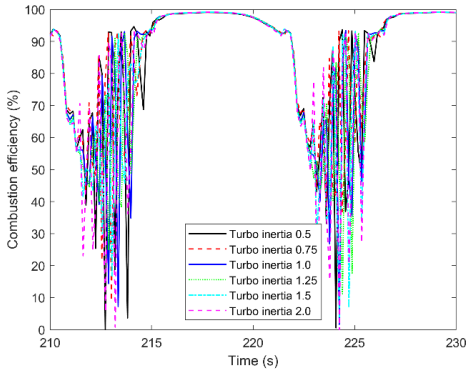


Fig. 18: Combustion efficiency showing the burned fuel fraction. A sudden drop to even zero is probable if the shaft inertia is too low.

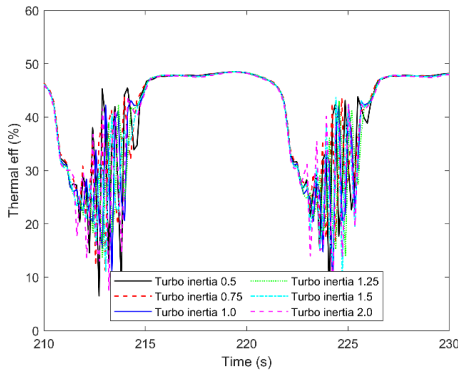


Fig. 19: Thermal efficiency drops with more air excess ratio and is almost constant with high loads.

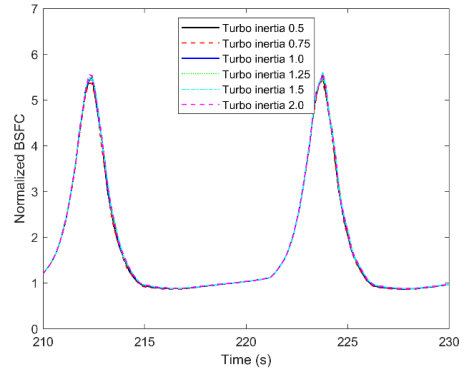


Fig. 20: Brake specific fuel consumption.

The same normalizing value was chosen for NO_x and methane slip, UHC. The UHC is defined as the unburned fuel of the combustion chamber, which has not participated in the main combustion and post-oxidation. It is used to evaluate how well a gas engine converts the natural gas to work and heat. This compound is a function of fuel-burning rate and main chamber temperature. When the air excess ratio increases, the burning rate of natural gas reduces, and the maximum temperature decreases: the extra air leads more lean mixture and further temperature reduction. Consequently, lots of the fuel will not burn during the main combustion process, and since the temperature during post oxidation is low, a striking increase of the methane slip is achievable. Comparing the air-fuel ratio in Fig. 17 and Fig. 21 confirms how influential is the air excess ratio. UHC increase to 100 means 100 times more quantity than the nominal value in steady-state. This is one of the main reasons for BSFC increase during lower loads. If this additional fuel is trapped in the chamber or be controlled before the load reduction, fuel consumption reduces significantly.

In contrast with the UHC, even though the higher inertia improved the engine combustion during load reduction, the engine's lag during load rise resulted in a richer mixture and extra maximum temperature. The higher temperature forms a more quantity of NO_x , and for this reason, there is more NO_x with the highest shaft inertia during load increment, the time between

216 to 222. Moreover, similar to the other figures, the long time scale variation of NO_x is in the same frequency as the other figures, and it changes from almost 0 in low loads to 7 in high loads. The trend is shown in Fig. 22.

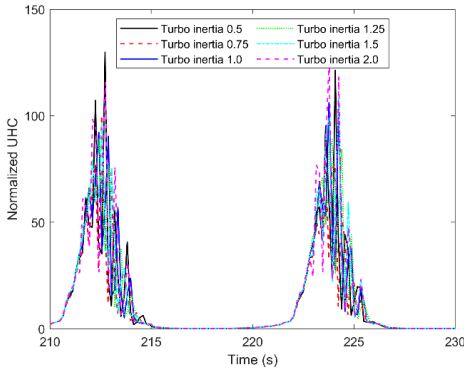


Fig. 21: Unburned hydrocarbon formation. The load sudden reduction resulted into higher fraction of fuel as unburned and leave the combustion chamber without participating the main combustion and post-oxidation.

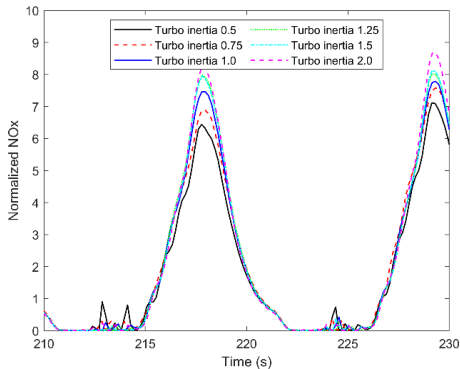


Fig. 22: NO_x formation. NO_x has a non variable value during lower loads due to lower temperature, while it increased to more than 7 times of steady-state. The higher the inertia, the higher the NO_x formation.

5. Conclusion

This work emphasized the engine performance, i.e., the dynamic response, combustion efficiency, and emission resulting from the constant load and oscillating propeller load. There was a particular interest in examining the throttle adjustment and turbocharger lag on the engine response. A thermodynamic spark-ignition engine model was developed, and based on the findings presented in this paper; the results can be summarized as:

- The engine was effectively regulated with the throttle during lower loads of the steady-state. The throttle exceptionally determines the fuel consumption and the emission formation and uninstalling the throttle valve results in incomplete combustion and lots of unburned hydrocarbons.
- For the transient condition when the frequency is high, the throttle did not recover the engine characteristics during lower loads. It was shown that the time scale of the throttle angle for the newly adjusted setpoint was longer than the waves' period.
- The created delay in providing the new throttle angle restricted a rapid response by the engine, especially in harsh weather conditions. Therefore, the application of the throttle valve in the fast-transient state is worthless.
- The mass moment of inertia directly influences the turbocharger speed and, consequently, boosts pressure and airflow.
- The lower the mass moment of inertia, the less stability on the turbocharger. This led the engine to fluctuate significantly due to variation in air excess ratio.
- A very high mass moment of inertia may improve the engine response when the load drops, but during load increment, the more lag resulted in higher NO_x formation due to increased response time.

References

- [1] M. Viana, P. Hammingh, A. Colette, X. Querol, B. Degraeuwe, I. de Vlieger, and J. van Aardenne, "Impact of maritime transport emissions on coastal

- air quality in europe,” *Atmospheric Environment*, vol. 90, pp. 96 – 105, 2014.
- [2] E. Fridell, E. Steen, and K. Peterson, “Primary particles in ship emissions,” *Atmospheric Environment*, vol. 42, no. 6, pp. 1160 – 1168, 2008.
- [3] V. Matthias, I. Bewersdorff, A. Aulinger, and M. Quante, “The contribution of ship emissions to air pollution in the north sea regions,” *Environmental Pollution*, vol. 158, no. 6, pp. 2241 – 2250, 2010. *Advances of air pollution science: from forest decline to multiple-stress effects on forest ecosystem services.*
- [4] S. Ushakov, D. Stenersen, and P. M. Einang, “Methane slip from gas fuelled ships: a comprehensive summary based on measurement data,” *Journal of Marine Science and Technology*, vol. 24, no. 4, pp. 1308–1325, 2019.
- [5] D. Stenersen and O. Thonstad, “Ghg and nox emissions from gas fuelled engines: Mapping, verification, reduction technologies,” Tech. Rep. OC2017 F-108, SIN-TEF Ocean AS, NO-7465 Trondheim NORWAY, 2017.
- [6] T. I. P. on Climate Change, “Global warming potential values,” 2016. IPCC Fifth Assessment Report.
- [7] “Project guide: Bergen engine type b, fuel gas operation,” tech. rep., Bergen Engines AS, 2018.
- [8] J. Reiß, C. Stürzebecher, C. Bohn, F. M’arzke, and R. Frase, “A diesel engine model including exhaust flap, intake throttle, lp-egr and vgt. part i: System modeling,” *IFAC-Papers On Line*, vol. 48, no. 15, pp. 52 – 59, 2015. 4th IFAC Workshop on Engine and Powertrain Control, Simulation and Modeling E-COSM 2015.
- [9] V. B. Pedrozo, I. May, T. D. Lanzanova, and H. Zhao, “Potential of internal egr and throttled operation for low load extension of ethanol–diesel dual-fuel reactivity controlled compression ignition combustion on a heavy-duty engine,” *Fuel*, vol. 179, pp. 391 – 405, 2016.
- [10] J. You, Z. Liu, Z. Wang, D. Wang, Y. Xu, G. Du, and X. Fu, “The exhausted gas recirculation improved brake thermal efficiency and combustion characteristics under different intake throttling conditions of a diesel/natural gas dual fuel engine at low loads,” *Fuel*, vol. 266, p. 117035, 2020.
- [11] M. Ojapah, Y. Zhang, and H. Zhao, “Part-load performance and emissions analysis of si combustion with eivc and throttled operation and cai combustion,” in *Internal Combustion Engines: Performance, Fuel Economy and Emissions*, pp. 19– 32, Woodhead Publishing, 2013.
- [12] N. Watson and M. S. Janota, *Introduction to Turbocharging and Turbochargers*, pp. 1–18. London: Macmillan Education UK, 1982.
- [13] C. Rakopoulos, A. Dimaratos, E. Giakoumis, and D. Rakopoulos, “Evaluation of the effect of engine, load and turbocharger parameters on transient emissions of diesel engine,” *Energy Conversion and Management*, vol. 50, no. 9, pp. 2381 –2393, 2009.
- [14] S. Tavakoli, M. V. Jensen, E. Pedersen, and J. Schramm, “Unburned hydrocarbon formation in a natural gas engine under sea wave load conditions,” *Journal of Marine Science and Technology*, 2020.
- [15] GT-SUITE, “Flow theory manual,” tech. rep., Gamma Technologies, 2017.
- [16] J. B. Heywood, *Internal Combustion Engines Fundamental*. New York: McGraw-Hill, Inc, 1988.
- [17] N. C. Blizzard and J. C. Keck, “Experimental and theoretical investigation of turbulent burning model for internal combustion engine,” *SAE*, p. 740191, 1974.
- [18] S. Tavakoli, E. Pedersen, and J. Schramm, “Natural gas engine thermodynamic modeling concerning offshore dynamic condition,” *Proceedings of the 14th International Symposium, PRADS 2019*, September 22-26, 2019, Yokohama, Japan, vol. II, 2019.
- [19] S. Tavakoli, S. Saettone, S. Steen, P. Andersen, J. Schramm, and E. Pedersen, “Modeling and analysis of performance and emissions of marine lean-burn natural gas engine propulsion in waves,” *Applied Energy*, vol. 279, p. 115904, 2020.
- [20] GT-SUITE, “Engine performance,” tech. rep., Gamma Technology, 2017.
- [21] A. Sidorow and R. Isermann, “Physical and experimental modeling of turbochargers with thermodynamic approach for calculation of virtual sensors,” (Rueil-Malmaison, France), 2012.
- [22] S. Saettone, B. Taskara, P. B. Regenera, S. Steen, and P. Andersen, “A comparison between fully-unsteady and quasi-steady approach for the prediction of the propeller performance in waves,” *Applied Ocean Research*, vol. 97, 2019

Paper 6

Effects of Propeller Load Fluctuation on Performance and Emission of a Lean-Burn Natural Gas Engine Operating at Part-Load Condition

Sadi Tavakoli, Jesper Schramm, and Eilif Pedersen


This paper is awaiting publication and is not included in NTNU Open

Paper 7

Emission Reduction of Marine Lean-Burn Gas Engine Employing a Hybrid Propulsion Concept

Sadi Tavakoli, Kamyar Maleki Bagherabadi, Jesper Schramm,
and Eilif Pedersen

Fuel consumption and emission reduction of marine lean-burn gas engine employing a hybrid propulsion concept

International J of Engine Research
1–11
© IMechE 2021
Article reuse guidelines:
sagepub.com/journals-permissions
DOI: 10.1177/14680874211016398
journals.sagepub.com/home/ijer


Sadi Tavakoli^{1,2} , Kamyar Maleki Bagherabadi¹, Jesper Schramm² and Eilif Pedersen¹

Abstract

As the emission legislation becomes further constraining, all manufacturers started to fulfill the future regulations about the prime movers in the market. Lean-burn gas engines operating under marine applications are also obligated to enhance the performance with a low emission level. Lean-burn gas engines are expressed as a cleaner source of power in steady loading than diesel engines, while in transient conditions of sea state, the unsteadiness compels the engine to respond differently than in the steady-state. This response leads to higher fuel consumption and an increase in emission formation. In order to improve the stability of the engine in transient conditions, this study presents a concept implementing a hybrid configuration in the propulsion system. An engine model is developed and validated in a range of load and speed by comparing it with the available measured data. The imposed torque into the developed engine model is smoothed out by implementing the hybrid concept, and its influence on emission reduction is discussed. It is shown that with the hybrid propulsion system, the NO_x reduces up to 40% because of the maximum load reduction. Moreover, eliminating the low load operation by a Power Take In during incomplete propeller immersion, the methane slip declines significantly due to combustion efficiency enhancement.

Keywords

Marine gas engine, hybrid propulsion system, combustion model, NO_x, methane slip

Date received: 11 January 2021; accepted: 19 April 2021

Introduction

High consideration is recently given to cleaner energy sources such as natural gas than other conventional fossil fuels. Natural gas has been used to reduce the carbon footprint in the transportation sector.¹ Besides, the potential of burning in a lean mixture gives the natural gas the opportunity of high thermal efficiency and low nitrogen oxides.^{2,3} Therefore, efforts to overcome the drawbacks of natural gas engines were made by numerous authors during the last decades. The flame speed of natural gas is lower than traditional fossil fuels,⁴ and the low combustion temperature of a lean mixture results in incomplete combustion. As a consequence, a significant part of the fuel may remain unburned. This unburned fuel has more greenhouse effects than CO₂. Methane has a 86 times higher 20-year global warming potential than carbon dioxide and 25 on a 100-year time.⁵ Sources of this emission in lean combustion are the crevice volume, gas exchange

process, and the quenched flame.⁶ A feasible method of unburned fuel reduction is reducing the crevice volume.⁷ However, minimizing the total volume must not lead the lubricating oil temperature to exceed the permitted temperature. Thus, there is always a dead volume in the combustion chamber where the flame can not propagate, and two-wall quenching occurs.⁸ Reducing the valve overlap duration limits the mixture short-circuiting and restricts issuing the fuel-air mixture directly into the atmosphere. Despite these two

¹Department of Marine Technology, Norwegian University of Science and Technology, Trondheim, Norway

²Department of Mechanical Engineering, Technical University of Denmark, Lyngby, Denmark

Corresponding author:

Sadi Tavakoli, Department of Marine Technology, Norwegian University of Science and Technology, Otto Nielsens, Trondheim, Sør-Trøndelag 7491, Norway.

Email: sadi.tavakoli@ntntu.no

parameters, flame quenching control and reduction are more complicated and require optimizing the combustion phenomenon. Installing a pre-chamber for stable initial combustion and stabilize the air excess ratio are promising strategies. By supplying a large quantity of turbulent hot gas to the combustion chamber, the pre-chamber ignites even a highly diluted mixture.^{9,10}

In marine applications, the propeller torque and engine load oscillate in time. The time-varying wake distribution, time-varying thrust deduction fraction, and the ship motions are primarily responsible for the propeller load variation.¹¹ With taking the engine propeller dynamics, wake variation, and thrust and torque losses into account, wave effect on ship propulsion performance showed a sharp decline in propulsion system performance.¹² Therefore, a dynamic or time-based simulation is required for coupled systems of engine-propeller-hulls operated in transient conditions.¹³

Stable combustion in a lean-burn marine gas engine is supported by rapid feedback controllers on air and fuel passages to adjust the air-fuel ratio and engine speed, but the controllers do not adequately provide the feedback to control the combustion during rapid load changes.¹⁴ Therefore, part of the fuel crosses into the exhaust manifold during the load reduction of transient sea conditions. Furthermore, a remarkable rise of NO_x formation occurs during load increase. The change of the load and the mechanical delay caused by the mass moment of inertia of the turbocharger shaft causes an almost one-second delay to the engine response, and a higher amount of NO_x.¹⁵ The conventional controlling approaches do not compensate for this delay. Therefore, new methodologies to improve the loading stability are proposed, such as control-oriented combustion models for continuously improving engine fuel economy.¹⁶

Hybrid Propulsion System for a marine application is one of the proposed ideas by integrating mechanical and electrical drive components on the propeller shaft. The main objective of this combination is to reduce fuel consumption and emission formation by approaching the optimum operation curve of the main engine.¹⁷ This integrated propulsion system improves engine performance during the low load operation and high load operation.¹⁸ Furthermore, hybrid propulsion provides an effective method to facilitate related issues of wear and tear, noise, vibration, and occupied space.¹⁹ The hybrid concept initiates by compensating part of the required load by an electrified section stored in the Energy Storage System.²⁰ Engines in marine propulsion are sized and designed based on the mean peak load demands. As a result, this approach gives an oversized engine for the low load conditions.²¹ Moreover, investigating a conventional propulsion system performance in low-speed mode demonstrates significant decrements in system efficiency. In order to overcome this drawback, the electric motor operates as a Power Take In (PTI) that can drive the propeller shaft in low load. Besides, during high load operation, the electric motor

can provide part of the required torques.²² The hybrid propulsion system can also be considered a proper alternative solution for vessels with fluctuating load profiles. In the case of redundancy requirements for the propulsion system, hybridization can be considered a feasible methodology.²³

Energy management systems (EMS) and advanced control strategy play an important role in optimum performance and efficiency improvement of this type of integrated system. Extensive research established on developing optimum EMS for Hybrid vehicles that can be implemented and inspired for marine hybrid propulsion application. Rule-based, optimal control and Model Predictive Controller can be implemented as the EMS in these systems. Among the mentioned controllers, rule-based is the most common and straightforward strategy. Rule-based methods can provide proper performance by appropriate tuning. Optimal controllers usually operate based on equivalent consumption minimization strategies.²⁴ It can be concluded that rule-based heuristic algorithms can obtain desirable performance. However, they require proper tuning and suffer from a lack of robustness in special cases. Model Predictive Controller (MPC) or predictive-based optimized strategies are proposed as a high-level control with a property of future prediction. These methods utilize future prediction and consider cost function to provide optimal decision makings.^{25,26} Considering feasible constraints and the plant control model is the main endeavor for implementing MPC as a high-level controller. Prediction-based optimization achieved a 9.31% improvement in performance than the baseline rule-based methods.²⁷ Moreover, the EMS performance is a function of the size and technical properties of components. The sizing of components can be defined as an optimization problem based on specific objectives and constraints. These objectives can be considered as the fuel consumption and emission of the main engine. The constraints could be the cost and weight of the electrical components, which are influenced by the intensity of the fluctuations. This proper sizing can improve the performance and efficiency of the system significantly.²⁸⁻³¹

The main objective of this study is to investigate the importance of load sharing on fuel consumption and emission formation of a lean-burn gas engine implemented for marine application. The load distribution is performed using a hybrid concept to reduce the maximum torque during high wave resistance and increase the minimum torque during load reduction of a harmonic sinusoidal load.

Simulation method

Engine modeling

Thermodynamic modeling is one of the most effective simulation methods of internal combustion engines widely used in the research field to predict fuel

Table 1. Engine specification.

Item	Unit	Amount
Number of cylinders		9
Cylinder bore	mm	350
Cylinder stroke	mm	400
Connecting rod length	mm	810
Rated power	kW	3940
Rated speed	rpm	750
Maximum torque at rated speed	N·m	50,200
Fuel type		Natural gas

Table 2. Vessel specification.

Item	Unit	Amount
Length oa	m	B 119.95
Length bpp	m	117.55
Width	m	20.80
Design draft	m	5.5
Design shaft submergence	m	3.3
Service speed	kts	15

consumption, combustion efficiency, intake and exhaust manifold optimization, and even tuning a control system. A robust thermodynamic-dynamic model has been proposed in this study. Measured data are available for validation and verifying the accuracy of the modeling. Specification of the gas engine named Bergen B35: 40L9 is presented in Table 1, and the ship specification where the marine engine is specifically designed for, is presented in Table 2.

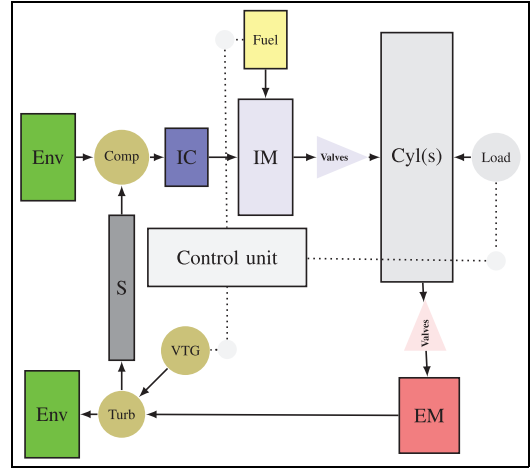
A detailed engine modeling plays a critical role in predicting the engine response during time-varying load, especially for transient conditions where the torque changes harmonically and even in a short duration of the time scale of seconds. The schematic of the structure and the connection of all essential components are shown in Figure 1.

A two-zone combustion model, the burned and unburned mixture, divides the combustion chamber into two separate zones during combustion. It is assumed that an infinitely fast reaction happens and contributes to considering the flame envisioned as a junction between fresh air/oxidizer and burnt gases. After the main combustion ended, all the burned and unburned gas is mixed into one zone. A more detailed discussion of the combustion modeling is presented.^{15,32} The rate of transformation of unburned to the burned zone is calculated by equations (1) and (2):

$$\frac{dM_e}{dt} = \rho_u A_c (S_T + S_L) \quad (1)$$

$$\frac{dM_b}{dt} = \frac{M_e - M_b}{\tau} \quad (2)$$

where index b symbolizes burned classification, u unburned classification, and e entrained classification.

**Figure 1.** All the essential components in the simulation platform.

It was also assumed that the reaction is quite fast with a thin layer of the burning zone.⁸ To calculate the laminar flame speed (S_L), Heywood³³ recommended equation (3) for several hydrocarbon fuels:

$$S_L = (B_m + B_f(\phi - \phi_m)^2) \left(\frac{T_u}{T_0}\right)^\alpha \left(\frac{P}{P_0}\right)^\beta \cdot f_{\text{Dilution}} \quad (3)$$

where for natural gas fuel

$$\alpha = 0.68\phi^2 - 1.7\phi + 3.18 \quad (4)$$

$$\beta = -0.52\phi^2 + 1.18\phi - 1.08 \quad (5)$$

and B_m is 0.490, B_f is -0.59, and ϕ_m is 1.390.³⁴ f_{Dilution} is the dilution effect and is employed as:

$$f_{\text{Dilution}} = 1 - 0.75 \cdot A(1 - (1 - 0.75 \cdot A)^7) \quad (6)$$

A is a multiplier, and Dilution is the mass fraction of the residuals in the unburned zone.

The time constant of combustion of fuel/air mixture entrained into the flame zone (τ) in equation (2) is calculated by equation (7):

$$\tau = \frac{\lambda}{S_L} \quad (7)$$

with the Taylor length scale of

$$\lambda = a \cdot \frac{L_i}{\sqrt{Re_t}} \quad (8)$$

and turbulent Reynolds number

$$Re_t = \frac{\rho_u \dot{u} L_i}{\mu_u} \quad (9)$$

Calculation of turbulent flame speed is done by equation (10):

$$S_T = b \cdot \dot{u} \left(1 - \frac{1}{1 + c \left(\frac{R_f}{L_i}\right)^2}\right) \quad (10)$$

where a , b , and c are constants. Moreover, \dot{u} and L_i are turbulent intensity and turbulent length scale, respectively. Surface area at the flame front (A_s) and flame radius (R_f) are presented in Blizard and Keck.³²

The boundary conditions at the inlet of the compressor and outlet of the turbine are the standard sea level condition.

The heat transfer of the flow through the piping of intake and exhaust is assumed to be either adiabatic or with a constant wall temperature. The heat transfer with a given wall temperature is calculated by Colburn analogy:

$$h_g = \left(\frac{1}{2}\right) C_f \rho U_{\text{eff}} C_p Pr^{(-\frac{2}{3})} \quad (11)$$

and, heat flux is calculated by:

$$q_{\text{convection}} = h_g (T_{\text{gas}} - T_{\text{wall}}) \quad (12)$$

Heat convection modeling in the main combustion chamber followed the method proposed by Woschni³⁵ in equation (13):

$$h_{c(\text{Woschni})} = \frac{K_1 P^{0.8} W^{0.8}}{B^{0.2} T^{K_2}} \quad (13)$$

where K_1 and K_2 are constant and W is average cylinder gas velocity (m/s). The equation for the average in-cylinder gas velocity is:

$$W = C_1 S_p + C_2 \frac{V_d T_r}{P_r V_r} (P - P_m) \quad (14)$$

C_1 and C_2 are constants, S_p mean piston speed (m/s), T_r unburned mixture temperature, P pressure, P_m motoring pressure, P_r unburned mixture pressure, V_d the total displacement and V_r is the volume before combustion.

The dimensions for all the pipes and junctions are implemented based on the designed components, and different discretized length scales for the straight pipes and bends were chosen.

$$\frac{dm}{dt} = \sum_{\text{boundaries}} \dot{m} \quad (15)$$

$$\frac{dme}{dt} = -\rho \frac{dv}{dt} + \sum_{\text{boundaries}} (\dot{m}H) - hA_s(T_{\text{fluid}} - T_{\text{wall}}) \quad (16)$$

$$\frac{d\dot{m}}{dt} = \frac{dpA + \sum_{\text{boundaries}} (\dot{m}u) - 4C_f \frac{\rho u |u| dx A}{2D} - K_p \left(\frac{1}{2} \rho u |u|\right) A}{dx} \quad (17)$$

Where m is mass of volume, and \dot{m} is the boundary mass flux. A is the cross-sectional flow area, and A_s is the heat transfer surface area.

In all discretized volume, the equations (15) and (16) yield the mass and energy in each volume.

The turbocharged performance, the compressor, turbine, and connecting shaft are calculated. A look-up table, including the pressure ratio, mass flow rate, efficiency, and rotational speed, was implemented for the compressor and turbine. The friction coefficient was implemented in a table for the connecting shaft. The turbocharger rotational speed in each time step is a function of the turbine, compressor, and friction torques and is calculated by equation (18).

$$\Delta\omega = \frac{\Delta t (T_{\text{turbine}} - T_{\text{compressor}} - T_{\text{friction}})}{I} \quad (18)$$

Where I is the turbocharger shaft inertia, and T is the torque.

Engine torque is an input to the model based on the wave characteristics discussed in the work of the authors,¹⁵ and the power is an output of the engine modeling based on torque, T_b , and speed, N :

$$P_{\text{brake}} = \left[\frac{\int T_b(t) N dt}{\int dt} \right] [2\pi] \quad (19)$$

A PID controller adjusts the engine speed for a set-point, 750 rpm. The fuel rack position controls the fuel valve lift upstream of the inlet valves to adjust the speed. Thus, a premixed mixture is added to each cylinder through two opening valves. The valves restrict the mass flow rate by a one-dimensional flow analysis model.³³ Accurate modeling of the valve models and quick response of the tuned PID controller is crucial in the engine response and the engine performance output. In addition, the high inertia of the connecting shaft from the engine to the propeller plays a striking impact on a stable engine speed during the transient condition. The engine brake torque relative to the propeller shaft acceleration is obtainable by the equation (20):

$$T_b(t) = T_s(t) - I\dot{\omega}_{ct}(t) \quad (20)$$

where, $\dot{\omega}_{ct}(t)$ is the instantaneous crank-train acceleration. The shaft torque, T_s , is also calculated by:

$$T_s(t) = T_i(t) + T_a(t) - T_f(\text{cyc}) \quad (21)$$

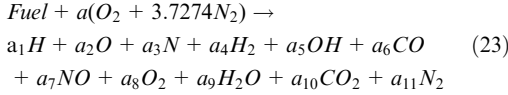
Where $T_a(t)$ accounts for all loads that are attached to the auxiliary port and $T_f(\text{cyc})$ friction torque in each cycle, and $T_i(t)$, is the indicated torque and is a function of the pressure distributed on piston surfaces by combustion modeling.

With the available power and injected fuel flow from the modeling, it is possible to calculate the amount of brake specific fuel consumption by equation (22).

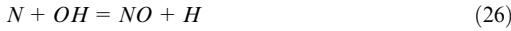
$$BSFC = \left[\frac{\text{fuel}_{\text{total}}}{\text{power}_{\text{brake}}} \right] \quad (22)$$

The combustion phase comprises the calculations of the flame burning rate during the main combustion, concentrations of the species by chemical equilibrium,

and emissions formation during post-oxidation. Throughout the main combustion, unburned and burned mass zones are maintained, and the burned zone composition is determined by equilibrium chemistry:



For the emission modeling, a general reaction, as presented in equation (23), never provides an acceptable output for the NO_x and UHC formation. Thus, NO_x is calculated using a reduced mechanism described by Zeldovich³⁶:



The reaction rate for the three mechanisms are respectively:

$$k1 = F_1 \cdot 7.60 \cdot 10^{10} \cdot e^{-38000 \frac{d_1}{T_b}} \quad (27)$$

$$k2 = F_2 \cdot 6.40 \cdot 10^6 \cdot T_b e^{-3150 \frac{d_2}{T_b}} \quad (28)$$

$$k3 = F_3 \cdot 4.10 \cdot 10^{10} \quad (29)$$

F_1 , F_2 , F_3 , A_1 and A_2 are constant coefficients for tuning the modeling. Since the concentration of N is much less than other species, there is an assumption of $\frac{d[N]}{dt} = 0$ with the steady-state approximation. A simplified one-way equilibrium is feasible for other species, and finally, a single rate of formation for NO is available. The reported value for NO_x is calculated by:

$$bsNO_x = \left[\frac{m_{NO_x, \text{exh}}}{b \cdot \text{power}} \right] \left[\frac{\text{avg. } r \text{ pm}}{n_r} \right] \quad (30)$$

where n_r is revolutions per cycle, two for 4-stroke engine.

The amount of methane slip or UHC is defined as the amount of fuel left unburned during the main combustion and during the post-oxidation in exhaust valve opening. The burning process for UHC calculation undergoes the following equation:

$$UHC_{total} = \int_{IVO}^{IVC} \dot{m}_f - \int_{comb} \dot{m}_f - \int_{post-comb} \dot{m}_f \quad (31)$$

where $\int_{post-comb} \dot{m}_f$ is calculated by reaction rate of Equation (32).³⁷

$$R_K = A \times R_S e^{-\frac{1600K \times B}{T}} [f_{HC}] [f_{O_2}] \quad (32)$$

Where A and B are multiplier, and T is the mass-averaged overall temperature, and R_S is the burn rate calculated by the combustion model.

The equation does only consider two sources of the UHC, including the quenched flame and crevice volume.

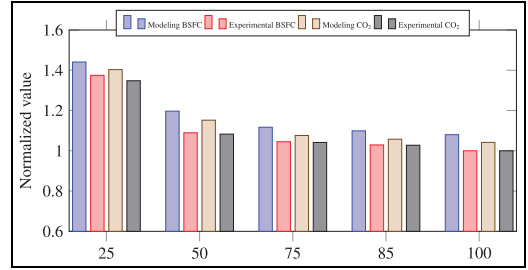


Figure 2. Comparison of measured data and engine simulation in steady-state. The X-axis shows the load percentage, and the Y-axis gives the normalized output.

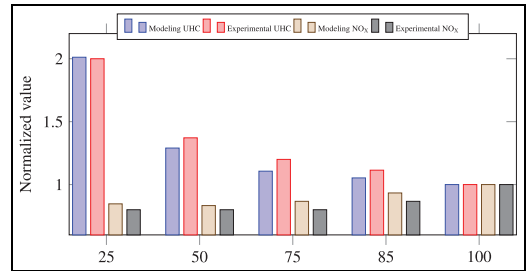


Figure 3. Comparison of measured data and simulation output in steady-state for emission compounds, NO_x and UHC.

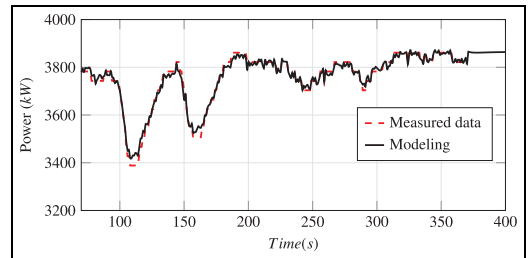


Figure 4. Validation of the model by comparing the output power.

The model is validated both in steady-state and transient conditions to verify the implemented equations predicting the engine response during the transient condition. Validation of the steady-state operating loads was chosen based on the available measure data, from 100% to 25% of the nominal torque in a constant engine speed, on 750 rpm. Comparison of the results is shown in Figures 2 and 3. As can be seen, there is a high degree of agreement between the measured and modeling data in the fuel-specific consumption and the produced CO_2 , and emission compounds including unburned hydrocarbon and NO_x .

Moreover, the effects of the dynamic loading for transient condition are presented in Figures 4 to 6. The

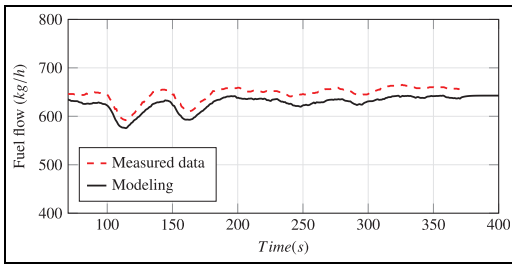


Figure 5. Fuel flow comparison between measured data and simulated model for verifying the model during the transient condition.

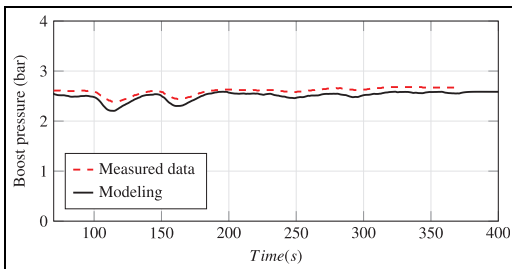


Figure 6. Boost pressure comparison between measured data and simulated model for verifying the model during the transient condition.

output power as a function of implemented torque and target speed is predicted with a negligible error under a torque range between 40,000 and 50,000 Nm. The maximum nominal torque for the engine is 50,200 Nm. In order to investigate the prediction accuracy of the fuel system, air supply system, and combustion efficiency, the fuel flow and boost pressure were compared. It is found that the model provides a powerful foresight and theoretical guidance for the engine performance in a range of load variation.¹⁵

Hybrid concept

Conventional propulsion systems consist of a main engine, gearbox, shaft, and propeller. In the case of hybridization of the propulsion system, as shown in Figure 7, three components, an electrical motor, shaft generator, and battery, are integrated into the system. The shaft generator has the role of Power Take Out (PTO), and the electrical motor is considered as Power Take In (PTI). The control system primary role is to provide load sharing for components to reduce the effect of load fluctuation on the main engine. This endeavor will be achieved by implementing a low pass filter on the main shaft predicted load. Furthermore, in the gearbox connection, the low varying load from filter output will be provided by the main engine. Therefore,

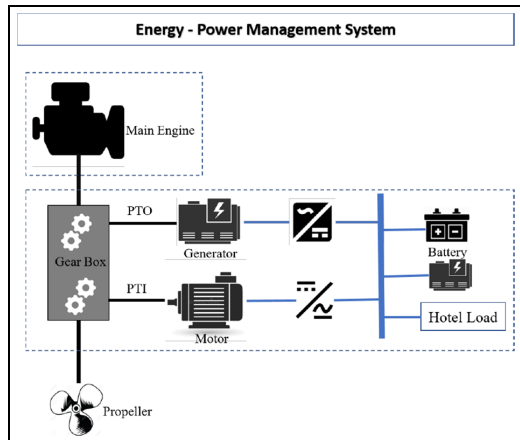


Figure 7. Hybrid propulsion system.

in a low and high-level load, the high-frequency fluctuations will be compensated by PTI and PTO regarding the load states. This technique is similar to the peak shaving of electrical hybrid power systems. The strategy of load sharing contributes to the optimum operation of the main engine. As a high-level controller, the energy management system monitors the system states and considers the constraints also. The decision on load sharing is based on the states and properties of the system. The states are defined as loads on the main shaft that is system requirements also, battery charge state as available stored electrical energy, and engine torque as the current operating point. The properties can be considered as the dynamic response that means main components behavior over the time domain. The transient response of the main engine, PTI, and PTO components determines their required time or inertia to satisfy the actuated load commands. Another system property is the charge and discharge current limitation of the battery that defines the maximum power value for the battery as input and output. Indeed, the optimum operation region of the main engine defines the proper torque range for the engine for better performance.

Implemented loads

Based on the project previous works, a range of wave characteristics may result in a variable frequency and amplitude of the torque on the propulsion shaft and, consequently, the engine. In this study, one of the periodic severe loads with high amplitude is chosen with the specification of wavelength (λ/L_{PP}) 1.2, amplitude 2 m, and direction (θ) 60° . The wave direction is relative to the ship, and 180° is considered as a head wave. The torque caused by the wave characteristics is shown in Figure 8.

With the hybrid concept, the new torque profile, as shown in Figure 8 named hybrid concept, is obtained

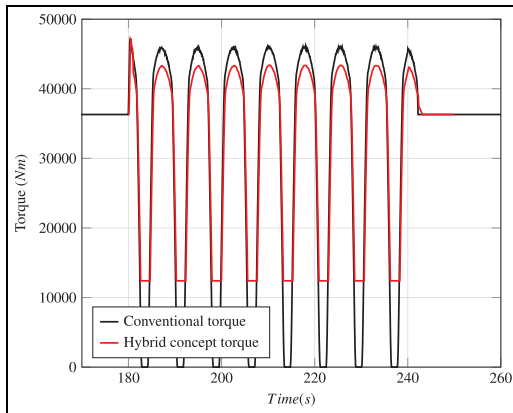


Figure 8. Implemented dynamic loading calculated by a wave amplitude of 2 m.¹¹

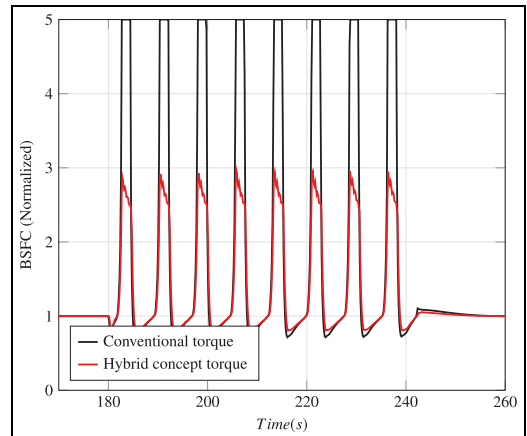


Figure 10. The brake specific fuel consumption. The values are normalized based on the quantity in steady-state.

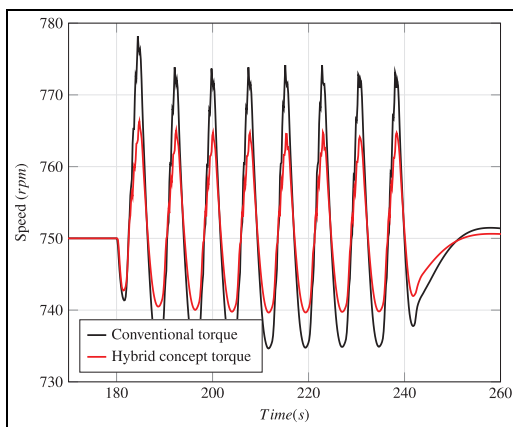


Figure 9. The engine speed variation on a nominal setpoint of 750 rpm. With the implemented hybrid system, the speed variation is in a limited range.

by implementing a second order low pass filter with bandwidth 3 Hz and power level cut-off regarding optimum engine operation point. Low pass filters make a delay comparing to their tuned frequency. The mentioned profile allows the main engine to produce the mean torque while the fluctuations were compensated by the PTI and PTO. With the new smoothed torque, the peak loads are eliminated, and the lower loads with less than 25% are also skipped.

Results and discussion

The effect of transient torque on engine speed is highly dependent on the magnitude and the frequency of the load. The higher the frequency of the load, the lower the variation of the speed domain. In addition, the higher wave amplitude results in more variation in

engine response. With the hybrid system implemented torque, the frequency was maintained as a severe case while the amplitude was reduced. Therefore, as shown in Figure 9, the speed variation has the same frequency as the Conventional load domain, but the magnitude of the speed value reduced from a maximum of almost 775 to 765 and a minimum of 735 to 740 rpm. It is worth mentioning that the target of the speed was 750 rpm for the case study; therefore, the relevant PID control system compensates the demanded fuel based on the deviation around 750 rpm.

The brake-specific fuel consumption (BSFC) of the engine is studied, and it is found that reducing the loading oscillation is beneficial to reduce the BSFC. It can be seen from Figure 10 that the BSFC reduction degree is remarkable with the load reduction part. It must be highlighted that due to the numerical error of the simulation, when the load drops to a brake torque almost zero for the propeller out of the water, the BSFC reached an infinity value. In the figure, this is limited to five. An understandable qualitative assessment of the fuel consumption comparison of our case study compares the fuel flow of the engine. As shown in the fuel flow trend by Figure 11, the fuel flow is almost 380 kg/h in minimum for the conventional mode. This quantity is a very high flow for the engine working on around zero brake torque, which is the main reason for the infinity value on BSFC. For the hybrid propulsion system, the brake torque is never reduced to loads lower than 25% of the nominal torque, and the engine works in higher combustion efficiency. The combustion efficiency is the ratio of released chemical energy in the exhaust gas to the total fuel energy and is shown in Figure 12. As illustrated, the combustion efficiency reduces in both installation modes in part of the load. The decrease in combustion efficiency reports an increase in volumetric efficiency or a very lean mixture. However, a significant improvement in combustion

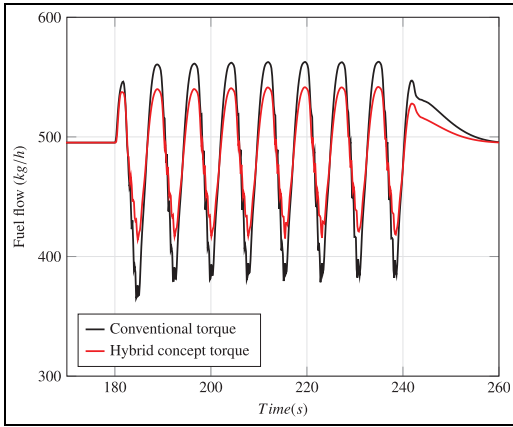


Figure 11. The fuel flow during the implemented torque. The average value for both of the cases is equal.

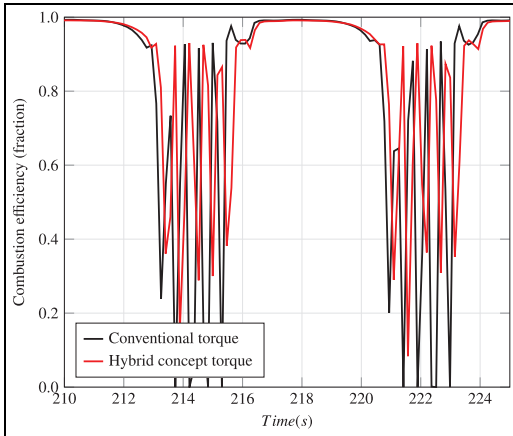


Figure 12. The combustion efficiency comparison between conventional installment and hybrid propulsion system.

efficiency can be seen by utilizing the hybrid propulsion system. On average, the fuel flow for both conditions is the same, while the hybrid system produces an average torque of 12% more than the conventional system. Hence, the lean-burn spark-ignition engine hybrid propulsion system shows a reduction in total fuel consumption.

The volumetric efficiency comparison assessment can be accomplished by utilizing the air excess ratio or λ . The higher volumetric efficiency led to the lower combustion efficiency is shown in Figure 13. There is a target setpoint for the turbocharging to fix the air excess ratio. With the load variation, due to the turbocharger mechanical delay, there is always a delay between the load change and the demanded air ratio. This delay leads the engine to have a permanent deviation on setpoint λ and the actual value. During the load increases, the λ value is less than the setpoint, and

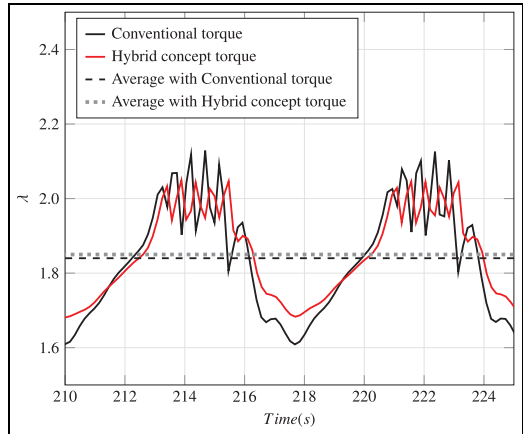


Figure 13. Less fluctuated air excess ratio is achievable by the hybrid propulsion system and cutting off the lower parts of the torque curve and peak shaving.

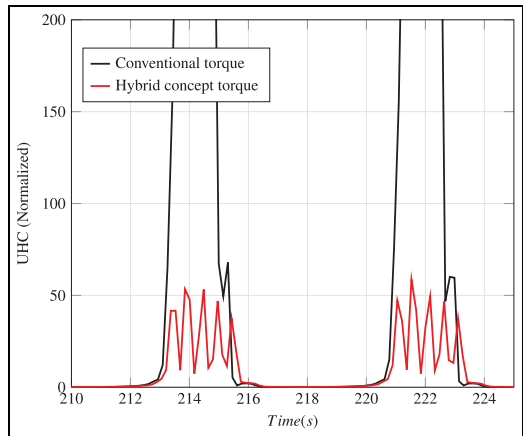


Figure 14. The amount of methane slip reduced considerably with the hybrid propulsion concept during transient conditions.

during the load drop, the λ value is higher than the setpoint. This extra volumetric efficiency of the engine during transient conditions results in lower combustion efficiency and higher fuel consumption. By involving the hybrid propulsion system, the load variation reduces, and consequently, the deviation domain reduces. However, there is still extra air available when the load is almost 25%, and the λ increases to 2.

Several noticeable hypotheses could be observed for the emission formation with the change of combustion efficiency and fuel consumption during the time-varying load. Figure 14 presents the marine gas engine methane slip. It is observed that the hybrid propulsion installment controlled the methane slip overshoot during the transient condition. It must be noted that the

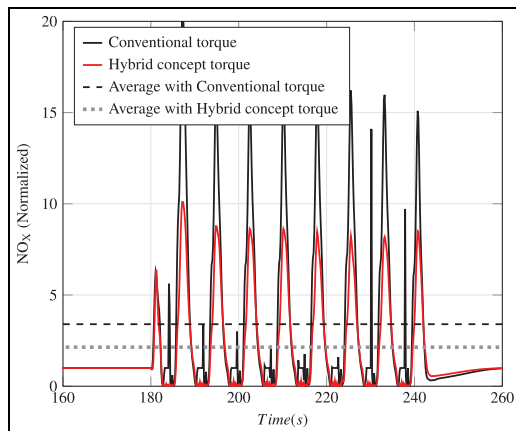


Figure 15. Formation of NO_x gives a remarkable reduction during load increment and in overall average value.

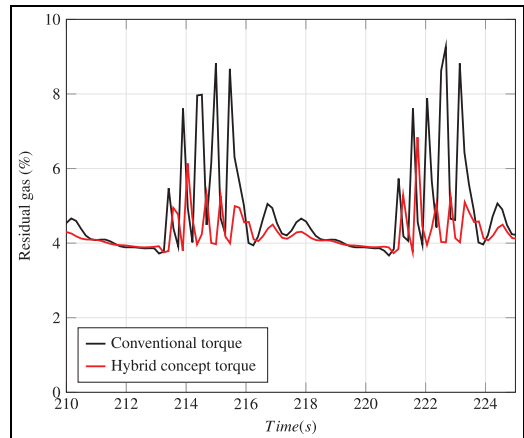


Figure 16. Percentage of residual gas captured in the cylinder number 1, before the combustion start.

UHC quantity is normalized with the value in steady loading. Therefore, the amount for the time before 170 equals one. Moreover, the maximum value is limited to 200. This value is chosen compared to the fuel consumption in order to prevent the infinity quantity achieved due to numerical error. It is also found that the relative deviation of the methane slip with and without the hybrid system is negligible during load increment when the UHC value is less than one. While the methane slip sources are short-circuited gas exchange, crevice volume, and quenched flame in the lean-burn gas engine, as discussed in the modeling section, the gas exchange is not considered in the modeling since the fraction of this source is negligible due to the short valve overlap of the intake and exhaust ports. With a constant volume considered for the crevice volume, it is expected that the methane slip of this section does not change significantly. However, the post oxidation may negatively influence increasing the methane slip from the crevice volume by less post-oxidation. The quenched flame is expected to be the primary source of this variation, especially with the available high volumetric efficiency and low combustion efficiency during lower loads.

NO_x is one of the most severe air pollutants produced by fossil fuel combustion. Although very low in the lean-burn gas engine, this compound is susceptible to any deviation to the air excess ratio, particularly to the rich combustion. Oxygen-rich mixtures resultant temperature causes the NO_x formation at high levels. Activating the hybrid system during higher loads and reducing the engine maximum power generation, the rich mixture zone mitigates, and a more balanced air excess ratio area is achievable. This area has a lower maximum temperature than the normal operating condition, and thus, as can be seen in Figure 15, a remarkable reduction of this compound is reached. The average value during the transient condition is also

added to the figure. With supposing the average NO_x quantity for the stable condition to one, the mean value for the entire transient condition without a hybrid propulsion system showed 3.4 times increasing. NO_x formation for the hybrid propulsion system, however, confirmed a 2.14 times increase. This means that the NO_x compound with the implemented hybrid system is reduced up to 40%. As can be seen from the figure, this reduction is only during the higher loads, where the peak NO_x reduced from the maximum value of 15 to 8. Due to a more stable condition with the hybrid system during load reduction, a higher value of NO_x is expected with the hybrid system in lower loads.

To reduce the NO_x formation in diesel engines, utilizing exhaust gas recirculation (EGR) is a common technique. The EGR is recycled into the combustion chamber at a high or cold temperature. The result is a lower temperature combustion and a lower level of NO_x formation. However, for a lean-burn gas engine, increasing EGR percentage has a negative consequence. The variation of EGR is shown in Figure 16. An undesirable increase of the residual gas percentage during the transient condition provided an over lean mixture. This amount of gas is the trapped burned mass of the previous cycle, which was consistent at 4% during steady-state (the time before 170s). The additional EGR during load reduction plus the extra λ resulted in the flame quench. Implementing the hybrid concept and a more stable air flow rate in the load reduction time, less EGR is available and presents more efficient combustion.

Conclusion

In this paper, a numerical model for a medium-speed lean-burn gas engine is developed. A 1-D model for the

air and fuel piping plus predictive 2-zone modeling for combustion is performed to deal with the rapid change of transient sea conditions. Non-variable coefficients for the control system tuning were employed, and the engine stability was examined with the coefficients during model preparation. The model was validated against measured data in steady-state and in transient conditions. By taking the experience from previous studies, the marine engine response was enhanced with a hybrid system. The simulation was conducted in a severe case scenario to demonstrate how a supplementary hybrid system influences the total fuel consumption and emission formation. The engine had a PTO to the hybrid system with loads lower than 25%, and PTI for the higher loads to smooth out the engine peak loads. The results of the demonstration are summarized as follows.

1. The average fuel consumption during rapid transient conditions with or without the hybrid system was identical, but the engine was totally providing 12% higher torque with the hybrid system.
2. Concerning the methane slip in transient condition, almost all the peak values were disappeared with the hybrid system, and the total quantity reduced notably.
3. It was shown that the amount of NO_x emission is reduced by 40% with the hybrid system due to lower peak torque and smoothing the rich mixture area.
4. EGR was non-desirable residual gas for the lean-burn gas engine, and rising the EGR fraction deteriorated the flame rate during lower loads and resulted in more instability in combustion.


Declaration of conflicting interests

The author(s) declared no potential conflicts of interest with respect to the research, authorship, and/or publication of this article.

Funding

The author(s) received no financial support for the research, authorship, and/or publication of this article.

ORCID iD

Sadi Tavakoli  <https://orcid.org/0000-0001-6345-1632>

References

1. Baratta M, Chiriches S, Goel P and Misul D. CFD modelling of natural gas combustion in IC engines under different EGR dilution and H₂-doping conditions. *Transp Eng* 2020; 2: 100018.
2. Caton JA. A comparison of lean operation and exhaust gas recirculation: thermodynamic reasons for the increases of efficiency. In: *SAE 2013 world congress exhibition*, 8 April 2013. SAE International.
3. Krishnasamy A, Gupta SK and Reitz RD. Prospective fuels for diesel low temperature combustion engine applications: a critical review. *Int J Engine Res*. Epub ahead of print 11 May 2020. DOI: 10.1177/1468087415621805.
4. Xu M, Cheng W, Zhang H, An T and Zhang S. Effect of diesel preinjection timing on combustion and emission characteristics of compression ignited natural gas engine. *Energy Convers Manag* 2016; 117: 86–94.
5. Burel F, Taccani R and Zuliani N. Improving sustainability of maritime transport through utilization of liquefied natural gas (LNG) for propulsion. *Energy* 2013; 57: 412–420.
6. Tavakoli S, Pedersen E and Schramm J. Natural gas engine thermodynamic modeling concerning offshore dynamic condition. In: *Proceedings of the 14th international symposium, PRADS 2019*, Yokohama, Japan, 22–26 September 2019, vol. 2.
7. Stenersen D and Thonstad O. GHG and NO_x emissions from gas fuelled engines: mapping, verification, reduction technologies. Technical report OC2017 F-108, SINTEF Ocean AS, NO-7465, Trondheim, Norway, 2017.
8. Turns SR. An introduction to combustion: concepts and applications. McGraw-Hill, 2012.
9. Müller C, Pischinger S, Tews S, Müller A and Habermann K. Analysis of experimental results with an active pre-chamber ultra-lean burn SI engine. *Int J Engine Res*. Epub ahead of print 6 December 2020. DOI: 10.1177/1468087420974544.
10. Yu S and Zheng M. Future gasoline engine ignition: a review on advanced concepts. *Int J Engine Res*. Epub ahead of print 19 September 2020. DOI: 10.1177/1468087420953085.
11. Saettone S, Tavakoli S, Taskar B, et al. The importance of the engine propeller model accuracy on the performance prediction of a marine propulsion system in the presence of waves. *Appl Ocean Res* 2020; 103: 102320.
12. Taskar B, Yum KK, Steen S and Pedersen E. The effect of waves on engine-propeller dynamics and propulsion performance of ships. *Ocean Eng* 2016; 122: 262–277.
13. Murphy A, Norman A, Pazouki K and Trodden D. Thermodynamic simulation for the investigation of marine diesel engines. *Ocean Eng* 2015; 102: 117–128.
14. Tavakoli S, Schramm J and Pedersen E. The effect of air throttle on combustion process and emission formation in marine lean-burn gas engines. In: *Proceedings of the 5th world congress on momentum, heat and mass transfer (MHMT'20)*, no. CSP 117. Virtual congress, Lisbon, Portugal, 14–16 October 2020.
15. Tavakoli S, Saettone S, Steen S, Andersen P, Schramm J and Pedersen E. Modeling and analysis of performance and emissions of marine lean-burn natural gas engine propulsion in waves. *Appl Energy* 2020; 279: 115904.
16. Tang J, Zhu GG and Men Y. Review of engine control-oriented combustion models. *Int J Engine Res*. Epub ahead of print 15 February 2021. DOI: 10.1177/1468087421992955.
17. Kalikatzarakis M, Geertsma R, Boonen E, Visser K and Negenborn R. Ship energy management for hybrid propulsion and power supply with shore charging. *Control Eng Pract* 2018; 76: 133–154.
18. Geertsma R, Negenborn R, Visser K and Hopman J. Design and control of hybrid power and propulsion systems for smart ships: a review of developments. *Appl Energy* 2017; 194: 30–54.

19. Altosole M, Campora U and Vigna V. Energy efficiency analysis of a flexible marine hybrid propulsion system. In: *2020 International symposium on power electronics, electrical drives, automation and motion (SPEEDAM)*, Sorrento, Italy, 24–26 June 2020, pp.436–441. IEEE.
20. Yum KK, Skjong S, Tasker B, Pedersen E and Steen S. Simulation of a hybrid marine propulsion system in waves. In: *Proceedings of 28th CIMAC World Congress*, Helsinki, Vol. 202. June 2016.
21. Capasso C, Veneri O, Notti E, Sala A, Figari M and Martelli M. Preliminary design of the hybrid propulsion architecture for the research vessel “G. Dallaporta”, In: *2016 International Conference on Electrical Systems for Aircraft, Railway, Ship Propulsion and Road Vehicles International Transportation Electrification Conference (ESARS-ITEC)*, 2016. pp. 1–16.
22. Castles G, Reed G, Bendre A and Pitsch R. Economic benefits of hybrid drive propulsion for naval ships. In: *2009 IEEE electric ship technologies symposium*, 2009. pp.515–520.
23. Barcellos R. The hybrid propulsion system as an alternative for off-shore vessels servicing and supporting remote oil field operations. In: *OTC Brasil, offshore technology conference*. Brazil: Rio de Janeiro, 29–31 October 2013.
24. Sciarretta A, Serrao L, Dewangan P, et al. A control benchmark on the energy management of a plug-in hybrid electric vehicle. *Control Eng Pract* 2014; 29: 287–298.
25. Bø TI and Johansen TA. Battery power smoothing control in a marine electric power plant using nonlinear model predictive control. *IEEE Trans Control Syst Technol* 2016; 25(4): 1449–1456.
26. Bø TI, Vaktkskjold E, Pedersen E and Mo O. Model predictive control of marine power plants with gas engines and battery. *IEEE Access* 2019; 7: 15706–15721.
27. Vu TL, Ayu AA, Dhupia JS, Kennedy L and Adnanes AK. Power management for electric tugboats through operating load estimation. *IEEE Trans Control Syst Technol* 2015; 23(6): 2375–2382.
28. Ostadi A and Kazerani M. Optimal sizing of the battery unit in a plugin electric vehicle. *IEEE Trans Veh Technol* 2014; 63(7): 3077–3084.
29. Zhang L, Hu X, Wang Z, Sun F, Deng J and Dorrell DG. Multiobjective optimal sizing of hybrid energy storage system for electric vehicles. *IEEE Trans Veh Technol* 2017; 67(2): 1027–1035.
30. Wang W, Peng Y, Li X, Qi Q, Feng P and Zhang Y. A two-stage framework for the optimal design of a hybrid renewable energy system for port application. *Ocean Eng* 2019; 191: 106555.
31. Yang J, Zhang D, Chen Y, Fan W, Liang H and Tan M. Feasibility analysis and trial of air-lift artificial upwelling powered by hybrid energy system. *Ocean Eng* 2017; 129: 520–528.
32. Blizard NC and Keck JC. Experimental and theoretical investigation of turbulent burning model for internal combustion engines. In: *1974 Automotive engineering congress and exposition*, Vol. 83 February 1974. pp. 846–864 SAE International.
33. Heywood JB. *Internal combustion engine fundamentals*. 2nd ed. McGraw-Hill series in mechanical engineering. New York, McGraw-Hill Education, 2018.
34. Hernandez JJ, Lapuerta M, Serrano C and Melgar A. Estimation of the laminar flame speed of producer gas from biomass gasification. *Energy Fuels* 2005; 19(5): 2172–2178.
35. Woschni G. A universally applicable equation for the instantaneous heat transfer coefficient in the internal combustion engine. In: *National fuels and lubricants, powerplants, transportation meetings*, 1 February 1967. SAE International.
36. Warnatz J, Maas U, Dibble RW and Warnatz J. *Combustion: physical and chemical fundamentals, modeling and simulation, experiments, pollutant formation*. 4th ed. Berlin, Heidelberg: Springer Berlin/Heidelberg, 2006.
37. Lavoie GA. Correlations of combustion data for S. I. engine calculations – laminar flame speed, quench distance and global reaction rates. SAE technical paper, SAE International, 02, 1978.

Appendix

Nomenclature

<i>EM</i>	Exhaust manifold
<i>EMS</i>	Energy management systems
<i>Env</i>	Environment
<i>IC</i>	Intercooler
<i>PTO</i>	Power Take Off
<i>BSFC</i>	Brake specific fuel consumption
<i>CO₂</i>	Carbon dioxide
<i>EGR</i>	Exhaust gas recirculation
<i>IM</i>	Intake manifold
<i>NG</i>	Natural gas
<i>NO_x</i>	Nitrogen oxide
<i>PTI</i>	Power Take In
<i>rpm</i>	Revolutions per minute
<i>S</i>	Shaft
<i>UHC</i>	Unburned hydrocarbon
<i>VTG</i>	Variable turbine geometry

Appendix B

List of previous PhD theses at Dept. of Marine Tech

**Previous PhD theses published at the Department of Marine Technology
(earlier: Faculty of Marine Technology)
NORWEGIAN UNIVERSITY OF SCIENCE AND TECHNOLOGY**

Report No.	Author	Title
	Kavlie, Dag	Optimization of Plane Elastic Grillages, 1967
	Hansen, Hans R.	Man-Machine Communication and Data-Storage Methods in Ship Structural Design, 1971
	Gisvold, Kaare M.	A Method for non-linear mixed -integer programming and its Application to Design Problems, 1971
	Lund, Sverre	Tanker Frame Optimalization by means of SUMT-Transformation and Behaviour Models, 1971
	Vinje, Tor	On Vibration of Spherical Shells Interacting with Fluid, 1972
	Lorentz, Jan D.	Tank Arrangement for Crude Oil Carriers in Accordance with the new Anti-Pollution Regulations, 1975
	Carlsen, Carl A.	Computer-Aided Design of Tanker Structures, 1975
	Larsen, Carl M.	Static and Dynamic Analysis of Offshore Pipelines during Installation, 1976
UR-79-01	Brigt Hatlestad, MK	The finite element method used in a fatigue evaluation of fixed offshore platforms. (Dr.Ing. Thesis)
UR-79-02	Erik Pettersen, MK	Analysis and design of cellular structures. (Dr.Ing. Thesis)
UR-79-03	Sverre Valsgård, MK	Finite difference and finite element methods applied to nonlinear analysis of plated structures. (Dr.Ing. Thesis)
UR-79-04	Nils T. Nordsve, MK	Finite element collapse analysis of structural members considering imperfections and stresses due to fabrication. (Dr.Ing. Thesis)
UR-79-05	Ivar J. Fylling, MK	Analysis of towline forces in ocean towing systems. (Dr.Ing. Thesis)
UR-80-06	Nils Sandsmark, MM	Analysis of Stationary and Transient Heat Conduction by the Use of the Finite Element Method. (Dr.Ing. Thesis)
UR-80-09	Sverre Haver, MK	Analysis of uncertainties related to the stochastic modeling of ocean waves. (Dr.Ing. Thesis)
UR-81-15	Odland, Jonas	On the Strength of welded Ring stiffened cylindrical Shells primarily subjected to axial Compression
UR-82-17	Engesvik, Knut	Analysis of Uncertainties in the fatigue Capacity of

Welded Joints

UR-82-18	Rye, Henrik	Ocean wave groups
UR-83-30	Eide, Oddvar Inge	On Cumulative Fatigue Damage in Steel Welded Joints
UR-83-33	Mo, Olav	Stochastic Time Domain Analysis of Slender Offshore Structures
UR-83-34	Amdahl, Jørgen	Energy absorption in Ship-platform impacts
UR-84-37	Mørch, Morten	Motions and mooring forces of semi submersibles as determined by full-scale measurements and theoretical analysis
UR-84-38	Soares, C. Guedes	Probabilistic models for load effects in ship structures
UR-84-39	Aarsnes, Jan V.	Current forces on ships
UR-84-40	Czujko, Jerzy	Collapse Analysis of Plates subjected to Biaxial Compression and Lateral Load
UR-85-46	Alf G. Engseth, MK	Finite element collapse analysis of tubular steel offshore structures. (Dr.Ing. Thesis)
UR-86-47	Dengody Sheshappa, MP	A Computer Design Model for Optimizing Fishing Vessel Designs Based on Techno-Economic Analysis. (Dr.Ing. Thesis)
UR-86-48	Vidar Aanesland, MH	A Theoretical and Numerical Study of Ship Wave Resistance. (Dr.Ing. Thesis)
UR-86-49	Heinz-Joachim Wessel, MK	Fracture Mechanics Analysis of Crack Growth in Plate Girders. (Dr.Ing. Thesis)
UR-86-50	Jon Taby, MK	Ultimate and Post-ultimate Strength of Dented Tubular Members. (Dr.Ing. Thesis)
UR-86-51	Walter Lian, MH	A Numerical Study of Two-Dimensional Separated Flow Past Bluff Bodies at Moderate KC-Numbers. (Dr.Ing. Thesis)
UR-86-52	Bjørn Sortland, MH	Force Measurements in Oscillating Flow on Ship Sections and Circular Cylinders in a U-Tube Water Tank. (Dr.Ing. Thesis)
UR-86-53	Kurt Strand, MM	A System Dynamic Approach to One-dimensional Fluid Flow. (Dr.Ing. Thesis)
UR-86-54	Arne Edvin Løken, MH	Three Dimensional Second Order Hydrodynamic Effects on Ocean Structures in Waves. (Dr.Ing. Thesis)
UR-86-55	Sigurd Falch, MH	A Numerical Study of Slamming of Two-Dimensional Bodies. (Dr.Ing. Thesis)
UR-87-56	Arne Braathen, MH	Application of a Vortex Tracking Method to the Prediction of Roll Damping of a Two-Dimension Floating Body. (Dr.Ing. Thesis)

UR-87-57	Bernt Leira, MK	Gaussian Vector Processes for Reliability Analysis involving Wave-Induced Load Effects. (Dr.Ing. Thesis)
UR-87-58	Magnus Småvik, MM	Thermal Load and Process Characteristics in a Two-Stroke Diesel Engine with Thermal Barriers (in Norwegian). (Dr.Ing. Thesis)
MTA-88-59	Bernt Arild Bremdal, MP	An Investigation of Marine Installation Processes – A Knowledge - Based Planning Approach. (Dr.Ing. Thesis)
MTA-88-60	Xu Jun, MK	Non-linear Dynamic Analysis of Space-framed Offshore Structures. (Dr.Ing. Thesis)
MTA-89-61	Gang Miao, MH	Hydrodynamic Forces and Dynamic Responses of Circular Cylinders in Wave Zones. (Dr.Ing. Thesis)
MTA-89-62	Martin Greenhow, MH	Linear and Non-Linear Studies of Waves and Floating Bodies. Part I and Part II. (Dr.Techn. Thesis)
MTA-89-63	Chang Li, MH	Force Coefficients of Spheres and Cubes in Oscillatory Flow with and without Current. (Dr.Ing. Thesis)
MTA-89-64	Hu Ying, MP	A Study of Marketing and Design in Development of Marine Transport Systems. (Dr.Ing. Thesis)
MTA-89-65	Arild Jæger, MH	Seakeeping, Dynamic Stability and Performance of a Wedge Shaped Planing Hull. (Dr.Ing. Thesis)
MTA-89-66	Chan Siu Hung, MM	The dynamic characteristics of tilting-pad bearings
MTA-89-67	Kim Wikstrøm, MP	Analysis av projekteringen for ett offshore projekt. (Licenciat-avhandling)
MTA-89-68	Jiao Guoyang, MK	Reliability Analysis of Crack Growth under Random Loading, considering Model Updating. (Dr.Ing. Thesis)
MTA-89-69	Arnt Olufsen, MK	Uncertainty and Reliability Analysis of Fixed Offshore Structures. (Dr.Ing. Thesis)
MTA-89-70	Wu Yu-Lin, MR	System Reliability Analyses of Offshore Structures using improved Truss and Beam Models. (Dr.Ing. Thesis)
MTA-90-71	Jan Roger Hoff, MH	Three-dimensional Green function of a vessel with forward speed in waves. (Dr.Ing. Thesis)
MTA-90-72	Rong Zhao, MH	Slow-Drift Motions of a Moored Two-Dimensional Body in Irregular Waves. (Dr.Ing. Thesis)
MTA-90-73	Atle Minsaas, MP	Economical Risk Analysis. (Dr.Ing. Thesis)
MTA-90-74	Knut-Aril Farnes, MK	Long-term Statistics of Response in Non-linear Marine Structures. (Dr.Ing. Thesis)
MTA-90-75	Torbjørn Sotberg, MK	Application of Reliability Methods for Safety Assessment of Submarine Pipelines. (Dr.Ing. Thesis)

		Thesis)
MTA-90-76	Zeuthen, Steffen, MP	SEAMAID. A computational model of the design process in a constraint-based logic programming environment. An example from the offshore domain. (Dr.Ing. Thesis)
MTA-91-77	Haagensen, Sven, MM	Fuel Dependant Cyclic Variability in a Spark Ignition Engine - An Optical Approach. (Dr.Ing. Thesis)
MTA-91-78	Løland, Geir, MH	Current forces on and flow through fish farms. (Dr.Ing. Thesis)
MTA-91-79	Hoen, Christopher, MK	System Identification of Structures Excited by Stochastic Load Processes. (Dr.Ing. Thesis)
MTA-91-80	Haugen, Stein, MK	Probabilistic Evaluation of Frequency of Collision between Ships and Offshore Platforms. (Dr.Ing. Thesis)
MTA-91-81	Sødahl, Nils, MK	Methods for Design and Analysis of Flexible Risers. (Dr.Ing. Thesis)
MTA-91-82	Ormberg, Harald, MK	Non-linear Response Analysis of Floating Fish Farm Systems. (Dr.Ing. Thesis)
MTA-91-83	Marley, Mark J., MK	Time Variant Reliability under Fatigue Degradation. (Dr.Ing. Thesis)
MTA-91-84	Krokstad, Jørgen R., MH	Second-order Loads in Multidirectional Seas. (Dr.Ing. Thesis)
MTA-91-85	Molteberg, Gunnar A., MM	The Application of System Identification Techniques to Performance Monitoring of Four Stroke Turbocharged Diesel Engines. (Dr.Ing. Thesis)
MTA-92-86	Mørch, Hans Jørgen Bjelke, MH	Aspects of Hydrofoil Design: with Emphasis on Hydrofoil Interaction in Calm Water. (Dr.Ing. Thesis)
MTA-92-87	Chan Siu Hung, MM	Nonlinear Analysis of Rotordynamic Instabilities in Highspeed Turbomachinery. (Dr.Ing. Thesis)
MTA-92-88	Bessason, Bjarni, MK	Assessment of Earthquake Loading and Response of Seismically Isolated Bridges. (Dr.Ing. Thesis)
MTA-92-89	Langli, Geir, MP	Improving Operational Safety through exploitation of Design Knowledge - an investigation of offshore platform safety. (Dr.Ing. Thesis)
MTA-92-90	Sævik, Svein, MK	On Stresses and Fatigue in Flexible Pipes. (Dr.Ing. Thesis)
MTA-92-91	Ask, Tor Ø., MM	Ignition and Flame Growth in Lean Gas-Air Mixtures. An Experimental Study with a Schlieren System. (Dr.Ing. Thesis)
MTA-86-92	Hessen, Gunnar, MK	Fracture Mechanics Analysis of Stiffened Tubular Members. (Dr.Ing. Thesis)

MTA-93-93	Steinebach, Christian, MM	Knowledge Based Systems for Diagnosis of Rotating Machinery. (Dr.Ing. Thesis)
MTA-93-94	Dalane, Jan Inge, MK	System Reliability in Design and Maintenance of Fixed Offshore Structures. (Dr.Ing. Thesis)
MTA-93-95	Steen, Sverre, MH	Cobblestone Effect on SES. (Dr.Ing. Thesis)
MTA-93-96	Karunakaran, Daniel, MK	Nonlinear Dynamic Response and Reliability Analysis of Drag-dominated Offshore Platforms. (Dr.Ing. Thesis)
MTA-93-97	Hagen, Arnulf, MP	The Framework of a Design Process Language. (Dr.Ing. Thesis)
MTA-93-98	Nordrik, Rune, MM	Investigation of Spark Ignition and Autoignition in Methane and Air Using Computational Fluid Dynamics and Chemical Reaction Kinetics. A Numerical Study of Ignition Processes in Internal Combustion Engines. (Dr.Ing. Thesis)
MTA-94-99	Passano, Elizabeth, MK	Efficient Analysis of Nonlinear Slender Marine Structures. (Dr.Ing. Thesis)
MTA-94-100	Kvålsvold, Jan, MH	Hydroelastic Modelling of Wetdeck Slamming on Multihull Vessels. (Dr.Ing. Thesis)
MTA-94-102	Bech, Sidsel M., MK	Experimental and Numerical Determination of Stiffness and Strength of GRP/PVC Sandwich Structures. (Dr.Ing. Thesis)
MTA-95-103	Paulsen, Hallvard, MM	A Study of Transient Jet and Spray using a Schlieren Method and Digital Image Processing. (Dr.Ing. Thesis)
MTA-95-104	Hovde, Geir Olav, MK	Fatigue and Overload Reliability of Offshore Structural Systems, Considering the Effect of Inspection and Repair. (Dr.Ing. Thesis)
MTA-95-105	Wang, Xiaozhi, MK	Reliability Analysis of Production Ships with Emphasis on Load Combination and Ultimate Strength. (Dr.Ing. Thesis)
MTA-95-106	Ulstein, Tore, MH	Nonlinear Effects of a Flexible Stern Seal Bag on Cobblestone Oscillations of an SES. (Dr.Ing. Thesis)
MTA-95-107	Solaas, Frøydis, MH	Analytical and Numerical Studies of Sloshing in Tanks. (Dr.Ing. Thesis)
MTA-95-108	Hellan, Øyvind, MK	Nonlinear Pushover and Cyclic Analyses in Ultimate Limit State Design and Reassessment of Tubular Steel Offshore Structures. (Dr.Ing. Thesis)
MTA-95-109	Hermundstad, Ole A., MK	Theoretical and Experimental Hydroelastic Analysis of High Speed Vessels. (Dr.Ing. Thesis)
MTA-96-110	Bratland, Anne K., MH	Wave-Current Interaction Effects on Large-Volume Bodies in Water of Finite Depth. (Dr.Ing. Thesis)
MTA-96-111	Herfjord, Kjell, MH	A Study of Two-dimensional Separated Flow by a Combination of the Finite Element Method and

		Navier-Stokes Equations. (Dr.Ing. Thesis)
MTA-96-112	Æsøy, Vilmar, MM	Hot Surface Assisted Compression Ignition in a Direct Injection Natural Gas Engine. (Dr.Ing. Thesis)
MTA-96-113	Eknes, Monika L., MK	Escalation Scenarios Initiated by Gas Explosions on Offshore Installations. (Dr.Ing. Thesis)
MTA-96-114	Erikstad, Stein O., MP	A Decision Support Model for Preliminary Ship Design. (Dr.Ing. Thesis)
MTA-96-115	Pedersen, Egil, MH	A Nautical Study of Towed Marine Seismic Streamer Cable Configurations. (Dr.Ing. Thesis)
MTA-97-116	Moksnes, Paul O., MM	Modelling Two-Phase Thermo-Fluid Systems Using Bond Graphs. (Dr.Ing. Thesis)
MTA-97-117	Halse, Karl H., MK	On Vortex Shedding and Prediction of Vortex-Induced Vibrations of Circular Cylinders. (Dr.Ing. Thesis)
MTA-97-118	Igland, Ragnar T., MK	Reliability Analysis of Pipelines during Laying, considering Ultimate Strength under Combined Loads. (Dr.Ing. Thesis)
MTA-97-119	Pedersen, Hans-P., MP	Levendefissteknologi for fiskefartøy. (Dr.Ing. Thesis)
MTA-98-120	Vikestad, Kyrre, MK	Multi-Frequency Response of a Cylinder Subjected to Vortex Shedding and Support Motions. (Dr.Ing. Thesis)
MTA-98-121	Azadi, Mohammad R. E., MK	Analysis of Static and Dynamic Pile-Soil-Jacket Behaviour. (Dr.Ing. Thesis)
MTA-98-122	Ulltang, Terje, MP	A Communication Model for Product Information. (Dr.Ing. Thesis)
MTA-98-123	Torbergsen, Erik, MM	Impeller/Diffuser Interaction Forces in Centrifugal Pumps. (Dr.Ing. Thesis)
MTA-98-124	Hansen, Edmond, MH	A Discrete Element Model to Study Marginal Ice Zone Dynamics and the Behaviour of Vessels Moored in Broken Ice. (Dr.Ing. Thesis)
MTA-98-125	Videiro, Paulo M., MK	Reliability Based Design of Marine Structures. (Dr.Ing. Thesis)
MTA-99-126	Mainçon, Philippe, MK	Fatigue Reliability of Long Welds Application to Titanium Risers. (Dr.Ing. Thesis)
MTA-99-127	Haugen, Elin M., MH	Hydroelastic Analysis of Slamming on Stiffened Plates with Application to Catamaran Wetdecks. (Dr.Ing. Thesis)
MTA-99-128	Langhelle, Nina K., MK	Experimental Validation and Calibration of Nonlinear Finite Element Models for Use in Design of Aluminium Structures Exposed to Fire. (Dr.Ing. Thesis)
MTA-99-	Berstad, Are J., MK	Calculation of Fatigue Damage in Ship Structures.

129		(Dr.Ing. Thesis)
MTA-99-130	Andersen, Trond M., MM	Short Term Maintenance Planning. (Dr.Ing. Thesis)
MTA-99-131	Tveiten, Bård Wathne, MK	Fatigue Assessment of Welded Aluminium Ship Details. (Dr.Ing. Thesis)
MTA-99-132	Søreide, Fredrik, MP	Applications of underwater technology in deep water archaeology. Principles and practice. (Dr.Ing. Thesis)
MTA-99-133	Tønnessen, Rune, MH	A Finite Element Method Applied to Unsteady Viscous Flow Around 2D Blunt Bodies With Sharp Corners. (Dr.Ing. Thesis)
MTA-99-134	Elvekrok, Dag R., MP	Engineering Integration in Field Development Projects in the Norwegian Oil and Gas Industry. The Supplier Management of Norne. (Dr.Ing. Thesis)
MTA-99-135	Fagerholt, Kjetil, MP	Optimeringsbaserte Metoder for Ruteplanlegging innen skipsfart. (Dr.Ing. Thesis)
MTA-99-136	Bysveen, Marie, MM	Visualization in Two Directions on a Dynamic Combustion Rig for Studies of Fuel Quality. (Dr.Ing. Thesis)
MTA-2000-137	Storteig, Eskild, MM	Dynamic characteristics and leakage performance of liquid annular seals in centrifugal pumps. (Dr.Ing. Thesis)
MTA-2000-138	Sagli, Gro, MK	Model uncertainty and simplified estimates of long term extremes of hull girder loads in ships. (Dr.Ing. Thesis)
MTA-2000-139	Tronstad, Harald, MK	Nonlinear analysis and design of cable net structures like fishing gear based on the finite element method. (Dr.Ing. Thesis)
MTA-2000-140	Kroneberg, André, MP	Innovation in shipping by using scenarios. (Dr.Ing. Thesis)
MTA-2000-141	Haslum, Herbjørn Alf, MH	Simplified methods applied to nonlinear motion of spar platforms. (Dr.Ing. Thesis)
MTA-2001-142	Samdal, Ole Johan, MM	Modelling of Degradation Mechanisms and Stressor Interaction on Static Mechanical Equipment Residual Lifetime. (Dr.Ing. Thesis)
MTA-2001-143	Baarholm, Rolf Jarle, MH	Theoretical and experimental studies of wave impact underneath decks of offshore platforms. (Dr.Ing. Thesis)
MTA-2001-144	Wang, Lihua, MK	Probabilistic Analysis of Nonlinear Wave-induced Loads on Ships. (Dr.Ing. Thesis)
MTA-2001-145	Kristensen, Odd H. Holt, MK	Ultimate Capacity of Aluminium Plates under Multiple Loads, Considering HAZ Properties. (Dr.Ing. Thesis)
MTA-2001-146	Greco, Marilena, MH	A Two-Dimensional Study of Green-Water

			Loading. (Dr.Ing. Thesis)
MTA-2001-147	Heggelund, Svein E., MK		Calculation of Global Design Loads and Load Effects in Large High Speed Catamarans. (Dr.Ing. Thesis)
MTA-2001-148	Babalola, Olusegun T., MK		Fatigue Strength of Titanium Risers – Defect Sensitivity. (Dr.Ing. Thesis)
MTA-2001-149	Mohammed, Abuu K., MK		Nonlinear Shell Finite Elements for Ultimate Strength and Collapse Analysis of Ship Structures. (Dr.Ing. Thesis)
MTA-2002-150	Holmedal, Lars E., MH		Wave-current interactions in the vicinity of the sea bed. (Dr.Ing. Thesis)
MTA-2002-151	Rognebakke, Olav F., MH		Sloshing in rectangular tanks and interaction with ship motions. (Dr.Ing. Thesis)
MTA-2002-152	Lader, Pål Furset, MH		Geometry and Kinematics of Breaking Waves. (Dr.Ing. Thesis)
MTA-2002-153	Yang, Qinzhen, MH		Wash and wave resistance of ships in finite water depth. (Dr.Ing. Thesis)
MTA-2002-154	Melhus, Øyvind, MM		Utilization of VOC in Diesel Engines. Ignition and combustion of VOC released by crude oil tankers. (Dr.Ing. Thesis)
MTA-2002-155	Ronæss, Marit, MH		Wave Induced Motions of Two Ships Advancing on Parallel Course. (Dr.Ing. Thesis)
MTA-2002-156	Økland, Ole D., MK		Numerical and experimental investigation of whipping in twin hull vessels exposed to severe wet deck slamming. (Dr.Ing. Thesis)
MTA-2002-157	Ge, Chunhua, MK		Global Hydroelastic Response of Catamarans due to Wet Deck Slamming. (Dr.Ing. Thesis)
MTA-2002-158	Byklum, Eirik, MK		Nonlinear Shell Finite Elements for Ultimate Strength and Collapse Analysis of Ship Structures. (Dr.Ing. Thesis)
IMT-2003-1	Chen, Haibo, MK		Probabilistic Evaluation of FPSO-Tanker Collision in Tandem Offloading Operation. (Dr.Ing. Thesis)
IMT-2003-2	Skaugset, Kjetil Bjørn, MK		On the Suppression of Vortex Induced Vibrations of Circular Cylinders by Radial Water Jets. (Dr.Ing. Thesis)
IMT-2003-3	Chezhan, Muthu		Three-Dimensional Analysis of Slamming. (Dr.Ing. Thesis)
IMT-2003-4	Buhaug, Øyvind		Deposit Formation on Cylinder Liner Surfaces in Medium Speed Engines. (Dr.Ing. Thesis)
IMT-2003-5	Tregde, Vidar		Aspects of Ship Design: Optimization of Aft Hull with Inverse Geometry Design. (Dr.Ing. Thesis)
IMT-	Wist, Hanne Therese		Statistical Properties of Successive Ocean Wave

2003-6		Parameters. (Dr.Ing. Thesis)
IMT-2004-7	Ransau, Samuel	Numerical Methods for Flows with Evolving Interfaces. (Dr.Ing. Thesis)
IMT-2004-8	Soma, Torkel	Blue-Chip or Sub-Standard. A data interrogation approach of identity safety characteristics of shipping organization. (Dr.Ing. Thesis)
IMT-2004-9	Ersdal, Svein	An experimental study of hydrodynamic forces on cylinders and cables in near axial flow. (Dr.Ing. Thesis)
IMT-2005-10	Brodtkorb, Per Andreas	The Probability of Occurrence of Dangerous Wave Situations at Sea. (Dr.Ing. Thesis)
IMT-2005-11	Yttervik, Rune	Ocean current variability in relation to offshore engineering. (Dr.Ing. Thesis)
IMT-2005-12	Fredheim, Arne	Current Forces on Net-Structures. (Dr.Ing. Thesis)
IMT-2005-13	Heggernes, Kjetil	Flow around marine structures. (Dr.Ing. Thesis)
IMT-2005-14	Fouques, Sebastien	Lagrangian Modelling of Ocean Surface Waves and Synthetic Aperture Radar Wave Measurements. (Dr.Ing. Thesis)
IMT-2006-15	Holm, Håvard	Numerical calculation of viscous free surface flow around marine structures. (Dr.Ing. Thesis)
IMT-2006-16	Bjørheim, Lars G.	Failure Assessment of Long Through Thickness Fatigue Cracks in Ship Hulls. (Dr.Ing. Thesis)
IMT-2006-17	Hansson, Lisbeth	Safety Management for Prevention of Occupational Accidents. (Dr.Ing. Thesis)
IMT-2006-18	Zhu, Xinying	Application of the CIP Method to Strongly Nonlinear Wave-Body Interaction Problems. (Dr.Ing. Thesis)
IMT-2006-19	Reite, Karl Johan	Modelling and Control of Trawl Systems. (Dr.Ing. Thesis)
IMT-2006-20	Smogeli, Øyvind Notland	Control of Marine Propellers. From Normal to Extreme Conditions. (Dr.Ing. Thesis)
IMT-2007-21	Storhaug, Gaute	Experimental Investigation of Wave Induced Vibrations and Their Effect on the Fatigue Loading of Ships. (Dr.Ing. Thesis)
IMT-2007-22	Sun, Hui	A Boundary Element Method Applied to Strongly Nonlinear Wave-Body Interaction Problems. (PhD Thesis, CeSOS)
IMT-2007-23	Rustad, Anne Marthine	Modelling and Control of Top Tensioned Risers. (PhD Thesis, CeSOS)
IMT-2007-24	Johansen, Vegar	Modelling flexible slender system for real-time simulations and control applications
IMT-2007-25	Wroldsen, Anders Sunde	Modelling and control of tensegrity structures.

(PhD Thesis, CeSOS)

IMT-2007-26	Aronsen, Kristoffer Høye	An experimental investigation of in-line and combined inline and cross flow vortex induced vibrations. (Dr. avhandling, IMT)
IMT-2007-27	Gao, Zhen	Stochastic Response Analysis of Mooring Systems with Emphasis on Frequency-domain Analysis of Fatigue due to Wide-band Response Processes (PhD Thesis, CeSOS)
IMT-2007-28	Thorstensen, Tom Anders	Lifetime Profit Modelling of Ageing Systems Utilizing Information about Technical Condition. (Dr.ing. thesis, IMT)
IMT-2008-29	Refsnes, Jon Erling Gorset	Nonlinear Model-Based Control of Slender Body AUVs (PhD Thesis, IMT)
IMT-2008-30	Berntsen, Per Ivar B.	Structural Reliability Based Position Mooring. (PhD-Thesis, IMT)
IMT-2008-31	Ye, Naiquan	Fatigue Assessment of Aluminium Welded Box-stiffener Joints in Ships (Dr.ing. thesis, IMT)
IMT-2008-32	Radan, Damir	Integrated Control of Marine Electrical Power Systems. (PhD-Thesis, IMT)
IMT-2008-33	Thomassen, Paul	Methods for Dynamic Response Analysis and Fatigue Life Estimation of Floating Fish Cages. (Dr.ing. thesis, IMT)
IMT-2008-34	Pákozdi, Csaba	A Smoothed Particle Hydrodynamics Study of Two-dimensional Nonlinear Sloshing in Rectangular Tanks. (Dr.ing.thesis, IMT/ CeSOS)
IMT-2007-35	Grytøyr, Guttorm	A Higher-Order Boundary Element Method and Applications to Marine Hydrodynamics. (Dr.ing.thesis, IMT)
IMT-2008-36	Drummen, Ingo	Experimental and Numerical Investigation of Nonlinear Wave-Induced Load Effects in Containerships considering Hydroelasticity. (PhD thesis, CeSOS)
IMT-2008-37	Skejic, Renato	Maneuvering and Seakeeping of a Singel Ship and of Two Ships in Interaction. (PhD-Thesis, CeSOS)
IMT-2008-38	Harlem, Alf	An Age-Based Replacement Model for Repairable Systems with Attention to High-Speed Marine Diesel Engines. (PhD-Thesis, IMT)
IMT-2008-39	Alsos, Hagbart S.	Ship Grounding. Analysis of Ductile Fracture, Bottom Damage and Hull Girder Response. (PhD-thesis, IMT)
IMT-2008-40	Graczyk, Mateusz	Experimental Investigation of Sloshing Loading and Load Effects in Membrane LNG Tanks Subjected to Random Excitation. (PhD-thesis, CeSOS)
IMT-2008-41	Taghypour, Reza	Efficient Prediction of Dynamic Response for Flexible amd Multi-body Marine Structures. (PhD-

thesis, CeSOS)

IMT-2008-42	Ruth, Eivind	Propulsion control and thrust allocation on marine vessels. (PhD thesis, CeSOS)
IMT-2008-43	Nystad, Bent Helge	Technical Condition Indexes and Remaining Useful Life of Aggregated Systems. PhD thesis, IMT
IMT-2008-44	Soni, Prashant Kumar	Hydrodynamic Coefficients for Vortex Induced Vibrations of Flexible Beams, PhD thesis, CeSOS
IMT-2009-45	Amlashi, Hadi K.K.	Ultimate Strength and Reliability-based Design of Ship Hulls with Emphasis on Combined Global and Local Loads. PhD Thesis, IMT
IMT-2009-46	Pedersen, Tom Arne	Bond Graph Modelling of Marine Power Systems. PhD Thesis, IMT
IMT-2009-47	Kristiansen, Trygve	Two-Dimensional Numerical and Experimental Studies of Piston-Mode Resonance. PhD-Thesis, CeSOS
IMT-2009-48	Ong, Muk Chen	Applications of a Standard High Reynolds Number Model and a Stochastic Scour Prediction Model for Marine Structures. PhD-thesis, IMT
IMT-2009-49	Hong, Lin	Simplified Analysis and Design of Ships subjected to Collision and Grounding. PhD-thesis, IMT
IMT-2009-50	Koushan, Kamran	Vortex Induced Vibrations of Free Span Pipelines, PhD thesis, IMT
IMT-2009-51	Korsvik, Jarl Eirik	Heuristic Methods for Ship Routing and Scheduling. PhD-thesis, IMT
IMT-2009-52	Lee, Jihoon	Experimental Investigation and Numerical in Analyzing the Ocean Current Displacement of Longlines. Ph.d.-Thesis, IMT.
IMT-2009-53	Vestbøstad, Tone Gran	A Numerical Study of Wave-in-Deck Impact using a Two-Dimensional Constrained Interpolation Profile Method, Ph.d.thesis, CeSOS.
IMT-2009-54	Bruun, Kristine	Bond Graph Modelling of Fuel Cells for Marine Power Plants. Ph.d.-thesis, IMT
IMT 2009-55	Holstad, Anders	Numerical Investigation of Turbulence in a Sekwed Three-Dimensional Channel Flow, Ph.d.-thesis, IMT.
IMT 2009-56	Ayala-Uraga, Efen	Reliability-Based Assessment of Deteriorating Ship-shaped Offshore Structures, Ph.d.-thesis, IMT
IMT 2009-57	Kong, Xiangjun	A Numerical Study of a Damaged Ship in Beam Sea Waves. Ph.d.-thesis, IMT/CeSOS.
IMT 2010-58	Kristiansen, David	Wave Induced Effects on Floaters of Aquaculture Plants, Ph.d.-thesis, CeSOS.

IMT 2010-59	Ludvigsen, Martin	An ROV-Toolbox for Optical and Acoustic Scientific Seabed Investigation. Ph.d.-thesis IMT.
IMT 2010-60	Hals, Jørgen	Modelling and Phase Control of Wave-Energy Converters. Ph.d.thesis, CeSOS.
IMT 2010- 61	Shu, Zhi	Uncertainty Assessment of Wave Loads and Ultimate Strength of Tankers and Bulk Carriers in a Reliability Framework. Ph.d. Thesis, IMT/ CeSOS
IMT 2010-62	Shao, Yanlin	Numerical Potential-Flow Studies on Weakly-Nonlinear Wave-Body Interactions with/without Small Forward Speed, Ph.d.thesis,CeSOS.
IMT 2010-63	Califano, Andrea	Dynamic Loads on Marine Propellers due to Intermittent Ventilation. Ph.d.thesis, IMT.
IMT 2010-64	El Khoury, George	Numerical Simulations of Massively Separated Turbulent Flows, Ph.d.-thesis, IMT
IMT 2010-65	Seim, Knut Sponheim	Mixing Process in Dense Overflows with Emphasis on the Faroe Bank Channel Overflow. Ph.d.thesis, IMT
IMT 2010-66	Jia, Huirong	Structural Analysis of Intact and Damaged Ships in a Collision Risk Analysis Perspective. Ph.d.thesis CeSoS.
IMT 2010-67	Jiao, Linlin	Wave-Induced Effects on a Pontoon-type Very Large Floating Structures (VLFS). Ph.D.-thesis, CeSOS.
IMT 2010-68	Abrahamsen, Bjørn Christian	Sloshing Induced Tank Roof with Entrapped Air Pocket. Ph.d.thesis, CeSOS.
IMT 2011-69	Karimirad, Madjid	Stochastic Dynamic Response Analysis of Spar-Type Wind Turbines with Catenary or Taut Mooring Systems. Ph.d.-thesis, CeSOS.
IMT - 2011-70	Erlend Meland	Condition Monitoring of Safety Critical Valves. Ph.d.-thesis, IMT.
IMT – 2011-71	Yang, Limin	Stochastic Dynamic System Analysis of Wave Energy Converter with Hydraulic Power Take-Off, with Particular Reference to Wear Damage Analysis, Ph.d. Thesis, CeSOS.
IMT – 2011-72	Visscher, Jan	Application of Particle Image Velocimetry on Turbulent Marine Flows, Ph.d.Thesis, IMT.
IMT – 2011-73	Su, Biao	Numerical Predictions of Global and Local Ice Loads on Ships. Ph.d.Thesis, CeSOS.
IMT – 2011-74	Liu, Zhenhui	Analytical and Numerical Analysis of Iceberg Collision with Ship Structures. Ph.d.Thesis, IMT.
IMT – 2011-75	Aarsæther, Karl Gunnar	Modeling and Analysis of Ship Traffic by Observation and Numerical Simulation. Ph.d.Thesis, IMT.

Imt – 2011-76	Wu, Jie	Hydrodynamic Force Identification from Stochastic Vortex Induced Vibration Experiments with Slender Beams. Ph.d.Thesis, IMT.
Imt – 2011-77	Amini, Hamid	Azimuth Propulsors in Off-design Conditions. Ph.d.Thesis, IMT.
IMT – 2011-78	Nguyen, Tan-Hoi	Toward a System of Real-Time Prediction and Monitoring of Bottom Damage Conditions During Ship Grounding. Ph.d.thesis, IMT.
IMT- 2011-79	Tavakoli, Mohammad T.	Assessment of Oil Spill in Ship Collision and Grounding, Ph.d.thesis, IMT.
IMT- 2011-80	Guo, Bingjie	Numerical and Experimental Investigation of Added Resistance in Waves. Ph.d.Thesis, IMT.
IMT- 2011-81	Chen, Qiaofeng	Ultimate Strength of Aluminium Panels, considering HAZ Effects, IMT
IMT- 2012-82	Kota, Ravikiran S.	Wave Loads on Decks of Offshore Structures in Random Seas, CeSOS.
IMT- 2012-83	Sten, Ronny	Dynamic Simulation of Deep Water Drilling Risers with Heave Compensating System, IMT.
IMT- 2012-84	Berle, Øyvind	Risk and resilience in global maritime supply chains, IMT.
IMT- 2012-85	Fang, Shaoji	Fault Tolerant Position Mooring Control Based on Structural Reliability, CeSOS.
IMT- 2012-86	You, Jikun	Numerical studies on wave forces and moored ship motions in intermediate and shallow water, CeSOS.
IMT- 2012-87	Xiang ,Xu	Maneuvering of two interacting ships in waves, CeSOS
IMT- 2012-88	Dong, Wenbin	Time-domain fatigue response and reliability analysis of offshore wind turbines with emphasis on welded tubular joints and gear components, CeSOS
IMT- 2012-89	Zhu, Suji	Investigation of Wave-Induced Nonlinear Load Effects in Open Ships considering Hull Girder Vibrations in Bending and Torsion, CeSOS
IMT- 2012-90	Zhou, Li	Numerical and Experimental Investigation of Station-keeping in Level Ice, CeSOS
IMT- 2012-91	Ushakov, Sergey	Particulate matter emission characteristics from diesel engines operating on conventional and alternative marine fuels, IMT
IMT- 2013-1	Yin, Decao	Experimental and Numerical Analysis of Combined In-line and Cross-flow Vortex Induced Vibrations, CeSOS

IMT-2013-2	Kurniawan, Adi	Modelling and geometry optimisation of wave energy converters, CeSOS
IMT-2013-3	Al Ryati, Nabil	Technical condition indexes doe auxiliary marine diesel engines, IMT
IMT-2013-4	Firoozkoohi, Reza	Experimental, numerical and analytical investigation of the effect of screens on sloshing, CeSOS
IMT-2013-5	Ommani, Babak	Potential-Flow Predictions of a Semi-Displacement Vessel Including Applications to Calm Water Broaching, CeSOS
IMT-2013-6	Xing, Yihan	Modelling and analysis of the gearbox in a floating spar-type wind turbine, CeSOS
IMT-7-2013	Balland, Océane	Optimization models for reducing air emissions from ships, IMT
IMT-8-2013	Yang, Dan	Transitional wake flow behind an inclined flat plate-----Computation and analysis, IMT
IMT-9-2013	Abdillah, Suyuthi	Prediction of Extreme Loads and Fatigue Damage for a Ship Hull due to Ice Action, IMT
IMT-10-2013	Ramirez, Pedro Agustin Pérez	Ageing management and life extension of technical systems- Concepts and methods applied to oil and gas facilities, IMT
IMT-11-2013	Chuang, Zhenju	Experimental and Numerical Investigation of Speed Loss due to Seakeeping and Maneuvering. IMT
IMT-12-2013	Etemaddar, Mahmoud	Load and Response Analysis of Wind Turbines under Atmospheric Icing and Controller System Faults with Emphasis on Spar Type Floating Wind Turbines, IMT
IMT-13-2013	Lindstad, Haakon	Strategies and measures for reducing maritime CO2 emissons, IMT
IMT-14-2013	Haris, Sabril	Damage interaction analysis of ship collisions, IMT
IMT-15-2013	Shainee, Mohamed	Conceptual Design, Numerical and Experimental Investigation of a SPM Cage Concept for Offshore Mariculture, IMT
IMT-16-2013	Gansel, Lars	Flow past porous cylinders and effects of biofouling and fish behavior on the flow in and around Atlantic salmon net cages, IMT
IMT-17-2013	Gaspar, Henrique	Handling Aspects of Complexity in Conceptual Ship Design, IMT
IMT-18-2013	Thys, Maxime	Theoretical and Experimental Investigation of a Free Running Fishing Vessel at Small Frequency of Encounter, CeSOS
IMT-19-2013	Aglen, Ida	VIV in Free Spanning Pipelines, CeSOS

IMT-1-2014	Song, An	Theoretical and experimental studies of wave diffraction and radiation loads on a horizontally submerged perforated plate, CeSOS
IMT-2-2014	Rogne, Øyvind Ygre	Numerical and Experimental Investigation of a Hinged 5-body Wave Energy Converter, CeSOS
IMT-3-2014	Dai, Lijuan	Safe and efficient operation and maintenance of offshore wind farms ,IMT
IMT-4-2014	Bachynski, Erin Elizabeth	Design and Dynamic Analysis of Tension Leg Platform Wind Turbines, CeSOS
IMT-5-2014	Wang, Jingbo	Water Entry of Freefall Wedged – Wedge motions and Cavity Dynamics, CeSOS
IMT-6-2014	Kim, Ekaterina	Experimental and numerical studies related to the coupled behavior of ice mass and steel structures during accidental collisions, IMT
IMT-7-2014	Tan, Xiang	Numerical investigation of ship's continuous- mode icebreaking in level ice, CeSOS
IMT-8-2014	Muliawan, Made Jaya	Design and Analysis of Combined Floating Wave and Wind Power Facilities, with Emphasis on Extreme Load Effects of the Mooring System, CeSOS
IMT-9-2014	Jiang, Zhiyu	Long-term response analysis of wind turbines with an emphasis on fault and shutdown conditions, IMT
IMT-10-2014	Dukan, Fredrik	ROV Motion Control Systems, IMT
IMT-11-2014	Grimsmo, Nils I.	Dynamic simulations of hydraulic cylinder for heave compensation of deep water drilling risers, IMT
IMT-12-2014	Kvittem, Marit I.	Modelling and response analysis for fatigue design of a semisubmersible wind turbine, CeSOS
IMT-13-2014	Akhtar, Juned	The Effects of Human Fatigue on Risk at Sea, IMT
IMT-14-2014	Syahroni, Nur	Fatigue Assessment of Welded Joints Taking into Account Effects of Residual Stress, IMT
IMT-1-2015	Böckmann, Eirik	Wave Propulsion of ships, IMT
IMT-2-2015	Wang, Kai	Modelling and dynamic analysis of a semi-submersible floating vertical axis wind turbine, CeSOS
IMT-3-2015	Fredriksen, Arnt Gunvald	A numerical and experimental study of a two-dimensional body with moonpool in waves and current, CeSOS
IMT-4-2015	Jose Patricio Gallardo Canabes	Numerical studies of viscous flow around bluff bodies, IMT

IMT-5-2015	Vegard Longva	Formulation and application of finite element techniques for slender marine structures subjected to contact interactions, IMT
IMT-6-2015	Jacobus De Vaal	Aerodynamic modelling of floating wind turbines, CeSOS
IMT-7-2015	Fachri Nasution	Fatigue Performance of Copper Power Conductors, IMT
IMT-8-2015	Oleh I Karpa	Development of bivariate extreme value distributions for applications in marine technology, CeSOS
IMT-9-2015	Daniel de Almeida Fernandes	An output feedback motion control system for ROVs, AMOS
IMT-10-2015	Bo Zhao	Particle Filter for Fault Diagnosis: Application to Dynamic Positioning Vessel and Underwater Robotics, CeSOS
IMT-11-2015	Wenting Zhu	Impact of emission allocation in maritime transportation, IMT
IMT-12-2015	Amir Rasekhi Nejad	Dynamic Analysis and Design of Gearboxes in Offshore Wind Turbines in a Structural Reliability Perspective, CeSOS
IMT-13-2015	Arturo Jesús Ortega Malca	Dynamic Response of Flexibles Risers due to Unsteady Slug Flow, CeSOS
IMT-14-2015	Dagfinn Husjord	Guidance and decision-support system for safe navigation of ships operating in close proximity, IMT
IMT-15-2015	Anirban Bhattacharyya	Ducted Propellers: Behaviour in Waves and Scale Effects, IMT
IMT-16-2015	Qin Zhang	Image Processing for Ice Parameter Identification in Ice Management, IMT
IMT-1-2016	Vincentius Rumawas	Human Factors in Ship Design and Operation: An Experiential Learning, IMT
IMT-2-2016	Martin Storheim	Structural response in ship-platform and ship-ice collisions, IMT
IMT-3-2016	Mia Abrahamsen Prsic	Numerical Simulations of the Flow around single and Tandem Circular Cylinders Close to a Plane Wall, IMT
IMT-4-2016	Tufan Arslan	Large-eddy simulations of cross-flow around ship sections, IMT

IMT-5-2016	Pierre Yves-Henry	Parametrisation of aquatic vegetation in hydraulic and coastal research,IMT
IMT-6-2016	Lin Li	Dynamic Analysis of the Instalation of Monopiles for Offshore Wind Turbines, CeSOS
IMT-7-2016	Øivind Kåre Kjerstad	Dynamic Positioning of Marine Vessels in Ice, IMT
IMT-8-2016	Xiaopeng Wu	Numerical Analysis of Anchor Handling and Fish Trawling Operations in a Safety Perspective, CeSOS
IMT-9-2016	Zhengshun Cheng	Integrated Dynamic Analysis of Floating Vertical Axis Wind Turbines, CeSOS
IMT-10-2016	Ling Wan	Experimental and Numerical Study of a Combined Offshore Wind and Wave Energy Converter Concept
IMT-11-2016	Wei Chai	Stochastic dynamic analysis and reliability evaluation of the roll motion for ships in random seas, CeSOS
IMT-12-2016	Øyvind Selnes Patricksson	Decision support for conceptual ship design with focus on a changing life cycle and future uncertainty, IMT
IMT-13-2016	Mats Jørgen Thorsen	Time domain analysis of vortex-induced vibrations, IMT
IMT-14-2016	Edgar McGuinness	Safety in the Norwegian Fishing Fleet – Analysis and measures for improvement, IMT
IMT-15-2016	Sepideh Jafarzadeh	Energy efficiency and emission abatement in the fishing fleet, IMT
IMT-16-2016	Wilson Ivan Guachamin Acero	Assessment of marine operations for offshore wind turbine installation with emphasis on response-based operational limits, IMT
IMT-17-2016	Mauro Candeloro	Tools and Methods for Autonomous Operations on Seabed and Water Coumn using Underwater Vehicles, IMT
IMT-18-2016	Valentin Chabaud	Real-Time Hybrid Model Testing of Floating Wind Tubines, IMT
IMT-1-2017	Mohammad Saud Afzal	Three-dimensional streaming in a sea bed boundary layer
IMT-2-2017	Peng Li	A Theoretical and Experimental Study of Wave-induced Hydroelastic Response of a Circular Floating Collar
IMT-3-2017	Martin Bergström	A simulation-based design method for arctic maritime transport systems

IMT-4-2017	Bhushan Taskar	The effect of waves on marine propellers and propulsion
IMT-5-2017	Mohsen Bardestani	A two-dimensional numerical and experimental study of a floater with net and sinker tube in waves and current
IMT-6-2017	Fatemeh Hoseini Dadmarzi	Direct Numerical Simulation of turbulent wakes behind different plate configurations
IMT-7-2017	Michel R. Miyazaki	Modeling and control of hybrid marine power plants
IMT-8-2017	Giri Rajasekhar Gunnu	Safety and efficiency enhancement of anchor handling operations with particular emphasis on the stability of anchor handling vessels
IMT-9-2017	Kevin Koosup Yum	Transient Performance and Emissions of a Turbocharged Diesel Engine for Marine Power Plants
IMT-10-2017	Zhaolong Yu	Hydrodynamic and structural aspects of ship collisions
IMT-11-2017	Martin Hassel	Risk Analysis and Modelling of Allisions between Passing Vessels and Offshore Installations
IMT-12-2017	Astrid H. Brodtkorb	Hybrid Control of Marine Vessels – Dynamic Positioning in Varying Conditions
IMT-13-2017	Kjersti Bruserud	Simultaneous stochastic model of waves and current for prediction of structural design loads
IMT-14-2017	Finn-Idar Grøtta Giske	Long-Term Extreme Response Analysis of Marine Structures Using Inverse Reliability Methods
IMT-15-2017	Stian Skjong	Modeling and Simulation of Maritime Systems and Operations for Virtual Prototyping using co-Simulations
IMT-1-2018	Yingguang Chu	Virtual Prototyping for Marine Crane Design and Operations
IMT-2-2018	Sergey Gavrilin	Validation of ship manoeuvring simulation models
IMT-3-2018	Jeevith Hegde	Tools and methods to manage risk in autonomous subsea inspection, maintenance and repair operations
IMT-4-2018	Ida M. Strand	Sea Loads on Closed Flexible Fish Cages
IMT-5-2018	Erlend Kvinge Jørgensen	Navigation and Control of Underwater Robotic Vehicles

IMT-6-2018	Bård Stovner	Aided Inertial Navigation of Underwater Vehicles
IMT-7-2018	Erlend Liavåg Grotle	Thermodynamic Response Enhanced by Sloshing in Marine LNG Fuel Tanks
IMT-8-2018	Børge Rokseth	Safety and Verification of Advanced Maritime Vessels
IMT-9-2018	Jan Vidar Ulveseter	Advances in Semi-Empirical Time Domain Modelling of Vortex-Induced Vibrations
IMT-10-2018	Chenyu Luan	Design and analysis for a steel braceless semi-submersible hull for supporting a 5-MW horizontal axis wind turbine
IMT-11-2018	Carl Fredrik Rehn	Ship Design under Uncertainty
IMT-12-2018	Øyvind Ødegård	Towards Autonomous Operations and Systems in Marine Archaeology
IMT-13-2018	Stein Melvær Nornes	Guidance and Control of Marine Robotics for Ocean Mapping and Monitoring
IMT-14-2018	Petter Norgren	Autonomous Underwater Vehicles in Arctic Marine Operations: Arctic marine research and ice monitoring
IMT-15-2018	Minjoo Choi	Modular Adaptable Ship Design for Handling Uncertainty in the Future Operating Context
MT-16-2018	Ole Alexander Eidsvik	Dynamics of Remotely Operated Underwater Vehicle Systems
IMT-17-2018	Mahdi Ghane	Fault Diagnosis of Floating Wind Turbine Drivetrain- Methodologies and Applications
IMT-18-2018	Christoph Alexander Thieme	Risk Analysis and Modelling of Autonomous Marine Systems
IMT-19-2018	Yugao Shen	Operational limits for floating-collar fish farms in waves and current, without and with well-boat presence
IMT-20-2018	Tianjiao Dai	Investigations of Shear Interaction and Stresses in Flexible Pipes and Umbilicals
IMT-21-2018	Sigurd Solheim Pettersen	Resilience by Latent Capabilities in Marine Systems
IMT-22-2018	Thomas Sauder	Fidelity of Cyber-physical Empirical Methods. Application to the Active Truncation of Slender Marine Structures
IMT-23-2018	Jan-Tore Horn	Statistical and Modelling Uncertainties in the Design of Offshore Wind Turbines

IMT-24-2018	Anna Swider	Data Mining Methods for the Analysis of Power Systems of Vessels
IMT-1-2019	Zhao He	Hydrodynamic study of a moored fish farming cage with fish influence
IMT-2-2019	Isar Ghamari	Numerical and Experimental Study on the Ship Parametric Roll Resonance and the Effect of Anti-Roll Tank
IMT-3-2019	Håkon Strandenes	Turbulent Flow Simulations at Higher Reynolds Numbers
IMT-4-2019	Siri Mariane Holen	Safety in Norwegian Fish Farming – Concepts and Methods for Improvement
IMT-5-2019	Ping Fu	Reliability Analysis of Wake-Induced Riser Collision
IMT-6-2019	Vladimir Krivopolianskii	Experimental Investigation of Injection and Combustion Processes in Marine Gas Engines using Constant Volume Rig
IMT-7-2019	Anna Maria Kozłowska	Hydrodynamic Loads on Marine Propellers Subject to Ventilation and out of Water Condition.
IMT-8-2019	Hans-Martin Heyn	Motion Sensing on Vessels Operating in Sea Ice: A Local Ice Monitoring System for Transit and Stationkeeping Operations under the Influence of Sea Ice
IMT-9-2019	Stefan Vilsen	Method for Real-Time Hybrid Model Testing of Ocean Structures – Case on Slender Marine Systems
IMT-10-2019	Finn-Christian W. Hanssen	Non-Linear Wave-Body Interaction in Severe Waves
IMT-11-2019	Trygve Olav Fossum	Adaptive Sampling for Marine Robotics
IMT-12-2019	Jørgen Bremnes Nielsen	Modeling and Simulation for Design Evaluation
IMT-13-2019	Yuna Zhao	Numerical modelling and dynamic analysis of offshore wind turbine blade installation
IMT-14-2019	Daniela Myland	Experimental and Theoretical Investigations on the Ship Resistance in Level Ice
IMT-15-2019	Zhengru Ren	Advanced control algorithms to support automated offshore wind turbine installation
IMT-16-2019	Drazen Polic	Ice-propeller impact analysis using an inverse propulsion machinery simulation approach
IMT-17-2019	Endre Sandvik	Sea passage scenario simulation for ship system performance evaluation

IMT-18-2019	Loup Suja-Thauvin	Response of Monopile Wind Turbines to Higher Order Wave Loads
IMT-19-2019	Emil Smilden	Structural control of offshore wind turbines – Increasing the role of control design in offshore wind farm development
IMT-20-2019	Aleksandar-Sasa Milakovic	On equivalent ice thickness and machine learning in ship ice transit simulations
IMT-1-2020	Amrit Shankar Verma	Modelling, Analysis and Response-based Operability Assessment of Offshore Wind Turbine Blade Installation with Emphasis on Impact Damages
IMT-2-2020	Bent Oddvar Arnesen Haugalokken	Autonomous Technology for Inspection, Maintenance and Repair Operations in the Norwegian Aquaculture
IMT-3-2020	Seongpil Cho	Model-based fault detection and diagnosis of a blade pitch system in floating wind turbines
IMT-4-2020	Jose Jorge Garcia Agis	Effectiveness in Decision-Making in Ship Design under Uncertainty
IMT-5-2020	Thomas H. Viuff	Uncertainty Assessment of Wave-and Current-induced Global Response of Floating Bridges
IMT-6-2020	Fredrik Mentzoni	Hydrodynamic Loads on Complex Structures in the Wave Zone
IMT-7-2020	Senthuran Ravinthrakumar	Numerical and Experimental Studies of Resonant Flow in Moonpools in Operational Conditions
IMT-8-2020	Stian Skaalvik Sandøy	Acoustic-based Probabilistic Localization and Mapping using Unmanned Underwater Vehicles for Aquaculture Operations
IMT-9-2020	Kun Xu	Design and Analysis of Mooring System for Semi-submersible Floating Wind Turbine in Shallow Water
IMT-10-2020	Jianxun Zhu	Cavity Flows and Wake Behind an Elliptic Cylinder Translating Above the Wall
IMT-11-2020	Sandra Hogenboom	Decision-making within Dynamic Positioning Operations in the Offshore Industry – A Human Factors based Approach
IMT-12-2020	Woongshik Nam	Structural Resistance of Ship and Offshore Structures Exposed to the Risk of Brittle Failure
IMT-13-2020	Svenn Are Tutturen Værnø	Transient Performance in Dynamic Positioning of Ships: Investigation of Residual Load Models and Control Methods for Effective Compensation
IMT-14-2020	Mohd Atif Siddiqui	Experimental and Numerical Hydrodynamic Analysis of a Damaged Ship in Waves
IMT-15-2020	John Marius Hegseth	Efficient Modelling and Design Optimization of Large Floating Wind Turbines

IMT-16-2020	Asle Natskår	Reliability-based Assessment of Marine Operations with Emphasis on Sea Transport on Barges
IMT-17-2020	Shi Deng	Experimental and Numerical Study of Hydrodynamic Responses of a Twin-Tube Submerged Floating Tunnel Considering Vortex-Induced Vibration
IMT-18-2020	Jone Torsvik	Dynamic Analysis in Design and Operation of Large Floating Offshore Wind Turbine Drivetrains
IMT-1-2021	Ali Ebrahimi	Handling Complexity to Improve Ship Design Competitiveness
IMT-2-2021	Davide Proserpio	Isogeometric Phase-Field Methods for Modeling Fracture in Shell Structures
IMT-3-2021	Cai Tian	Numerical Studies of Viscous Flow Around Step Cylinders
IMT-4-2021	Farid Khazaeli Moghadam	Vibration-based Condition Monitoring of Large Offshore Wind Turbines in a Digital Twin Perspective
IMT-5-2021	Shuaishuai Wang	Design and Dynamic Analysis of a 10-MW Medium-Speed Drivetrain in Offshore Wind Turbines
IMT-6-2021	Sadi Tavakoli	Ship Propulsion Dynamics and Emissions